

Advances in Civil Engineering

# Natural Hazards Challenges to Civil Engineering

Special Issue Editor in Chief: Hugo Rodrigues

Guest Editors: Lars Abrahamczyk, André Barbosa, Haiyun Shi, and Tiago Ferreira





---

# **Natural Hazards Challenges to Civil Engineering**

Advances in Civil Engineering

---

## **Natural Hazards Challenges to Civil Engineering**

Special Issue Editor in Chief: Hugo Rodrigues

Guest Editors: Lars Abrahamczyk, André Barbosa, Haiyun Shi,  
and Tiago Ferreira



---

Copyright © 2019 Hindawi. All rights reserved.

This is a special issue published in “Advances in Civil Engineering.” All articles are open access articles distributed under the Creative Commons Attribution License, which permits unrestricted use, distribution, and reproduction in any medium, provided the original work is properly cited.

## Editorial Board

- Khalid Abdel-Rahman, Germany  
José Aguiar, Portugal  
Reza Akhavian, USA  
Maria Cruz Alonso, Spain  
Serji N. Amirkhanian, USA  
P. Ch. Anastasopoulos, USA  
Venu G. M. Annamdas, Singapore  
Mehrdad Arashpour, Australia  
Pedro Arias-Sánchez, Spain  
Farhad Aslani, Australia  
Daniele Baraldi, Italy  
Emilio Bastidas-Arteaga, France  
Chiara Bedon, Italy  
Rafik Belarbi, France  
Rafael J. Bergillos, Spain  
Giovanni Biondi, Italy  
Hugo C. Biscaia, Portugal  
Giosuè Boscato, Italy  
Melina Bosco, Italy  
Jorge Branco, Portugal  
Emanuele Brunesi, Italy  
Alberto Campisano, Italy  
Francesco Canestrari, Italy  
Paolo Castaldo, Italy  
Giulio Castori, Italy  
Robert Černý, Czech Republic  
Constantin Chalioris, Greece  
Noel Challamel, France  
Daniel W.M. Chan, Hong Kong  
Edwin H W Chan, Hong Kong  
Carlos Chastre, Portugal  
Ghassan Chehab, Lebanon  
Wensu Chen, Australia  
Nicholas Chileshe, Australia  
Heap-Yih (John) Chong, Australia  
Francesco Colangelo, Italy  
Ottavia Corbi, Italy  
Marco Corradi, Italy  
Mario D'Aniello, Italy  
Jorge de Brito, Portugal  
Gianmarco de Felice, Italy  
Stefano de Miranda, Italy  
Tayfun Dede, Turkey  
Angelo Di Egidio, Italy
- Luigi Di Sarno, Italy  
Giulio Dondi, Italy  
Mohamed ElGawady, USA  
Ahmed Elghazouli, UK  
Behzad Esmaeili, USA  
Flora Faleschini, Italy  
Harry Far, Australia  
Antonio Formisano, Italy  
Giovanni Garcea, Italy  
Emilio García-Taengua, UK  
Elhem Ghorbel, France  
Agathoklis Giaralis, UK  
Rodrigo Gonçalves, Portugal  
Arturo Gonzalez, Ireland  
Belén González-Fonteboa, Spain  
Salvatore Grasso, Italy  
Fan Gu, UK  
Kirk Hatfield, USA  
Khandaker Hossain, Canada  
Zahid Hossain, USA  
Mohammad R. Hosseini, Australia  
Bon-Gang Hwang, Singapore  
Dong-Sheng Jeng, Australia  
Jian Ji, China  
Andreas Lampropoulos, UK  
Raffaele Landolfo, Italy  
Eul-Bum Lee, Republic of Korea  
Chun-Qing Li, Australia  
Dongsheng Li, China  
Li Li, Canada  
Xuemei Liu, Australia  
Zaobao Liu, China  
Davide Lo Presti, UK  
Cristiano Loss, Canada  
Sui Pheng Low, Singapore  
Lyan-Ywan Lu, Taiwan  
Eric Lui, USA  
Zhongguo John Ma, USA  
Lorenzo Macorini, UK  
Yann Malecot, France  
John Mander, USA  
Giuseppe Carlo Marano, Italy  
Fabio Mazza, Italy  
Claudio Mazzotti, Italy
- Ahmed Mebarki, France  
Shazim A. Memon, Kazakhstan  
Giovanni Minafò, Italy  
Hossein Moayed, Iran  
Abbas Mohajerani, Australia  
Fabrizio Mollaioli, Italy  
Rosario Montuori, Italy  
Ayman S. Mosallam, USA  
Roberto Nascimbene, Italy  
Luís C. Neves, UK  
Trung Ngo, Australia  
Sanjay Nimbalkar, Australia  
Giuseppe Oliveto, Italy  
Alejandro Orfila, Spain  
Togay Ozbakkaloglu, Australia  
Hayri Baytan Ozmen, Turkey  
Alessandro Palmeri, UK  
Fabrizio Paolacci, Italy  
Fulvio Parisi, Italy  
Arnaud Perrot, France  
Christophe Petit, France  
Giuseppe Piccardo, Italy  
Prodromos Psarropoulos, Greece  
Giuseppe Quaranta, Italy  
Carlo Rainieri, Italy  
Damien Rangeard, France  
Dimitris Rizos, USA  
Geoffrey W. Rodgers, New Zealand  
Hugo Rodrigues, Portugal  
Hamid Reza Ronagh, Australia  
Pier Paolo Rossi, Italy  
Lukasz Sadowski, Poland  
Anna Saetta, Italy  
Timo Saksala, Finland  
Evangelos J. Sapountzakis, Greece  
Vasilis Sarhosis, UK  
Halil Sezen, USA  
M. Shahria Alam, Canada  
Faiz U.A. Shaikh, Australia  
Mostafa Sharifzadeh, Australia  
Sanjay Kumar Shukla, Australia  
Amir Si Larbi, France  
Stefano Sorace, Italy  
Flavio Stochino, Italy



---

Claudio Tamagnini, Italy  
Yaya Tan, China  
Patrick W.C. Tang, Australia  
Yinshan Tang, UK  
Huu-Tai Thai, Australia  
Filippo Ubertini, Italy  
Humberto Varum, Portugal  
Castorina S. Vieira, Portugal  
C. Vipulanandan, USA  
Claudia Vitone, Italy  
Hao Wang, USA

Lei Wang, USA  
Linbing Wang, USA  
Wayne Yu Wang, UK  
Roman Wan-Wendner, Austria  
Bo Xia, Australia  
Wei-Chau Xie, Canada  
Michael Yam, Hong Kong  
Libo Yan, Germany  
Jian Yang, China  
Xu Yang, Australia  
Hui Yao, China

Victor Yepes, Spain  
Gürol Yildirim, Turkey  
Qingliang Yu, Netherlands  
Mariano Angelo Zanini, Italy  
Xiong Zhang, USA  
Yuqing Zhang, UK  
Dong Zhao, USA  
Xianbo Zhao, Australia  
Annan Zhou, Australia  
Abdul Aziz bin Abdul Samad, Malaysia

# Contents

## **Natural Hazards Challenges to Civil Engineering**

Hugo Rodrigues , Lars Abrahamczyk , André R. Barbosa, Haiyun Shi, and Tiago Miguel Ferreira   
Editorial (2 pages), Article ID 4365075, Volume 2019 (2019)

## **Seismic Stability Analysis of Saturated and Unsaturated Soil Slopes Using Permanent Displacement**

Shuai Huang  and Yanju Peng   
Research Article (9 pages), Article ID 1786392, Volume 2018 (2019)

## **Development of Empirical Fragility Curves in Earthquake Engineering considering Nonspecific Damage Information**

Jung J. Kim   
Research Article (13 pages), Article ID 6209137, Volume 2018 (2019)

## **Probabilistic Prediction of Maximum Tensile Loads in Soil Nails**

Yongqiang Hu and Peiyuan Lin   
Research Article (12 pages), Article ID 3410146, Volume 2018 (2019)

## **Rapid Disaster Data Dissemination and Vulnerability Assessment through Synthesis of a Web-Based Extreme Event Viewer and Deep Learning**

P. Shane Crawford , Mohammad A. Al-Zarrad, Andrew J. Graettinger, Alexander M. Hainen, Edward Back, and Lawrence Powell  
Research Article (13 pages), Article ID 7258156, Volume 2018 (2019)

## **Error Source Analysis and Precision Assessment of Limit Equilibrium Methods for Rock Slopes**

Xiaofan An , Ning Li , Peng Zhang, and Wenbo Sun  
Research Article (13 pages), Article ID 3280734, Volume 2018 (2019)

## **Landslide Susceptibility Mapping in Darjeeling Himalayas, India**

Amit Chawla , Sowmiya Chawla, Srinivas Pasupuleti , A. C. S. Rao, Kripamoy Sarkar, and Rajesh Dwivedi  
Research Article (17 pages), Article ID 6416492, Volume 2018 (2019)

## **Reproducing Field Measurements Using Scaled-Down Hydraulic Model Studies in a Laboratory**

Seung Oh Lee and Seung Ho Hong   
Research Article (11 pages), Article ID 9091506, Volume 2018 (2019)

## **Heat Treatment and Ventilation Optimization in a Deep Mine**

Xingxin Nie , Xiaobin Wei , Xiao Chen Li, and Caiwu Lu   
Research Article (12 pages), Article ID 1529490, Volume 2018 (2019)

## **Probabilistic Analysis of Weathered Soil Slope in South Korea**

Taeho Bong and Younghwan Son   
Research Article (12 pages), Article ID 2120854, Volume 2018 (2019)

**Beneficial and Detrimental Effects of Soil-Structure Interaction on Probabilistic Seismic Hazard and Risk of Nuclear Power Plant**

Shinyoung Kwag, BuSeog Ju , and Wooyoung Jung 

Research Article (18 pages), Article ID 2698319, Volume 2018 (2019)

**Can Repetitive Small Magnitude-Induced Seismic Events Actually Cause Damage?**

Oliver-Denzil S. Taylor , Alanna P. Lester, Theodore A. Lee III, and Mihan H. McKenna

Review Article (5 pages), Article ID 2056123, Volume 2018 (2019)

**Seismic Response of Tunnel Lining for Shallow-Bias Tunnel with a Small Clear Distance under Wenchuan Earthquake**

Yang Hui , Jiang Xueliang, and Lian Pengyuan

Research Article (10 pages), Article ID 2578062, Volume 2018 (2019)

**A Modified Newmark Methodology for Permanent Deformation Analysis of Rock-Fill Dams**

Hongjun Li , Hong Zhong, Zuwen Yan, and Jianming Zhao

Research Article (10 pages), Article ID 3129471, Volume 2018 (2019)

## Editorial

# Natural Hazards Challenges to Civil Engineering

**Hugo Rodrigues** <sup>1</sup>, **Lars Abrahamczyk** <sup>2</sup>, **André R. Barbosa**,<sup>3</sup> **Haiyun Shi**,<sup>4</sup>  
**and Tiago Miguel Ferreira** <sup>5</sup>

<sup>1</sup>RISCO, Polytechnic Institute of Leiria, Leiria, Portugal

<sup>2</sup>EDAC/GRK1462, Bauhaus-Universität Weimar, Weimar, Germany

<sup>3</sup>School of Civil and Construction Engineering, Oregon State University, Oregon, USA

<sup>4</sup>The University of Hong Kong, Pokfulam, Hong Kong

<sup>5</sup>ISISE, Institute of Science and Innovation for Bio-Sustainability (IB-S), Department of Civil Engineering, University of Minho, Guimarães, Portugal

Correspondence should be addressed to Hugo Rodrigues; hugo.f.rodrigues@ipleiria.pt

Received 13 December 2018; Accepted 14 December 2018; Published 27 March 2019

Copyright © 2019 Hugo Rodrigues et al. This is an open access article distributed under the Creative Commons Attribution License, which permits unrestricted use, distribution, and reproduction in any medium, provided the original work is properly cited.

In recent decades, research on natural hazards has moved into a new era driven by the rise of new technologies and techniques with potential use in risk assessment, management, and mitigation. Nevertheless, in spite of these significant advances, it is recognised that the effects of natural hazards are rapidly increasing in frequency and extension, having to be understood in the context of an unprecedentedly complex and populated world. To tackle this global issue, there is a central need for developing basic and applied multidisciplinary research that can lead to the development and implementation of more efficient risk mitigation strategies.

The present special issue contributes to this goal by gathering a diverse set of recent studies, which provide original papers and review articles addressing the current challenges related to natural hazards linked, when possible, with climate change adaptation and their impacts on applications in planning, design, construction, and management of the built environment, and mitigations to reduce the effects of natural hazards. The collection of papers also aims to present the effects of individual natural hazards as well as their relationships with other correlated and uncorrelated hazards and study the vulnerability and resilience of the built environment when subjected to multiple hazards, with a particular focus on future challenges to civil engineering.

This special issue focuses on the civil engineering procedures that promote safety assessment of the built

environment when subjected to natural hazard events. The natural hazard events considered are concurrent, isolated, or correlated events, such as wind and surge; cascading events, such as landslides following earthquakes; and extreme events, occurring at different timescales along the infrastructure life time, such as earthquakes and wind.

A total of 48 papers were submitted, from which a total of 12 papers have been finally selected to integrate the present issue, which underscores the need, interest, and importance of this special issue topic.

The topics addressed in the papers are from several fields across civil engineering, including the analysis of the response of infrastructure such as dams, tunnels, nuclear power plants, mines, and buildings to different hazards. In addition, topics covered relate to the analysis of soil and soil-structure interaction, landslides, and lastly the study of seismic hazards using different analytical and computational approaches.

The editorial team is sure that the papers reflect significant contributions to the research and development in the various topics addressed. We hope that readers will find all articles of the special issue useful and exciting and that the articles will stimulate further research activities in the area of damage assessment, risk mitigation, and the new and complex challenges in natural hazards and their impacts on civil engineering.

**Conflicts of Interest**

The guest editors have no conflicts of interest regarding the publication of this special issue.

*Hugo Rodrigues*  
*Lars Abrahamczyk*  
*André R. Barbosa*  
*Haiyun Shi*  
*Tiago Miguel Ferreira*

## Research Article

# Seismic Stability Analysis of Saturated and Unsaturated Soil Slopes Using Permanent Displacement

Shuai Huang  and Yanju Peng 

*Institute of Crustal Dynamics, China Earthquake Administration, Beijing 100085, China*

Correspondence should be addressed to Shuai Huang; [huangshuai3395@163.com](mailto:huangshuai3395@163.com)

Received 20 August 2018; Revised 2 November 2018; Accepted 28 November 2018; Published 19 December 2018

Academic Editor: Hugo Rodrigues

Copyright © 2018 Shuai Huang and Yanju Peng. This is an open access article distributed under the Creative Commons Attribution License, which permits unrestricted use, distribution, and reproduction in any medium, provided the original work is properly cited.

The permanent displacement has been widely used for slope seismic stability in practical engineering; however, the effect of the dynamic pore water pressure on the saturated and unsaturated soil slopes could not be neglected. In this paper, we propose a calculation method of dynamic pore water pressure by the hollow cylinder apparatus (GCTS) which is the most advanced and complicated device in lab testing on soil dynamics. Then, based on the proposed calculation method of dynamic pore water pressure combined with the limit equilibrium and finite element methods, we introduce a simple calculation method of permanent displacement, which avoids solving complex nonlinear equations and greatly simplifies the computational effort. Shaking table test results demonstrate the effectiveness and efficiency of the simple calculation method of permanent displacement, which could rapidly assess the soil slope seismic stability considering the effect of dynamic pore water pressure.

## 1. Introduction

The landslide induced by earthquake is a common geological disaster. According to preliminary statistics, more than 15,000 landslides were triggered by the Wenchuan earthquake [1]. The slopes which were designed in accordance with the seismic codes were still destroyed a lot, and a series of new features appeared in slope failure. How to prevent the failure of slope under earthquake has become one of the key techniques in slope stability analysis [2, 3]. Safety factor is often used for the slope stability evaluation at present. In fact, the slope is considered to be damaged when the safety factor is less than 1. And at this time, the slope may be in a new equilibrium, which is common in practical engineering. Thus, the safety factor will not be used for further evaluation of the slope stability when it is less than 1. Fortunately, the permanent displacement of the slope is accumulated when the safety factor is less than 1. And permanent displacement could evaluate the slope stability when the safety factor is less than 1. In addition, with the further research on slope dynamic stability, the dynamic stability evaluation method using the single

seismic coefficient has been found to be insufficient. The core issue of seismic resistance of geotechnical structures has gradually transformed from the strength standard into the deformation standard. The seismic design method based on deformation is currently one of the important design theories. Thus, permanent displacement is more suitable for slope seismic stability, and how to use permanent displacement for accurate assessment of the slope stability needs further research.

Different soil slopes affected by different rainfall amounts are in different groundwater levels during the earthquake or aftershocks, and the slopes suffered from a combination of factors, including earthquake and groundwater. Seismic stability evaluation methods of slopes are the core of the slope seismic stability analysis. Therefore, it is especially important to use a reasonable safety evaluation method for slope seismic stability analysis. At present, the slope stability analysis methods mainly include the quasi-static method, Newmark sliding block method, and time-history method. The quasi-static method [4] transforms the dynamic problem into a static problem by using the dynamic coefficient, which avoids the solution

of complex nonlinear equations and greatly simplifies the computational effort. The horizontal and vertical inertial forces transformed from dynamic loads act on the center of the slope gravity, and the safety factor can be calculated fast by the quasi-static method. The quasi-static method has been widely used in engineering projects and written into the regulations in many countries. However, seismic wave characteristics, such as vibration frequency and duration of earthquake, were not considered in the quasi-static method [5]. The time-history method [6] is used to analyze the dynamic property of the slope during the seismic process considering the soil dynamic property and seismic characters. And the dynamic safety factors of the slope could be calculated under earthquake. However, the instability criterion is mostly solved by statistical methods, such as the average safety coefficient method and reliability dynamic safety factor method. How to evaluate the slope stability with dynamic safety factors at different times of earthquake action needs further research. The Newmark sliding block method [7] was first put forward by Newmark, and the soil was assumed as the ideal one which is a rigid, perfectly plastic body. The yield acceleration of the landslide mass is a constant. The landslide mass tends to start sliding when the seismic accelerations exceed the yield acceleration. Then, the permanent displacement can be obtained by a double integration of the portions of the acceleration time-history exceeding the yield acceleration [8]. Rabie [9] researched the slope stability based on the quasi-static method and time-history method and found that the quasi-static method is more conservative for slope stability analysis; Lu et al. [10] researched the seismic stability of a three-dimensional slope using the permanent displacement and found that permanent displacement was more reasonable for slope stability analysis. Therefore, in this study, the seismic stability of the soil slope is evaluated by permanent displacement. Great attention will be paid to the issue of seismic stability of the saturated and unsaturated soil slopes using permanent displacement considering the influence of the groundwater level.

In recent years, a large number of landslide disaster cases especially the slope failure phenomena in the Wenchuan earthquake show that the current evaluation method of slope stability could not meet the safety performance evaluation of the slope. The design method based on deformation is one of the most important theories of seismic design [11, 12]. The study for slope stability using permanent displacement is the hot issue in slope seismic response analysis, and the traditional method for evaluating the soil slope stability has many limits. Marzorati et al. [13] and Carro et al. [14] completed the seismic and landslide zoning maps of Umbria and Marche regions with the Newmark permanent displacement prediction model. Bray and Travasarou [15] proposed a fully coupled permanent displacement calculation method considering the dynamic effect of the slope. Shenglin et al. [16] proposed an algorithm for seismic permanent displacement of the slope considering structural surface degradation. Han et al. [17] analyzed the permanent displacement of the slope and found that the

variation curve of the permanent displacement has a threshold value, and the permanent displacement increased and then became stable when the acceleration values were greater than the threshold value. Liu and Kong [18] calculated the permanent displacement of the slope using discontinuous deformation analysis; however, certain simplification has been made on the method. Although some research has been done on the slope stability using the permanent displacement, the effect of the dynamic pore water pressure under earthquake on the permanent displacement was neglected. The effect of the dynamic pore water pressure on the saturated or unsaturated soil slope stability is significant [19]. Thus, a soil slope located in Inner Mongolia Autonomous Region in China was selected to investigate the seismic stability analysis using permanent displacement.

## 2. Calculation Model of the Slope

*2.1. Establishing the Slope Model.* An actual slope which is along the Zhunshuo railway in Inner Mongolia Autonomous Region in China is selected as the research object, as shown in Figure 1. The soil types of the slope are mainly sandy. The groundwater level changes with the season, and the mean water level is above 2.0 m. The slope length is 17 m, the slope height is 12 m, and the slope angle is 35°.

The slope model in reference [20] is referred and established with the finite element software MIDAS GTS NX 2018, and the height of the finite element model is twice the slope height, as shown in Figure 2. In order to reduce the error of the calculation results, the maximum finite element mesh size is smaller than 1/10~1/8 of the input seismic wavelength. The Mohr–Coulomb constitutive model is adopted in this study. The free field boundaries are used for the model boundaries.

The calculation parameters of the slope model are obtained by the indoor test and referenced in the *Geotechnical Engineering Handbook* [21], as shown in Table 1.

*2.2. Sliding Failure Evaluation Index of the Slope.* By comparison of the slope codes of the earthquake-prone countries (China, Japan, European countries, and California in the United States), evaluation methods of the slope seismic stability in different specifications were determined at home and abroad, as shown in Table 2.

By comparing slope codes in different countries, we used the safety factor and permanent displacement to evaluate the slope stability, which are closer to the actuals.

*2.3. Numerical Procedure.* Referring to Japanese *Specifications for Highway Bridges*, we used three real recorded seismic waves, including T1-II-1 which is a far-field seismic wave, T2-II-1 which is a near-field seismic wave, and El Centro seismic wave, to analyze the slope stability, as shown in Table 3. The peak acceleration values of the three seismic waves are scaled to 0.21 g, while the frequencies remain unchanged, as shown



FIGURE 1: Engineering field figure.

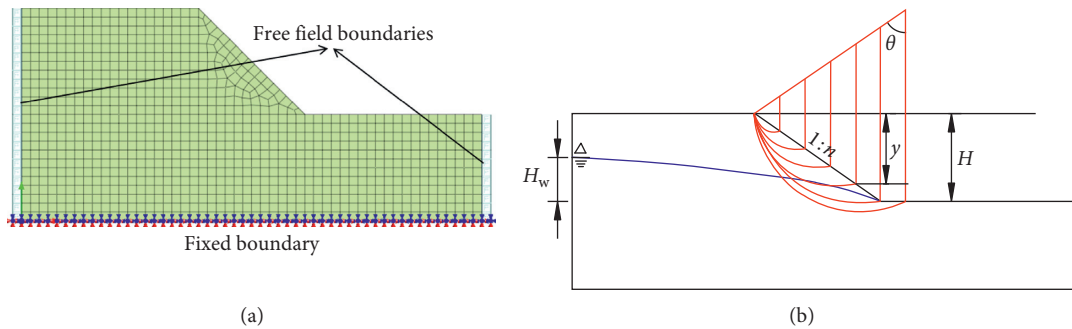


FIGURE 2: Analysis model of the slope (reproduced from the study of Huang et al. [20], under the Creative Commons Attribution License/public domain).

TABLE 1: Calculation parameters of the model.

Soil type	Gravity ( $\text{kN}\cdot\text{m}^{-3}$ )	Poisson's ratio	Elastic modulus (MPa)	Friction angle ( $^\circ$ )	Cohesion (kPa)	Permeability coefficient ( $\text{cm}\cdot\text{s}^{-1}$ )	Saturated water content (%)
Sandy	17.5	0.3	50.4	35.23	11.42	$5\text{e-}5$	30

TABLE 2: Slope codes of the earthquake-prone countries.

Nation	Codes	Evaluation methods	Evaluation indicators
China	“Technical code for building slope engineering” (GB50330-2013)	Quasi-static method [22, 23]	Safety factor
	“Design code for engineered slopes in water resources and hydropower projects” (SL386-2007)	Quasi-static method	Safety factor
	“Specifications for design of highway Subgrades” (JTG D30-2004)	Quasi-static method	Safety factor
	“Code for seismic design of railway engineering” (GB50111-2006)	Quasi-static method	Safety factor
	“Code for design on subgrade of railway” (TB10001-2005)	Quasi-static method	Safety factor
	“Code for design of high speed railway” (TB10621-2009)	Quasi-static method	Safety factor
Japan	“Design standards for railway structures”	Quasi-static method and Newmark method	Safety factor and permanent displacement
European countries	Eurocode 7: geotechnical design	Quasi-static method	Safety factor
California in the United States	California Geological Survey’s guidelines (2008)	Quasi-static method	Safety factor

TABLE 3: Parameters of the earthquake motions.

Seismic wave	Recorded location	Earthquake name	Magnitude	Epicentral distance (km)
T1-II-1	Foundation of Itajima bridge	Hyūganada earthquake (1968)	7.5	100
El Centro	El Centro	Emperor Valley earthquake (1940)	7.7	12
T2-II-1	JR Takatori station	Kobe (1995)	7.2	16

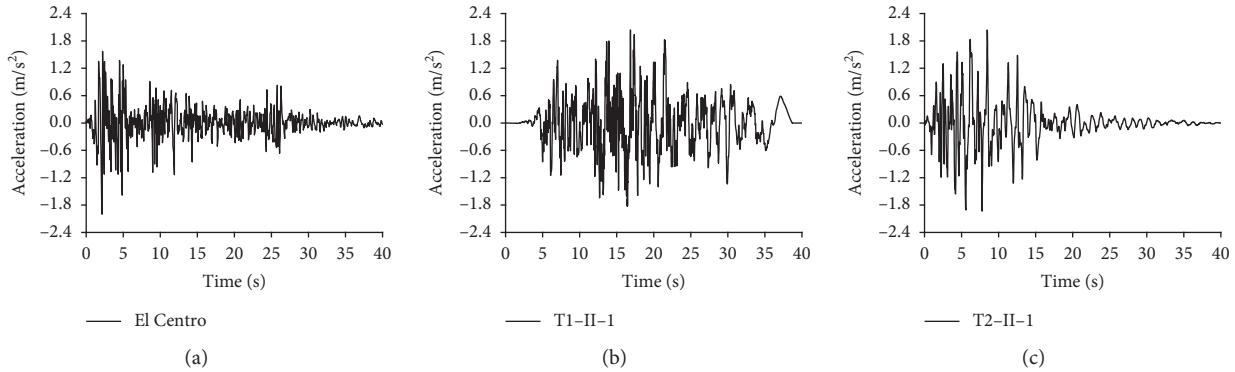


FIGURE 3: Time-history of earthquakes (reproduced from the study of Huang et al. [20], under the Creative Commons Attribution License/public domain).

in Figure 3. The earthquake motions are used as the horizontal excitations and input from the fixed bottom boundary.

Different factors are changed, respectively, on the basis of the original slope. Effects of various factors including slope rates, slope heights, groundwater levels, peak accelerations, and earthquake types on the safety factor and the permanent displacement of the slope are studied, as shown in Table 4.

### 3. Fitting Relationship of Permanent Displacement and Safety Factor

**3.1. Determination of Permanent Displacement.** The permanent displacement is calculated by the finite element method at a certain groundwater level considering the effect of the large deformation nonlinearity. And we calculated the permanent displacement of the slope under El Centro (2 m/s<sup>2</sup>) at the groundwater level 5 m, as shown in Figure 4.

As shown in Figure 4, we could calculate the permanent displacement affected by different factors using the finite element method considering the effect of the large deformation nonlinearity. And the maximum permanent displacement of the slope under El Centro is 5.2 cm, when the groundwater level is 5 m.

**3.2. Determination of the Safety Factor Calculation Method considering Dynamic Pore Water Pressure.** Generation of the dynamic pore water pressure is mainly caused by the changes in the deviatoric stress and the average effective stress. Thus, the maximum dynamic pore water pressure could be calculated by the deviatoric stress and the average effective stress of the soil, as shown in Table 5. The dynamic hollow cylinder torsional shear test is carried out by the American dynamic hollow cylinder apparatus (GCTS), as shown in Figure 5.

TABLE 4: Numerical procedure.

Slope rate	Slope height (m)	Underground water level $H_w$ (m)	Peak acceleration (m·s <sup>-2</sup> )	Seismic waves
1 : 1.5	12	5	2, 3, 4, 5, 6, 7, 8, 9, 10	El Centro
1 : 1.4	12	5	4, 5, 6	El Centro
1 : 1.5	12	5	4, 5, 6	
1 : 1.6	12	5	4, 5, 6	
1 : 1.5	12	7	4, 5, 6	El Centro
	12	8	4, 5, 6	
1 : 1.5	12	5	4, 5, 6	El Centro
	24	10	4, 5, 6	El Centro
	36	15	4, 5, 6	El Centro
1 : 1.5	12	5	4, 5, 6	El Centro, T1-II-1, T2-II-1

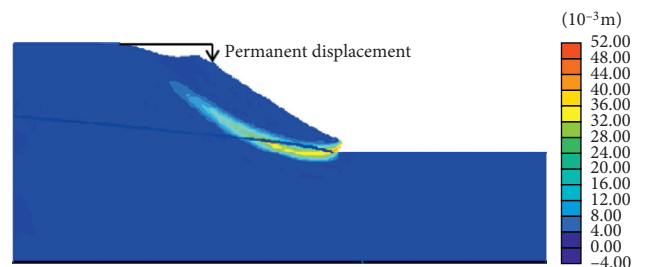


FIGURE 4: Permanent displacement calculated by the finite element method.

The relations of the maximum dynamic pore water pressure and the maximum deviatoric stress and the average effective stress under different earthquakes and sine waves are analyzed, as shown in Figures 5 and 6.

TABLE 5: Test results under earthquakes and sine waves.

Vertical stress (kPa)	Soil compaction			Seismic waves	Working condition			Cycle times
	Horizontal stress (kPa)	Average effective stress (kPa)	Initial deviatoric stress (kPa)		Maximum deviatoric stress (kPa)	Stress ratio	Dynamic pore water pressure (kPa)	
300	150	200	150	T1-II-1	56.02	0.09	24	2
255	170	198	85	El Centro	51.56	0.26	25	2
300	150	200	150		62.36	0.10	29	2
255	170	198	85		40.01	0.20	16	2
300	150	200	150	T2-II-1	57.96	0.10	26	2
255	170	198	85	Sine wave 1 Hz	48.27	0.24	23	2
300	150	200	150		70.73	0.12	35	2
255	170	198	85		59.21	0.30	30	2
300	150	200	150	Sine wave 2 Hz	57.5	0.095	25	2
255	170	198	85	Sine wave 3 Hz	40.51	0.20	17	2
300	150	200	150		58.60	0.098	26	2
255	170	198	85		50.90	0.26	24	2
300	150	200	150	Sine wave 4 Hz	66.42	0.098	32	2
255	170	198	85	Sine wave 5 Hz	52.70	0.27	26	2
300	150	200	150		57.47	0.096	25	2
255	170	198	85		48.87	0.25	23	2
300	150	200	150	Sine wave 6 Hz	52.47	0.13	28	2

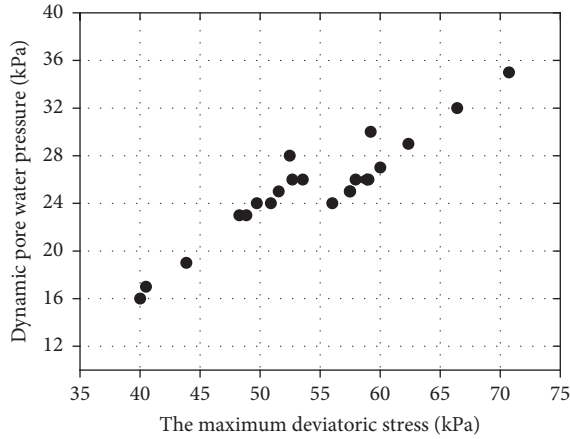


FIGURE 5: Relationship curve of the maximum dynamic pore water pressure and the maximum deviatoric stress.

As shown in Figures 5 and 6, the maximum dynamic pore water pressure increases linearly with the increasing maximum deviatoric stress, while the maximum dynamic pore water pressure is decreasing with the increasing average effective stress.

Through the nonlinear regression analysis, the simple calculation method of the maximum dynamic pore water pressure could be obtained, as shown in the following equation:

$$\Delta u = 9 - 0.07\sigma'_{pj} + 0.7(\sigma'_y - \sigma'_x)_d, \quad (1)$$

where  $\Delta u$  is the maximum dynamic pore water pressure,  $\sigma'_{pj}$  is the average effective stress, and  $(\sigma'_y - \sigma'_x)_d$  is the maximum deviatoric stress.

The simple calculation method of the maximum dynamic pore pressure is plugged into the limit equilibrium

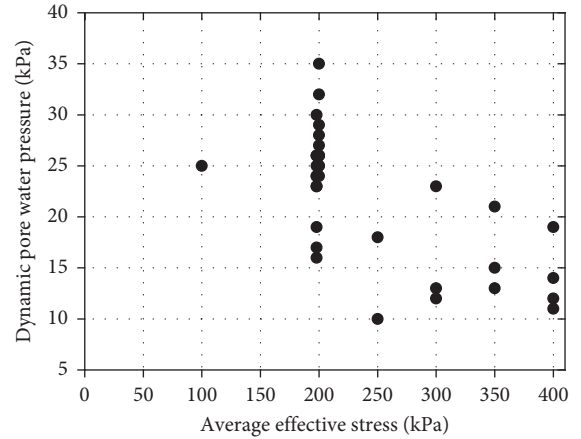


FIGURE 6: Relationship curve of the maximum dynamic pore water pressure and the average effective stress.

equation, and the safety factor which could consider the effect of the dynamic pore pressure is obtained, as shown in Figure 7 and equation (2).

By analyzing the stress state of the isolator in the slope, the limit equilibrium method is shown as follows:

$$F_s = \frac{\sum\{c'L(W \cos \theta - u_0L - \Delta uL - WK_h \sin \theta)\tan \varphi\}}{\sum(W \sin \theta + WK_h \cos \theta)}, \quad (2)$$

where  $F_s$  is the safety factor;  $W$  is the weight of the free body;  $\theta$  is the slope angle;  $\varphi$  is the internal friction angle;  $c'$  is the cohesion;  $L$  is the length of the free body parallel to the slope;  $u_0$  is the hydrostatic pressure;  $\Delta u$  is the maximum dynamic pore pressure;  $K_h$  is the horizontal seismic coefficient,  $K_h = a/g$ ;  $N$  is the normal stress of the sliding plane including the normal stress produced by  $W \cos \theta$ ,  $WK_h \sin \theta$ ,

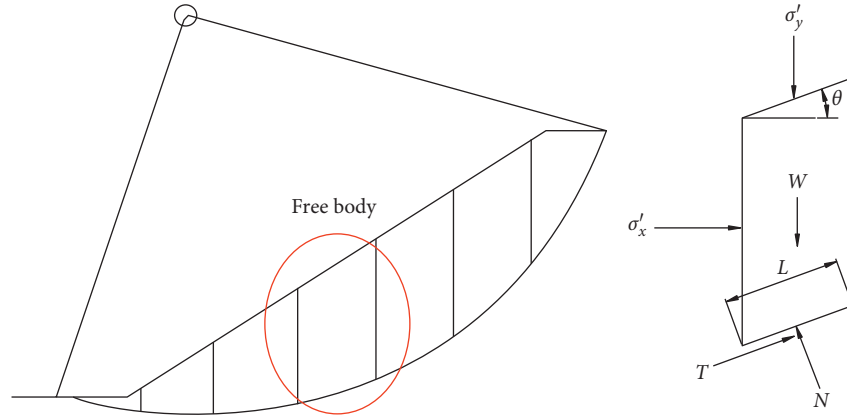


FIGURE 7: Stress state of a free body in the slope.

$u_0$ , and  $\Delta u$ ; and  $T$  is the tangential stress of the sliding plane including the tangential stress produced by  $c'L$ ,  $W \sin \theta$ , and  $WK_h \cos \theta$ .

By using balance equation (2) of the free body,  $\sigma'_y$  and  $\sigma'_x$  could be obtained, as shown in the following equations:

$$\sigma'_y = (W \cos \theta - u_0 L) + \left( \frac{(W \sin \theta + W' \sin \theta)(1 - \cos 2\theta)}{\sin 2\theta} \right), \quad (3)$$

$$\sigma'_x = (W \cos \theta - u_0 L) + \left( \frac{(W \sin \theta + W' \sin \theta)(1 + \cos 2\theta)}{\sin 2\theta} \right), \quad (4)$$

where  $W'$  is the thrust of the upper soil to the lower soil.

By using equations (3) and (4), equations (5) and (6) could be obtained:

$$\sigma'_{pj} = \frac{(\sigma'_y + 2\sigma'_x)}{3} = (2(W \cos \theta - u_0 L)) - \left( \frac{\{(W \sin \theta + W' \sin \theta) + 3(W \sin \theta + W' \sin \theta) \cos 2\theta\}}{\sin 2\theta} \right), \quad (5)$$

$$(\sigma'_y - \sigma'_x)_d = \frac{2WK_h \cos \theta}{\sin 2\theta}. \quad (6)$$

Equations (5) and (6) are plugged into equation (1), and the maximum dynamic pore pressure  $\Delta u$  could be obtained. Then,  $\Delta u$  is plugged into equation (2), and the limit equilibrium method considering the effect of the maximum dynamic pore water pressure is obtained.

**3.3. Simple Calculation Method of the Permanent Displacement.** Fitting relationship of the permanent displacement and safety factor is shown in Figure 8.

As shown in Figure 8, the safety factor and the permanent displacement change exponentially with the different factors. And the permanent displacements decrease with the increasing safety factor. By fitting analysis of the permanent displacement

and the safety factor, the relationship between the permanent displacement and the safety factor could be obtained.

Thus, fitting relationship of the permanent displacement and the safety factor could be obtained, as shown in the following equation:

$$\delta_{\max} = 1000e^{-6.6F_s} - 2, \quad (7)$$

where  $\delta_{\max}$  is the permanent displacement of the slope and  $F_s$  is the safety factor of the slope.

Equation (7) considers the influence of peak acceleration, slope height, slope rate, groundwater levels, and spectrum characteristics of the seismic wave, so the permanent displacement could be calculated by this method, which could provide the reference for the seismic reinforcement of engineering designers.

#### 4. Application Analysis of the Permanent Displacement of a Slope

In order to determine the accuracy of the proposed simple calculation method, a shaking table test of a small soil slope is carried out, as shown in Figure 9. The detailed test process can be obtained by referring to reference [20]. The groundwater levels of the slope model are 0 m, 0.6 m, 0.7 m, and 0.8 m. The length, width, and height of the model are 1.96 m, 0.96 m, and 1.4 m. The slope ratio is 1:1.5. We use sponge to reduce the seismic reflectance, and the sponge thickness is 20 mm.

In this study, a one-way shaking table (ES-15/KE-2000) is used for testing. There are four technical indicators in this equipment. The maximum test load and acceleration are 5000 kg and 20 m/s<sup>2</sup>, respectively. The rated speed is 0.5 m/s. And the equipment is shown in Figure 10.

The permanent displacements are obtained from the shaking table test under T1-II-1 when the peak acceleration value is 0.4 g, as shown in Figure 11.

As shown in Figure 11, the slope starts to slide at the groundwater level 0.6 m, and the safety factor is less than 1 at this time. Permanent displacement reaches the maximum value until the groundwater level is 0.8 m. The slope

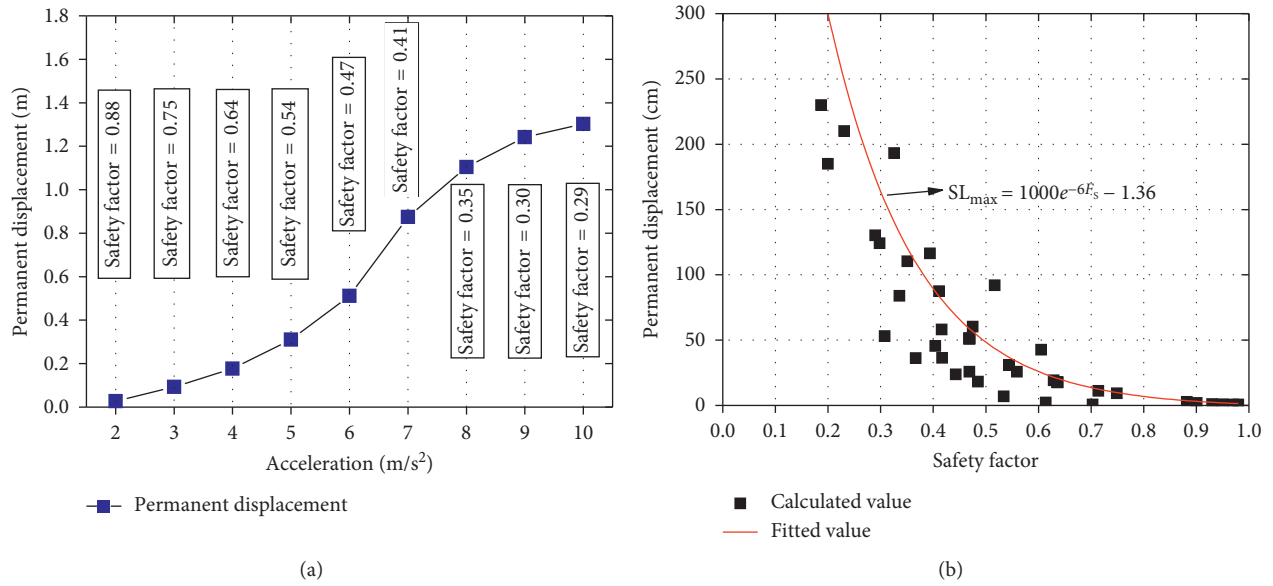


FIGURE 8: (a) Relationship of the safety factor and the peak acceleration. (b) Fitting relationship of the permanent displacement and safety factor.

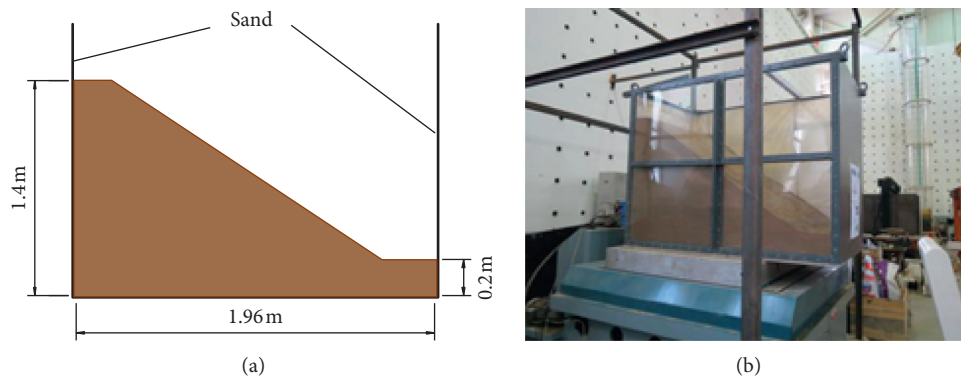


FIGURE 9: The small slope model (reproduced from the study of Huang et al. [20], under the Creative Commons Attribution License/public domain).



FIGURE 10: Vibration equipment (reproduced from the study of Huang et al. [20], under the Creative Commons Attribution License/public domain).

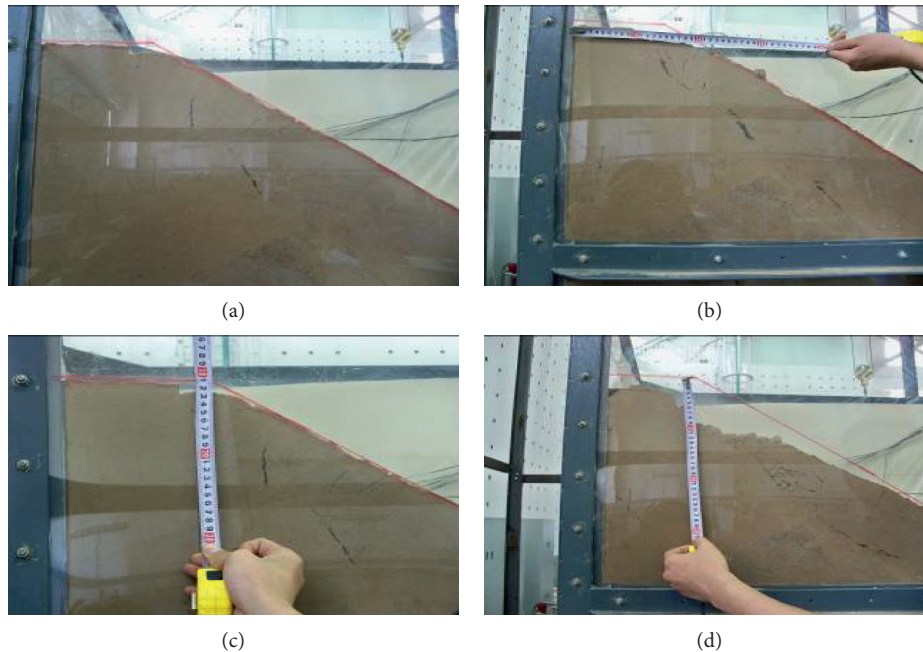


FIGURE 11: Permanent displacements during the test. (a)  $H_w = 0$  m. (b)  $H_w = 0.6$  m. (c)  $H_w = 0.7$  m. (d)  $H_w = 0.8$  m.

just slides but it does not collapse, and the slope is in a new equilibrium, which is usual in practical engineering. The safety factor will not be used for further evaluation of the slope stability when it is less than 1; however, the permanent displacement of the slope is accumulated. Therefore, the permanent displacement could be used for further evaluation of the slope stability. It is found that, with the increasing groundwater levels, the permanent displacement increases. The permanent displacement values will be 3.8 cm, 5.2 cm, and 8.3 cm, respectively, when the groundwater levels are 0.6 m, 0.7 m, and 0.8 m. It shows that the effect of the groundwater level on the permanent displacement should be paid more attention, and certain definitive steps should be taken to maintain the stability of the slope.

The permanent displacement obtained from the shaking table test is compared with that calculated by the simple calculation method, as shown in Figure 12.

As shown in Figure 12, the permanent displacements increase with the increasing groundwater levels. The permanent displacement obtained from the shaking table test at the groundwater level 0.8 m is about 4.0 times the permanent displacement at the groundwater level 0 m, which shows that the increase of the groundwater level has a significant effect on the permanent displacement of the slope. Also, we found that the permanent displacements obtained by the simple calculation method are greater than the permanent displacements obtained from the shaking table test. The maximum deviation value obtained from the two methods, respectively, is within 18% when the groundwater level is 0.8 m. Therefore, the simple calculation method is feasible, and it could be used to calculate the permanent displacement of the soil slope in different groundwater levels.

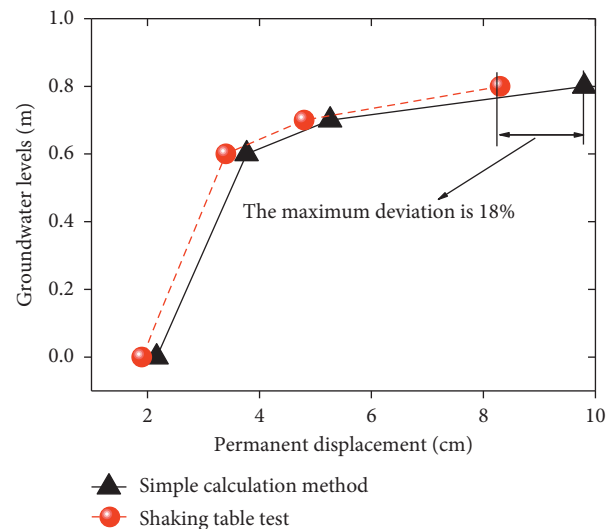


FIGURE 12: Permanent displacements of different methods.

## 5. Conclusion

The aim of this research is to lay a foundation for the stability evaluation of the saturated and unsaturated soil slopes using permanent displacement. A series of dynamic hollow cylinder torsional shear tests were conducted under different confining and deviatoric stresses, and a calculation method of dynamic pore water pressure associated with deviatoric and average effective stresses is proposed. The calculation method avoids the solution of complex nonlinear equations and greatly simplifies the computational effort.

Based on the proposed calculation method of dynamic pore water pressure combined with the limit equilibrium and finite element methods, we introduced a simple

calculation method of permanent displacement, which could provide a reference to the slope seismic reinforcement for engineering designers and be used as a rapid assessment method to the slope seismic stability. Unlike traditional calculation methods of permanent displacement, the proposed calculation method considered the effect of the dynamic pore water pressure.

The superior performance of the simple calculation method of the permanent displacement was demonstrated based on the shaking table test. The shaking table test results indicated that the calculation method could rapidly assess the seismic stability of the soil slope considering the effect of dynamic pore water pressure. The permanent displacement values obtained from the simple calculation method were greater than the permanent displacement values obtained from the shaking table test; however, the maximum deviation was within 18%, which verified the simple calculation method is feasible.

### Data Availability

The data used to support the findings of this study are included within the article.

### Conflicts of Interest

There are no conflicts of interest regarding the publication of this paper.

### Acknowledgments

This work was financially supported by the Beijing Natural Science Foundation (Grant No. 8174078), National Natural Science Foundation of China (Grant No. 51708516), and National Key R&D Program of China (2017YFC1500404) and the research grant from Institute of Crustal Dynamics, China Earthquake Administration (No. ZDJ2016-12).

### References

- [1] Y. Yin, "Features of landslide triggered by the Wenchuan earthquake," *Journal of Engineering Geology*, vol. 17, no. 1, pp. 30–38, 2009.
- [2] S. A. Sepúlveda, W. Murphy, R. W. Jibson, and D. N. Petley, "Seismically induced rock slope failures resulting from topographic amplification of strong ground motions: the case of Pacoima canyon, California," *Engineering Geology*, vol. 80, no. 3/4, pp. 336–348, 2005.
- [3] E. Eberhardt, K. Thuro, and M. Luginbuehl, "Slope instability mechanisms in dipping interbedded conglomerates and weathered marls—the 1999 Ruffin landslide, Switzerland," *Engineering Geology*, vol. 77, no. 1/2, pp. 35–56, 2005.
- [4] L. Liu, Z. Lei, and F. Zhou, "The evaluation of seismic slope stability analysis methods," *Journal of Chongqing Jiaotong University*, vol. 20, no. 3, pp. 83–88, 2001.
- [5] Z. ping Fan and Li hua Zhang, "Analysis on slope stability during earthquake," *Northwestern Seismological Journal*, vol. 32, no. 4, pp. 339–343, 2010.
- [6] H. Liu, F. Kang, and Y. Gao, "Time history analysis method of slope seismic stability," *Rock and Soil Mechanics*, vol. 24, no. 4, pp. 553–560, 2003.
- [7] N. M. Newmark, "Effects of earthquakes on dams and embankments," *Géotechnique*, vol. 15, no. 2, pp. 139–160, 1965.
- [8] A. Liu, Z. Lu, T. X. Liu, and L. Yang, "Study seismic slope permanent displacements with dynamic critical acceleration," *China Earthquake Engineering Journal*, vol. 39, no. 5, pp. 876–882, 2017.
- [9] M. Rabie, "Comparison study between traditional and finite element methods for slopes under heavy rainfall," *HBRC Journal*, 2014, In press.
- [10] K. Lu, D. Zhu, Y. Zhu et al., "Preliminary study of seismic permanent displacement of 3D slope," *Rock and Soil Mechanics*, vol. 32, no. 5, pp. 1425–1429, 2011.
- [11] W. Randall, "Jibson. Methods for assessing the stability of slopes during earthquakes—A retrospective," *Engineering Geology*, vol. 122, pp. 43–50, 2011.
- [12] E. M. Rathje and G. Antonakos, "A unified model for predicting earthquake-induced sliding displacements of rigid and flexible slopes," *Engineering Geology*, vol. 122, no. 1-2, pp. 51–60, 2011.
- [13] S. Marzorati, L. Luzi, and M. De Amicis, "Rock falls induced by earthquakes: a statistical approach," *Soil Dynamics and Earthquake Engineering*, vol. 22, no. 7, pp. 565–577, 2002.
- [14] M. Carro, M. De Amicis, L. Luzi, and S. Marzorati, "The application of predictive modeling techniques to landslides induced by earthquakes: the case study of the 26 September 1997 Umbria-Marche earthquake (Italy)," *Engineering Geology*, vol. 69, no. 1-2, pp. 139–159, 2003.
- [15] J. D. Bray and T. Travasarou, "Simplified procedure for estimating earthquake-induced deviatoric slope displacements," *Journal of Geotechnical and Geoenvironmental Engineering*, vol. 133, no. 4, pp. 381–392, 2007.
- [16] Q. Shenglin, Q. Shengwen, W. Faquan et al., "On permanent displacement of earthquake induced slide based on residual pushing force method," *Journal of Engineering Geology*, vol. 12, no. 1, pp. 63–68, 2004.
- [17] J. Han, W. Lv, and Y. Ou, "Study on analysis method for permanent displacement of slope under seismic action," *Subgrade Engineering*, vol. 4, pp. 37–41, 2016.
- [18] J. Liu and X. Kong, "Seismic stability and permanent displacement analysis of a solid waste landfill slope containing geomembrane," *Rock and Soil Mechanics*, vol. 25, no. 5, pp. 778–782, 2004.
- [19] S. Malla, "Consistent application of horizontal and vertical earthquake components in analysis of a block sliding down an inclined plane," *Soil Dynamics and Earthquake Engineering*, vol. 101, pp. 176–181, 2017.
- [20] S. Huang, Y. Lv, Y. Peng et al., "Permanent displacement analysis of soil slope considering dynamic pore water pressure under severe earthquakes," *Electronic Journal of Geotechnical Engineering*, vol. 20, no. 4, pp. 1529–1539, 2015s.
- [21] *Geotechnical Engineering Handbook Editorial Board. Geotechnical Engineering Handbook*, China Architecture & Building Press, Beijing, China, 4th edition, 2007.
- [22] S. L. Kramer, *Geotechnical Earthquake Engineering*, Prentice-Hall, Upper Saddle River, NJ, USA, 1995.
- [23] H. Liu, B. Jingshan, and D. Liu, "Development on study of seismic stability evaluation methods of rock-soil slopes," *Journal of Institute of Disaster-Prevention Science and Technology*, vol. 9, no. 3, pp. 20–27, 2007.

## Research Article

# Development of Empirical Fragility Curves in Earthquake Engineering considering Nonspecific Damage Information

Jung J. Kim 

*Professor, Department of Civil Engineering, Kyungnam University, Changwon-si 51767, Republic of Korea*

Correspondence should be addressed to Jung J. Kim; [jungkim@kyungnam.ac.kr](mailto:jungkim@kyungnam.ac.kr)

Received 3 September 2018; Revised 4 November 2018; Accepted 11 November 2018; Published 13 December 2018

Guest Editor: Tiago Ferreira

Copyright © 2018 Jung J. Kim. This is an open access article distributed under the Creative Commons Attribution License, which permits unrestricted use, distribution, and reproduction in any medium, provided the original work is properly cited.

As a function of fragility curves in earthquake engineering, the assessment of the probability of exceeding a specific damage state according to the magnitude of earthquake can be considered. Considering that the damage states for fragility curves are generally nested to each other, the possibility theory, a special form of the evidence theory for nested intervals, is applied to generate fragility information from seismic damage data. While the lognormal distributions are conventionally used to generate fragility curves due to their simplicity and applicability, the methodology to use the possibility theory does not require the assumption of distributions. Seismic damage data classified by four damage levels were used for a case study. The resulted possibility-based fragility information expressed by two monotone measures, “possibility” and “certainty,” are compared with the conventional fragility curves based on probability. The results showed that the conventional fragility curves provide a conservative estimation at the relatively high earthquake magnitude compared with the possibility-based fragility information.

## 1. Introduction

In earthquake engineering, fragility curves have been used to estimate damages of infrastructures according to the magnitude of earthquake. While fragility curves can provide reasonable estimation of earthquake damages with damage levels, those might neglect the possible slight damage occurrence at the relatively low earthquake magnitude due to the nature of probability density functions consists of two parameters, expected mean value and dispersion.

Traditionally, probability theory has been used to model uncertainties in structural engineering, especially when addressing reliability for structural safety [1, 2]. However, the types of uncertainties considered in probability theory are random, chance, and likelihood, and there are limitations to model other types of uncertainties such as nonspecificity, fuzziness, and strife, using probability theory [3, 4]. Random uncertainty known as aleatory uncertainty is from inherent randomness and therefore is irreducible. However, other types of uncertainties known as epistemic uncertainties arise from lack of knowledge and therefore are reducible and subjective. Research on generalized information theory (GIT)

[5, 6] showed that three types of epistemic uncertainties due to lack of knowledge and/or variability thrive when modeling complex environments [7]. While nonspecificity represents the difficulty to choose from many modeling alternatives, fuzziness represents the uncertainty due to lack of sharpness (imprecise boundaries) of the modeling parameter. Strife expresses the uncertainty due to conflict among alternatives. Given are there various types of uncertainties, appropriate modeling of uncertainty has been an interesting and challenging topic in many areas during the last few decades [8–10]. A number of theories to model uncertainties adequately have been introduced: evidence theory [11, 12], possibility theory [3, 13] and fuzzy set theory [14, 15].

In earthquake engineering, empirical fragility curves were generally presented in the form of lognormal cumulative distribution function (CDF) with respect to peak ground acceleration (PGA) representing the ground motion intensity due to earthquake [16]. To generate empirical fragility curve for a damage state, the damage reports by experts are used. The damage reports usually present the damage states in linguistic ways such as “no damage,” “slight damage,” “moderate damage,” “extensive damage,” and

“collapse” for a structure experiencing earthquake of a PGA. As the fragility curve of a damage state represents the fragility of “at least” of the damage level, the evidence for a damage state includes possible higher damage states. For example, the evidence for “moderate damage” of a structure by an earthquake means that the structure is damaged at least moderately, and it might be possible for the structure to be damaged extensively or collapsed. As there exist ambiguous boundaries between the damage states, fuzzy logic and possibility theory were applied to resolve the ambiguity [17, 18].

Recently, extensive earthquake damage data are used to generate fragility curves [19–25]. Postearthquake surveys of approximately 340000 reinforced concrete structures were used to derive fragility curves for a European seismic risk assessment scenario [19]. A database of 7597 reinforced concrete buildings located in the city and the province of L’Aquila in Italy was used in order to derive fragility curves [20]. The observed damage to 9500 of low-rise residential buildings from earthquakes in South Iceland was studied by typological fragility curves [21]. Moreover, fragility curves were developed from millions of data on the basis of 665,515 building damage cases by earthquake in Nepal [22, 23]. In Italy, the postearthquake damage surveys of approximately 90,000 buildings in order to derive fragility curves were considered [24, 25]. Even with the increase of damage data to generate fragility curves, there is still an uncertainty of nonspecificity, the difficulty to choose from many modeling functions of fragility curves such as lognormal, extreme type I, extreme type II functions, and so on.

In this study, the evidence of damage state is dealt with possibility theory. It is noticeable that the fragility curves from possibility distribution representing the certainty of damage state and those are generated without any assumption of distributions. Therefore, there is no uncertainty of nonspecificity to choose functions of fragility curves.

## 2. Possibility Information in Fragility Curves

Theories for modeling uncertainties present different types of uncertainty assignment and monotone measures. As uncertainty assignment terms, the degree of belief, probability distribution, and possibility distribution are used for evidence theory, probability theory, and possibility theory, respectively. To quantify the assigned uncertainties, monotone measures are used such as dual monotone measures of plausibility and belief, dual monotone measures of possibility and certainty, and single monotone measure of probability for evidence theory, probability theory, and possibility theory, respectively [26–28]. Considering the relationship between uncertainty assignment terms and monotone measures used for each theory, it can be known as probability theory and possibility theory are special forms of evidence theory [6]. Consider a discrete universe  $D$  that consists of a set of damage levels,

$$D = \{d_N, d_S, d_M, d_E, d_C\}, \quad (1)$$

where  $d_N$ ,  $d_S$ ,  $d_M$ ,  $d_E$ , and  $d_C$  represent no damage, slight damage, moderate damage, extensive damage, and collapse of a structure due to a seismic force level respectively.

In evidence theory, which is also known as Dempster–Shafer theory [11, 12], the degree of belief  $m$  based on evidence is assigned to all countable subsets  $A$  (e.g.,  $\emptyset, \{d_N\}, \{d_N, d_S\}, \dots, \{d_N, \dots, d_C\}$ ) with the constraint of

$$\sum_{A \subset D} m(A) = 1. \quad (2)$$

Dual monotone measures, belief  $\text{bel}(A)$  and plausibility  $\text{pl}(A)$ , for a subset  $A$  are calculated as

$$\text{bel}(A) = \sum_{B \in A} m(B), \quad (3)$$

$$\text{pl}(A) = \sum_{B \cap A \neq \emptyset} m(B). \quad (4)$$

While belief measure represents the degree of evidence for a subset  $A$ , plausibility measure is defined as “Complement of the belief of the complement of a subset  $A$ ” as

$$\text{pl}(A) = 1 - \text{bel}(\bar{A}). \quad (5)$$

As belief measure is based on the degree of belief with its evidence, belief measure of “Complement of a subset  $A$ ” also needs its evidence. Therefore, if there is no evidence for “Complement of a subset  $A$ ,” one cannot determine the belief of “Complement of a subset  $A$ ” as  $1 - \text{bel}(A)$ . The difference between these two measures can represent our ignorance (lack of knowledge) of a subset  $A$  (denoted  $\text{ign}$ ) as

$$\text{ign}(A) = \text{pl}(A) - \text{bel}(A) = 1 - [\text{bel}(\bar{A}) + \text{bel}(A)]. \quad (6)$$

In probability theory, probability distribution, which is equivalent to the degree of belief  $m$  in evidence theory, is assigned to a single variable (e.g.  $d_N, \dots, d_C$ ) on universe  $D$  such as

$$\sum_{d_i \in D} p(d_i) = 1, \quad (7)$$

where  $d_i$  denotes the damage state,  $d_N, d_S, d_M, d_E$ , and  $d_C$ . Only one monotone measure, probability  $\text{prob}(A)$ , for a subset  $A$  is defined as

$$\text{prob}(A) = \sum_{d_i \in A} p(d_i), \quad (8)$$

and probability measure of “Complement of a subset  $A$ ” is defined as

$$\text{prob}(\bar{A}) = 1 - \text{prob}(A), \quad (9)$$

with the *excluded middle axioms* [4]. Unlike evidence theory, “Complement of a subset  $A$ ” can be determined as  $1 - \text{prob}(A)$ . Therefore, our lack of knowledge measured by  $\text{ign}(A)$  in equation (6) cannot be measured in probability theory.

In possibility theory, possibility distribution  $\pi$  is assigned to a single damage level in possibility theory such as

$$\pi(d_i) = \sum_{d_i \in A} m(A), \quad (10)$$

$$\max\{\pi(d_i)\} = 1.$$

The relationship between the uncertainty assignment  $\pi$  and the degree of belief  $m$  in equation (10) indicates that possibility theory is a special form of evidence theory when the collective body of evidence is consonant [26–28] (see Figure 1).

Dual monotone measures, certainty  $\text{cert}(A)$  and possibility  $\text{pos}(A)$ , for a subset  $A$  are determined as

$$\text{pos}(A) = \sup\{\pi(d_i) : x_i \in A\}, \quad (11)$$

$$\text{cert}(A) = 1 - \text{pos}(\bar{A}). \quad (12)$$

This relationship can be converted to a single measure that represents the degree of confirmation  $C(A)$  of a subset  $A$ , whose range is from  $-1$  to  $1$  [5]:

$$C(A) = \text{cert}(A) + \text{pos}(A) - 1. \quad (13)$$

Negative value of the degree of confirmation expresses the degree of disconfirmation of a subset  $A$ . It is noticeable that the assignment of possibility distribution of 1 to a single variable means that the occurrence of the variable is possibly 1 but certainly “no evidence,” while the assignment of degree of possibility of zero confirms that the occurrence of the variable is possibly zero and certainly zero. For a consonant body of evidence, the following relationship for two different subsets,  $A$  and  $B$ , can be proven [6]:

$$\text{pos}(A \cup B) = \max[\text{pos}(A), \text{pos}(B)], \quad (14)$$

$$\text{cert}(A \cap B) = \min[\text{cert}(A), \text{cert}(B)]. \quad (15)$$

When the ignorance in equation (6) is zero, the *excluded middle axioms* are satisfied and the evidence can be described using one monotone measure called the probability measure. Moreover, when body of evidence is consonant, monotone measures in evidence theory, belief and plausibility, can be represented as those in possibility theory, certainty and possibility, respectively (see Appendix for examples).

As the fragility curve of a damage state represents the fragility of “at least” of the damage level, probable damage information for higher damage state is included in a damage state. For example, the evidence for “no damage” means that a structure seems undamaged, but there might be possible damages for the structure: slight, moderate, extensive, or collapsed damages. Considering the characteristics of evidence, “at least,” we can define subsets  $N, S, M, E$ , and  $C$  for “at least no damage,” “at least slight damage,” “at least moderate damage,” “at least extensive damage,” and “at least collapse” as shown in equation (16). It can be recognized that a damage subset includes higher than and equal to the damage levels.

$$\begin{aligned} N &= \{d_N, d_S, d_M, d_E, d_C\}, \\ S &= \{d_S, d_M, d_E, d_C\}, \\ M &= \{d_M, d_E, d_C\}, \\ E &= \{d_E, d_C\}, \\ C &= \{d_C\}. \end{aligned} \quad (16)$$

It is seen that the subsets in equation (16) are nested to each other such as  $C \subset E \subset M \subset S \subset N$ . Based on the degree

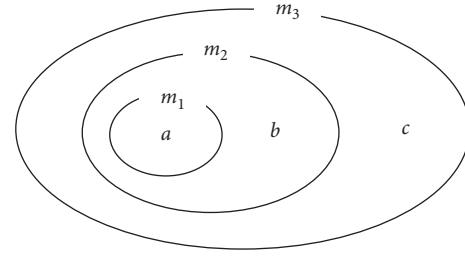


FIGURE 1: Consonant body of evidence.

of belief,  $m$  is assigned to a consonant set of damage levels, possibility distributions for predetermined PGA region are generated using the assignment of the degree of belief. The sequence of monotone measures of each damage level with respect to PGA is presented and compared with conventional fragility curves generated by maximum likelihood estimation. It is noticeable that the evidence for at least no damage,  $N$ , is considered as any damage level.

### 3. Case Study

A schematic representation of the proposed framework to generate fragility curves using possibility distributions is shown in Figure 2. At the first step, the empirical damage data are rearranged in the shape of binomial damage data for damage states. In this step, the damage data are rearranged in the ascending order with respect to PGA. As this procedure is out of scope of this study, the arranged data by other researchers [16] are used for case study. Some part of the arranged data is presented in Table 1. Using the arranged data set, PGA intervals are determined based on the inclusion of damage levels at the second step. At the third step, the degree of belief  $m$  is assigned to the sets in equation (16) based on the occurrence of damage levels in each PGA interval. At the fourth step, possibility distribution is generated based on the degree of belief. At the final step, monotone measures for PGA intervals are calculated and the sequence of monotone measures with respect to PGA is determined.

For the case study, the damage data of bridges from the 1994 Northridge earthquake are used to develop empirical fragility curves [16]. The PGA value at the location of bridges is interpolated and extrapolated from the PGA data [16]. The binomial damage information of damage states “no damage,” “at least minor,” “at least moderate,” “at least major,” and “collapse” in original reference [16] are used to generate possibility-based empirical fragility curves of “no damage fragility curve,” “slight damage fragility curve,” “moderate damage fragility curve,” “extensive damage fragility curve,” and “collapse fragility curve,” respectively, in this study.

For the comparison, the binomial information for the damage state at PGA is used to generate empirical fragility curves by maximum likelihood estimation with the assumption of lognormal and extreme type I and II distributions. The results of the four families of fragility curves are presented in Figure 3.

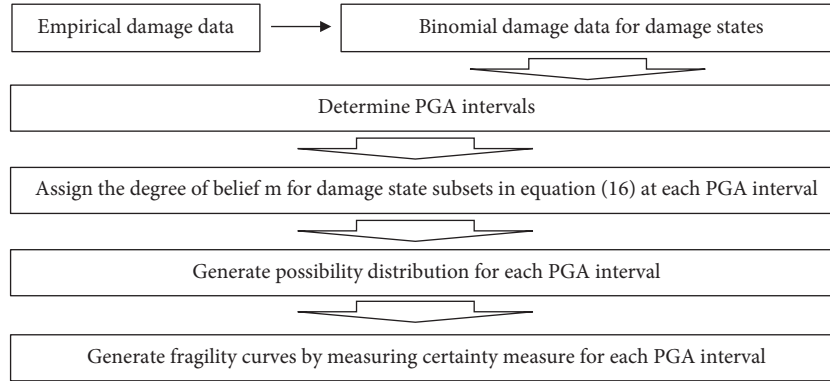


FIGURE 2: Procedure to generate empirical fragility curves using possibility distributions.

TABLE 1: Some part of the arranged binomial data to generate empirical fragility curves for the case study [16].

No.	PGA	None	$\geq$ Min	$\geq$ Mod	$\geq$ Maj	$\geq$ Col	First appearance
1	0.069	1	0	0	0	0	
⋮	⋮	⋮	⋮	⋮	⋮	⋮	
57	0.079	1	0	0	0	0	
⋮	⋮	⋮	⋮	⋮	⋮	⋮	
62	0.080	1	1	0	0	0	Minor damage
⋮	⋮	⋮	⋮	⋮	⋮	⋮	
397	0.137	1	0	0	0	0	
⋮	⋮	⋮	⋮	⋮	⋮	⋮	
415	0.138	1	1	1	0	0	Moderate damage
⋮	⋮	⋮	⋮	⋮	⋮	⋮	
1303	0.322	1	0	0	0	0	
⋮	⋮	⋮	⋮	⋮	⋮	⋮	
1307	0.323	1	1	1	1	0	Major damage
⋮	⋮	⋮	⋮	⋮	⋮	⋮	
1555	0.384	1	0	0	0	0	
⋮	⋮	⋮	⋮	⋮	⋮	⋮	
1561	0.385	1	1	1	1	1	Collapse
⋮	⋮	⋮	⋮	⋮	⋮	⋮	
1859	0.680	1	1	1	1	0	
1860	0.682	1	1	1	0	0	
1861	0.682	1	1	1	1	1	Collapse
⋮	⋮	⋮	⋮	⋮	⋮	⋮	
1998	0.889	1	1	1	1	0	

## 4. Results and Discussions

From the binomial information of damage state data, PGA intervals are determined based on the inclusion of damage levels and presented in Table 2. For the last PGA interval, it is divided into two regions as the first collapse evidence at PGA of 0.385 g seems possible, but the next evidence is far from the PGA such as 0.682 g. During the 0.385 g to 0.682 g, as there is no evidence for collapse, the PGA interval is divided for engineering sense.

Based on the occurrence of damage levels in each PGA interval, the degree of belief  $m$  is assigned to the sets in equation (16) and presented in Table 3. The possibility distributions for each PGA intervals are generated as shown in Figure 4. The possibility distribution  $\pi$  values for each

damage level are calculated based on the degree of belief and presented in Table 4. For example,  $\pi$  for  $d_M$  for the interval [0.385, 0.680] is calculated as the summation of the degree of belief for  $N$ ,  $S$ ,  $M$  in the respective interval of Table 3. It follows the definition of  $\pi$  as presented in equation (10).

Using the generated possibility distributions in Figure 4, monotone measures for  $N$ ,  $S$ ,  $M$ ,  $E$ , and  $C$  can be measured. An example to measure the dual monotone measures in possibility theory, certainty  $\text{cert}(M)$  and possibility  $\text{pos}(M)$ , for  $M$  of the interval [0.323, 0.384] is presented in Figure 5. The maximum possibility distribution  $\pi$  inside of the interval will be the measure of  $\text{pos}$  as 100% as defined in equation (11) and the complement of the maximum possibility distribution  $\pi$  outside of the interval will be the measure of  $\text{cert}$  as 8% as defined in equation (12). The *degree of confirmation* is calculated using the dual monotone measures as 8% as shown in equation (13). The certainty and possibility measures are presented in Tables 5 and 6, respectively. It is noticeable that the belief and plausibility measures for the sets in equation (16) are same with the certainty and possibility measures, respectively, as possibility theory is a special form of evidence theory. The belief and plausibility measures in evidence theory are presented in Tables 7 and 8.

As the possibility measures for all intervals are 100% as presented in Table 6, the degree of confirmation is going to be the same with the certainty measure in Table 5. The empirical fragility curves can be constructed by plotting certainty or the degree of confirmation with respect to the corresponding intervals as shown in Figure 6.

Comparisons with the conventional fragility curves that generated by assuming a distribution are presented in Figures 7–10. It is noticeable that the caption for  $y$ -axis in the figures, “fragility” represents “probability” in probability theory and “certainty” in possibility theory. For the comparison of “Slight” damage state as shown in Figure 7, the conventional fragility curves underestimate the failure probability at the PGA interval between 0.323 g and 0.5 g. For the comparison of “Moderate” and “Extensive” damage states as shown in Figures 8 and 9, respectively, the conventional fragility curves underestimate the failure probability at the PGA interval between 0.385 g and 0.5 g. Finally,

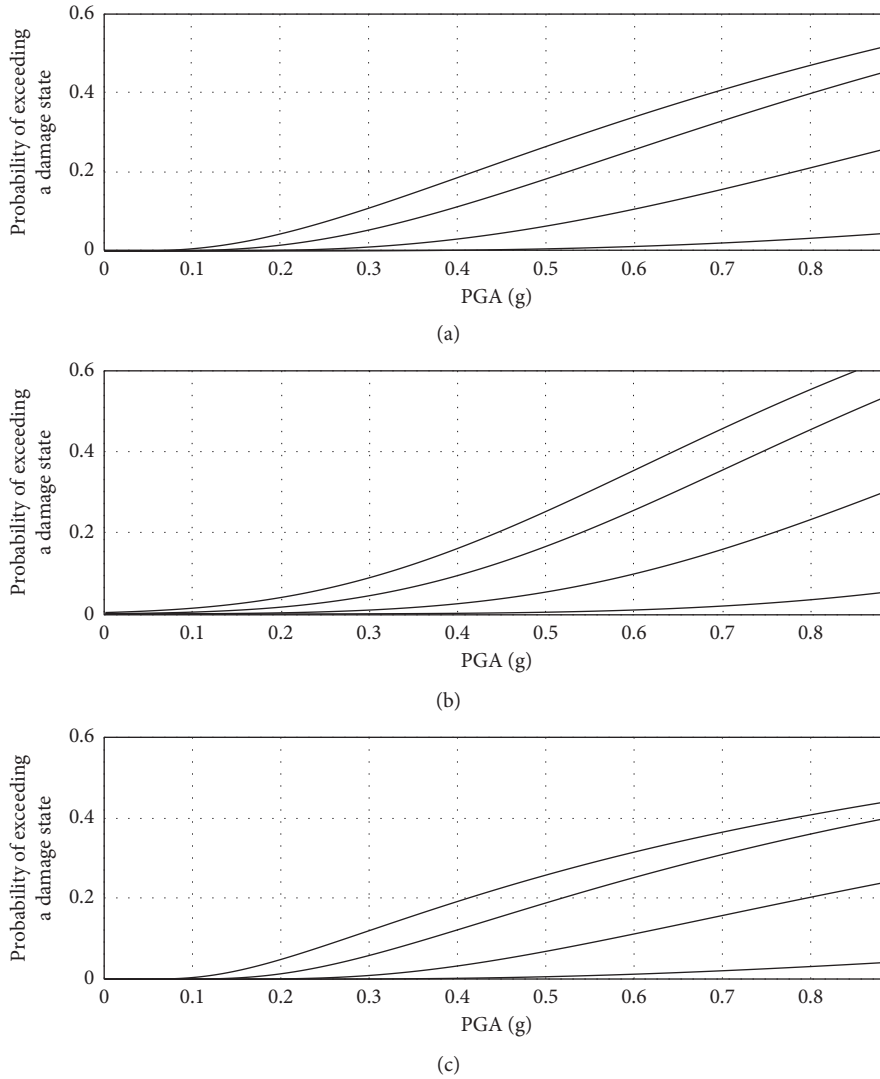


FIGURE 3: Empirical fragility curves determined by maximum likelihood estimation using different distribution functions. At each figure, curves from top to bottom are fragility curves for damage state subsets of  $S$ ,  $M$ ,  $E$ , and  $C$ , respectively. (a) Lognormal CDF. (b) Extreme type I (Gumbel) CDF. (c) Extreme type II (Frechet) CDF.

TABLE 2: Number of damage information at each damage state in PGA intervals.

PGA interval (g) $[\theta_1, \theta_2]$	None ( $N$ )	Slight ( $S$ )	Moderate ( $M$ )	Extensive ( $E$ )	Collapse ( $C$ )	No. of evidence
[0.069, 0.079]	56	0	0	0	0	56
[0.080, 0.137]	350	8	0	0	0	358
[0.138, 0.322]	862	14	16	0	0	892
[0.323, 0.384]	205	24	14	6	0	249
[0.385, 0.680]	221	23	39	20	1	304
[0.682, 0.889]	74	14	25	21	5	139
Sum	1768	83	94	47	6	1998

for the comparison of “Collapse” damage state as shown in Figure 10, the conventional fragility curves underestimate the failure probability at the PGA interval between 0.682 g and 0.8 g. While there is no evidence for damage over the PGA of 0.889 g, the conventional fragility curves for all damage states clearly overestimate the failure probability over the PGA of 0.889 g. These results are obvious as the

conventional fragility curves are generated by assuming the distributions with mathematical formulations such as log-normal and extreme type I and type II distributions.

With extensive earthquake damage database, the uniform PGA interval, so called as “PGA bin,” can be used instead of the PGA intervals determined by experts in Table 2. In this case, the shape of fragility curve also can be

TABLE 3: Degree of belief  $m$  based on the fraction of each damage state in PGA intervals.

PGA interval (g) $[\theta_1, \theta_2]$	None (N)	Slight (S)	Moderate (M)	Extensive (E)	Collapse (C)	Sum
[0.069, 0.079]	1.000	0.000	0.000	0.000	0.000	1.000
[0.080, 0.137]	0.978	0.022	0.000	0.000	0.000	1.000
[0.138, 0.322]	0.966	0.016	0.018	0.000	0.000	1.000
[0.323, 0.384]	0.823	0.096	0.056	0.024	0.000	1.000
[0.385, 0.680]	0.727	0.076	0.128	0.066	0.003	1.000
[0.682, 0.889]	0.532	0.101	0.180	0.151	0.036	1.000

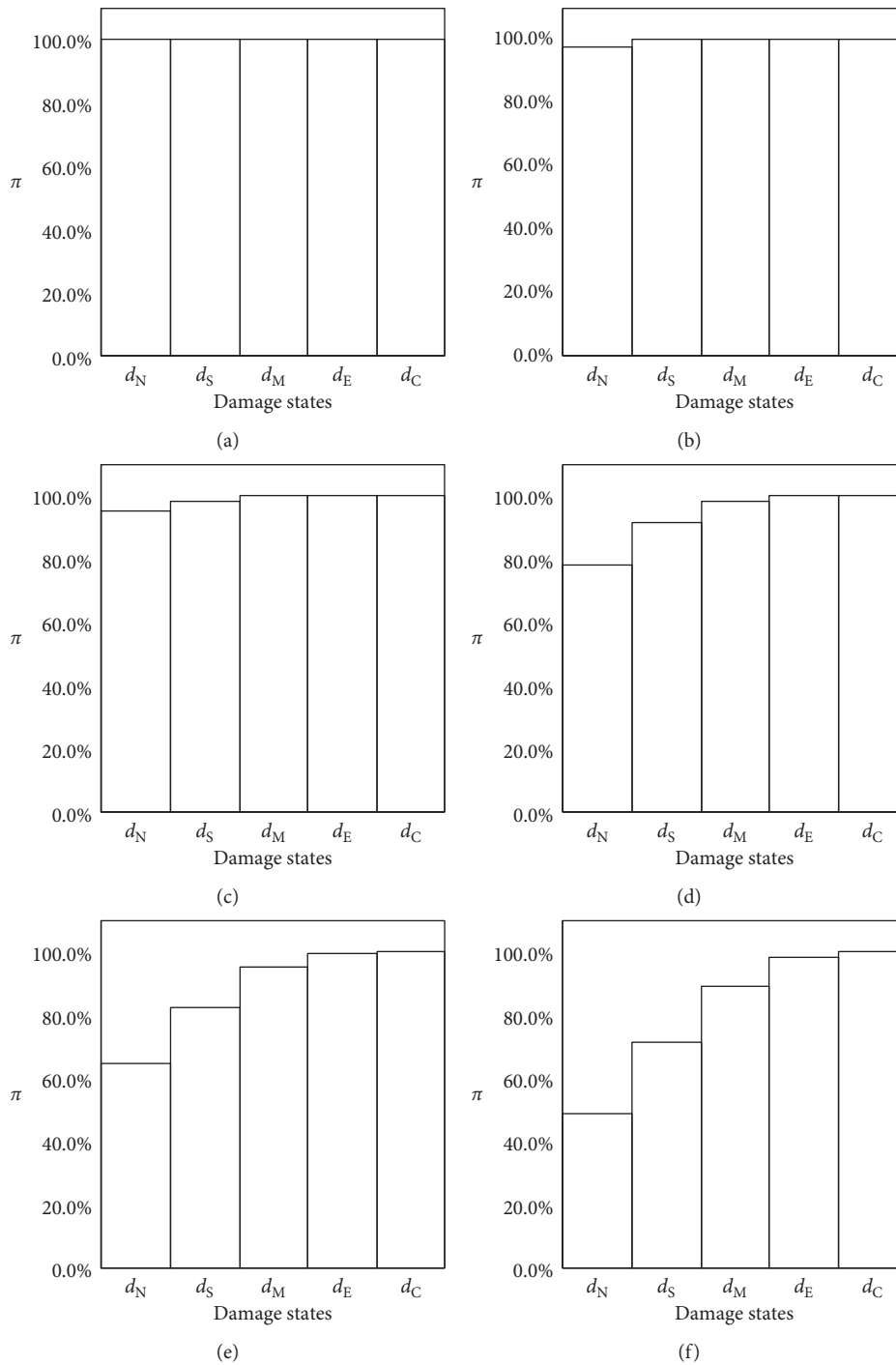


FIGURE 4: Possibility distributions of damage states for the corresponding PGA (g) intervals. (a) [0.069, 0.079]g. (b) [0.080, 0.137]g. (c) [0.138, 0.322]g. (d) [0.323, 0.384]g. (e) [0.385, 0.680]g. (f) [0.682, 0.889]g.

TABLE 4: Assigning  $\pi$  based on the degree of belief  $m$  in Table 3.

PGA interval (g) $[\theta_1, \theta_2]$	$d_N$ (%)	$d_S$ (%)	$d_M$ (%)	$d_E$ (%)	$d_C$ (%)	Max. (%)
[0.069, 0.079]	100.0	100.0	100.0	100.0	100.0	100
[0.080, 0.137]	97.8	100.0	100.0	100.0	100.0	100
[0.138, 0.322]	96.6	98.2	100.0	100.0	100.0	100
[0.323, 0.384]	82.3	92.0	97.6	100.0	100.0	100
[0.385, 0.680]	72.7	80.3	93.1	99.7	100.0	100
[0.682, 0.889]	53.2	63.3	81.3	96.4	100.0	100

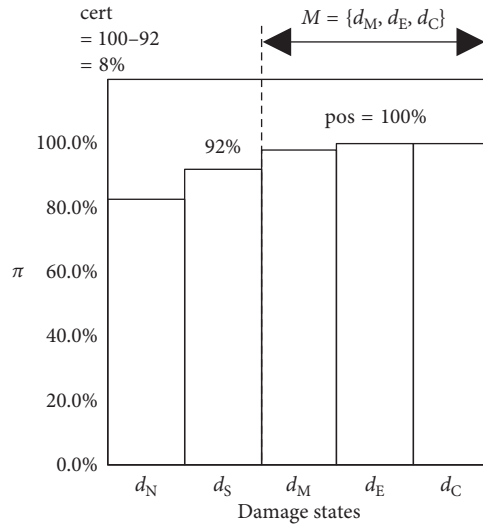


FIGURE 5: Calculated certainty measure,  $\text{cert} = 8\%$ , and possibility measure,  $\text{pos} = 100\%$ , of the set  $M = \{d_M, d_E, d_C\}$  for the PGA (g) interval of [0.323, 0.384]g.

TABLE 5: Certainty measure of damage sets in equation (16) using equation (12) based on the possibility distribution in Figure 4.

PGA interval (g) $[\theta_1, \theta_2]$	None (N) (%)	Slight (S) (%)	Moderate (M) (%)	Extensive (E) (%)	Collapse (C) (%)
[0.069, 0.079]	100.0	0.00	0.0	0.0	0.0
[0.080, 0.137]	100.0	2.23	0.0	0.0	0.0
[0.138, 0.322]	100.0	3.36	1.8	0.0	0.0
[0.323, 0.384]	100.0	17.67	8.0	2.4	0.0
[0.385, 0.680]	100.0	27.30	19.7	6.9	0.3
[0.682, 0.889]	100.0	46.76	36.7	18.7	3.6

TABLE 6: Possibility measure of damage sets in equation (16) using equation (11) based on the possibility distribution in Figure 4.

PGA interval (g) $[\theta_1, \theta_2]$	None (N) (%)	Slight (S) (%)	Moderate (M) (%)	Extensive (E) (%)	Collapse (C) (%)
[0.069, 0.079]	100.0	100.0	100.0	100.0	100.0
[0.080, 0.137]	100.0	100.0	100.0	100.0	100.0
[0.138, 0.322]	100.0	100.0	100.0	100.0	100.0
[0.323, 0.384]	100.0	100.0	100.0	100.0	100.0
[0.385, 0.680]	100.0	100.0	100.0	100.0	100.0
[0.682, 0.889]	100.0	100.0	100.0	100.0	100.0

TABLE 7: Belief measure of damage subsets in equation (16) using equation (3) based on the degree of belief  $m$  in Table 3.

PGA interval (g) $[\theta_1, \theta_2]$	N (%)	S (%)	M (%)	E (%)	C (%)
[0.069, 0.079]	100.0	0.00	0.0	0.0	0.0
[0.080, 0.137]	100.0	2.23	0.0	0.0	0.0
[0.138, 0.322]	100.0	3.36	1.8	0.0	0.0
[0.323, 0.384]	100.0	17.67	8.0	2.4	0.0
[0.385, 0.680]	100.0	27.30	19.7	6.9	0.3
[0.682, 0.889]	100.0	46.76	36.7	18.7	3.6

TABLE 8: Plausibility measure of damage subsets in equation (16) using equation (4) based on the degree of belief  $m$  in Table 3.

PGA interval (g) $[\theta_1, \theta_2]$	N (%)	S (%)	M (%)	E (%)	C (%)
[0.069, 0.079]	100.0	100.0	100.0	100.0	100.0
[0.080, 0.137]	100.0	100.0	100.0	100.0	100.0
[0.138, 0.322]	100.0	100.0	100.0	100.0	100.0
[0.323, 0.384]	100.0	100.0	100.0	100.0	100.0
[0.385, 0.680]	100.0	100.0	100.0	100.0	100.0
[0.682, 0.889]	100.0	100.0	100.0	100.0	100.0

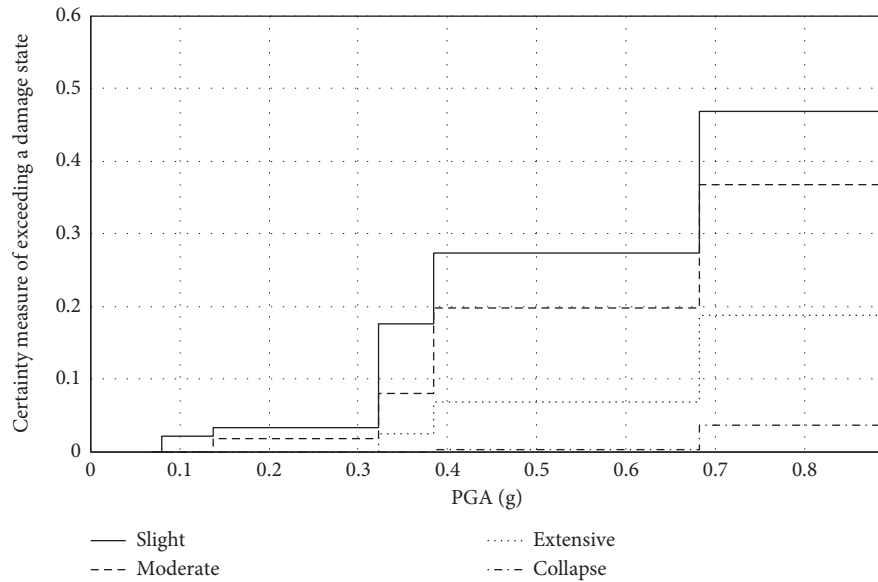


FIGURE 6: Empirical fragility curves of damage state subsets determined by measuring *certainty* of possibility distributions for PGA (g) intervals.

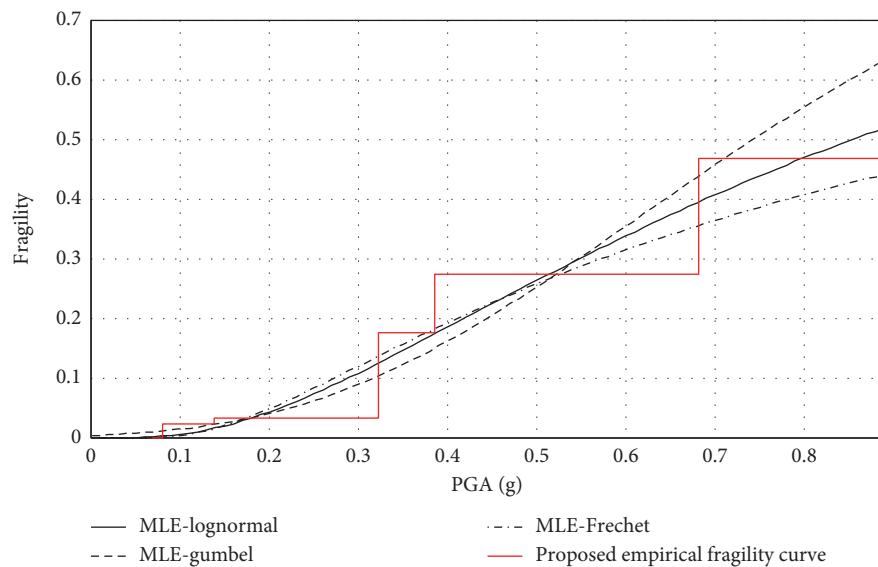


FIGURE 7: Comparison of empirical fragility curves of damage state with Slight.

formulated by connecting the necessity measure at the center of bin instead of using step function that has the same value in a PGA interval (bin). An example using “PGA bin” of 0.1 g is presented in Figures 11–14 for the respective damage state of “Slight,” “Moderate,” “Extensive,” and “Collapse”. In the figures, the proposed fragility curves using expert’s interval are compared with those using the uniform interval. The alternative formulation of the proposed fragility curves by connecting the certainty measure at the center of PGA interval is also presented in Figures 11–14. The comparisons in the figures showed that the uniform interval would be used to generate the proposed fragility curves in this study with a large number of damage data.

## 5. Conclusions

A framework to consider the “nonspecificity” of damage data is presented. Considering that the damage states for fragility curves are generally nested to each other, the possibility theory, a special form of the evidence theory for nested intervals, is applied to generate fragility information from seismic damage data. Seismic damage data classified by four damage levels were used for a case study. Based on the damage state evidence, the degree of belief is assigned to a consonant set of damage levels. Possibility distributions for predetermined PGA region are generated using the assignment of the degree of belief. The sequence of monotone measures of each damage level

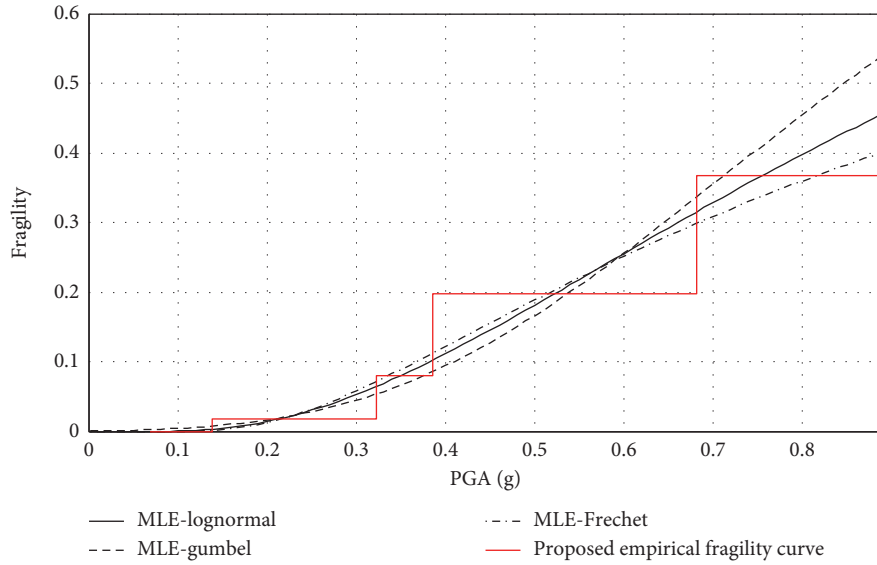


FIGURE 8: Comparison of empirical fragility curves of damage state with Moderate.

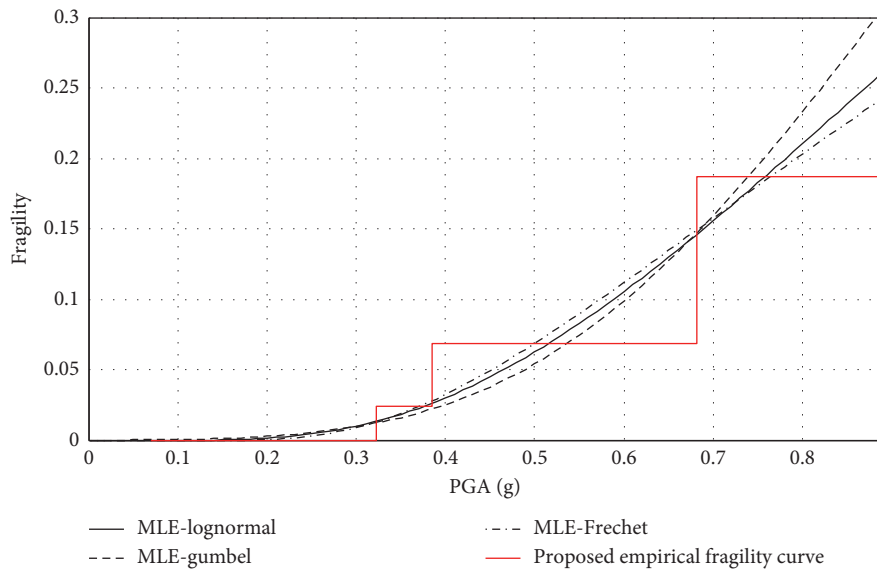


FIGURE 9: Comparison of empirical fragility curves of damage state with Extensive.

with respect to PGA is presented and compared with conventional fragility curves generated by maximum likelihood estimation. It was shown that the generated sequence of certainty measure could be used as fragility curves in alternative perspective. Noticeably, the fragility curves from possibility distribution represent the certainty of damage state, and those are generated without any assumption of distributions. The empirical fragility curves using possibility theory were compared with those generated by maximum likelihood estimation. The results showed that the conventional fragility curves generated by assuming the distributions overestimate the failure probability at the relatively high PGA, while those underestimate the failure probability at the medium range of PGA. Therefore, the proposed empirical fragility curves

using possibility theory can be used as an alternative methodology for earthquake engineering.

### Appendix

All possible subsets of a set constitute a special set defined as power set.

$$X = \{a, b, c\},$$

$$P(X) = \{\emptyset, \{a\}, \{b\}, \{c\}, \{a, b\}, \{b, c\}, \{a, c\}, \{a, b, c\}\}. \tag{17}$$

Example 1. Evidence theory.

Consider a discrete universe  $X = \{1, 2, 3\}$ . The degree of belief (evidence)  $m$  is assigned to the corresponding power set

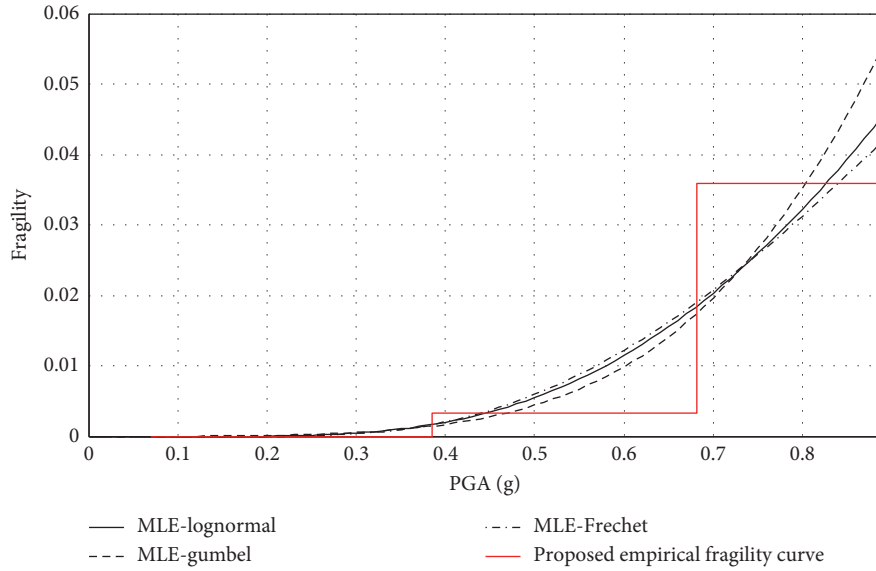


FIGURE 10: Comparison of empirical fragility curves of damage state with Collapse.

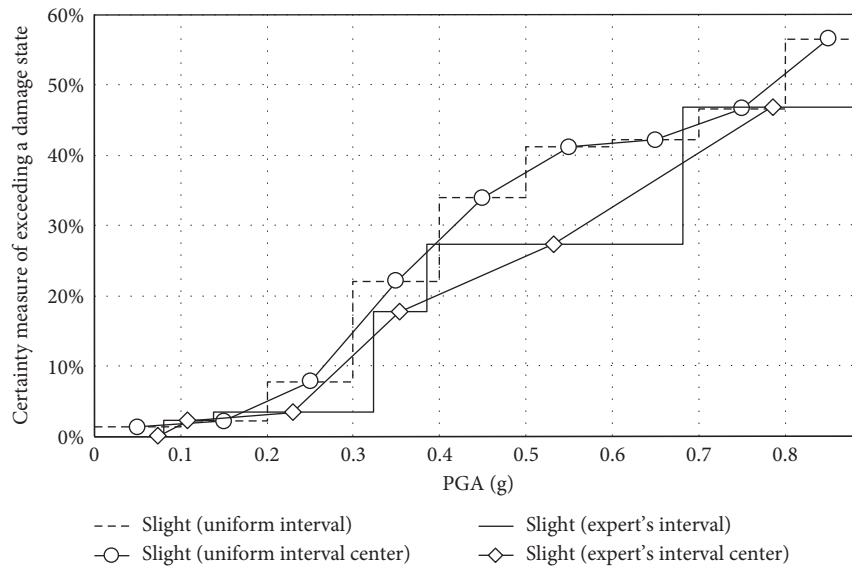


FIGURE 11: Comparison of the proposed fragility curves for Slight about the different interval selections with alternative formulation of the proposed fragility curves by using step function and connecting the necessity measure at the center of PGA interval.

with the summation of  $m$  as unity as shown in equation (2) such as

$$\begin{aligned}
 P(X) &= \{\emptyset, \{1\}, \{2\}, \{3\}, \{1, 2\}, \{2, 3\}, \{1, 3\}, \{1, 2, 3\}\} \\
 \longrightarrow m &= [0, 0.1, 0.1, 0.1, 0.2, 0.1, 0.1, 0.3].
 \end{aligned}
 \tag{18}$$

The monotone measures for a subset are calculated by equation (3) for belief and equation (4) for plausibility as presented in Table 9.

*Example 2.* Special case of evidence theory (same with probability theory).

For the same universe  $X$  in example 2, the degree of belief (evidence)  $m$  is assigned to the corresponding power set such as

$$\begin{aligned}
 P(X) &= \{\emptyset, \{1\}, \{2\}, \{3\}, \{1, 2\}, \{2, 3\}, \{1, 3\}, \{1, 2, 3\}\} \\
 \longrightarrow m &= [0, 0.3, 0.3, 0.4, 0, 0, 0, 0].
 \end{aligned}
 \tag{19}$$

The monotone measures, belief and plausibility, are calculated as presented in Table 10.

As shown in results, belief and plausibility measures have the same values for all subsets, and ignorance measures are

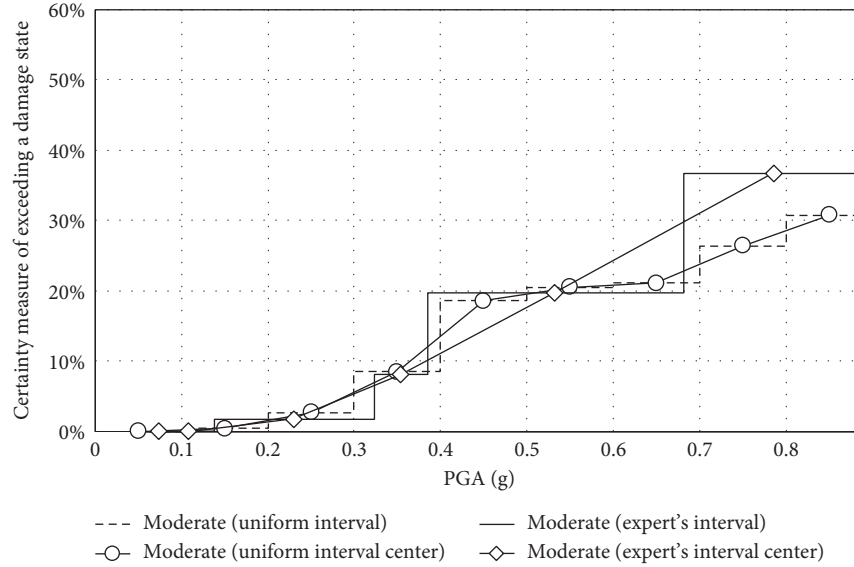


FIGURE 12: Comparison of the proposed fragility curves for Moderate about the different interval selections with alternative formulation of the proposed fragility curves by using step function and connecting the necessity measure at the center of PGA interval.

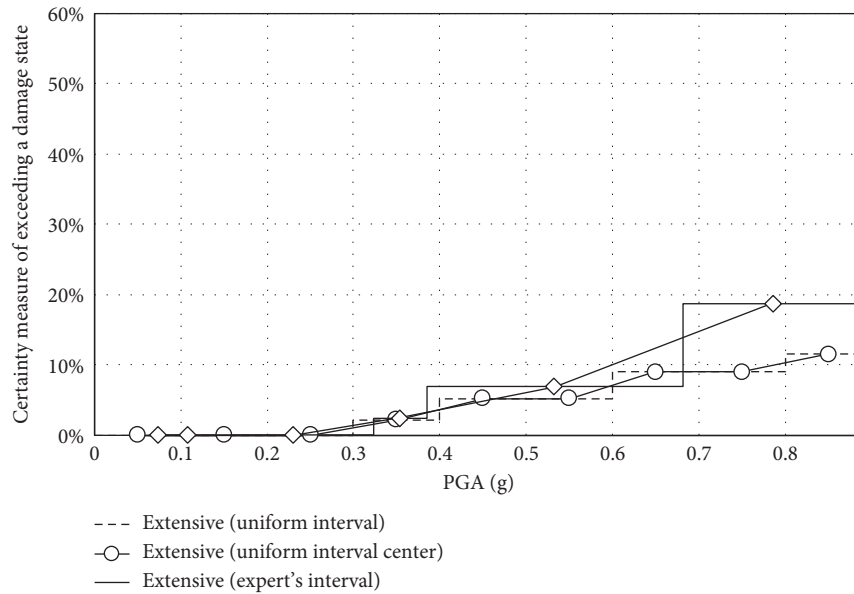


FIGURE 13: Comparison of the proposed fragility curves for Extensive about the different interval selections with alternative formulation of the proposed fragility curves by using step function and connecting the necessity measure at the center of PGA interval.

going to be zero. Therefore, belief and plausibility measures can be represented as one monotone measure such as probability.

*Example 3.* Special case of evidence theory (same with possibility theory).

As shown in Figure 1, if a body of evidence is nested within each other for a discrete universe  $\{a, b, c\}$ , this body of evidence is called "consonant body of evidence". For a consonant body of evidence, belief and plausibility are equal to necessity and possibility, respectively.

For the same universe  $X$  in example 2, when the degree of belief (evidence)  $m$  is assigned to the corresponding power set such as

$$P(X) = \{\emptyset, \{1\}, \{2\}, \{3\}, \{1, 2\}, \{2, 3\}, \{1, 3\}, \{1, 2, 3\}\}$$

$$\rightarrow m = [0, 0.3, 0, 0, 0.3, 0, 0, 0.4].$$

(20)

The monotone measures, belief and plausibility, are calculated as presented in Table 11. Moreover, possibility distributions can be generated using equation (10) as presented in Table 12. Using these possibility distributions in

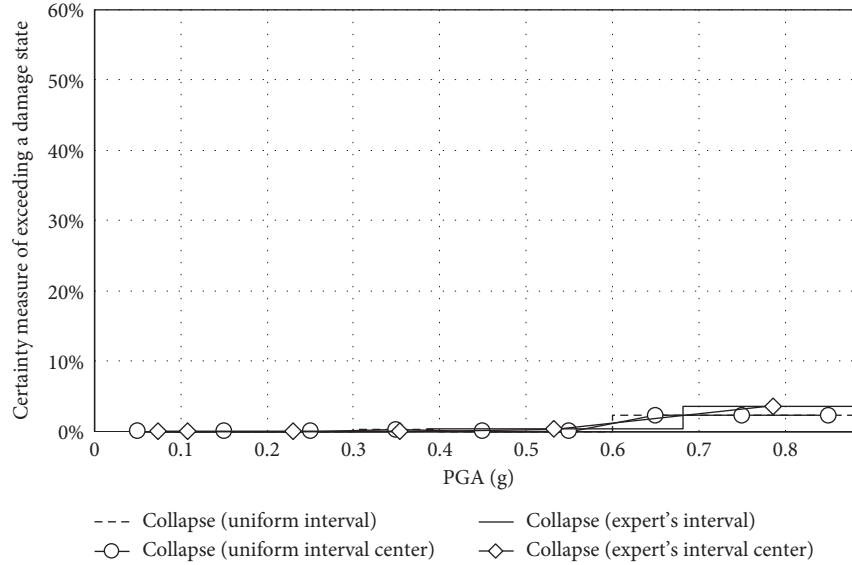


FIGURE 14: Comparison of the proposed fragility curves for Collapse about the different interval selections with alternative formulation of the proposed fragility curves by using step function and connecting the necessity measure at the center of PGA interval.

TABLE 9: The calculated monotone measures in evidence theory.

Subset	Monotone measures in evidence theory
	$bel(\{1\}) = m(\{1\}) = 0$
{1}	$pl(\{1\}) = m(\{1\}) + m(\{1, 2\}) + m(\{1, 3\}) + m(\{1, 2, 3\})$ $= 0.1 + 0.2 + 0.1 + 0.3 = 0.7$ $ign(\{1\}) = pl(\{1\}) - bel(\{1\}) = 0.7 - 0.1 = 0$
	$bel(\{1, 2\}) = m(\{1\}) + m(\{2\}) + m(\{1, 2\}) = 0.4$
{1, 2}	$pl(\{1, 2\}) = m(\{1\}) + m(\{2\}) + m(\{1, 2\}) + m(\{2, 3\}) +$ $m(\{1, 3\}) + m(\{1, 2, 3\}) = 1$ $ign(\{1, 2\}) = pl(\{1, 2\}) - bel(\{1, 2\}) = 1 - 0.4 = 0.6$
	$bel(\{1, 2, 3\}) = all = 1$
{1, 2, 3}	$pl(\{1, 2, 3\}) = all = 1$ $ign(\{1, 2, 3\}) = pl(\{1, 2, 3\}) - bel(\{1, 2, 3\}) = 1 - 1 = 0$

TABLE 10: The calculated monotone measures in a special case of evidence theory which is the same with probability theory.

Subset	Monotone measures in evidence theory
	$bel(\{1\}) = m(\{1\}) = 0.3$
{1}	$pl(\{1\}) = m(\{1\}) + m(\{1, 2\}) + m(\{1, 3\}) + m(\{1, 2, 3\})$ $= 0.3 + 0 + 0 + 0 = 0.3$ $ign(\{1\}) = pl(\{1\}) - bel(\{1\}) = 0.3 - 0.3 = 0$
	$bel(\{1, 2\}) = m(\{1\}) + m(\{2\}) + m(\{1, 2\}) = 0.3 + 0.3 +$ $0 = 0.6$
{1, 2}	$pl(\{1, 2\}) = m(\{1\}) + m(\{2\}) + m(\{1, 2\}) + m(\{2, 3\}) +$ $m(\{1, 3\}) + m(\{1, 2, 3\}) = 0.3 + 0.3 + 0 + 0 + 0 + 0 = 0.6$ $ign(\{1, 2\}) = pl(\{1, 2\}) - bel(\{1, 2\}) = 0.6 - 0.6 = 0$
	$bel(\{1, 2, 3\}) = all = 1$
{1, 2, 3}	$pl(\{1, 2, 3\}) = all = 1$ $ign(\{1, 2, 3\}) = pl(\{1, 2, 3\}) - bel(\{1, 2, 3\}) = 1 - 1 = 0$

Table 12, certainty and possibility measures in possibility theory are calculated using equations (11) and (12) as presented in Table 13. As expected, the belief and plausibility measures in Table 11 are equal to the certainty and possibility measures in Table 13 respectively.

TABLE 11: The calculated monotone measures in a special case of evidence theory which is the same with possibility theory.

Subset	Monotone measures in evidence theory
	$bel(\{1\}) = m(\{1\}) = 0.3$
{1}	$pl(\{1\}) = m(\{1\}) + m(\{1, 2\}) + m(\{1, 3\}) + m(\{1, 2, 3\})$ $= 0.3 + 0.3 + 0 + 0.4 = 1$ $ign(\{1\}) = pl(\{1\}) - bel(\{1\}) = 1 - 0.3 = 0.7$
	$bel(\{1, 2\}) = m(\{1\}) + m(\{2\}) + m(\{1, 2\}) = 0.3 + 0 +$ $0.3 = 0.6$
{1, 2}	$pl(\{1, 2\}) = m(\{1\}) + m(\{2\}) + m(\{1, 2\}) + m(\{2, 3\}) +$ $m(\{1, 3\}) + m(\{1, 2, 3\}) = 0.3 + 0 + 0.3 + 0 + 0 + 0.4 = 1$ $ign(\{1, 2\}) = pl(\{1, 2\}) - bel(\{1, 2\}) = 1 - 0.6 = 0.4$
	$bel(\{1, 2, 3\}) = all = 1$
{1, 2, 3}	$pl(\{1, 2, 3\}) = all = 1$ $ign(\{1, 2, 3\}) = pl(\{1, 2, 3\}) - bel(\{1, 2, 3\}) = 1 - 1 = 0$

TABLE 12: The possibility distributions.

Subset	Monotone measures in evidence theory
{1}	$\pi(\{1\}) = m(\{1\}) + m(\{1, 2\}) + m(\{1, 3\}) + m(\{1, 2, 3\}) =$ $0.3 + 0.3 + 0 + 0.4 = 1$
{2}	$\pi(\{2\}) = m(\{2\}) + m(\{1, 2\}) + m(\{2, 3\}) + m(\{1, 2, 3\}) =$ $0 + 0.3 + 0 + 0.4 = 0.7$
{3}	$\pi(\{3\}) = m(\{3\}) + m(\{1, 3\}) + m(\{2, 3\}) + m(\{1, 2, 3\}) =$ $0 + 0 + 0 + 0.4 = 0.4$

TABLE 13: The calculated monotone measures in possibility theory.

Subset	Monotone measures in possibility theory
{1}	$cert(\{1\}) = 1 - \sup [\pi(\{2\}), \pi(\{3\})] = 1 - \sup [0.7, 0.4]$ $= 0.3$ $pos(\{1\}) = \pi(\{1\}) = 1$
{1, 2}	$cert(\{1, 2\}) = 1 - \pi(\{3\}) = 1 - 0.4 = 0.6$ $pos(\{1, 2\}) = \sup [\pi(\{1\}), \pi(\{2\})] = \sup [1, 0.7] = 1$
{1, 2, 3}	$cert(\{1, 2, 3\}) = 1$ $pos(\{1, 2, 3\}) = \sup [\pi(\{1\}), \pi(\{2\}), \pi(\{3\})] = \sup [1,$ $0.7, 0.4] = 1$

## Data Availability

The data used for the case study of this study can be found in Reference [16].

## Conflicts of Interest

The author declares that there are no conflicts of interest.

## Acknowledgments

This work was supported by Kyungnam University Foundation Grant, 2016.

## References

- [1] C. O. Li and R. E. Melchers, "Time-dependent reliability analysis of corrosion-induced concrete cracking," *ACI Structural Journal*, vol. 102, no. 4, pp. 543–549, 2005.
- [2] J. Seo, G. Hatfield, and J.-H. Kimn, "Probabilistic structural integrity evaluation of a highway steel bridge under unknown trucks," *Journal of Structural Integrity and Maintenance*, vol. 1, no. 2, pp. 65–72, 2016.
- [3] D. Dubois, "Possibility theory and statistical reasoning," *Computational Statistics and Data Analysis*, vol. 51, no. 1, pp. 47–69, 2006.
- [4] T. J. Ross, *Fuzzy Logic with Engineering Applications*, John Wiley & Sons, Hoboken, NJ, USA, 3rd edition, 2010.
- [5] G. J. Klir and B. Yuan, *Fuzzy Sets and Fuzzy Logic, Theory and Applications*, Prentice-Hall, Upper Saddle River, NJ, USA, 1995.
- [6] G. J. Klir, *Uncertainty and Information*, John Wiley & Sons, Hoboken, NJ, USA, 2006.
- [7] O. F. Hoffman and J. S. Hammonds, "Propagation of uncertainty in risk assessment: the need to distinguish between uncertainty due to lack of knowledge and uncertainty due to variability," *Risk Analysis*, vol. 14, no. 5, pp. 707–712, 1994.
- [8] J. C. Helton and D. E. Burmaster, "Guest editorial: treatment of aleatory and epistemic uncertainty in performance assessments for complex systems," *Reliability Engineering and System Safety*, vol. 54, no. 2–3, pp. 91–94, 1996.
- [9] H. G. Matthies, C. E. Brenner, C. G. Bucher, and C. Guedes Soares, "Uncertainties in probabilistic numerical analysis of structures and solids-stochastic finite elements," *Structural Safety*, vol. 19, no. 3, pp. 283–336, 1997.
- [10] W. L. Oberkampf, S. M. DeLand, B. M. Rutherford, K. V. Diegert, and K. F. Alvin, "Error and uncertainty in modeling and simulations," *Engineering and System Safety*, vol. 75, no. 3, pp. 333–357, 2002.
- [11] A. P. Dempster, "Upper and lower probabilities induced by a multivalued mapping," *Annals of Mathematical Statistics*, vol. 38, no. 2, pp. 325–339, 1967.
- [12] G. Shafer, *Mathematical Theory of Evidence*, Princeton University Press, Princeton, NJ, USA, 1976.
- [13] D. Dubois and H. Prade, *Possibility Theory: An Approach to Computerized Processing of Uncertainty*, Plenum Press, New York, NY, USA, 1988.
- [14] L. A. Zadeh, "Fuzzy sets," *Information and Control*, vol. 8, no. 3, pp. 338–353, 1965.
- [15] L. A. Zadeh, "Fuzzy sets as a basis for a theory of possibility," *Fuzzy Sets and Systems*, vol. 1, no. 1, pp. 3–28, 1978.
- [16] M. Shinozuka, M. O. Feng, H. Kim, T. Uzawa, and T. Ueda, *Statistical Analysis of Fragility Curves*, Technical report MCEER, Federal Highway Administration, Washington, DC, USA, 2001.
- [17] F. Colangelo, "A simple model to include fuzziness in the seismic fragility curve and relevant effect compared with randomness," *Earthquake Engineering and Structural Dynamics*, vol. 41, no. 5, pp. 969–986, 2012.
- [18] J. Rohmer and C. Baudrit, "The use of the possibility theory to investigate the epistemic uncertainties within scenario-based earthquake risk assessments," *Natural Hazards*, vol. 56, no. 3, pp. 613–632, 2010.
- [19] T. Rossetto and A. Elnashai, "Derivation of vulnerability functions for European-type RC structures based on observational data," *Engineering Structures*, vol. 25, no. 10, pp. 1241–1263, 2003.
- [20] C. Del Gaudio, G. De Martino, M. De Ludovico et al., "Empirical fragility curves from the damage data on RC buildings after the 2009 L'Aquila earthquake," *Bulletin of Earthquake Engineering*, vol. 15, no. 4, pp. 1425–1450, 2017.
- [21] B. Besson and J. O. Bjarnason, "Seismic vulnerability of low-rise residential buildings based on damage data from three earthquakes (MW 6.5, 6.5 and 6.3)," *Engineering Structures*, vol. 111, pp. 64–79, 2016.
- [22] D. Gautam, G. Fabbrocino, and F. Santucci de Magistris, "Derive empirical fragility functions for Nepali residential buildings," *Engineering Structures*, vol. 171, pp. 612–628, 2018.
- [23] D. Gautam, "Observational fragility functions for residential stone masonry buildings in Nepal," *Bulletin of Earthquake Engineering*, vol. 16, no. 10, pp. 4661–4673, 2018.
- [24] M. Rota, A. Penna, and C. L. Strobbia, "Processing Italian damage data to derive typological fragility curves," *Soil Dynamics and Earthquake Engineering*, vol. 28, no. 10–11, pp. 933–947, 2008.
- [25] M. Colombi, B. Borzi, H. Crowley, M. Onida, F. Meroni, and R. Pinho, "Deriving vulnerability curves using Italian earthquake damage data," *Bulletin of Earthquake Engineering*, vol. 6, no. 3, pp. 485–504, 2006.
- [26] J. J. Kim, "Uncertainty quantification in serviceability of reinforced concrete structures," PhD Dissertation in University of New Mexico, USA, 2009.
- [27] J. J. Kim, M. M. Reda Taha, and T. J. Ross, "Establishing concrete cracking strength interval using possibility theory with an application to predict the possible reinforced concrete deflection interval," *Engineering Structures*, vol. 32, no. 11, pp. 3592–3600, 2010.
- [28] J. J. Kim, M. M. Reda Taha, and T. J. Ross, "Binary damage classification in SHM using possibility distributions," in *Proceedings of the Second International Conference on Vulnerability and Risk Analysis and Management (ICV-RAM) and the Sixth International Symposium on Uncertainty Modeling and Analysis, (ISUMA)*, Liverpool, UK, July 2014.

## Research Article

# Probabilistic Prediction of Maximum Tensile Loads in Soil Nails

Yongqiang Hu<sup>1</sup> and Peiyuan Lin<sup>2</sup>

<sup>1</sup>Assistant Professor, School of Civil Engineering, Guangzhou University, Guangzhou, Guangdong 510 006, China

<sup>2</sup>Postdoctoral Fellow, Department of Civil Engineering & Ryerson Institute of Infrastructure Innovation, Ryerson University, Toronto, ON, Canada M5B 2K3

Correspondence should be addressed to Peiyuan Lin; [peiyuan.lin@ryerson.ca](mailto:peiyuan.lin@ryerson.ca)

Received 21 August 2018; Revised 29 October 2018; Accepted 6 November 2018; Published 22 November 2018

Guest Editor: Haiyun Shi

Copyright © 2018 Yongqiang Hu and Peiyuan Lin. This is an open access article distributed under the Creative Commons Attribution License, which permits unrestricted use, distribution, and reproduction in any medium, provided the original work is properly cited.

This paper presents the development of a simplified model for estimation of maximum nail loads during or at completion of construction of soil nail walls. The developed simplified nail load model consists of two multiplicative components: the theoretical nail load and the correction factor. The theoretical nail load is computed as the product of lateral active Earth pressure at nail depth and the nail tributary area. The correction factor is introduced to account for the difference between the theoretical and the measured nail loads. A total of 85 measured nail load data were collected from the literature; out of which, 74 were used to develop a simple formulation for the correction factor, whereas the remaining 11 were used for validation. After the validation, the model was updated using all 85 data. The updated simplified nail load model was demonstrated to be accurate on average (mean of model factor equal to 1), and the spread in prediction quantified as the coefficient of variation of the model factor was about 40%. Here, model factor is the ratio of measured to estimated nail load. The randomness of the model factor was also verified. Finally, the model factor was demonstrated to be a lognormal random variable. The proposed simplified nail load model is beneficial due to its simplicity and quantified model uncertainty; thus it is practically valuable to both direct reliability-based design and load and resistance factor design of soil nail wall internal limit states.

## 1. Introduction

Estimation of maximum tensile loads for soil nails during or at completion of construction of soil nail walls is of great practical interests to wall design engineers. Due to the nail-soil interactions, tensile loads develop along soil nails as the nailed soil mass deforms. Failures due to nail pullout or yield in tension take place when the maximum tensile load in a nail exceeds its ultimate pullout capacity or yield tensile strength [1].

There have been several models proposed in the literature for estimation of maximum loads of soil nails during or at completion of wall construction. Juran and Elias [2] developed a modified apparent Earth pressure diagram model which was later found to be not practical as the estimated nail loads are very sensitive to input parameters such as soil friction angle and soil cohesion. Juran et al. [3] proposed a kinematical approach to compute nail loads as the wall construction proceeds and validated their approach using one case study. The underlying model uncertainty of the kinematical approach is not reported in the literature. The Federal Highway Administration

(FHWA) soil nail wall design manuals [1, 4, 5] provide a simplified model for nail load estimation. Lin et al. [6] evaluated the model uncertainty of the FHWA simplified model using 45 measured maximum nail load data they collected from the literature and concluded that the default FHWA simplified nail load equation is excessively conservative on average and the estimation scatters widely. Moreover, the model factor of the FHWA equation is not a random variable as it is statistically correlated to some of the input parameters and the calculated nail load. Here, model factor is the ratio of measured to calculated nail load. They then modified the FHWA simplified nail load model to improve on-average accuracy, reduce spreads in prediction accuracy, and remove the dependency between model factor and input parameters and calculated nail load. Indeed, the dependency issue has been reported for various geotechnical models, e.g., bearing capacity of foundations [7–9], both pullout capacities and tensile loads of reinforcing elements in reinforced soil walls [6, 10–13], and deflection of cantilever walls [14]. Removal of this type of dependency is important for geotechnical reliability-based

design as emphasized in ISO2394:2015 Annex D [15] and Phoon [16]. Influence of the dependency on reliability analysis outcomes was discussed by Lin and Bathurst [17].

In this study, a total of 85 measured data for maximum nail tensile loads during or at completion of wall construction are first collected from the literature and divided into two data groups. The first data group is used to develop a simplified model for nail load estimation based on the two regression approaches introduced in Dithinde et al. [18]. The developed simplified model is then validated using the other data group. The simplified model proposed by the present study is advantageous when compared to the default and modified FHWA simplified nail load models from the perspectives of number of empirical constants (i.e., two versus three and five), on-average accuracy (i.e., accurate versus conservative), spread in prediction accuracy (i.e., about 40% versus about 45% and 50%), and dependency between model factor and input parameters or computed nail load. Finally, the distribution of the model factor of the proposed equation is also discussed.

## 2. Formulation of Simplified Model for Calculation of Maximum Nail Loads

A soil nail wall system is typically divided into an active zone and a passive zone by a potential slip surface, as shown in

Figure 1. Nails are installed immediately after excavation of each level to provide both pullout resistance against global failure and restraint against lateral deformation of the excavated ground. Tensile loads are then developed along nails mainly due to the frictional interaction between nails and the surrounding soil and the soil-structure interaction between the facing and the soil at nail heads [19]. The lateral Earth pressure ( $\sigma_h$ ) acting within a tributary area ( $S_h S_v$ ) where a soil nail center is carried by that nail. Based on this mechanism, the tensile load in a soil nail can be calculated as follows:

$$T_N = \eta T_t = \eta \sigma_h S_h S_v = \eta K_a (\gamma h + q_s) S_h S_v, \quad (1)$$

where  $T_t$  is the theoretical nail load computed as  $T_t = \sigma_h S_h S_v = K_a (\gamma h + q_s) S_h S_v$ ;  $\sigma_h = K_a (\gamma h + q_s)$  is the horizontal Earth pressure at depth of nail head  $h$  as defined in Figure 1;  $K_a$  is the active Earth pressure coefficient computed using Coulomb theory;  $\gamma$  is the soil unit weight;  $q_s$  is the surcharge load;  $S_h$  and  $S_v$  are the horizontal and vertical nail spacing, respectively; and  $\eta$  is the empirical correction factor introduced to account for errors arising from underlying model errors, variability in soil properties, and all types of uncertainties in sites, etc. The Coulomb  $K_a$  is computed as follows:

$$K_a = \frac{\cos^2(\beta + \phi)}{\cos^2 \beta \cos(\beta - \delta) [1 + \sqrt{(\sin(\phi + \delta) \sin(\phi - \alpha)) / (\cos(\beta - \delta) \cos(\alpha + \beta))}]^2}, \quad (2)$$

where  $\beta$  = face batter angle;  $\phi$  = effective soil friction angle;  $\alpha$  = back slope angle; and  $\delta$  = interface friction angle between the wall face and soil.

The formulation structure of Equation (1) is consistent to those currently used in AASHTO [20] and FHWA [21] for estimation of loads in reinforcing elements such as steel strip, steel grid, and geosynthetic sheet (geogrid or geotextile). The only difference is the expression of the empirical term  $\eta$  which is dependent on the type of reinforcing elements. One of the advantages of Equation (1) is the compatibility in formulation with those for design of different types of reinforced soil walls per AASHTO [20] and FHWA [21]. The remaining of this study is focused on the development of simple expression of  $\eta$  for soil nails.

## 3. Database of Maximum Soil Nail Loads under Working Conditions

This study developed a large database of measured soil nail loads based on two components. The first is the database that was developed by Lin et al. [6] (walls W1 to W9 in Table 1), and the second is new data that we collected from the literature (walls W10 to W19 in Table 1). Summary of the wall geometry, soil type and properties, nail arrangement, and surcharge loading conditions for those soil nail walls are shown in Table 1; while detailed descriptions are provided in the following.

Lin et al. [6] developed a database of measured short-term maximum tensile loads of soil nails. Here, short-term means that the nail loads were recorded during or at completion of wall construction. There were 45 data points from nine soil nail walls included in their database; all the walls were constructed, instrumented, and monitored within the United States for different applications. In Table 1, walls W1 and W2 by Banerjee et al. [22] were nearby each other; W1 was constructed below an existing bridge abutment, whereas W2 was not beneath the bridge abutment but about 15 m to the west. Wall W3 by Shen et al. [23] was a full-scale field prototype built as a part of the systematic studies on in situ Earth retaining structures. Wall W4 by Juran and Elias [2] was featured by both the inclined facing and upper ground back slope. Temporary walls W5 to W7 by Holman and Tuozzolo [24] were used to support the construction of a large electrical vault, for which the site accessibility was very limited in size and the construction schedule was aggressive. Walls W8 and W9 by Wei [25] were from an MSE/soil nail hybrid project where the soil nail walls were sitting beneath the MSE walls for an overpass of a road.

It is noted that for a soil nail, there were several strain gauges mounted along its length, and only the one that gave the maximum nail load was adopted. In the database by Lin et al. [6], the soil nail walls were typically less than 10 m high with horizontal back slope and vertical facing structure. Those walls were built in a wide variety of cohesive and

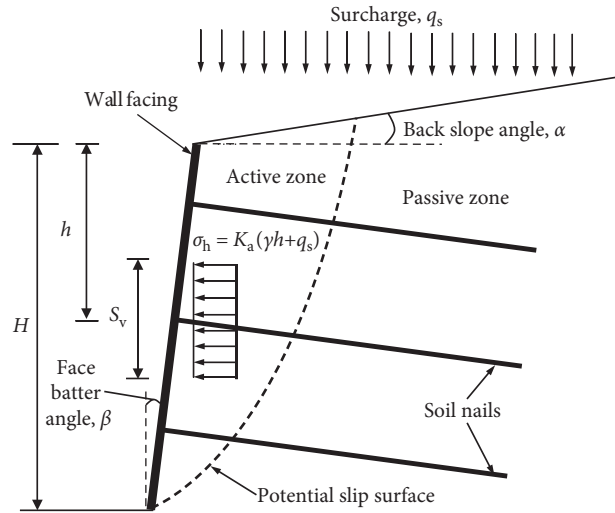


FIGURE 1: Geometry of soil nail walls and horizontal stress of soil acting on the wall.

TABLE 1: Summary of wall geometry, soil properties, and nail arrangement for soil nail walls reported in the source documents.

Data group	Wall	Source	Soil	Wall geometry			Surcharge $q_s$ (kPa)	Soil strength parameters			Nail spacing		No. of data
				$H$ (m)	$\alpha$ ( $^\circ$ )	$\beta$ ( $^\circ$ )		$\phi$ ( $^\circ$ )	$c$ (kPa)	$\gamma$ (kN/m <sup>3</sup> )	$S_h$ (m)	$S_v$ (m)	
1	W1	[22]	Medium dense, poorly graded sand	5.3	0	0	55	33	4.8	18.0	1.4	1.0	5
	W2	[22]	Silty sand, clayey silt	5.6	0	27	0	33	4.8	18.0	1.4	1.0	5
	W3	[23]	Heterogeneous SM	9.2	0	0	0	36.5	18.5	16.3	1.85	1.85	3
	W4	[2]	Residual soil and weathered rock	9–12	16	25	0	38	7.2	18.9	1.5	1.5	7
	W5	[24]	Fill, silt, sand	7.6	0	0	0	38	0	19.6	1.83	1.22–1.83	4
	W6	[24]	Fill, silt, sand	5.9	0	0	0	38	0	19.6	1.83	1.22–1.52	3
	W7	[24]	Fill, silt, sand	5.9	0	0	0	38	0	19.6	1.83	1.22–1.52	3
	W8	[25]	Gravelly silty sand	4–5	0	0	0–127	35	0	19.6	1.0	1.05	3
	W9	[25]	Gravelly silty sand	4–5	0	0	0–127	35	0	19.6	1.0	1.05	12
	W10	[26]	Silty clay	9.2	8.5	0	0	10	0	19.6	1.5	1.5	4
	W11	[27]	Silty sand, fine sand	10	0	0	35	30.6	0	19.1	1	1–1.2	3
	W12	[28]	Clay, silty clay	12	0	0	15	16–20	16–18	19	1.5	1.5	4
	W13	[29]	Silty clay	8	0	0	0	16.4	12	19.7	1.2	1.2	6
	W14	[30]	Sand	6	11.3	0	0	35	0	21	1.5	1.5	4
	W15	[31]	Silty clay	8.5	11.3	0	0	18.9	21	19.8	1.5	1.5	5
	W16	[31]	Silty clay	8.5	15.8	0	0	18.9	21	19.8	1.5	1.5	3
2	W17	[32]	Sand	6	12	0	16	33	0	16	1.25	1.46	4
	W18	[33]	Clayey or silty gravel	5.8–10.6	30	0	0	27	3	18	1.7, 1.8	1.2, 2.1	7
	W19	[34]	Residual andesite	10	0	0	0	38	0	19	2.0	1.5	1

noncohesive soils, including sand, silty sand, clayey silt, residual soil, and weather rock. Despite various soil types, the soil friction angles varied in a relatively narrow ranges, i.e., from 33° to 38°. Three walls were surcharged with an equivalent soil height less than 6 m; the majority were under self-weight-loading conditions.

In this study, by surveying the literature, we expanded their database to include another 40 data points from ten soil nail walls (i.e., walls W10 to W19 in Table 1), resulting in a larger database that includes a total of 85 short-term nail load data. Importantly, these additional data were collected from soil nail walls built in the United States, China, Poland, and South Africa. Therefore, the larger database developed

in this study is more international. Walls W10 to W16 were soil nail walls built in China mainly for support of foundation pits for high-rise buildings (i.e., [26, 28–31]), except for W11 by Duan et al. [27] for supporting excavation in a tunnel project. Wall W17 by Sawicki et al. [32] was the first wall built in Poland to protect and strengthen a steep slope of an excavation in loose sandy subsoil. Wall W18 by Turner and Jensen [33] was from an MSE/soil nail wall hybrid project in the United States aiming at demonstrating the feasibility of using soil nails for stabilization of active landslides. Wall 19 by Jacobsz and Phalanndwa [34] was used to support an excavation for a railway line in South Africa.

The newly added data were from soil nail walls that were typically built in clayey silt and sand. In general, the friction angles varied widely, i.e., from  $10^\circ$  to  $38^\circ$  but typically less than  $30^\circ$ . The wall heights were from about 6 m to 12 m, which were typical. All the walls had horizontal back slopes while most had inclined facing. The walls were typically subjected to self-weight loads.

By examining the source documents carefully, we found that two maximum load measurements in Turner and Jensen [33] were anomalously large compared to other measurements in the same nails. The strain gauges giving these two large nail loads were mounted near the facing, leading to the possibility that the anomalously large measurements could have been due to the bending of the nails due to the facing installation. As a result, these two questionable data were not adopted; instead, the second largest measurements in the same nails were adopted.

In addition, the source documents do not specify whether or not the strain gauge measurements had been calibrated against temperature. Hence, the effect of temperature is not considered in the development of the simplified nail load model in this study. It is also revealed that some source documents also reported long-term nail loads which were recorded several years after completion of wall construction. However, since this study is exclusively focused on prediction of short-term nail loads, those long-term data are thus not included in the analyses to follow.

The larger database ( $n = 85$ ) developed in this study are divided into two data groups: a verification group (group 1) and a validation group (group 2). The verification group contains 74 data and is used to determine the  $\eta$  expressions for the simplified nail load estimation model. Then, the developed simplified nail load model is validated using the validation group, which contains 11 data points. After the validation, the empirical constants appearing in the simplified model are updated using all collected data (i.e., data groups 1 and 2). This final updated simplified model is the model that is proposed by the present study. The model factor of this final updated model is then characterized.

Last, it should be pointed out that the importance of compiling a larger database for model evaluation and calibration should not be undervalued. The number of data points in the present database is almost doubled compared to the previous one by [6]. It contains nail load data from wider working conditions. When a model is scrutinized within a larger context, the merits and demerits of the model can be seen more clearly. From a statistical and also practical point of view, a larger database is desirable as it provides more confidence on the quantitative model estimation and calibration outcomes.

#### 4. Formulation of the Empirical Correction Term $\eta$

Dithinde et al. [18] summarize two regression approaches that are widely used in the literature for determination of  $\eta$ . The first approach is the generalized model factor framework which regresses measured nail loads against theoretical values, and  $\eta$  is a function of  $T_t$  expressed as  $\eta = f(T_t)$ . The

second approach is to regress measured nail loads against each input parameter of  $T_t$ , and  $\eta$  is expressed as  $\eta = f(K_a) \times f(\gamma) \times f(h) \times f(q_s) \times f(S_h S_v)$ . Both approaches are adopted for determination of  $\eta$  in Equation (1).

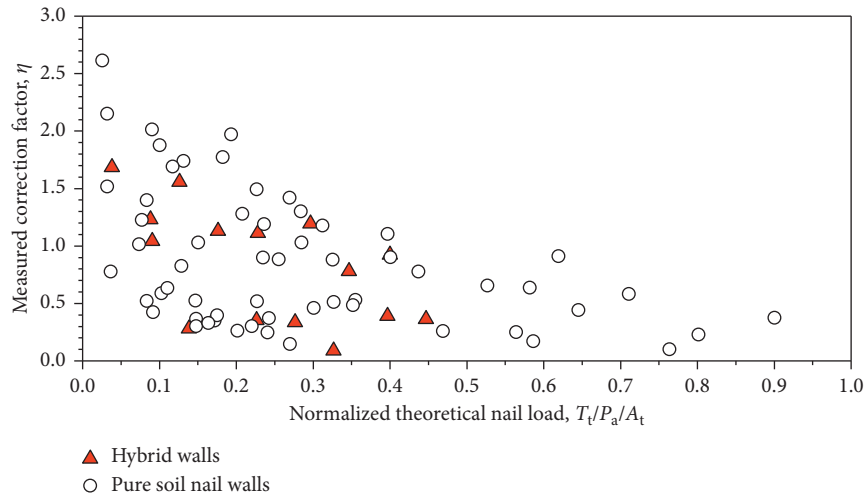
*4.1. Generalized Model Factor Approach.* The parameter  $\delta$  in Equation (2) must be specified before further analyses can be carried out. The range of ratio of  $\delta$  to  $\phi$  is commonly assumed to be from 1/2 to 2/3 for different types of retaining walls (e.g., [35]). Based on this range,  $\delta/\phi = 1/2$  is first selected in this study for analysis while the justification is presented later.

As the nail load data were collected from soil nail walls under different working conditions, for example, some data were from nails in hybrid soil-nail/MSE walls while others were not; it should first check that whether or not the formulation of  $\eta$  depends significantly on the wall-working conditions. To do the check, this study divides the verification data group ( $n = 74$ ) into different data subsets based on three criteria: (1) data from hybrid walls or pure soil nail walls; (2) data from soil nail walls with or without surcharge; and (3) data from walls in cohesive or cohesionless soils. Ideally, the data should be grouped concurrently according to these three criteria; however, as there are only 74 data in total, such a detailed data-grouping approach would make each individual data subset very small, i.e., on average less than 10 points. As a result, this study groups the data based on one criterion at one time. That being said, the 74 data are divided into two data subsets, corresponding to either criterion 1, or 2, or 3.

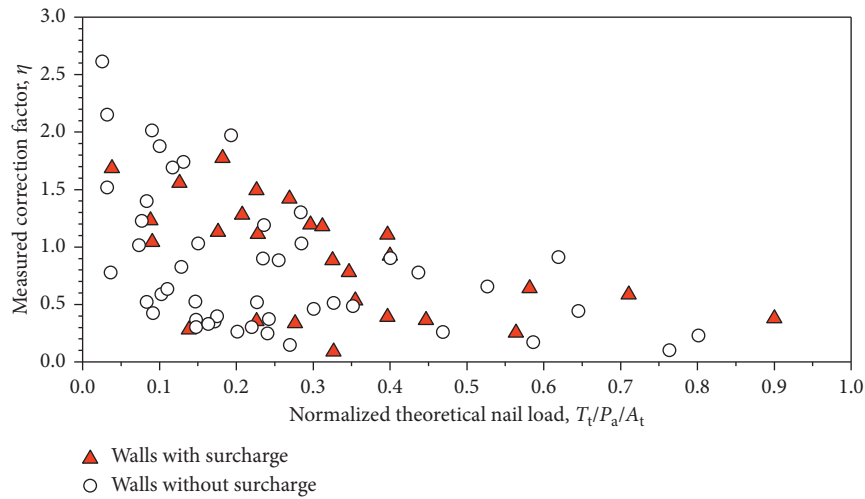
With measured nail loads  $T_m$ , the measured empirical correction factors can be computed as  $\eta = T_m/T_t$ , where  $T_t = K_a(\gamma h + q_s)S_h S_v$  is theoretical nail load as defined in Equation (1). By using the generalized model factor approach, in this study,  $\eta$  is regressed against  $T_t/P_a/A_t$ , where  $P_a = 101$  kPa is the atmospheric pressure and  $A_t = 1.5 \times 1.5 \text{ m}^2 = 2.25 \text{ m}^2$  is typical nail tributary area computed using typical horizontal and vertical nail spacing of 1.5 m [6]. The introduction of  $P_a$  and  $A_t$  is for normalization of  $T_t$  and makes it dimensionless. Figure 2 shows the plots of  $\eta$  versus  $T_t/P_a/A_t$  with respect to different data subsets for soil nail walls under different working conditions.

The first observation from Figure 2 is that the measured  $\eta$  values in general decrease monotonically (at least visually) and nonlinearly with increasing  $T_t/P_a/A_t$  values. The measured  $\eta$  is more likely to be larger than 1 for  $T_t/P_a/A_t < 0.1$ , meaning that the true nail load is more likely to be underestimated if taken as  $T_t$ . For larger  $T_t/P_a/A_t$  values, e.g.,  $>0.2$ , the true nail load is more frequently overpredicted if taken as  $T_t$  since the  $\eta$  value is much likely smaller than 1. The second observation is that the overall trend between  $\eta$  and  $T_t/P_a/A_t$  holds regardless of wall-working conditions, i.e., nails in pure soil nail walls or in hybrid walls, walls with or without surcharge, and walls in cohesive and cohesionless soils. Hence, in the following analyses for the formulations for  $\eta = f(T_t/P_a/A_t)$ , all the measured data ( $n = 74$ ) will be used.

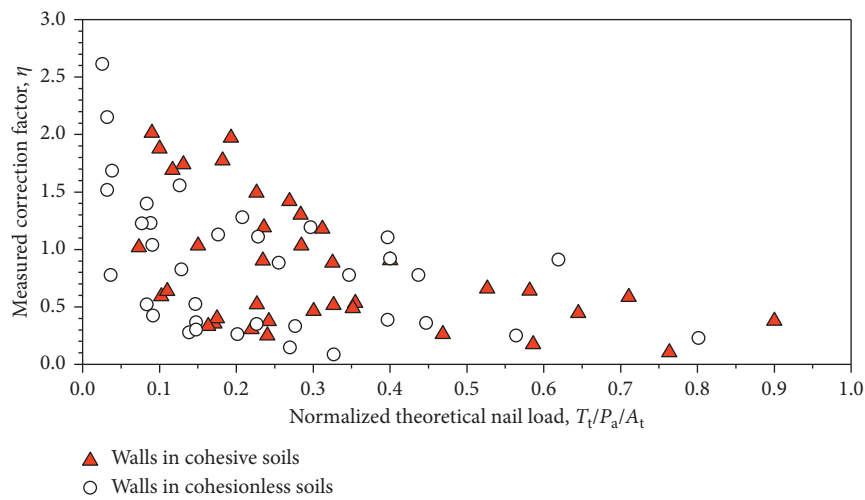
Various formulations could be proposed for  $\eta$ , e.g., nonmonotonic, higher-order functions. Sophisticated



(a)



(b)



(c)

FIGURE 2: Measured correction factor  $\eta$  versus normalized theoretical nail load  $T_t/P_a/A_t$  for different data subsets grouped based on soil nail wall-working conditions.

functions, although might fit the data better, are undesirable due to the complexity. In addition, they could result in overfitting issues. This study advocates the adoption of simple formulations for practical purpose. Therefore, four simple candidate expressions were examined, including exponential, linear, logarithmic, and power functions. The four expressions can be written as follows:

$$\eta = a \times \exp(b \times T_t/P_a/A_t), \quad \text{exponential,} \quad (3a)$$

$$\eta = a \times (T_t/P_a/A_t) + b, \quad \text{linear,} \quad (3b)$$

$$\eta = a \times \ln(T_t/P_a/A_t) + b, \quad \text{logarithmic,} \quad (3c)$$

$$\eta = a \times (T_t/P_a/A_t)^b, \quad \text{power,} \quad (3d)$$

where  $a$  and  $b$  are the empirical constants to be determined. The determination of  $a$  and  $b$  must satisfy three criteria: (1) the mean of model factor,  $\mu_M$ , for Equation (1) should be equal to one; (2) the COV of model factor,  $COV_M$ , should be as small as possible; and (3) the model factor,  $M$ , should be a random variable, which means that  $M$  is not statistically correlated to any input parameters or the calculated  $T_N$  values using Equation (1).

The steps to determine the optimal values of  $a$  and  $b$  are as follows: (1) select an expression for  $\eta$  (e.g., Equation (3a)) and substitute into Equation (1); (2) compute model factors as  $M = T_m/T_N$  where  $T_m$  are the measured nail load values and  $T_N$  are matching calculated values using Equation (1); and (3) determine the values of  $a$  and  $b$  as the pair that minimizes  $COV_M$  (Criterion 2) while keeps  $\mu_M = 1.00$  (Criterion 1).

Table 2 summarizes the analysis outcomes using the generalized model factor framework and data group 1 ( $n = 74$ ). The minimal  $COV_M$  was 0.535 corresponding to  $\eta$  being a power function of  $T_t$  (Equation (3d)) with  $a = 0.34$  and  $b = -0.47$ . To verify the randomness of  $M$  for this case, Spearman's rank correlation test was applied to  $M$  against  $T_N$  which gave the  $p$  value of 0.54 ( $>0.05$ ), indicating rejection of the null hypothesis that the two datasets are statistically correlated at a level of significance of 5%. Further examinations showed that there is correlation at a level of significance of 5% between  $M$  and the nail depth  $h$ . This independency between  $M$  and  $h$  was doubly confirmed by the outcome of Pearson's correlation test. Hence, the calibrated  $\eta$  expression in this case is judged to be unsatisfactory.

For  $\eta$  with other formulations (i.e., exponential, linear, and logarithmic), the  $COV_M$  values for Equation (1) are all higher, and  $M$  is also correlated to  $h$  for all the three cases. This suggests inadequacy for calibrating  $\eta$  to the level of  $T_t$  as the generalized model framework provides no physical insight on the sources of statistical correlations [18]. Calibration to the level of each input parameter is needed.

#### 4.2. Correction Term $\eta$ as a Function of Input Parameters.

This approach assumes that  $\eta$  is a function of input parameters of Equation (1) and can be generally expressed as  $\eta = f(K_a) \times f(\gamma) \times f(h) \times f(q_s) \times f(S_h S_v)$ . The formulation of  $\eta$  could be too complicated to be practical if all the

input parameters are taken into account. A common strategy to simplify the formulation of  $\eta$  is to identify and address the most important influential factors, while ignoring those that are of secondary significance. This can be easily done by carrying out correlation tests between measured  $\eta$  values and values of input parameters. Note that the measured  $\eta$  value is computed as  $T_m/T_t$  based on Equation (1) where  $T_m$  is the measured nail load and  $T_t = K_a(\gamma h + q_s)S_h S_v$  is the theoretical value as defined earlier in this paper.

Table 3 shows the  $\rho$  and  $p$  values between  $\eta$  and each input parameter using both Spearman's rank and Pearson's correlation tests. It appears that the measured  $\eta$  values are strongly correlated to the depths of nail head  $h$ , but independent of  $K_a$ ,  $q_s$ , and  $S_h S_v$  at the level of significance of 5%. For the soil unit weight,  $\gamma$ , the  $p$  value from Spearman's rank test was 0.04, slightly lower than 0.05, suggesting a correlation between  $\eta$  and  $\gamma$ . On the contrary, Pearson's correlation test result suggested the opposite,  $p$  value = 0.32 (far exceed 0.05). To further investigate whether or not  $\gamma$  should be formulated into  $\eta$ , the four simple expressions adopted earlier were used to fit  $\eta$  against  $\gamma$ , and the coefficients of determination ( $R^2$ ) were computed. The results showed that the  $R^2$  values were 0.015, 0.014, 0.011, and 0.012 for exponential, linear, logarithmic, and power functions of  $\eta = f(\gamma)$ , respectively. These  $R^2$  values were very small, indicating that including  $\gamma$  into the formulation of  $\eta$  is reluctant to improve the accuracy at a noticeable extent. Moreover, in reality, the unit weight of soils that are suitable for soil nailing applications usually varies in a relative small range. As a result, in this study, the formulation of  $\eta$  was greatly simplified to be as  $\eta = f(h/H)$ . The introduction of wall height  $H$  is intended to make  $\eta$  dimensionless. It should be pointed out that this is a different normalization treatment from that for the first case as in the first case,  $P_a$  and  $A_t$  are both constants regardless of walls, whereas in this second case,  $H$  varies from one wall to another. Expectedly, different normalization strategies could result in different calibration outcomes; nevertheless, the differences are insignificant and thus not quantitatively analyzed here.

Figure 3 shows the plot of measured  $\eta$  values ( $T_m/T_t$ ) versus normalized depths ( $h/H$ ) using data subsets grouped based on wall-working conditions as defined earlier. The measured  $\eta$  appears to decrease monotonically with increasing  $h/H$ . The trend differentiates insignificantly among different wall-working conditions. Hence, further analyses are based on all data points ( $n = 74$ ).

It has been shown, e.g., [1, 5, 6], that  $T_m$  typically increases with  $h/H$  within the upper quarter of wall height and roughly keeps constant before  $h/H$  reaching about 0.7-0.8, then decreases with larger  $h/H$  until at round zero at the bottom of the wall. While for  $T_t$ , it increases monotonically with increasing  $h/H$ . They together result in the decreasing of measured  $\eta$  values against increasing  $h/H$ . On average, the measured  $\eta$  values are greater than 1.0 within  $h/H = 0$  and about  $h/H = 0.50$ , suggesting underestimation of nail loads if taken as  $T_t$ . For greater depth (i.e.,  $h/H > 0.50$ ), nail loads would generally be overestimated if taken as  $T_t$ . The reason for this is that the nail load data were collected from soil nail walls built following the top-down construction procedure,

TABLE 2: Calibration outcomes based on both  $\eta = f(T_t/P_a/A_t)$  and  $\eta = f(h/H)$  using data group 1 ( $n = 74$ ).

Case	Simple formulation		Constants		Model factor, M		Spearman's $\rho$ value between model factor M and						
	Name	Expression*	$a$	$b$	$\mu_M$	$COV_M$	$\eta$	$K_a$	$\gamma$	$h$	$q_s$	$S_h S_v$	$T_N$
Generalized model factor approach	Exponential	$\eta = a \times \exp(b \times T_t/P_a/A_t)$	1.19	-1.77	1.00	0.558	0.09	0.20	0.08	0.00	0.47	0.89	0.06
	Linear	$\eta = a \times (T_t/P_a/A_t) + b$	-0.92	1.05	1.00	0.580	0.01	0.45	0.11	0.00	0.44	0.90	0.00
	Logarithmic	$\eta = a \times \ln(T_t/P_a/A_t) + b$	-0.33	0.26	1.00	0.538	0.23	0.14	0.11	0.00	0.36	0.91	0.23
	Power	$\eta = a \times [T_t/P_a/A_t]^b$	0.34	-0.47	1.00	0.535	0.54	0.09	0.13	0.00	0.32	0.98	0.54
Calibration to $h/H$	Exponential	$\eta = a \times \exp(b \times h/H)$	2.05	-2.11	1.00	0.439	0.18	0.64	0.12	0.15	0.18	0.04	0.27
	Linear	$\eta = a \times (h/H) + b$	<b>-1.45</b>	<b>1.53</b>	<b>1.00</b>	<b>0.424</b>	<b>0.25</b>	<b>0.34</b>	<b>0.08</b>	<b>0.13</b>	<b>0.16</b>	<b>0.05</b>	<b>0.06</b>
	Logarithmic	$\eta = a \times \ln(h/H) + b$	-0.71	0.20	1.00	0.434	0.52	0.77	0.10	0.42	0.16	0.03	0.33
	Power	$\eta = a \times (h/H)^b$	0.39	-0.72	1.00	0.474	0.01	1.00	0.07	0.01	0.19	0.04	0.23

Note: \*  $P_a$  (101 kPa) is the atmospheric pressure, and  $A_t$  ( $1.5\text{ m} \times 1.5\text{ m} = 2.25\text{ m}^2$ ) is the typical tributary area. They are introduced to make the empirical correction term  $\eta$  dimensionless.

TABLE 3: Outcomes of correlation tests between measured  $\eta$  values and values of input parameters based on data group 1 ( $n = 74$ ).

Input parameter	Spearman's rank correlation test		Pearson's correlation test	
	$\rho$	$p$ value	$\rho$	$p$ value
Coulomb Earth pressure coefficient, $K_a$	-0.09	0.43 > 0.05	-0.20	0.09 > 0.05
Soil unit weight, $\gamma$	-0.24	0.04 < 0.05	-0.12	0.32 > 0.05
Depth of nail head, $h$	<b>-0.71</b>	<b>0.00 &lt; 0.05</b>	<b>-0.64</b>	<b>0.00 &lt; 0.05</b>
Surcharge, $q_s$	0.07	0.54 > 0.05	0.02	0.88 > 0.05
Tributary area, $S_h S_v$	-0.10	0.38 > 0.05	-0.03	0.80 > 0.05

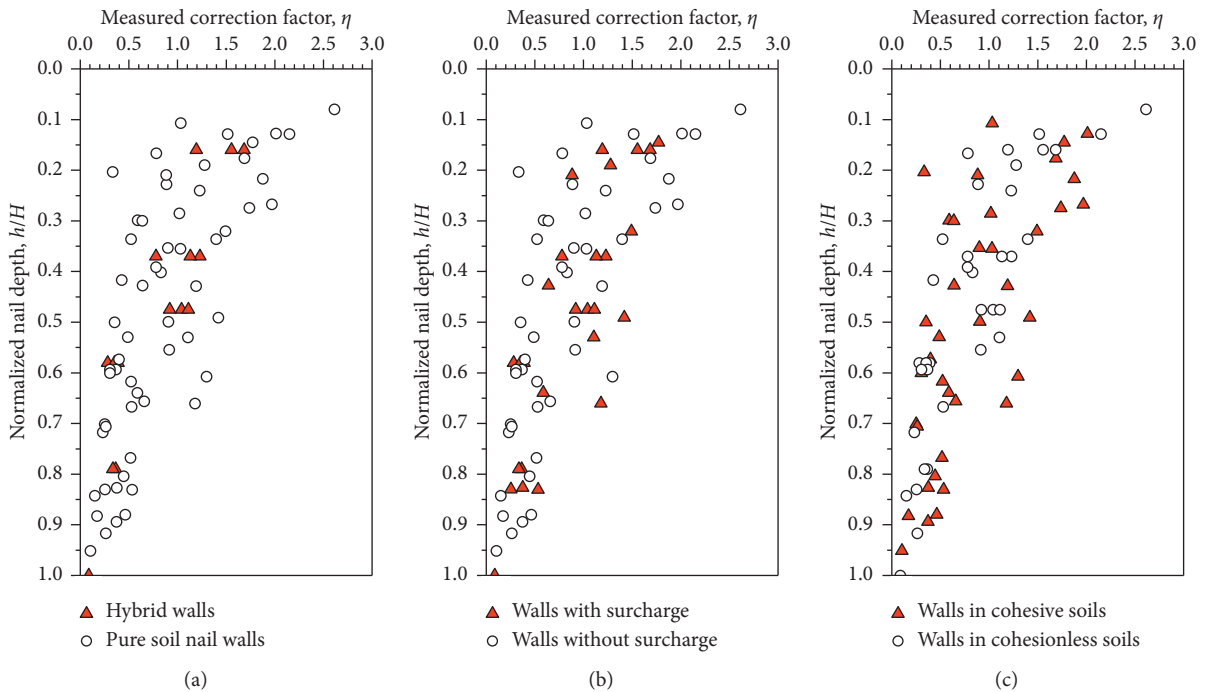


FIGURE 3: Measured correction factor  $\eta$  versus normalized nail depth  $h/H$  for different data subsets grouped based on soil nail wall-working conditions.

which resulted in larger lateral deformations and hence more mobilization of nail tensile loads at shallower depth (i.e., closer to the top of the walls).

Again, the four simple expressions were adopted, i.e., exponential, linear, logarithmic, and power functions. Steps to determine the formulation of  $\eta = f(h/H)$  are similar to those for  $\eta = f(T_t/P_a/A_t)$ . Calibration outcomes

using data group 1 ( $n = 74$ ) are summarized in Table 2. The smallest  $COV_M$  is achieved as 0.424 when  $\eta$  is a linear function of  $h/H$ . Spearman's rank correlation test outcomes showed that, in this case, the model factor  $M$  is not correlated to  $T_N$  and any input parameters at a level of significance of 5%. Therefore, the calibration outcomes are satisfactory.

Figure 4(a) shows the plots of measured versus computed nail loads using Equation (1) with  $\eta = a \times (h/H) + b$  and  $a = -1.45$  and  $b = 1.53$  (from Table 2). The majority of the data points scatter within  $M = T_m/T_N = 0.5$  and 2. The causes of deviation of data points from the line of  $T_m/T_N = 1$  include the randomness and spatial variability of soil properties, variation in time to record the strain gauge readings, systematic errors in conversion from strain gauge readings to nail loads, and underlying model errors of Equation (1), as explained in [6]. Figure 4(b) shows the plots of model factors against computed nail loads, and expectedly, there is no visual trend between  $M$  and  $T_N$  as the  $p$  value is larger than 0.05.

Based on Table 2, taking the correction term  $\eta$  in Equation (1) as a linear function of  $h/H$  gives the best outcomes in terms of  $COV_M$ . As such, Equation (1) is now expressed as follows:

$$T_N = \left( a \times \left( \frac{h}{H} \right) + b \right) K_a (\gamma h + q_s) S_h S_v, \quad (4)$$

where  $a = -1.45$  and  $b = 1.53$  based on data group 1.

**4.3. Validation and Update of the Developed Simplified Nail Load Model.** The measured nail loads in data group 2 are plotted against the corresponding computed nail loads using Equation (4) with  $a = -1.45$  and  $b = 1.53$ , as shown in Figure 4(a). The data points basically fall between  $M = 0.5$  and  $M = 1.5$ . Based on data group 2, the model factor of Equation (4) is found to have a mean of  $\mu_M = 1.19$  with a COV of  $COV_M = 0.325$ . These values are comparable to those using data group 1, which are 1.00 and 0.424, respectively. A two-sample Kolmogorov–Smirnov test was applied to the two model factor datasets. The results showed that the two distributions are not significantly different at a level of significance of 0.05. Furthermore, Spearman's rank correlation test is applied to the computed model factors against the computed nail loads, giving Spearman's  $\rho = -0.25$  and  $p$  value = 0.47 > 0.05 as shown in Figure 4(b). The correctness of Equation (4) is thus demonstrated.

Data group 2 is now merged into data group 1 to form a larger data group ( $n = 74 + 11 = 85$ ). This larger data group is then used to update the empirical constants  $a$  and  $b$  in Equation (4). The final optimal values are  $a = -1.45$  and  $b = 1.55$  after rounded up to two decimal places, which are very close to those previously determined based on data group 1. The corresponding mean and COV of the model factor are  $\mu_M = 1.00$  and  $COV_M = 0.412$ . No dependencies between  $M$  and  $T_N$  or any input parameters are detected. Equation (4) with  $a = -1.45$  and  $b = 1.55$  is the proposed simplified nail load model in the present study.

**4.4. Influence of Ratio of  $\delta/\phi$  on  $\eta$ .** The ratio of friction angle at facing-soil interface ( $\delta$ ) and soil friction angle ( $\phi$ ) was taken as 1/2 in the analyses presented above. The influence of ratio of  $\delta/\phi$  on the calibration outcomes is examined using all data groups. Figure 5 shows that as the  $\delta/\phi$  ratio increases from 0 to 1.0, the minimal  $COV_M$  decreases from 0.419 to 0.403, given  $\mu_M$  is maintained at 1.00. The reduction is even smaller within the typical range of interest, i.e.,  $\delta/\phi$  from 1/2

to 2/3. From a practical point of view, the influence of  $\delta/\phi$  on the minimal  $COV_M$  value is judged to be negligible. Hence, using  $\delta/\phi = 1/2$  in the previous analyses is justified.

**4.5. Characterization of Distribution of Model Factor.** The model uncertainty of Equation (4) with  $a = -1.45$  and  $b = 1.55$  for estimation of nail loads was shown to have  $\mu_M = 1.00$  and  $COV_M = 0.412$ . Figure 6 shows the cumulative distribution function plot of the model factors. The vertical axis is the standard normal variable,  $z$ . The horizontal axis is in log scale.

Visually, a first-order polynomial seems adequate to capture the overall data trend. This is quantitatively confirmed by the outcomes of Kolmogorov–Smirnov (K-S) test that was applied to the logarithm of the model factor ( $M$ ) values. The K-S test results suggested that the logarithm of the  $M$  values can be considered to be significantly drawn from normally distributed populations. This means that  $M$  can be taken as a lognormal random variable. The K-S test was also applied directly to the  $M$  values, which suggested that  $M$  can also be taken as a normal random variable. However, the main disadvantage of using normal distribution model is that negative  $M$  values could be generated using the Monte Carlo simulation technique, which is physically impossible based on the definition of  $M$  (i.e., measured to computed nail load). From this perspective, model factor  $M$  is always considered lognormally distributed in the literature (e.g., [36–38]). Cautions are required when taking  $M$  as a normal random variable in reliability-based design or calibration of resistance factors for load and resistance factor design methods.

## 5. Comparisons to Default and Modified FHWA Simplified Nail Load Models

The default FHWA simplified model to estimate maximum loads in soil nails is based on an empirical trapezoid envelope roughly fitted to the data collected by Banerjee et al. [22]. The model equation is written as follows [1, 4, 5]:

$$T_N = \eta K_a (\gamma H + q_s) S_h S_v. \quad (5)$$

Parameters in the equation are as defined earlier in this paper. Equations (4) and (5) are similar in formulation but there are two differences. First, the height of wall,  $H$ , is used in Equation (5), while for Equation (4), the depth of nail head,  $h$ , is used. Second, the expression of the empirical correction term,  $\eta$ , is different.  $\eta$  for the default FHWA simplified model is a piecewise function of  $h/H$  expressed as follows:

$$\eta = \begin{cases} a \times \left( \frac{h}{H} \right) + b, & \text{for } 0 < \left( \frac{h}{H} \right) \leq 0.2, \\ c, & \text{for } 0.2 < \left( \frac{h}{H} \right) \leq 0.7, \text{ and} \\ d - e \times (h/H), & \text{for } 0.7 < \left( \frac{h}{H} \right) \leq 1, \end{cases} \quad (6)$$

where the function  $\eta$  contains a total of five empirical constants, including  $a = 1.25$ ,  $b = 0.50$ ,  $c = 0.75$ ,  $d = 2.03$ , and

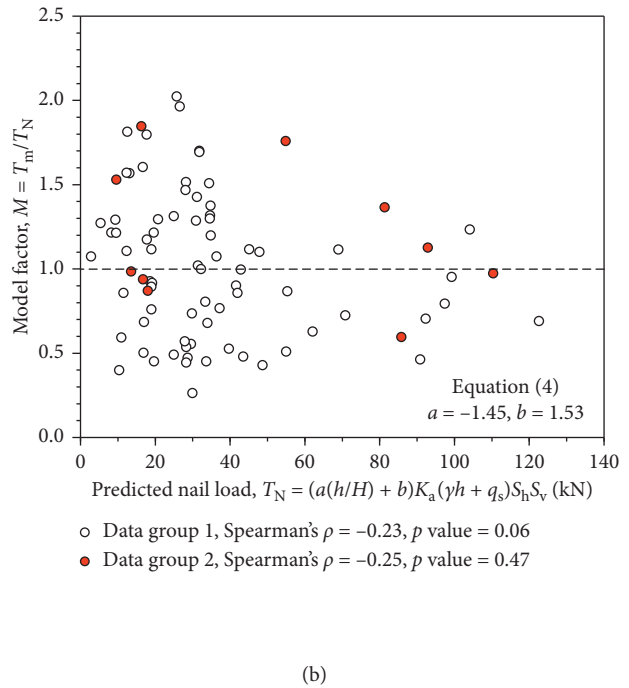
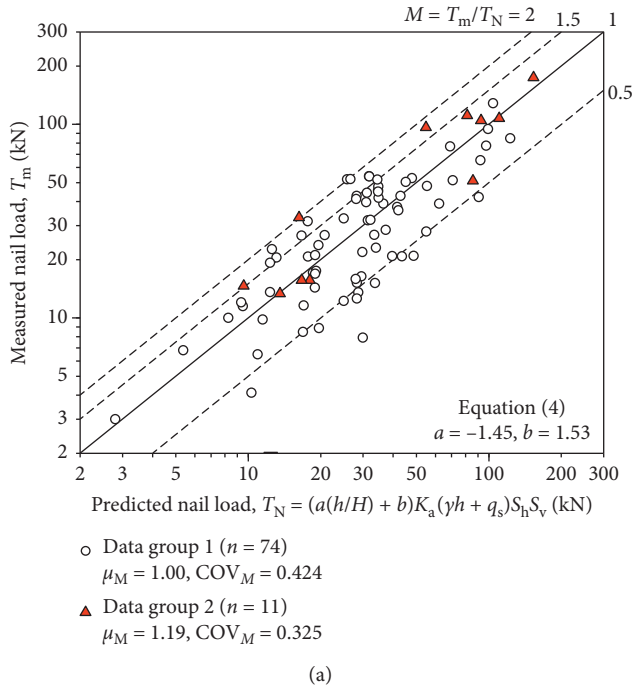


FIGURE 4: Analyses of Equation (4) using different data groups: (a) measured versus calculated nail load; (b) model factor versus calculated nail load.

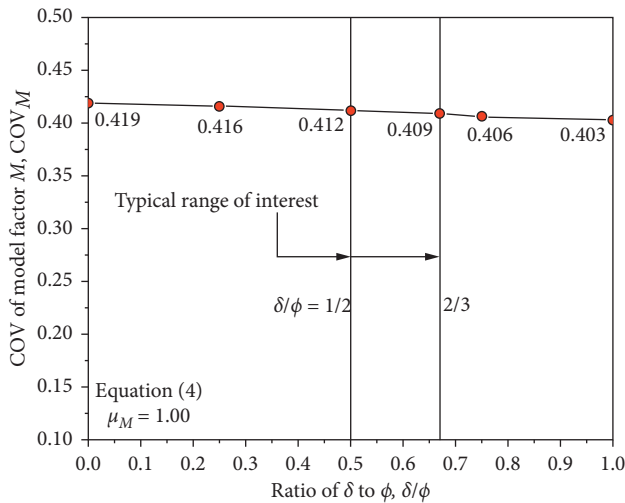


FIGURE 5: Influence of ratio of  $\delta$  to  $\phi$  on optimization outcomes of COV of model factor ( $COV_M$ ) for Equation (4).

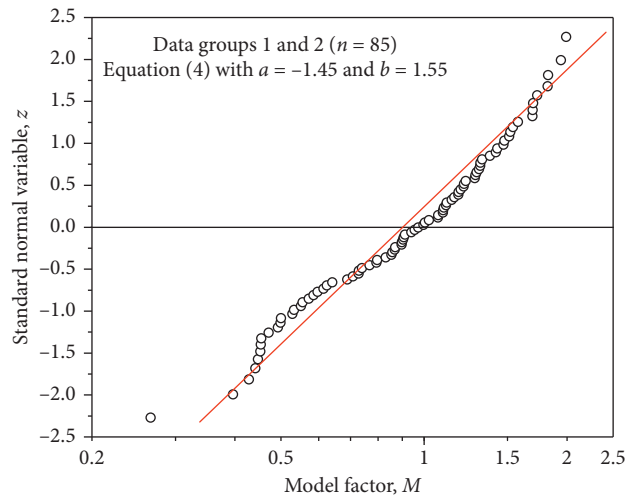


FIGURE 6: Cumulative distribution function plots of model factor of Equation (4) using all nail load data ( $a = -1.45$ ;  $b = 1.55$ ).

$e = -1.83$ . The model uncertainty of the default FHWA simplified model was evaluated by [6]. They concluded that the performance of Equation (5) jointly with Equation (7) is unsatisfactory, and then they modified the expression of  $\eta$  for accuracy improvement as follows:

$$\eta = \left[ \frac{S_h S_v}{A_t} \right]^a \times \left[ -\left( \frac{h}{H} \right)^2 + b \left( \frac{h}{H} \right) + c \right]. \quad (7)$$

The number of empirical constants were reduced to three, i.e.,  $a$ ,  $b$ , and  $c$ . The values of the empirical constants are  $a = -0.67$ ,  $b = 0.84$ , and  $c = 0.25$  for nails during or at

completion of wall construction. Equation (5) jointly with Equation (7) is called modified FHWA simplified nail load estimation model in this paper.

The empirical constants  $a$ ,  $b$ , and  $c$  in Equation (7) were calibrated using a subset of the database presented in this study, i.e.,  $n = 45$  [6]. Now the total number of data points has been expanded to 85. To allow a fair comparison, Equation (7) was recalibrated using the present expanded database. The optimal set of  $a$ ,  $b$ , and  $c$  values was computed as  $a = 0.04$ ,  $b = -0.14$ , and  $c = 1.20$ , after rounded to two decimal places. The model factor of the modified FHWA simplified nail load equation was then reestimated. After

TABLE 4: Comparisons of model accuracy in estimation of maximum nail loads among different models.

Method	Model equation	Empirical term, $\eta^*$	Empirical constants					$\mu_M^{**}$	COV $_M^{**}$	M correlated to	
			$a$	$b$	$c$	$d$	$e$			$T_N$	Input para.
The present study	$T_N = \eta K_a (\gamma h + q_s) S_h S_v$	$\eta = a \times (h/H) + b$	-1.45	1.55	—	—	—	1.00	0.412	No	None
Default FHWA simplified model	$T_N = \eta K_a (\gamma h + q_s) S_h S_v$	(1) $\eta = a \times (h/H) + b$ , if $0 < h/H \leq 0.2$ , (2) $\eta = c$ , if $0.2 < h/H \leq 0.7$ , (3) $\eta = d - e \times h/H$ , if $0.7 < h/H \leq 1$ .	1.25	0.50	0.75	2.03	-1.83	0.59	0.516	Yes	$S_h S_v, K_a$
Modified FHWA simplified model	$T_N = \eta K_a (\gamma h + q_s) S_h S_v$	$\eta = [(S_h S_v)/A_t]^a \times [-(h/H)^2 + b(h/H) + c]$	0.04	-0.14	1.20	—	—	1.00	0.454	No	None

Note:  $*A_t$  ( $1.5 \text{ m} \times 1.5 \text{ m} = 2.25 \text{ m}^2$ ) is the typical tributary area;  $**$  based on both data groups, i.e., data groups 1 and 2 ( $n = 85$ ).

recalibration, the model factor of the modified FHWA simplified model has a mean of 1.00 and a COV of 0.454.

A comparison of model uncertainty of each nail load estimation model using all data groups is presented in Table 4. The default FHWA simplified model is excessively conservative since on average it overestimates the maximum nail loads by about 40%. The spread in prediction quantified as COV $_M$  is over 50%. Moreover, the model factor of the default FHWA simplified model is statistically correlated to calculated  $T_N$  values and input parameters of  $S_h S_v$  and  $K_a$ . All these suggest unsatisfactory performance of the default FHWA simplified model in prediction of nail loads during or at completion of wall construction. While for the recalibrated modified FHWA simplified model and the simplified model proposed by the present study, based on the collected data (i.e., data groups 1 and 2), both models are much better than the default FHWA model as they are accurate on average, and the dependency issue of the model factors is not present. Nonetheless, the present model is more advantageous as it has less scatter in prediction, i.e., COV $_M = 0.412$  for the present model versus COV $_M = 0.454$  for the recalibrated modified FHWA model. Last, the present model has only two empirical constants, compared to five and three for the default and modified FHWA simplified models, respectively.

## 6. Concluding Remarks

A simplified model for estimation of maximum tensile loads for soil nails during or at completion of wall construction is developed in this study based on a total of 85 measured data collected from instrumented soil nail walls reported in the literature. The formulation of the developed simplified model has two multiplicative components: one is the theoretical nail loads expressed as the product of lateral active Earth pressure at depth of the nail head and the tributary area where the nail head centers; the other is a simple correction term (function) with two empirical constants introduced for improvement of estimation accuracy. The 85 collected measured nail load data are divided into two data groups. Data group 1 is used to determine the optimal values of the two empirical constants in the simple correction term using both the generalized model factor framework

approach and the approach of model factor as a function of input parameters introduced in Dithinde et al. [18]. Here, model factor is defined as the ratio of measured to calculated nail load. Then the developed simplified nail load model is validated using data group 2. After validation, the two data groups are merged into one larger dataset and used to update the values of the two empirical constants in the proposed simplified nail load equation.

Based on the collected nail load data, the model factor of the developed simplified nail load estimation equation has a mean of 1.00 and a COV of about 40%. Moreover, the model factor is not statistically correlated to the magnitude of the calculated nail load or any input parameters of the proposed nail load equation. In addition, there are less empirical constants in the present simplified nail load model equation compared to the default and modified FHWA simplified models [1, 4–6], i.e., the number of empirical constants is two versus five and three. Finally, the model factor of the proposed simplified model is characterized as a lognormal random variable based on the result of the Kolmogorov–Smirnov test.

The simplified nail load model developed in this study is compatible with the current soil nail wall design framework proposed in the FHWA soil nail wall design manual [1]. Also, the model uncertainty of the simplified model has been quantified and therefore the model is practically valuable to both direct reliability-based design and load and resistance factor design (LRFD) of internal limit states of soil nail walls, i.e., nail pullout limit state and nail tensile yield strength limit state.

Last, it is reminded that design methodologies, construction techniques, and site conditions differ from one soil nail wall project to another. Hence, the nail load database developed in this study should be taken as a “general” database. The proposed model based on such a database does not necessarily apply to any specific soil nail wall projects. In practice, design engineers must review and compare all the conditions against those specified in the present database and utilize their expertise to judge the suitability of the proposed default model. Moreover, for cases where project-specific nail load data are available, the Bayesian updating approaches (e.g., [39–41]) can be employed to refine the proposed default model to reflecting the specific site conditions of the projects.

## Data Availability

The data used to support the findings of this study are available from the corresponding author upon request.

## Conflicts of Interest

The authors declare that they have no conflicts of interest.

## References

- [1] C. A. Lazarte, H. Robinson, J. E. Gómez, A. Baxter, A. Cadden, and R. Berg, *Geotechnical Engineering Circular No. 7 Soil Nail Walls—Reference Manual*, U.S. Department of Transportation Publication No. FHWA-NHI-14-007, Federal Highway Administration (FHWA), Washington, DC, USA, 2015.
- [2] I. Juran and V. Elias, *Soil Nailed Retaining Structures: Analysis of Case Histories*, Geotechnical Special Publication No. 12, ASCE, New York, NY, USA, 1987.
- [3] I. Juran, G. Baudrand, K. Farrag, and V. Elias, “Kinematical limit analysis for design of soil-nailed structures,” *Journal of Geotechnical Engineering*, vol. 116, no. 1, pp. 54–72, 1990.
- [4] C. A. Lazarte, *Proposed Specifications for LRFD Soil-Nailing Design and Construction*, NCHRP Report 701, Transportation Research Board, National Research Council, Washington, DC, USA, 2011.
- [5] C. A. Lazarte, V. Elias, D. Espinoza, and P. J. Sabatini, *Geotechnical Engineering Circular No. 7 Soil Nail Walls*, U.S. Department of Transportation Publication No. FHWA0-IF-03-017, Federal Highway Administration (FHWA), Washington, DC, USA, 2003.
- [6] P. Lin, R. J. Bathurst, and J. Liu, “Statistical evaluation of the FHWA simplified method and modifications for predicting soil nail loads,” *Journal of Geotechnical and Geoenvironmental Engineering*, vol. 143, no. 3, article 04016107, 2017b.
- [7] K. K. Phoon and F. H. Kulhawy, “Characterization of model uncertainties for laterally loaded rigid drilled shafts,” *Géotechnique*, vol. 55, no. 1, pp. 45–54, 2005.
- [8] K. K. Phoon and C. Tang, “Model uncertainty for the capacity of strip footings under positive combined loading,” in *Proceedings of Geotechnical Safety and Reliability: Honoring Wilson H. Tang (GSP 286)*, J. Huang, G. A. Fenton, L. Zhang, and D. V. Griffiths, Eds., pp. 40–60, ASCE, Reston, VA, USA, June 2017.
- [9] C. Tang and K. K. Phoon, “Model uncertainty of cylindrical shear method for calculating the uplift capacity of helical anchors in clay,” *Engineering Geology*, vol. 207, pp. 14–23, 2016.
- [10] P. Lin, R. J. Bathurst, S. Javankhoshdel, and J. Liu, “Statistical analysis of the effective stress method and modifications for prediction of ultimate bond strength of soil nails,” *Acta Geotechnica*, vol. 12, no. 1, pp. 171–182, 2017a.
- [11] R. J. Bathurst, T. M. Allen, and A. S. Nowak, “Calibration concepts for load and resistance factor design (LRFD) of reinforced soil walls,” *Canadian Geotechnical Journal*, vol. 45, no. 10, pp. 1377–1392, 2008.
- [12] T. M. Allen and R. J. Bathurst, “Improved simplified method for prediction of loads in reinforced soil walls,” *Journal of Geotechnical and Geoenvironmental Engineering*, vol. 141, no. 11, article 04015049, 2015.
- [13] Y. Yu and R. J. Bathurst, “Analysis of soil-steel bar mat pullout models using a statistical approach,” *Journal of Geotechnical and Geoenvironmental Engineering*, vol. 141, no. 5, article 04015006, 2015.
- [14] D. M. Zhang, K. K. Phoon, H. W. Huang, and Q. F. Hu, “Characterization of model uncertainty for cantilever deflections in undrained clay,” *Journal of Geotechnical and Geoenvironmental Engineering*, vol. 141, no. 1, article 04014088, 2015.
- [15] International Organization for Standardization, *General Principles on Reliability of Structures*, ISO2394, Geneva, Switzerland, 2015.
- [16] K. K. Phoon, “Role of reliability calculations in geotechnical design,” *Georisk: Assessment and Management of Risk for Engineered Systems and Geohazards*, vol. 11, no. 1, pp. 4–21, 2017.
- [17] P. Lin and R. J. Bathurst, “Influence of cross-correlation between nominal load and resistance on reliability-based design for simple linear soil-structure limit states,” *Canadian Geotechnical Journal*, vol. 55, no. 2, pp. 279–295, 2018.
- [18] M. Dithinde, K. K. Phoon, J. Ching, L. M. Zhang, and J. V. Retief, “Statistical characterization of model uncertainty,” in *Chapter 5, Reliability of Geotechnical Structures in ISO2394*, K. K. Phoon and J. V. Retief, Eds., pp. 127–158, CRC Press/Balkema, Boca Raton, FL, USA, 2016.
- [19] R. J. Byrne, D. Cotton, J. Porterfield, C. Wolschlag, and G. Ueblacker, *Manual for Design and Construction Monitoring of Soil Nail Wall*, U.S. Department of Transportation Publication No. FHWA-SA-96-069R, Federal Highway Administration (FHWA), Washington, DC, USA, 1998.
- [20] AASHTO, *AASHTO LRFD Bridge Design Specifications*, AASHTO, Washington, DC, USA, 7th edition, 2014.
- [21] FHWA, *Design and Construction of Mechanically Stabilized Earth Walls and Reinforced Soil Slopes—Volume I*, FHWA-NHI-10-024, FHWA GEC 011-Vol I, Federal Highway Administration (FHWA), Washington, DC, USA, 2009.
- [22] S. Banerjee, A. Finney, T. D. Wentworth, and M. Bahiradhan, “Evaluation of design methodologies for soil-nailed walls,” in *Volume 2: Distribution of Axial Forces in Soil Nails Based on Interpolation of Measured Strains*, Washington State Department of Transportation (WA-RD 371.2), Olympia, WC, USA, 1998.
- [23] C. K. Shen, S. Bang, J. M. Romstad, L. Kulchin, and J. S. Denatale, “Field measurement of an earth support system,” *Journal of the Geotechnical Engineering Division*, vol. 107, no. GT12, pp. 1625–1642, 1981.
- [24] T. Holman and T. Tuozzolo, “Load development in soil nails from a strain-gauge instrumented wall,” in *Proceedings of 2009 International Foundation Congress and Equipment Expo Contemporary Topics in Ground Modification, Problem Soils, and Geo-Support*, pp. 25–32, Orlando, FL, USA, March 2009.
- [25] Y. Q. Wei, *Development of equivalent surcharge loads for the design of soil nailed segment of MSE/Soil nail hybrid retaining walls based on results from full-scale wall instrumentation and finite element analysis*, Ph.D. thesis, Texas Tech University, Lubbock, TX, USA, 2013.
- [26] M. J. Zhang and Z. X. Guo, “Research on behaviors of soil nailing by field test,” *Chinese Journal of Geotechnical Engineering*, vol. 23, no. 3, pp. 319–323, 2001, in Chinese.
- [27] J. L. Duan, Y. H. Tan, Y. W. Fan, and F. Lu, “Field testing study on composite soil nailing,” *Chinese Journal of Mechanical Engineering*, vol. 23, no. 12, pp. 2128–2132, 2004, in Chinese.
- [28] G. H. Yang, “Calculation of soil nail forces and displacement in soil nailing retaining wall,” *Rock and Soil Mechanics*, vol. 33, no. 1, pp. 137–146, 2012, in Chinese.
- [29] J. Cao, M. G. Xiao, and X. H. Xu, “Estimating of the axial nailing stress in soil nailed walls,” *Soils and Foundations*, vol. 27, no. 3, pp. 80–82, 2013, in Chinese.

- [30] A. N. Liu, Q. Z. Lai, R. G. Wu, and C. Y. Su, "Monitoring and analysis of soil nail axial force on the upper part of a soil nail wall for the deep foundation," *Journal of Sichuan University (Natural Science Edition)*, vol. 28, no. 1, pp. 59–62, 2015, in Chinese.
- [31] S. G. Wang, Q. W. Duan, and Y. Y. Wang, "Research on the soil nail wall by field tests," *Building Science*, vol. 26, no. 1, pp. 90–92, 2010, in Chinese.
- [32] A. Sawicki, D. Lesniwvska, and M. Kulczykowski, "Measured and predicted stresses and bearing capacity of a full scale slope reinforced with nails," *Soils and Foundations*, vol. 28, no. 4, pp. 47–56, 1998.
- [33] J. P. Turner and W. G. Jensen, "Landslide stabilization using soil nail and mechanically stabilized earth walls: case study," *Journal of Geotechnical and Geoenvironmental Engineering*, vol. 131, no. 2, pp. 141–150, 2005.
- [34] S. W. Jacobsz and T. S. Phalanndwa, "Observed axial loads in soil nails," in *Proceedings of 15th African Regional Conference on Soil Mechanics and Geotechnical Engineering*, Maputo, Mozambique, July 2011.
- [35] B. M. Das, *Principles of Foundation Engineering*, Cengage Learning, Boston, MA, USA, 2018.
- [36] D. Kim and R. Salgado, "Load and resistance factors for external stability checks of mechanically stabilized earth walls," *Journal of Geotechnical and Geoenvironmental Engineering*, vol. 138, no. 3, pp. 241–251, 2012a.
- [37] D. Kim and R. Salgado, "Load and resistance factors for internal stability checks of mechanically stabilized earth walls," *Journal of Geotechnical and Geoenvironmental Engineering*, vol. 138, no. 8, pp. 910–921, 2012b.
- [38] P. Lin, J. Liu, and X. Yuan, "Reliability analysis of soil nail walls against external failures in layered ground," *Journal of Geotechnical and Geoenvironmental Engineering*, vol. 143, no. 1, article 04016077, 2017d.
- [39] Y. Wang, Z. Cao, and D. Li, "Bayesian perspective on geotechnical variability and site characterization," *Engineering Geology*, vol. 203, pp. 117–125, 2016.
- [40] L. Zhang, D. Q. Li, X. S. Tang, Z. J. Cao, and K. K. Phoon, "Bayesian model comparison and characterization of bivariate distribution for shear strength parameters of soil," *Computers and Geotechnics*, vol. 95, pp. 110–118, 2018.
- [41] W. H. Zhou, F. Tan, and K. V. Yuen, "Model updating and uncertainty analysis for creep behavior of soft soil," *Computers and Geotechnics*, vol. 100, pp. 135–143, 2018.

## Research Article

# Rapid Disaster Data Dissemination and Vulnerability Assessment through Synthesis of a Web-Based Extreme Event Viewer and Deep Learning

**P. Shane Crawford** <sup>1</sup>, **Mohammad A. Al-Zarrad**<sup>1</sup>, **Andrew J. Graettinger**<sup>1</sup>,  
**Alexander M. Hainen**<sup>1</sup>, **Edward Back**<sup>1</sup> and **Lawrence Powell**<sup>2</sup>

<sup>1</sup>Department of Civil, Construction and Environmental Engineering, The University of Alabama, Tuscaloosa, AL 35401, USA

<sup>2</sup>Alabama Center for Insurance Information and Research, The University of Alabama, Tuscaloosa, AL 35401, USA

Correspondence should be addressed to P. Shane Crawford; [pscrawford@crimson.ua.edu](mailto:pscrawford@crimson.ua.edu)

Received 22 July 2018; Revised 16 October 2018; Accepted 17 October 2018; Published 13 November 2018

Guest Editor: André Barbosa

Copyright © 2018 P. Shane Crawford et al. This is an open access article distributed under the Creative Commons Attribution License, which permits unrestricted use, distribution, and reproduction in any medium, provided the original work is properly cited.

Infrastructure vulnerability has drawn significant attention in recent years, partly because of the occurrence of low-probability and high-consequence disruptive events such as 2017 hurricanes Harvey, Irma, and Maria, 2011 Tuscaloosa and Joplin tornadoes, and 2015 Gorkha, Nepal, and 2017 Central Mexico earthquakes. Civil infrastructure systems support social welfare, thus viability and sustained operation is critical. A variety of frameworks, models, and tools exist for advancing infrastructure vulnerability research. Nevertheless, providing accurate vulnerability measurement remains challenging. This paper presents a state-of-the-art data collection and information extraction methodology to document infrastructure at high granularity to assess preevent vulnerability and postevent damage in the face of disasters. The methods establish a baseline of preevent infrastructure functionality that can be used to measure impacts and temporal recovery following a disaster. The Extreme Events Web Viewer (EEWV) presented as part of the methodology is a GIS-based web repository storing spatial and temporal data describing communities before and after disasters and facilitating data analysis techniques. This web platform can store multiple geolocated data formats including photographs and 360° videos. A tool for automated extraction of photography from 360° video data at locations of interest specified in the EEWV was created to streamline data utility. The extracted imagery provides a manageable data set to efficiently document characteristics of the built and natural environment. The methodology was tested to locate buildings vulnerable to flood and storm surge on Dauphin Island, Alabama. Approximately 1,950 buildings were passively documented with vehicle-mounted 360° video. Extracted building images were used to train a deep learning neural network to predict whether a building was elevated or nonelevated. The model was validated, and methods for iterative neural network training are described. The methodology, from rapidly collecting large passive datasets, storing the data in an open repository, extracting manageable datasets, and obtaining information from data through deep learning, will facilitate vulnerability and postdisaster analyses as well as longitudinal recovery measurement.

## 1. Introduction

Capturing pre- and postevent disaster data is critical in furthering the measurement science for disaster resilience as well as assessing vulnerable aspects of the built environment. Preevent data provide the fundamental ground-truth of the built and natural environment before a disaster strikes which is used as a baseline to measure impact and performance

following an event. Additionally, these data are used to assess vulnerable areas of a community and direct mitigation strategies in these areas, which can lessen the effects of extreme events. To adequately assess the built and natural environment, data must be collected in granular spatial and temporal formats. Although significant progress has been made in the application of science and technology to reduce disaster effects, there are still many challenges related to

preparation, response, and recovery. In 2004, the National Science Board recognized the need for a cyber-integrated scientific research platform for collection, transfer, mining, and storage of perishable data [1]. In 2008, The National Science and Technology Council (NSTC) Subcommittee on Disaster Reduction put forth a list of grand challenges for disaster reduction. The first of these challenges is to provide hazard and disaster information where and when that information is needed. The subcommittee also recommended that disaster information should be provided through a real-time mechanism of data collection and interpretation that is readily available and usable by all scientists instead of a select few [2]. Collecting data and information are critical in addressing additional grand challenges that include developing hazard mitigation strategies and technologies, reducing the vulnerability of infrastructure, and assessing disaster resilience [2].

Currently, data collected by disaster reconnaissance teams for a particular study are not typically integrated, distributed, or stored and made available for use by others in the scientific community; they are used primarily in isolation by separate research teams and may be published in a limited capacity with the results of investigations carried out with the data. Current strategies have advanced research in postdisaster studies for earthquakes [3–6], tornadoes [7–11], and hurricanes [12–15]. Reuse of the collected information is typically in the form of the meta-analysis of literature and not the collected data. Advances in data collection and storage technologies offer the ability to meet these needs with modern sensors, platforms, and data collection techniques. However, emerging data collection equipment requires standards, protocols, and workflows, and data storage technology and software require data management strategies to be effectively implemented to further research goals. Big data issues often accompany the new technology and make management and extraction of salient information difficult [16]. The processes of information extraction from these datasets are critical for researchers to further measurement science. Additionally, long-term storage and dissemination of data across organizational platforms and stakeholders is needed to break down siloed research fields and benefit public understanding of disasters and mitigation strategies. A methodology of disaster data collection is needed, from developing data collection standards and protocols to storing and disseminating the collected data across organizational boundaries. Extracting information from collected data will enhance measurement science and fuel fundamental research for community vulnerability as well as other research areas where ground-truth information of the natural and manmade environment promotes research.

The methodology presented consists of an approach to collecting highly granular spatial and temporal data and storing the collected data in a web-based repository. Figure 1 presents the workflow. Large image datasets are collected using vehicle-mounted 360° video. The web-based repository, called the Extreme Events Web Viewer (EEWV), stores geolocated data in a temporal format. It is

an open platform where data can be uploaded in the location collected and provided with label data, for example vulnerability metrics for community infrastructure. The EEWV provides tools to extract manageable image datasets from large video files which can be efficiently analyzed. Implementing deep learning approaches to combine labelled imagery with a pretrained model architecture allows new models to be derived to classify unlabelled images. The approach can be useful in disaster and failure scenarios as well as recovery studies. The methodology is meant to facilitate development of hazard mitigation strategies to reduce vulnerability to infrastructure and assess disaster resilience. A case study of flood vulnerability on Dauphin Island in Alabama, a barrier island in the Gulf of Mexico that has experienced major damage from past hurricanes, is presented to illustrate the methodology. Flood vulnerability analyses, such as the case study presented for Dauphin Island, can aid in disaster and mitigation planning for these communities. Federal money has been spent to purchase homes in flood-prone areas [17] and establish the National Flood Insurance Program [18] along with various other mitigation techniques. A federal report released in 2005 showed that every \$1 spent on disaster mitigation saved \$4 in future costs of disasters [19]. Effectively prioritizing mitigation strategies requires knowledge of where the vulnerabilities in communities exist. Multiple vulnerability models, such as the Disaster Resilience of Place model [20], have been created to provide a framework for vulnerability assessment. The methods described here can quickly provide the fundamental information needed to drive these mitigation plans and vulnerability assessments in a format which is easily accessible to all community stakeholders.

## 2. Methodology

*2.1. Extreme Events Web Viewer.* The Extreme Events Web Viewer (EEWV) has been created at The University of Alabama to facilitate data storage, dissemination, and analysis of community and extreme event data. The EEWV is a web-based Internet clearinghouse using geographic information systems (GIS) tools to facilitate fundamental research and disseminate data to a broad user base. Data describing a community before or after an event is uploaded and displayed geographically and provided with attribute data to facilitate geospatial analyses. Survey locations storing photographs, PDFs, audio files, or other data types, are added to the EEWV in a spatial and temporal format and symbolically display attribute metadata. Building locations are marked separate from survey locations and can be used for data integration and analysis. Integration includes consolidating all survey location data describing a single building. One analysis technique, which will be presented as part of the methodology detailed here, extracts images from passive, vehicle-mounted 360° video data. The EEWV is set up to accept new analysis tools to broaden the resources available to researchers. Figure 2(a) shows the data types stored in the EEWV, including survey locations shown in magenta (when highlighted, survey

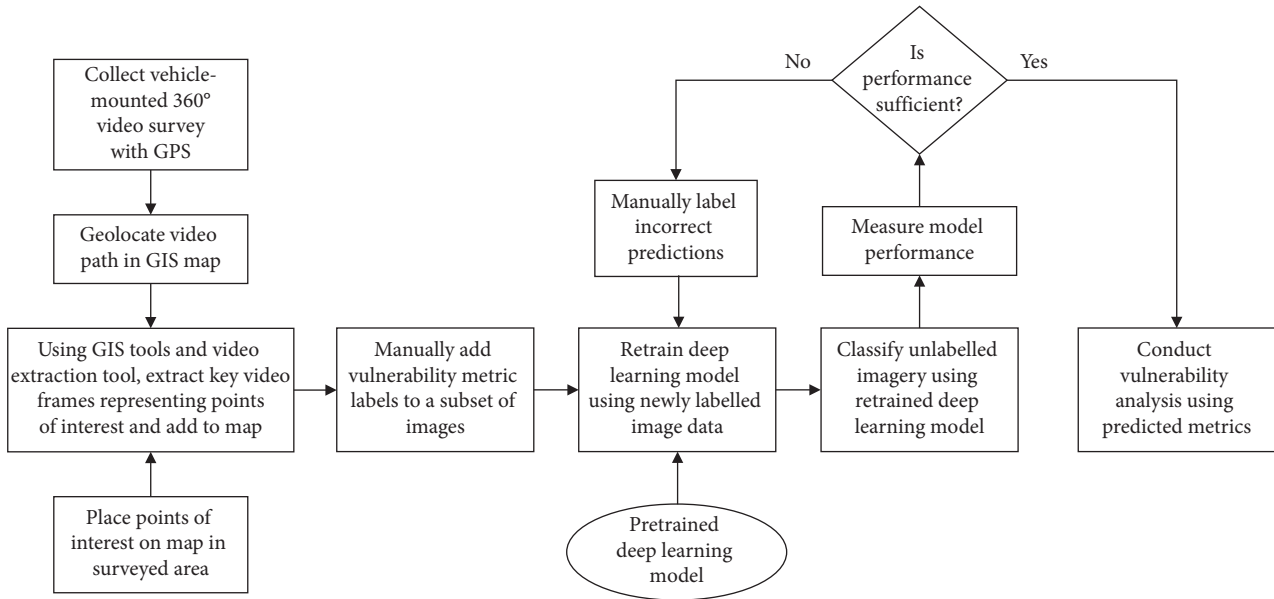


FIGURE 1: Workflow for vulnerability analysis using presented methodology.



FIGURE 2: Data visualization in the Extreme Events Web Viewer for survey locations and 360° videos.

locations change to cyan, as shown in the figure), building locations shown in blue, and video paths depicted as green lines. When a survey location is selected, a data view window, shown in Figure 2(b), opens to display data stored in the survey location.

Postdisaster reconnaissance has typically been conducted by groups of researchers traversing a damaged area on foot and collecting digital photography, video, or human subject surveys, describing infrastructure performance, social impacts, or other effects of the studied

disaster. This approach works well for studies requiring close-range inspection with photography to highlight specific details, such as determining component failure mechanisms, but this method requires large investments of personnel and time if data describing a large area are required. This often leads to expensive reconnaissance trips or studies focused on a small portion of the affected area. Additionally, information describing the preevent functionality of the community is often not prioritized, even in high-risk areas such as coastal communities that are

vulnerable to hurricanes, flooding, and tornado and Dixie Alleys, which have high vulnerability to tornadoes. Many communities in seismic regions track infrastructure with seismic design or retrofits. Recently, researchers have explored using drone videos to capture larger areas in smaller amounts of time [21]. This method is beneficial, but drone platforms suffer from short battery life, legal requirements such as the need for pilots to maintain line-of-sight with the platform, airspace permission, and pushback from community members due to privacy concerns. An approach for rapid, passive, and large-volume data collection using vehicle-mounted 360° cameras with onboard Global Positioning System (GPS) sensors has been created to meet the needs of researchers following an event as well as before a disaster occurs.

The EEWV facilitates visualization of collected videos using GPS latitude, longitude, and timestamp values. Figure 3(a) shows GPS location points collected using a vehicle-mounted camera. GPS point locations can vary from up to subfoot accuracy in the costliest units to lower accuracy depending on the model used [22, 23]. Many modern cameras are GPS-integrated, but external GPS sensors can be paired to increase the positioning accuracy when GPS-integrated camera accuracy is not sufficient for analysis. GPS location points typically vacillate around the true driven path with varying error based on the GPS used (GPS locations were measured up to nearly 10 meters from true locations in Figure 3), but large errors can be encountered when collecting video in the presence of disrupting infrastructure such as large buildings or trees, highway overpasses, etc. To increase the positioning accuracy in this study, location values were snapped to roadway lines obtained from the publicly available United States Census Bureau Topologically Integrated Geographic Encoding and Referencing (TIGER) data repository, as shown in Figure 3(b). Snapping moved points closer to the exact location where GPS points were taken in this study, as evidenced in Figure 3. This procedure may not be necessary in situations where highly accurate GPS is used. In this study, photo extraction was more accurate when GPS locations were snapped. A video path polyline was created by connecting snapped GPS points with sequential timestamps, which captured the correct trajectory even when multiple passes are conducted on a roadway. The video path line typically follows TIGER roadway line geometry exactly, but in some cases inaccuracies exist due to the snapping procedure. Due to location inaccuracy, GPS points were snapped to incorrect roadway lines in some cases. This occurred when a GPS point was located closer to an incorrect roadway line than the roadway where the point was collected. In most cases, this occurred at roadway intersections and where dual carriageways were represented in the TIGER data with single carriageways. GPS locations at intersections were rarely used for image extraction, due to images typically being extracted only at the nearest GPS location to a building, and the error at dual carriageways was reduced because buildings are typically located further from these roadway types than single carriageways.

A potential source of error in the geolocation process used here occurs where TIGER linework does not match the actual roadways, for example if a new road has been constructed and TIGER roadway lines have not been updated to accommodate the change. Leveraging alternative open-source roadway line repositories, such as OpenStreetMap [24], may reduce the error stemming from this effect. Additionally, many communities maintain highly accurate roadway lines of their own. These should be used when available as they typically constitute the most accurate account of roadway location in that community. Additionally, inaccurate data can be manually corrected using GIS software packages.

It should be noted that these approaches have been tested and calibrated for suburban and moderate-density urban environments. High-density urban environments provide their own difficulty in locating and extracting data with high accuracy, and more extensive testing in these regions is needed. Furthermore, due to the highly variable nature of global infrastructure, especially in postdisaster scenarios when roadways may not be accessible or viable, a single geolocation methodology may not be applicable in all contexts, but the current work is a substantial contribution to current data collection methods.

The geolocation approach enhances visualization of collected videos in the EEWV by updating vehicle location on a map while a video is playing. Figure 4 shows the vehicle-mounted 360° video display approach with the map and vehicle location in Figure 4(a). A video player opens in the EEWV when a video path is selected, as shown in Figure 4(b). The video player includes pan and zoom features which allow users to manually inspect collected videos to analyze the environment captured in the video. The video GPS locations are initially invisible to the user. Each GPS location includes a timestamp which is synced to the video time. When the video time matches the timestamp of a GPS location, the GPS location is selected and becomes visible as a cyan point (similar to survey locations which highlight cyan when selected) on the video path to show the location of the vehicle. The field of view corresponding to the selected video is shown in Figure 4(a) as a yellow triangle. Survey and building locations can be added in the EEWV, either manually or through upload of GIS shapefiles, to store information gained from videos.

The vehicle-mounted camera approach allows researchers to rapidly capture large passive datasets describing buildings, distribution networks, and other infrastructure. This approach creates a large volume of remotely sensed data that require a large time investment to manually analyze. Data can be uploaded from the field to the EEWV when Internet connection is available, although in postevent scenarios data should be managed locally when the state of the impacted community prevents large data transmission. While the open format of the EEWV allows multiple researchers to conduct an assessment simultaneously, which would make the data mining process more efficient, automated data extraction tools significantly improve assessment speed. The Extreme Events Video



FIGURE 3: Geolocated GPS points (a) before being snapped to roadway lines and (b) after being snapped to roadway lines.

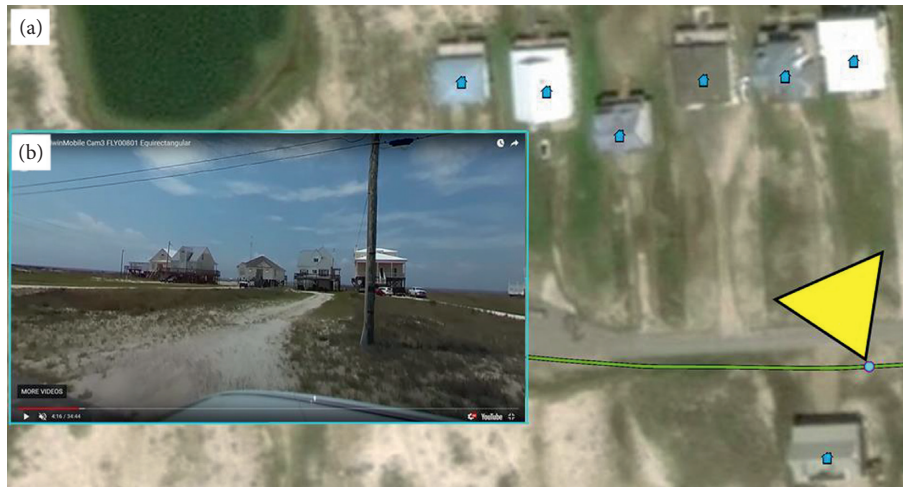


FIGURE 4: Geolocated vehicle-mounted 360° video visualization technique in the EEVW.

Capture (EEVC) tool allows users to automatically extract images from the 360° video at locations of interest.

*2.2. Extreme Events Video Capture Tool.* A video display window for the EEVC tool was created using Unity, a graphic development platform, and provides an interface to interact with 360° video geometry and extract images at specified video geometric orientations. The tool can function manually but is intended to interact with the EEVW to automate image extraction and upload processes. Figure 5 shows the video display window of the EEVC tool. The video time is displayed, and buttons allow the user to pause, slow the video down to quarter or half speed, or speed up to two or five times normal playback speed. Users can pan horizontally and vertically, and the orientation of the video geometry along both axes is displayed. Screenshots of the displayed window can be extracted and saved as Portable Network Graphics (PNG) image files.

A custom tool was created to automate extraction of images from 360° videos by calling the video player and providing parameters which allow the tool to interface with the EEVW. The parameters include a video path identifier, a maximum distance boundary, a camera direction relative to the direction of travel, and a processing method for photo extraction. Figure 6 provides a graphical illustration of the image extraction process. The video path identifier corresponds to the intended video path stored in the EEVW, for the example provided in Figure 6, Video Path 1 would be used as the input parameter. The maximum distance boundary is the distance from the camera to the furthest point of interest in the video, measured in meters. This parameter defines a boundary around the video path that specifies only building points visible in the video specified by the video path identified. The maximum distance boundary is shown in red in Figure 6, where one side of the boundary is shown. The boundary also extends the same distance on the opposite side of the video path, though is not shown.

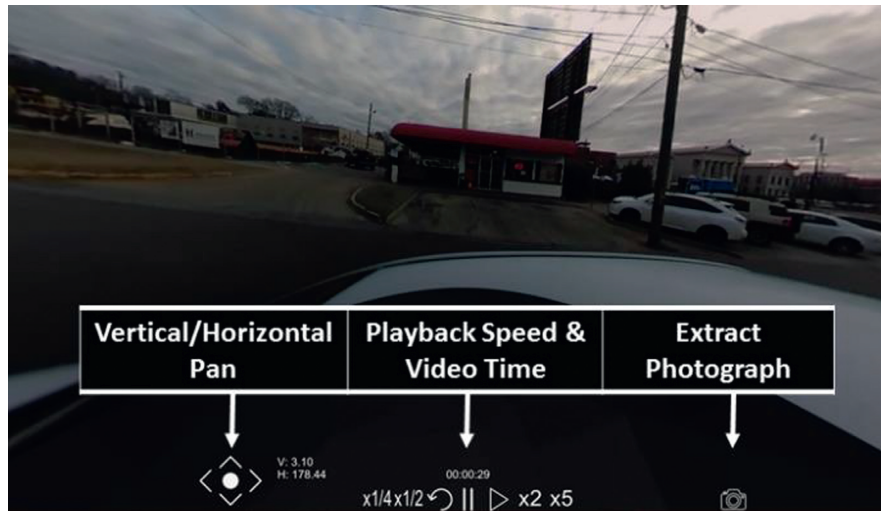


FIGURE 5: Extreme Events Video Capture tool video display window.

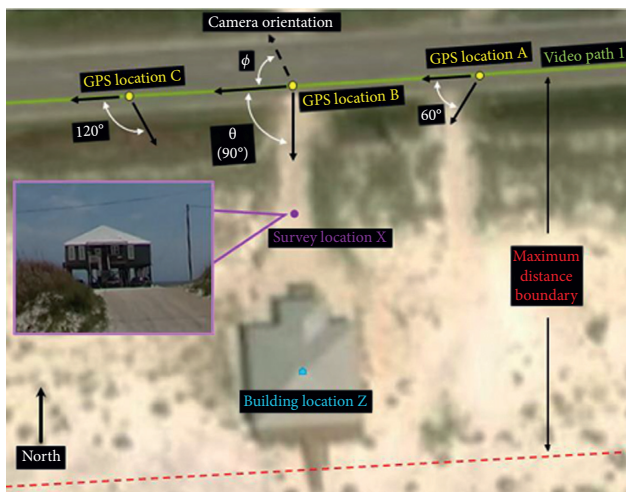


FIGURE 6: Illustration of the automated image extraction process.

Latitude and longitude values for building locations within the maximum distance boundary are used to calculate rotation angles between vehicle direction of travel and building point locations. The camera orientation relative to direction of travel parameter is used to calibrate the direction of travel to  $0^\circ$  in the horizontal plane of the video. Many commercial  $360^\circ$  cameras do not specify the orientation on the device, therefore the camera can be mounted to the car at various angles (e.g., with  $0^\circ$  pointed backwards, etc.). This parameter is optional; technicians are typically trained before data collection, but errors in camera mounting are possible. To illustrate this scenario, the camera direction relative to direction of travel in Figure 6 is illustrated as the  $\phi$  variable. The processing method parameter allows users to extract images from the closest vehicle GPS location (typically located at a  $90^\circ$  between the direction of travel and building location), or at specified angles provided as a list. Providing a list of angles allows images to be extracted showing different sides of the point of interest, for example, if images of

the front façade and both side walls of Building Location Z in Figure 6 are desired, the user could input  $60^\circ$ ,  $90^\circ$ , and  $120^\circ$  to extract images from GPS locations A, B, and C, respectively. Specifying angles is also useful in scenarios where occlusions occur in the image extracted at the closest GPS location. The process shown in Figure 6 would iterate through all building locations within the maximum distance boundary specified for the identified video path to extract images at all angles specified. Once the process has completed, survey locations are created at a location half of the distance between the building location and the GPS location used for the photo extraction. If multiple angles are specified in the processing method parameter, multiple survey locations will be created for each building point. If the area is visited multiple times to document temporal change, survey locations will multiply and potentially become difficult to manage. To streamline data management, all survey locations extracted for a building location are automatically related to the building location. When the building location is selected, all images stored in related survey locations will be displayed.

This methodology allows researchers to rapidly collect data for large areas to document a community before a disaster occurs to benchmark infrastructure functionality or determine vulnerability just after a disaster to preserve perishable data describing infrastructure performance in a disaster scenario or at multiple times after a disaster to document recovery progress. The methodology was developed to capture large passive video datasets, parse the data into manageable image files, and provide the ability to store, visualize, and add value to the collected data through the EEVW. The image extraction technique can be applied to supplement other data collection equipment such as static  $360^\circ$  photography offered by the Natural Hazards Engineering Research Infrastructure RAPID Facility [25]. While these methods provide data where and when needed, meeting the grand challenge posed by the NSTC subcommittee, there arises a big data issue. In general, big data refers to high volume and high variety data that require cost-effective and advanced forms of information

processing to enable better understanding of the data [16]. The EEVC tool extracts manageable datasets from collected videos, but for a researcher or community official to manually inspect these large volumes of data to obtain useful information, especially at multiple time intervals, a large time investment is required.

*2.3. Deep Learning Approaches.* Recent advances in machine and deep learning approaches have facilitated automated information extraction techniques from image data. To meet the needs of the research community as well as communities located in vulnerable areas, an approach has been developed to synthesize the data collection tools described earlier with a deep learning application. The use of deep learning can automate measurements in image data, thereby reducing big data issues created by production of large image datasets.

Deep learning, a branch of the wider machine learning research field, has shown recent advancements in image classification, in some cases producing results with higher accuracy than humans [26]. Deep learning models use neural networks to process and classify images. TensorFlow, a free and open-source software library facilitating machine learning frameworks has been developed by Google and is implemented to classify imagery stored in the EEWV. TensorFlow was created to support and implement machine learning models [27]. Image classification is conducted using the Inception model [28, 29]. The Inception model trains a convolutional neural network (CNN) to classify images, where each layer of the neural network classifies an aspect of the image using feature representation and similarity measurement (e.g., one layer may implement an edge detection algorithm, while another layer may group similar pixel color values). Features created in each layer of the CNN are general enough to account for image variation. Outputs from each layer are fed into subsequent layers, increasing abstraction throughout (e.g., edge detection layers feed into shape detection layers). The Inception model was originally trained on 100,000 images in 1,000 classification labels. To adopt the Inception model for new image classifications, transfer learning can be used to retrain the model using new imagery.

An application has been developed at the University of Alabama to facilitate transfer learning using the TensorFlow architecture and Inception model to train CNNs using images with new labels. The newly trained neural network can then be used to classify new imagery into the label classes specified in retraining. The output includes a label class prediction and a label class likelihood for each image. Classification accuracy is dependent on the number of images used in training as well as variation present in the training images. Common sources of image variation include resolution, light, and color. To create a robust classification model, training images should include an adequate amount of variation to account for the variation encountered in the images being classified by the model. Once classification predictions have been made, the information

can be associated with building locations to provide a spatial perspective of the classified information.

#### *2.4. Dauphin Island Case Study, Results, and Discussion.*

The data collection and deep learning approaches were applied to a case study on Dauphin Island, Alabama. Dauphin Island is a barrier island in the Gulf of Mexico located at the south end of Mobile County. The west side of the island is made up primarily of vacation and rental property, while the east end holds more permanent residents [30]. The west side is entirely beachfront while the east side contains maritime forests, as shown in Figure 7(a). The island is vulnerable to hurricanes that form in the Gulf of Mexico, with infrastructure damage due to wind and flooding as well as coastal erosion common aftereffects of these severe storms. Hurricane Camille in 1969 flooded over half of the island. Hurricane Frederic, which made landfall on Dauphin Island in 1979 as a Category 4 hurricane, swept away the viaduct connecting Dauphin Island to mainland Alabama. Recently, Hurricane Ivan caused nearly one-fourth of the island to be flooded by two feet of water, Hurricane Katrina damaged homes on the west side of the island with high winds and storm surge [31], and damage was also reported from Hurricane Nate in 2017. Hurricanes Ivan and Katrina destroyed over 300 homes on the island [30]. The island has decreased in size by an estimated 16% since 1958 due to coastal erosion [32]. Despite the island's natural vulnerability and changing shorelines, construction has continued and residents tolerate the disruptions caused by these events [33].

Vehicle-mounted 360° video was collected covering nearly all roadways and all buildings on the island. Data collection procedures required less than one day. The EEVC tool played videos at normal playback speed, therefore the image extraction process equaled the video time. Image extraction was unsupervised; therefore no investment of researcher time was necessary. The small time investment relative to conventional approaches verifies the efficiency of the methodology and promotes temporal data collection at regular intervals to monitor change. Figure 7(b) shows the video paths, denoted by green lines, collected for the island. Figure 7(c) shows building locations on the island. In total, almost 2000 building locations were manually placed in the EEWV. Figure 7(d) shows survey locations created to store building images extracted from the 360° videos. Data were not collected in gated communities in the southeast of the island or in government-owned compounds on the east edge of the island. Over 2,150 images were collected at building locations in the EEWV, with multiple images extracted for buildings which were documented in multiple videos. Images were extracted for 1,752 building locations on Dauphin Island.

The extracted photographs were used to train a deep learning image classification model. The model included three class labels: elevated building, nonelevated building, and unknown class. The model is intended to locate buildings vulnerable to storm surge, which can be catastrophic for nonelevated buildings. The unknown class



FIGURE 7: Dauphin Island with (a) aerial overview, (b) collected video paths, (c) building locations, and (d) survey locations storing extracted images.

label accounts for images where no building is visible; without this class, images with no visible buildings would be classified as elevated or nonelevated, leading to decreased model performance. The existence of images with no building present is due to the maximum distance boundary specified for the videos. Buildings on the west side of the island are typically located farther from the roadway than buildings on the east side of the island. The maximum distance provided to the EEVC tool was large enough to capture buildings on the west side, but in cases on the east side of the island images were extracted from roadways where vegetation occluded visibility. Additional obstructions, such as vehicles in dual carriageways, sometimes occluded building visibility. Figure 8 displays images representing each class label.

The initial deep learning model was trained using 50 images per class. A classification test was run on a set of 120 images. The test set was created by collecting images representative of the image variation encountered on the island, with an equal representation between classes.

Images collected from the west side of the island typically show buildings constructed on elevated piers with open soft story and sandy soil with little to no vegetation, such as the elevated class image in Figure 8(a). Images collected from the east side of the island show buildings where construction typically varies between elevated piers with open soft story, elevated piers with enclosed soft story, and either slab-on-grade or crawlspace foundations, with grass and trees visible in the images, as shown in the nonelevated class image in Figure 8(b). Images in the unknown class were typically collected from the east side of the island where vegetation occluded building visibility, as shown in the unknown class image in Figure 8(c). Images containing multiple buildings were collected in areas with high building density. In these images, buildings centered in the image seemed to govern predictions, but lower likelihood values were noticed. Images that were incorrectly predicted in the classification test were inspected and an explanation of model inaccuracy is detailed below.



FIGURE 8: Image classes for deep learning model describing buildings on Dauphin Island. (a) Elevated, (b) nonelevated, and (c) unknown.

There exists a “semantic gap” between image pixels used in machine learning and semantic concepts perceived by humans [34] that causes inaccuracy in deep learning image classification. Inaccuracy can be difficult to locate and understand because the inception module contains many layers, and the output of each layer is withheld, with only a class prediction and likelihood provided for each image. Understandably, more complex images require more complexity in the image classification model. To illustrate potential sources of error in the model, Figure 9 presents a representative set of incorrectly predicted images. Figure 9(a) shows a nonelevated building which was predicted to be elevated. The columns supporting the walkway have similar geometry to piers used in elevated buildings, which would likely signify an elevated building. Figure 9(b) shows an elevated building which is off center in the image. The center of the image contains a high concentration of trees, commonly seen in unknown images, likely leading to the unknown prediction. The lower Figure 9(c) shows an elevated building classified as a nonelevated building. There are no discernible piers, and the sides of the building are not visible. Therefore, building geometry is evident but no distinguishing geometry would signify elevation in the classification algorithm, leading to a prediction of nonelevated building.

The natural variation in building design and construction material is expected to require a model with many training images to produce an accurate deep learning model. To increase model accuracy, an iterative approach to retraining was used. Images that were incorrectly predicted by the model trained on 50 images per class were manually classified and used to retrain the model. Two retrained models were created, using 75 images per class and 100 images per class. Figure 10 presents the precision-recall curves for the three models. A decreasing trend in model performance is seen as the number of images in the training set increases. As training sets increase in size, image variation is introduced for each class which may cause disrupt model classification instead of increasing model performance. At a certain point, the model will be able to isolate the image signal in the presence of increased variation, which will lead to increased model performance.

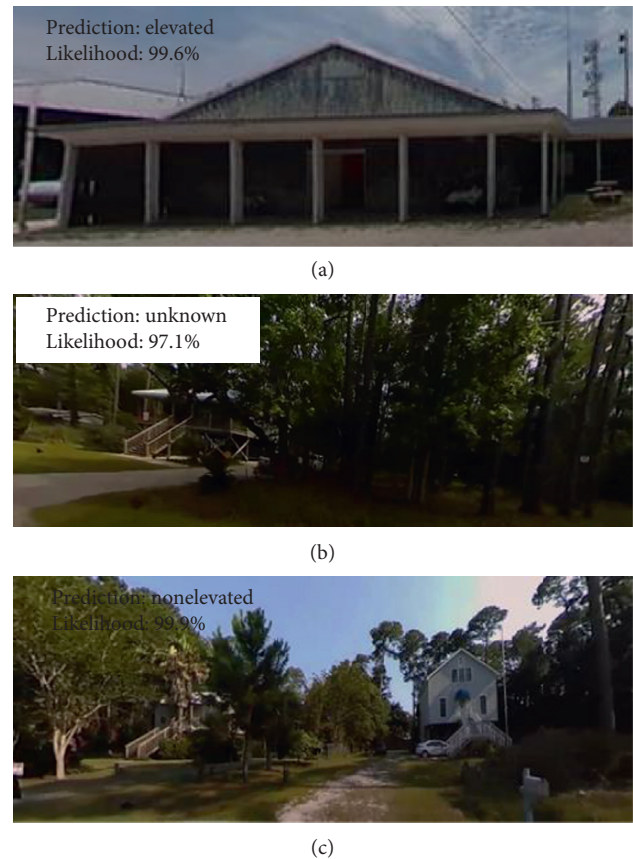


FIGURE 9: Incorrectly predicted images of buildings on Dauphin Island with class predictions of (a) elevated, (b) unknown, and (c) nonelevated structures.

Deep learning approaches typically require a large number of training images to reach a desired accuracy. The ImageNet project, designed to promote and enhance deep learning image classification by creating a large-scale image ontology, defines a set of 1,000 labels with an average of 500–1000 images per classification [35]. Therefore, the comparatively small set of images available for model training in this case study is insufficient to develop a high-performing deep learning model. Alternatively, the ability

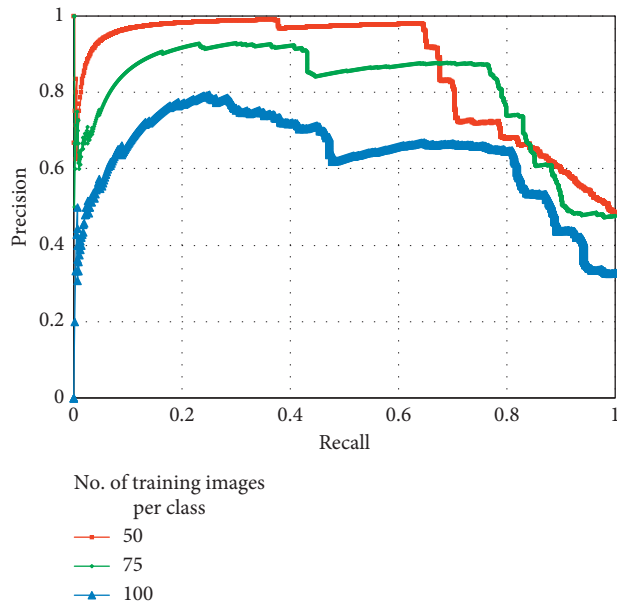


FIGURE 10: Precision-recall result of iterative model approach.

to capture large image datasets describing community infrastructure through an efficient data collection methodology and storage in a public portal provides the fundamental image data that researchers need to arrive at these high-performing models. Additionally, deep learning models have shown increased performance in image classification recently. For example, the annual ImageNet Large Scale Visual Recognition Challenge resulted in significant image classification error reduction from 2010 to 2015 [36]. Increased performance in emerging deep learning model architectures could facilitate the use of the models in vulnerability analyses.

Spatial analysis can be conducted with the information created in the data collection and deep learning approaches to support vulnerability analysis. Figure 11 presents the spatial results of the manual and deep learning approaches to building classification on Dauphin Island. The manual classification presented in Figure 11(a) shows that the west side of the island contains only elevated buildings, while the east side contains a mixture of elevated and nonelevated buildings. The deep learning predictions from a model trained on 100 images are presented in Figure 11(b). In general, the model predicted mostly elevated buildings on the west side of the island and a mixture of elevated and nonelevated buildings on the east side. Buildings in the unknown class prediction were excluded as they are not useful in vulnerability analysis. Buildings that were predicted to be unknown would require manual inspection to determine the building type, but the inspection process could be planned efficiently using the spatial results of the model. Elevated buildings incorrectly predicted to be nonelevated are problematic in a vulnerability analysis because they incorrectly signify higher vulnerability. The incorrect prediction becomes more problematic when nonelevated buildings are predicted as elevated, because

the comparatively higher level of vulnerability for these buildings would not be understood. Figure 11(c) shows the locations of the incorrect predictions. Red locations indicate nonelevated buildings predicted as elevated and yellow locations indicate elevated buildings predicted as nonelevated. The images at these locations can be labelled and used in the next iteration of deep learning model training.

Most elevated buildings on Dauphin Island are single-family residential structures. While a large percentage of the nonelevated buildings are also single-family residential, many are commercial, multifamily residential, government, and other building types. Disaster impacts to the non-residential building types have the potential to trigger cascading effects in the community. For example, damage to commercial buildings causing business disruptions can impact employment for residents of the island, and damage to schools can cause educational disruption and social problems for affected children. These represent a few of the community interdependencies which can be adversely affected by the disaster of flood vulnerability for nonelevated buildings.

### 3. Conclusions

Understanding the vulnerability of communities and measuring their changes through time are important for community leaders, governmental decision-makers, industry, and community stakeholders when creating plans for mitigation activities. A methodology to rapidly collect large, passive datasets in a spatial and temporal format was presented. The Extreme Events Web Viewer was created to store the collected data in a spatial, temporal, and publicly available format and add value to the data through analysis techniques. The Extreme Events Video Capture tool was created to facilitate extraction of image data from passively collected, vehicle-mounted 360° video. A deep learning application employing the Google TensorFlow architecture with the inception image classification model was created to obtain information from the extracted image data. A case study was presented to showcase how these tools could be combined to assess the vulnerability of buildings on Dauphin Island, Alabama. Reconnaissance was conducted on the island by driving accessible streets to document buildings. The collected data were geolocated and uploaded to the Extreme Events Web Viewer, and building images were extracted from the videos. A set of deep learning models was trained to classify building images as elevated, nonelevated, or unknown. Buildings on the island were manually classified, and a geospatial analysis of the deep learning model results was presented. An approach to quickly determine where incorrect classifications occurred was presented to show how the geospatial nature of the presented methodology would facilitate an iterative approach to deep learning model creation. The results of the case study conclude that the data collection, storage, and extraction approaches support deep learning model creation. An iterative approach to model training is required to

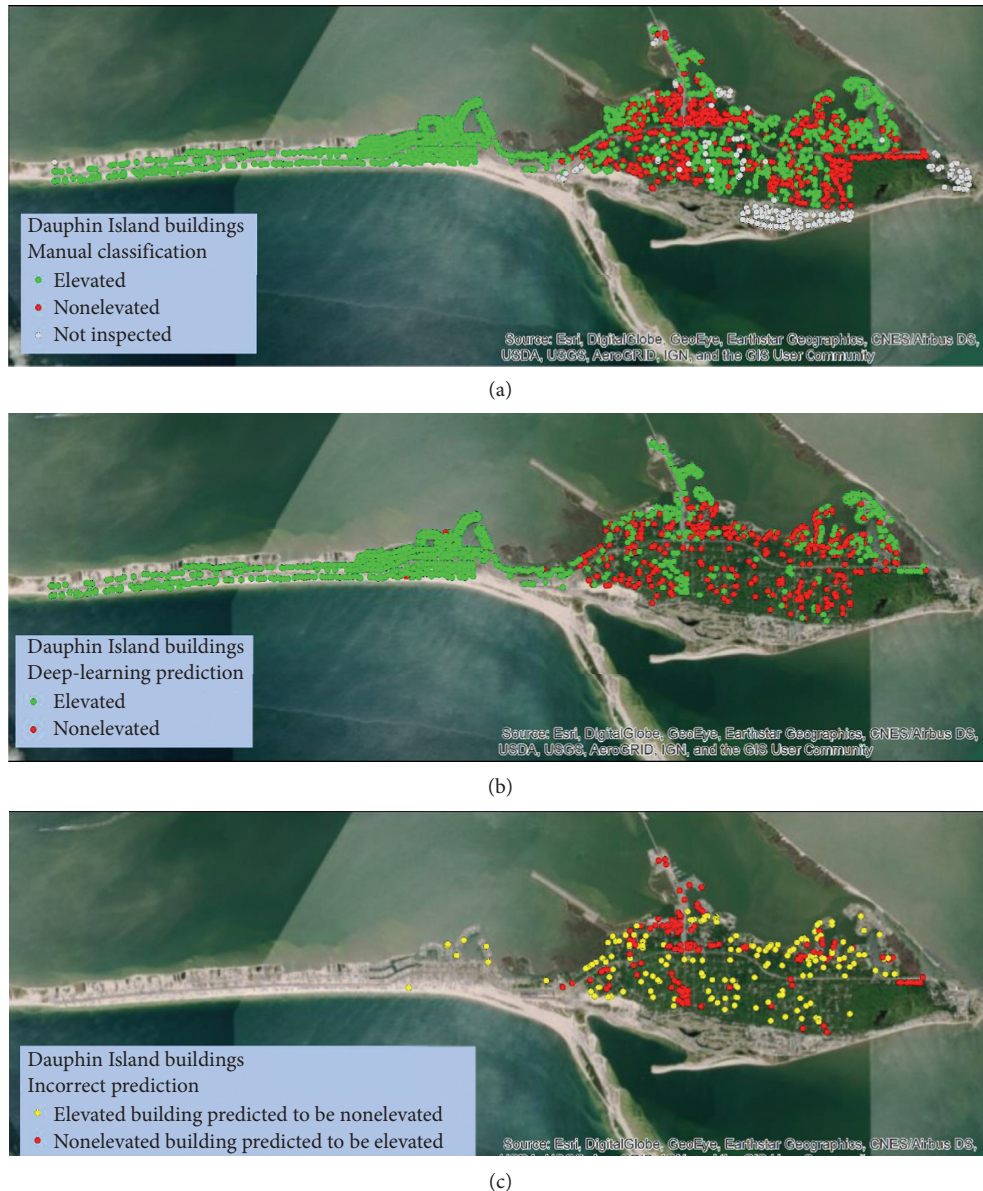


FIGURE 11: Buildings on Dauphin Island (a) manually classified and (b) predicted by a deep learning model, with (c) incorrectly classified building locations.

increase accuracy, and the model should be trained with images collected at varying daylight and seasonal stages and across communities.

The vulnerability assessment for Dauphin Island was restricted to a single vulnerability indicator for a single built environment system. The passive data collected in the methodology allow many systems of the built environment to be captured, including transportation and distribution networks and erosion control measures, among others. Deep learning image classification models created to assess vulnerability in these systems and track temporal changes due to vulnerability mitigation or disaster impacts could lead to increased community resilience. The ability to store large, passively collected data in the Extreme Events Web Viewer and extract information from the datasets using automated approaches for assessing and measuring changes to these

distinct, interdependent systems vulnerable to disasters will provide information where and when needed in a format that is available to the broader research community as well as decision-makers and community stakeholders to meet the needs of the NSB recommendations and NSTC grand challenges.

**Data Availability**

Data used in this study can be accessed at <http://extremeevents.caps.ua.edu/Maps/6>.

**Conflicts of Interest**

The authors declare that there are no conflicts of interest regarding the publication of this paper.

## Acknowledgments

This research has been jointly funded by The Center for Sustainable Infrastructure and The Alabama Center for Insurance Information and Research at the University of Alabama. The authors are thankful for the support from these research centers as well as the support from The Center for Advanced Public Safety at the University of Alabama.

## References

- [1] NSB (National Science Board), "Long-lived digital data collections: enabling research and education in the 21st century," June 2018, <http://www.nsf.gov/pubs/2005/nsb0540/nsb0540.pdf>.
- [2] NSTC (National Science and Technology Council), "Grand challenges for disaster reduction," June 2018, <https://www.sdr.gov/docs/SDRGrandChallengesforDisasterReduction.pdf>.
- [3] G. Brando, D. Rapone, E. Spacone et al., "Damage reconnaissance of unreinforced masonry bearing wall buildings after the 2015 Gorkha, Nepal, earthquake," *Earthquake Spectra*, vol. 33, no. S1, pp. S243–S273, 2017.
- [4] G. Brando, G. De Matteis, and E. Spacone, "Predictive model for the seismic vulnerability assessment of small historic centres: application to the inner Abruzzi Region in Italy," *Engineering Structures*, vol. 153, pp. 81–96, 2017.
- [5] H. Yu, M. A. Mohammed, M. E. Mohammadi et al., "Structural identification of an 18-story RC building in Nepal using post-earthquake ambient vibration and lidar data," *Frontiers in Built Environment*, vol. 3, p. 11, 2017.
- [6] D. Zekkos, M. Clark, M. Whitworth et al., "Observations of landslides caused by the April 2015 Gorkha, Nepal, earthquake based on land, UAV, and satellite reconnaissance," *Earthquake Spectra*, vol. 33, no. S1, pp. S95–S114, 2017.
- [7] A. J. Graettinger, D. Grau, J. Van De Lindt, and D. O. Prevatt, "GIS for the geo-referenced analysis and rapid dissemination of forensic evidence collected in the aftermath of the Tuscaloosa tornado," in *Proceedings of Construction Research Congress 2012: Construction Challenges in a Flat World*, pp. 2170–2179, West Lafayette, IN, USA, May 2012.
- [8] A. G. Kashani, P. S. Crawford, S. K. Biswas, A. J. Graettinger, and D. Grau, "Automated tornado damage assessment and wind speed estimation based on terrestrial laser scanning," *Journal of Computing in Civil Engineering*, vol. 29, no. 3, article 04014051, 2014.
- [9] E. D. Kuligowski, F. T. Lombardo, L. T. Phan, M. L. Levitan, and D. P. Jorgensen, *Final Report, National Institute of Standards and Technology (NIST) Technical Investigation of the May 22, 2011, Tornado in Joplin, Missouri*, No. National Construction Safety Team Act Reports (NIST NCSTAR-3), National Institute of Standards and Technology, Gaithersburg, MD, USA, 2014.
- [10] D. O. Prevatt, J. W. van de Lindt, A. Graettinger et al., *Damage Study and Future Direction for Structural Design following the Tuscaloosa Tornado of 2011*, University of Alabama, Tuscaloosa, AL, USA, 2011.
- [11] D. O. Prevatt, J. W. van de Lindt, E. W. Back et al., "Making the case for improved structural design: tornado outbreaks of 2011," *Leadership and Management in Engineering*, vol. 12, no. 4, pp. 254–270, 2012.
- [12] B. J. Adams, J. A. Womble, M. Z. Mio, J. B. Turner, K. C. Mehta, and S. Ghosh, *Collection of Satellite-Referenced Building Damage Information in the Aftermath of Hurricane Charley*, Natural Hazards Center, Boulder, CO, USA, 2004.
- [13] T. Comes and B. Van de Walle, "Measuring disaster resilience: the impact of hurricane sandy on critical infrastructure systems," *ISCRAM*, vol. 11, pp. 195–204, 2014.
- [14] K. R. Gurley, D. B. Roueche, G. Wong-Parodi et al., *Survey and Investigation of Buildings Damaged by Category III Hurricanes in FY 2016-17—Hurricane Matthew 2016*, Florida Department of Business and Professional Regulation, Tallahassee, FL, USA, 2017.
- [15] F. Lombardo, D. B. Roueche, R. J. Krupar, D. J. Smith, and M. G. Soto, "Observations of building performance under combined wind and surge loading from hurricane Harvey," in *Proceedings of AGU Fall Meeting Abstracts*, Orleans, LA, USA, December 2017.
- [16] A. De Mauro, M. Greco, and M. Grimaldi, "A formal definition of big data based on its essential features," *Library Review*, vol. 65, no. 3, pp. 122–135, 2016.
- [17] FEMA (Federal Emergency Management Agency), "Purchasing flood-prone property," June 2018, <https://www.fema.gov/news-release/2008/08/28/purchasing-flood-prone-property>.
- [18] E. O. Michel-Kerjan, "Catastrophe economics: the national flood insurance program," *Journal of Economic Perspectives*, vol. 24, no. 4, pp. 165–86, 2010.
- [19] MM Council, *Natural Hazard Mitigation Saves: An Independent Study to Assess the Future Savings from Mitigation Activities*, Vol. 68, National Institute of Building Sciences, Washington, DC, USA, 2005.
- [20] S. L. Cutter, L. Barnes, M. Berry et al., "A place-based model for understanding community resilience to natural disasters," *Global Environmental Change*, vol. 18, no. 4, pp. 598–606, 2008.
- [21] C. A. F. Ezequiel, M. Cua, N. C. Libatique et al., "UAV aerial imaging applications for post-disaster assessment, environmental management and infrastructure development," in *Proceedings of 2014 International Conference on Unmanned Aircraft Systems (ICUAS)*, pp. 274–283, IEEE, Orlando, FL, USA, May 2014.
- [22] J. F. Zumberge, M. B. Heflin, D. C. Jefferson, M. M. Watkins, and F. H. Webb, "Precise point positioning for the efficient and robust analysis of GPS data from large networks," *Journal of Geophysical Research: Solid Earth*, vol. 102, no. B3, pp. 5005–5017, 1997.
- [23] P. August, J. Michaud, C. Labash, and C. Smith, "GPS for environmental applications: accuracy and precision of locational data," *Photogrammetric Engineering and Remote Sensing*, vol. 60, no. 1, pp. 41–45, 1994.
- [24] OpenStreetMap, "OpenStreetMap," June 2018, <http://www.openstreetmap.org>.
- [25] NHERI (Natural Hazards Engineering Research Infrastructure), "Five year science plan: multi-hazard research to make a more resilient world," July 2017, [http://www.designsafe-ci.org/media/filer\\_public/20/6f/206f5d4a-5f7d-4ab6-b837-7c5f89c7b251/varwwwdesignsafe-ciorgmediacms\\_page\\_media595nheri\\_science\\_plan\\_july\\_2017.pdf](http://www.designsafe-ci.org/media/filer_public/20/6f/206f5d4a-5f7d-4ab6-b837-7c5f89c7b251/varwwwdesignsafe-ciorgmediacms_page_media595nheri_science_plan_july_2017.pdf).
- [26] D. Cireşan, U. Meier, and J. Schmidhuber, "Multi-column deep neural networks for image classification," arXiv preprint arXiv:1202.2745, 2012.
- [27] M. Abadi, P. Barham, J. Chen et al., "Tensorflow: a system for large-scale machine learning," in *Proceedings of 12th USENIX Symposium on Operating Systems Design and Implementation, OSDI 2016*, vol. 16, pp. 265–283, Savannah, GA, USA, June 2016.
- [28] C. Szegedy, V. Vanhoucke, S. Ioffe, J. Shlens, and Z. Wojna, "Rethinking the inception architecture for computer vision,"

- in *Proceedings of IEEE Conference on Computer Vision and Pattern Recognition*, pp. 2818–2826, Las Vegas, NV, USA, June 2016.
- [29] C. Szegedy, S. Ioffe, V. Vanhoucke, and A. A. Alemi, “Inception-v4, inception-resnet and the impact of residual connections on learning,” in *Proceedings of AAAI*, vol. 4, p. 12, San Francisco, CA, USA, February 2017..
- [30] C. M. Janasie and S. Deal, “Increasing climate resilience on Dauphin Island through land use planning,” June 2018, <http://masgjp.olemiss.edu/Advisory/dauphin-island-report-land-use-planning.pdf>.
- [31] NWS (National Weather Service), “Hurricane Katrina photos, Dauphin island and Mon luis island (southern Mobile County),” June 2018, [https://www.weather.gov/mob/katrina\\_part2](https://www.weather.gov/mob/katrina_part2).
- [32] R. A. Morton, “Historical changes in the Mississippi-Alabama barrier-island chain and the roles of extreme storms, sea level, and human activities,” *Journal of Coastal Research*, vol. 246, pp. 1587–1600, 2008.
- [33] NPR (National public Radio), “Alabama’s Tiny Dauphin island Cleaning up after hurricane Nate’s wallop,” June 2018, <https://www.npr.org/2017/10/09/556701153/alabamas-tiny-dauphin-island-cleaning-up-after-hurricane-nates-wallop>.
- [34] J. Wan, D. Wang, S. C. H. Hoi et al., “Deep learning for content-based image retrieval: a comprehensive study,” in *Proceedings of the 22nd ACM International Conference on Multimedia*, ACM, pp. 157–166, Orlando, FL, USA, 2014.
- [35] J. Deng, W. Dong, R. Socher, L. J. Li, K. Li, and L. Fei-Fei, “Imagenet: a large-scale hierarchical image database,” in *Proceedings of IEEE Conference on Computer Vision and Pattern Recognition, 2009 (CVPR 2009)*, IEEE, pp. 248–255, Miami, FL, USA, June 2009.
- [36] O. Russakovsky, J. Deng, H. Su et al., “Imagenet large scale visual recognition challenge,” *International Journal of Computer Vision*, vol. 115, no. 3, pp. 211–252, 2015.

## Research Article

# Error Source Analysis and Precision Assessment of Limit Equilibrium Methods for Rock Slopes

Xiaofan An <sup>1,2</sup>, Ning Li <sup>1</sup>, Peng Zhang,<sup>3</sup> and Wenbo Sun<sup>1</sup>

<sup>1</sup>Institute of Geotechnical Engineering, Xi'an University of Technology, Xi'an, China

<sup>2</sup>Department of Earth, Ocean and Atmospheric Sciences, University of British Columbia, Vancouver, Canada

<sup>3</sup>College of Transportation Science and Engineering, Nanjing Tech University, Nanjing, China

Correspondence should be addressed to Ning Li; [ningli@xaut.edu.cn](mailto:ningli@xaut.edu.cn)

Received 15 June 2018; Revised 21 August 2018; Accepted 18 September 2018; Published 29 October 2018

Academic Editor: Hugo Rodrigues

Copyright © 2018 Xiaofan An et al. This is an open access article distributed under the Creative Commons Attribution License, which permits unrestricted use, distribution, and reproduction in any medium, provided the original work is properly cited.

The approximate assumptions of limit equilibrium methods are the fundamental cause of the deviation between their calculation results and actual situation. This study proposes a new finite-element evaluation method to reflect the progressive failure characteristics of rock slopes. By comparing the results of limit equilibrium and finite-element methods, the influence factors of stability for planar landslides are systematically studied. The factors include the plastic parameters of sliding surfaces in progressive failure, the elastic parameters of sliding mass, the elastic deformation of sliding beds, and excavation stress release. Moreover, the stress distribution rules on sliding surfaces and the diversity of safety factors are explored. Finally, the error source and calculation accuracy of the limit equilibrium method in slope analysis are obtained. The study provides scientific references for analyzing and evaluating the stability of such slopes.

## 1. Introduction

With the development of computers, numerical techniques are widely used in the analysis of landslides and engineered slopes, especially the application of the finite-element (FE) method. However, conventional limit equilibrium (LE) approaches still play important roles. These methods have clear mechanical concepts and a wide variety of software available for different failure modes (planar, wedge, toppling, etc.). The calculation results of LE methods are exact analytical solutions under the conditions that satisfy their basic assumptions. These unavoidable approximate assumptions and the lack of balance equations can lead to some errors between the methods and actual situations [1–3].

In contrast, numerical methods are able to provide more accurate solutions to problems, which would not be solvable using LE techniques alone. The problems of rock slope stability involve complexities related to geometry, material anisotropy, nonlinear behavior, in situ stresses, and coupling processes (pore pressures, seismic loads, etc.) [4, 5]. Stead

et al. [6] compared in detail the advantages and disadvantages of LE and numerical methods to rock slope analysis.

Many researchers have studied the inherent defects of LE methods and the calculation errors of the methods in practical application. For methods that satisfied all equilibrium conditions (e.g., Janbu, Morgenstern–Spencer, Spencer), Duncan [7] believed that the differences between calculated results would not exceed 12% and the error should be less than 6%, which was considered accurate. Liu et al. [8] contrasted the LE methods with two FE methods (strength reduction and overloading). The results show that the FE methods have a good consistency, and the safety factors of LE methods were slightly lower than those of the FE methods. Yu et al. [9] compared the results of the Bishop method with rigorous upper- and lower-bound solutions, resulting in that LE methods were reliable for homogeneous slopes. However, the methods tended to underestimate the stability of inhomogeneous slopes with a low slope angle. Huang et al. [10] discussed the influence of the lack of some simplified and static equilibrium conditions of LE methods on calculation results. Safety factors of elastic-plastic FE methods could be

close to those of LE methods. Zheng et al. [11] pointed out that the premise was that Poisson's ratio must be adjusted with the reduction of the cohesion and friction angle. Lane and Griffiths [12] claimed that traditional analysis methods could not include all boundary conditions, as well as fully reflect the heterogeneity of slopes and the complexity of forces. Hammouri et al. [13] suggested that critical slopes should be analyzed by both FE and LE methods.

Most of the existing studies are compared with the final calculation results of FE and LE methods, and only the comprehensive errors under various assumptions are obtained. However, fundamental causes of the generated error under each assumption and the impact of relevant factors have not been analyzed. Moreover, the mechanical mechanism and error range of LE methods are rarely involved.

In this study, we regard the basic assumptions that cause deviations between LE methods and actual situations as a starting point. By comparative analysis of FE and LE methods, the assumptions are separated to study the effect of each assumption on calculation results. Therefore, the error source, mechanism, and error range of LE methods are further explored.

## 2. Analysis and Evaluation Methods for Planar Landslides

Planar sliding, which has a universal characteristic of existing planar discontinuities, is very common in natural and engineered slopes [14]. The 2D case of such slopes should not be ignored, as many valuable lessons can be learned considering the mechanics of this simple failure mode. Planar failure is particularly useful for demonstrating the sensitivity of the slope to changes in shear strength and ground water conditions. These changes are not obvious when dealing with 3D slope failure [15].

**2.1. Limit Equilibrium Analysis.** For all shear failure slopes, the rock can be assumed to be the Mohr–Coulomb material, and its shear strength is represented by the cohesion  $c$  and friction angle  $\phi$ . If the effective normal stress on a sliding surface is  $\sigma'$ , the shear stress  $\tau$  developed on this surface is expressed as

$$\tau = c + \sigma' \cdot \tan \phi. \quad (1)$$

The effective normal stress is the normal component of the vertical stress due to the weight of the sliding bed. Figure 1 shows a slope containing a continuous joint dipping out of the face and forming a sliding body. Calculation of the safety factor for the body involves resolution of the force acting on the sliding surface into two components that are perpendicular and parallel to this surface. If the dip of the sliding surface is  $\alpha$ , its area is  $A$ , and the weight of the sliding body is  $W$ , then the normal and shear stresses on the sliding surface are

$$\begin{aligned} \sigma &= \frac{W \cdot \cos \alpha}{A}, \\ \tau_s &= \frac{W \cdot \sin \alpha}{A}, \end{aligned} \quad (2)$$

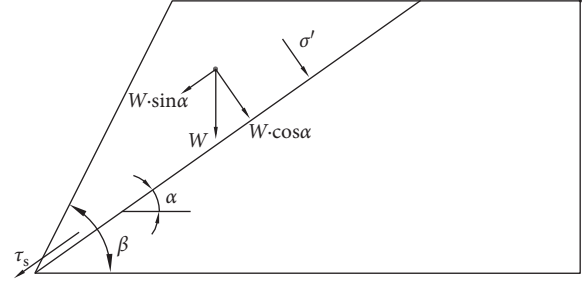


FIGURE 1: Force states of the sliding body in LE analysis.

and Equation (1) can be expressed as

$$\tau = c + \frac{W \cdot \cos \alpha \cdot \tan \phi}{A}, \quad (3)$$

or

$$\begin{aligned} \tau_s \cdot A &= W \cdot \sin \alpha, \\ \tau \cdot A &= c \cdot A + W \cdot \cos \alpha \cdot \tan \phi. \end{aligned} \quad (4)$$

In Equation (4), the expression  $(W \cdot \sin \alpha)$  defines the resultant force acting down the sliding surface and is termed the sliding force  $(\tau_s \cdot A)$ . The expression  $(c \cdot A + W \cdot \cos \alpha \cdot \tan \phi)$  defines the total shear strength forces acting up the surface and is termed the antisliding force  $(\tau \cdot A)$ . The safety factor of the slope can be quantified by the ratio of the antisliding and sliding forces, which is expressed as

$$F_s = \frac{c \cdot A + W \cos \alpha \tan \phi}{W \sin \alpha}. \quad (5)$$

If the sliding surface is smooth and contains no infilling, the cohesion is zero and the above equation is simplified as Equation (6). When the slope is in a limit equilibrium state  $(\phi = \alpha)$ , the safety factor  $F_s = 1$ :

$$F_s = \frac{\tan \phi}{\tan \alpha}. \quad (6)$$

**2.2. A Finite-Element Evaluation Method.** In numerical modelling of slopes, strength reduction and overloading techniques are commonly used methods for calculating safety factors [16, 17]. For comparison with the LE method and manifesting the actual stress states of sliding surfaces, a stability evaluation method is proposed to reflect the progressive failure characteristics of rock slopes based on FE calculation results. The method still defines safety factors as a ratio of antisliding forces to sliding forces on a whole sliding surface and uses the concept of material safety reservation. In the calculation of safety factors, peak strength is used for unbroken materials and residual strength is selected for damaged materials [18]. For planar-type slopes, the antisliding and sliding forces of a sliding surface are on a same line; thus, vector superposition can be performed. In summary, the global safety factor for the slope is calculated as

$$F_s = \frac{\sum (\sigma_i \cdot \tan \phi_i + c_i) \cdot l_i + \sum (\sigma'_i \cdot \tan \phi'_i + c'_i) \cdot l_i}{\sum \tau_i \cdot l_i + \sum \tau'_i \cdot l_i}, \quad (7)$$

where  $\sigma_i$  is the normal stress of the unbroken sliding surface element,  $\sigma'_i$  is the normal stress of the damaged sliding

surface element,  $\tau_i$  is the shear stress of the unbroken sliding surface element,  $\tau'_i$  is the shear stress of the damaged sliding surface element,  $c_i$  is the peak cohesion of the unbroken sliding surface element,  $\phi_i$  is the friction angle of the unbroken sliding surface element,  $c'_i$  is the residual cohesion of the damaged sliding surface element,  $\phi'_i$  is the residual friction angle of the damaged sliding surface element, and  $l_i$  is the length of sliding surface elements.

In general, the cohesion of slip-zone rocks decays relatively fast during the shear-sliding process of rock slopes, but the change of the friction angle is not very severe [19]. Therefore, residual shear strength is mainly provided by the friction angle. For this study, the parameters are assumed to be  $c'_i = 0.2 \cdot c_i$  and  $\tan \phi'_i = 0.8 \cdot \tan \phi_i$  in error analysis experiments. The selection of residual strength values in actual slope calculation should be based on laboratory tests.

### 3. Introduction of Interface Elements

The traditional joint model Goodman elements [20] is used to simulate faults, shear fracture zones, and discontinuities in rock mass. However, because the virtual normal stiffness and tangential stiffness of fractures are not easily determined, the practical application of the elements is greatly restricted [21]. Katona [22] proposed a friction-contact interface element without stiffness coefficients to simulate the sliding friction and opening and closing processes between two contact surfaces. However, the element uses a two-node simple element with constant contact forces, which makes it difficult to adapt to complex interface problems.

According to Katona's work, Swoboda and Marenc [23, 24] developed a new contact-friction interface element (COJO). The element can directly select the normal and tangential stresses on a contact surface as additional unknowns and simulate the complex geometry of the contact surface with a six-node triangular isoparametric element, which overcomes the shortcomings of traditional fracture elements. This study uses COJO elements to simulate the potential sliding surface of slopes. Geometric models are shown in Figure 2, where  $K_n$  and  $K_s$  are the normal and tangential stiffness of contact surfaces,  $u$  and  $v$  are the displacements of nodes, and  $\lambda_s$  and  $\lambda_n$  are the coupling forces of nodes.

Contact conditions of COJO elements are divided into three categories: fixed, sliding, and opening. Fixed means that the contact surfaces of rock mass are closed without relative displacements. Sliding indicates that the overall shear stress on contact surfaces exceeds their shear strength, and there is a relative displacement between the interfaces. Opening indicates that the tensile stress of an interface exceeds its tensile strength.

Frictional contact problems require repeated iterations to obtain correct solutions [25]. In calculation, first assume that elements are in a certain contact state and thus calculate the equivalent element stiffness matrix and load vector. After solving the FE equation, a set of test solutions can be obtained to check the contact state. If the state is the same as the original assumption, it is proven to be correct and the

calculation is complete. If they are different, the test solution is selected as a new hypothesis state and the load vector is modified to perform a new iteration until convergence. Table 1 shows the contact states of COJO elements. In the table,  $[\sigma]$  and  $[\tau]$  are the normal and tangential allowable stresses, where  $[\tau] = c - \nu \sigma_i^k$ .  $c$  and  $\nu$  are the cohesion and friction coefficient of contact surfaces, the positive value of  $\sigma_i^k$  is specified as tensile stress, and  $g$  is the initial displacement in the normal direction.

### 4. Numerical Tests for Error Analysis

Slope instability is a result of the interaction between the elastic-plastic deformation of sliding mass (or sliding beds) and the plastic sliding of sliding surfaces. In this study, we select the FE method to analyze slope stability under the basic assumptions of LE methods. Safety factors calculated by the two methods are used to calibrate the error caused by each assumption [26].

The planar sliding method has the following basic assumptions: (1) The sliding body is rigid. (2) Points of the sliding surface are destroyed at the same time. (3) The sliding surface follows the Mohr-Coulomb strength theory.

As shown in Figure 3, this research is carried out based on the following five aspects:

- (i) The FE method is used to simulate a slope under the above assumptions, and the systematic errors of a simulation platform are compared and verified.
  - (ii) Removing assumption (2) makes a progressive failure of the slope, and the errors caused by plastic sliding of the sliding surface are compared and analyzed.
  - (iii) We continue to remove assumption (1) and regard the sliding body as an elastic-plastic mass, and the errors caused by elastic-plastic deformation of the sliding body are comparatively analyzed.
- Normally, sliding surfaces are the weakest positions of planar landslides, and slopes are likely to be unstable before the sliding body has not entered a plastic stage. Therefore, we only discuss the effect of elastic deformation of the sliding body on calculation results.
- (iv) The errors caused by changes in sliding bed stiffness are further studied.
  - (v) Based on the above research, the influence of stress release due to excavation on slope stability is analyzed.

**4.1. Comparative Analysis Models.** FE models are shown in Figure 4, which can be regarded as 2D plane-strain problems. Geometric parameters of the slope are shown in Table 2. Boundary conditions of the models are as follows: the slope surface is a free boundary, and the bottom and left sides are zero-displacement boundaries. The sliding body and sliding bed are regarded as elastic-plastic isotropic materials. The sliding surface is simulated by the interface elements, and the Mohr-Coulomb criterion is used to judge

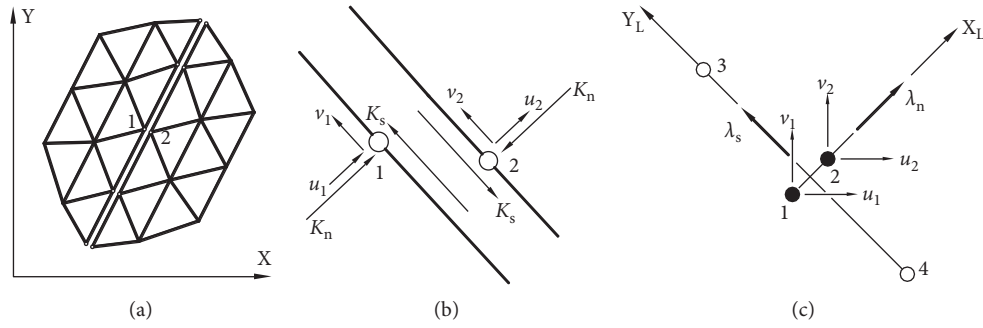


FIGURE 2: Models of the sliding surface element: (a) FE mesh model; (b) traditional joint model; (c) COJO element.

TABLE 1: Contact states of COJO elements.

Iteration step $i-1$ to $i$	Fixed	Sliding	Opening
Fixed	$\sigma_i^k < [\sigma] \quad \tau_i^k < [\tau]$	$\sigma_i^k < [\sigma] \quad \tau_i^k \geq [\tau]$	$\sigma_i^k \geq [\sigma]$
Sliding	$\sigma_i^k < [\sigma] \quad  (\Delta v')_i  < \epsilon$	$\sigma_i^k < [\sigma] \quad  (\Delta v')_i  \geq \epsilon$	$\sigma_i^k \geq [\sigma]$
Opening	$(\Delta u')_i + g < 0$		$(\Delta u')_i + g \geq 0$

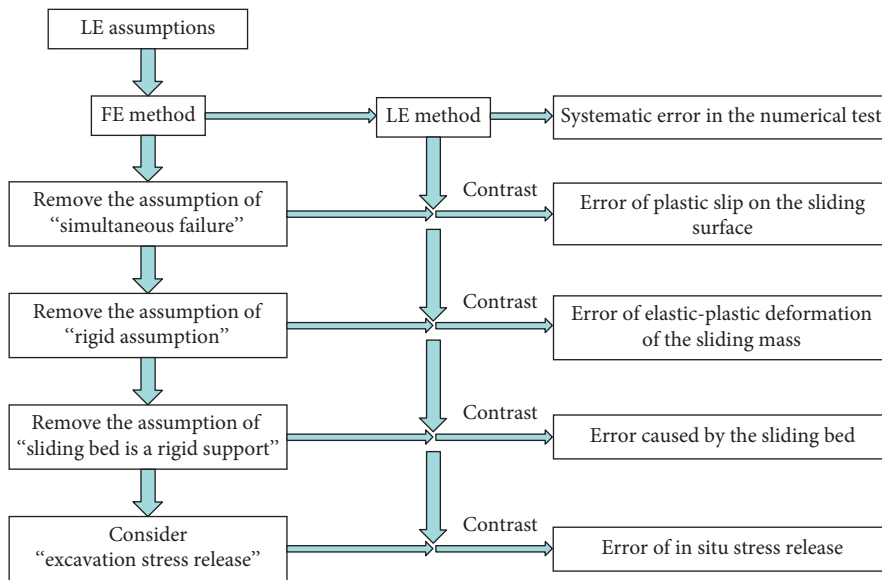


FIGURE 3: Research ideas and processes.

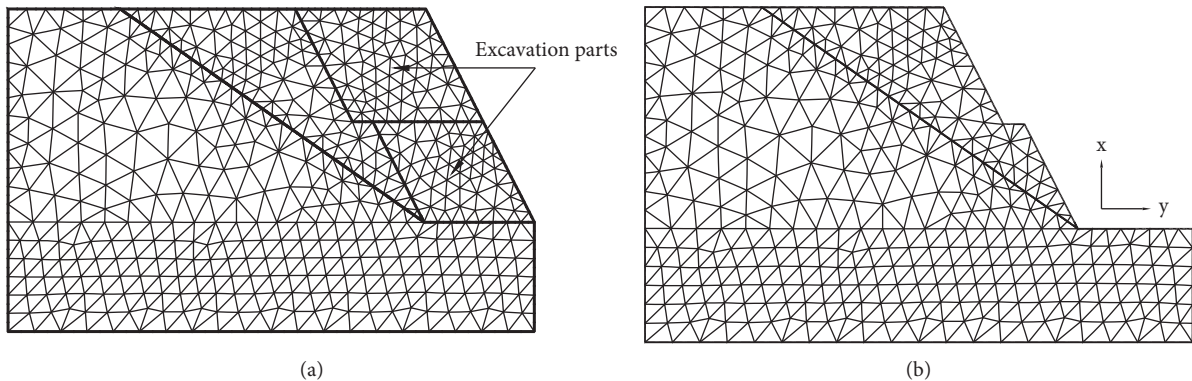


FIGURE 4: FE mesh models of the slope before (a) and after (b) excavation. Model (a) is used for the study in Section 4.6, and the other sections select Model (b).

TABLE 2: Geometric parameters of slope.

Type	Height (m)	Slope angle (°)	Dip angle of the sliding surface (°)	Width of the back edge (m)
Planar landslide without tension cracks	53	63	35	71.4

the friction states. There is no interface element between the excavation parts and the bed rock.

*4.2. Systematic Error of the Simulation Platform.* Although the LE method cannot reflect the actual states of slopes to a certain extent, the analytical solution under its basic assumption is an accurate value.

#### 4.2.1. FE Simulation Approaches

- (i) Sliding body is assumed to be rigid: in FE analysis, we select a large value of the elastic modulus and a small value of Poisson's ratio for rocks; thus, they are approximated as rigid bodies. The sliding bed is reflected by the form of forces in LE methods; therefore, it is considered as a rigid support to simulate the assumption in finite elements. Linear-elastic analysis is used for the sliding body and sliding bed in solutions, which can avoid the plastic effect of  $c$  and  $\varphi$ .
- (ii) Points of the sliding surface are destroyed simultaneously: to make the points of the sliding surface reach the limit equilibrium (or instability) state at the same time, we set the friction angle of interface elements equal to the dip angle of the sliding surface and select the cohesion of zero. The interface elements are analyzed by the elastic-plastic model in FE solution. Calculation parameters of rock mass and the sliding surface are shown in Table 3.

*4.2.2. Results Analysis.* It can be seen from Figure 5 that the normal stress and shear stress on the sliding surface obtained by FE calculation increase linearly from top to bottom of the slope. The shear stress  $\tau$  on the sliding surface is  $\tau = c + \sigma \tan \phi$ , which accords with the Mohr-Coulomb criterion and shows that the points reach the limit state at the same time. Thus, the setting that the friction angle of the sliding surface is equal to its dip angle (35°) and the cohesion is zero is correct.

As shown in Table 4, the safety factor calculated by the FE method is 0.99 and the error with the LE method is only 1%, which can prove the reliability of the numerical simulation platform.

*4.3. Error Analysis of "Simultaneous Failure and Progressive Failure".* Removing the assumption of "simultaneous failure" for the planar sliding method, the influence of progressive failure on slope stability is studied. The plastic slip of

TABLE 3: Physical and mechanical parameters of rock mass and sliding surface.

Rock mass (sliding body and sliding bed)			Sliding surface	
Elastic modulus (GPa)	Poisson's ratio	Bulk density (kN/m <sup>3</sup> )	Cohesion (kPa)	Friction angle (°)
15.0e6	0.01	23.0	0	35

the sliding surface is closely related to the cohesion and friction angle of interface elements, so the above problem is reflected by changing the value of  $c$  and  $\varphi$  of the sliding surface.

#### 4.3.1. Analysis Schemes

- (i) Assuming that the value of  $\varphi$  is equal to the dip angle of the sliding surface, the effect to calculation errors is studied by changing the value of  $c$ , as shown in Schemes 1–6
- (ii) When the value of  $\varphi$  is less than the dip angle of the sliding surface, calculation errors are affected by a combination of  $c$  and  $\varphi$ , as shown in Schemes 7–9
- (iii) When the value of  $c$  is a constant, the effect to calculation errors is explored by changing the value of  $\varphi$ , as shown in Schemes 10–12

Physical and mechanical parameters of the sliding body and sliding bed are the same as in Table 3, and parameters of the sliding surface and calculation schemes are shown in Table 5.

*4.3.2. Results Analysis.* When the sliding body and sliding bed are rigid, normal stress increases linearly along with the sliding surface from top to bottom of the slope. The magnitude of normal stress on the sliding surface is irrelevant to plastic parameters but only relates to the weight of the sliding body.

Figures 6(a)–6(c) show the shear stress on the sliding surface of Schemes 1–6, 7–9, and 10–12, respectively. The values of  $c$  and  $\varphi$  of the sliding surface directly affect the magnitude and distribution of the shear stress. According to the Mohr-Coulomb criterion, the sliding surface is in a steady state when shear stress is horizontal and linearly distributed. When the shear stress distribution appears in a partial oblique line, it indicates that the corresponding points of the oblique line reach limit instability states and local failure occurs in the slope. A complete oblique line illustrates that the whole sliding surface reaches the limit state and the slope is entirely unstable.

The shear stress distribution of Schemes 1–6 ( $\varphi = 35^\circ$ ) can obviously reflect the progressive failure characteristics of the slope. As the cohesion decreases, sliding zones gradually expand from top to bottom of the sliding surface. Meanwhile, the slope presents a state from overall stability to local instability and eventually evolves into complete failure.

Table 6 shows the safety factors and errors of each scheme. Safety factors obtained by the FE method are less than those by the planar sliding method. In Schemes 5, 6, 9, and 12, slopes are steady and calculation errors are basically controlled within

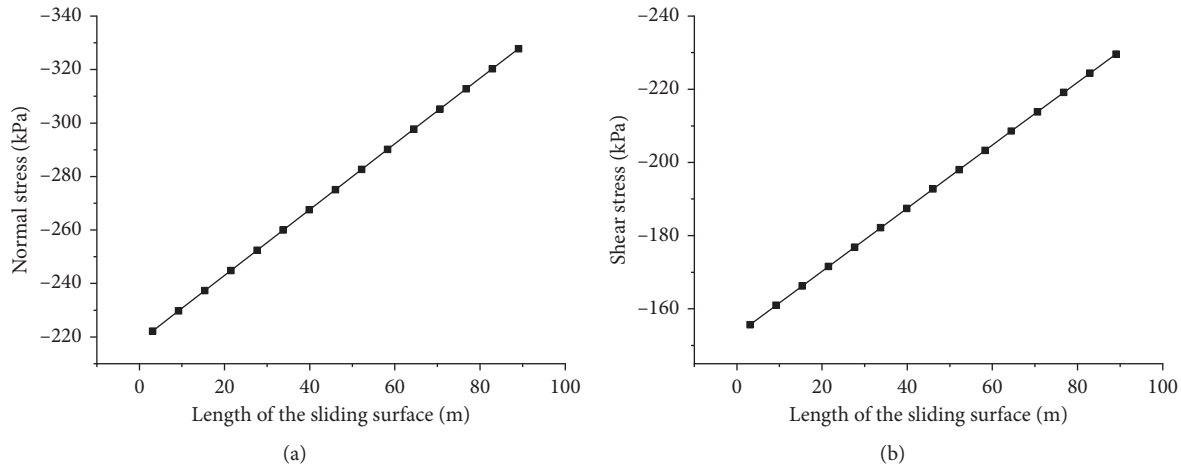


FIGURE 5: Stress distribution on the sliding surface. (a) Normal stress. (b) Shear stress.

TABLE 4: Calculation results and error of two methods.

Schemes	FE method	LE method	Error (%)
Results	0.99	1.00	-1

Note: negative error means that the safety factor of the LE method is greater than that of the FE method; on the contrary, it is positive.

TABLE 5: Plastic parameters of the sliding surface and numerical test schemes.

Schemes	Sliding surface	
	Friction angle (°)	Cohesion (kPa)
1	35	10
2	35	20
3	35	30
4	35	40
5	35	50
6	35	150
7	25	50
8	25	75
9	25	100
10	20	100
11	22.5	100
12	35	100

10%. The reason of the errors is that the planar sliding method regards the sliding body as a particle without considering the inhomogeneity of forces. However, the errors of safety factors for local and overall failure slopes are relatively large. Due to the different roles played by the cohesion and friction angle, the calculation errors vary between 5% and 88%.

When the value of  $\varphi$  is equal to the dip angle of the sliding surface, the error range retains within 10% (Schemes 1–6 and Scheme 12). When the value of  $\varphi$  is less than the dip angle of the sliding surface, the influence of plastic parameters of the sliding surface on calculation errors increases significantly (Schemes 7–11).

In summary, the progressive failure effect of slopes on calculation errors between the two methods is that the ultimate failure modes of slopes depend on a combined

strength of  $c$  and  $\varphi$  of the sliding surface. A basic reason is that safety factors solved by the FE method use peak and residual strengths to reflect different states of sliding surface elements. However, LE methods can only select a unified strength parameter, and the stable (or unstable) state of a whole sliding surface is consistent.

4.4. Error Analysis of “Rigid and Elastic Assumptions”. Removing the “rigid assumption” of the LE method, calculation results of the two methods based on progressive failure and elastic assumptions are analyzed. Elastic parameters of the sliding body are reflected by the elastic modulus  $E$  and Poisson’s ratio  $\mu$ .

4.4.1. Analysis Schemes. The  $E$  and  $\mu$  values of the sliding body are changed from rigid to general parameters of rock mass. At this time, the sliding body is gradually adjusted from rigid to elastic, and the sliding bed is still considered as a rigid support.

The bulk density of rock mass is  $\gamma = 23 \text{ kN/m}^3$ . Parameters of the sliding surface for stable slopes are  $c = 150 \text{ kPa}$  and  $\phi = 20^\circ$ ; for local failure slopes, they are  $c = 80 \text{ kPa}$  and  $\phi = 25^\circ$ . Calculation schemes and results are shown in Tables 7 and 8, respectively.

4.4.2. Influence of the Elastic Modulus on Slope Stability. Figure 7 shows the influence of the sliding body elastic modulus on the stress distribution of the sliding surface. The distributions of the normal and shear stresses are roughly consistent. When the elastic modulus of the sliding body is large (close to the sliding bed), stress distribution behaves linear and the stress value of various parts of the sliding surface has little difference. As the value of  $E$  continues to decrease, stress distribution changes from linear to “valleys” and the inhomogeneity gradually increases. Besides, the maximum normal stress and shear stress are basically increasing. When the elastic modulus of the sliding body is equal to or less than that of actual rock mass, it has almost no effect on stress distribution.

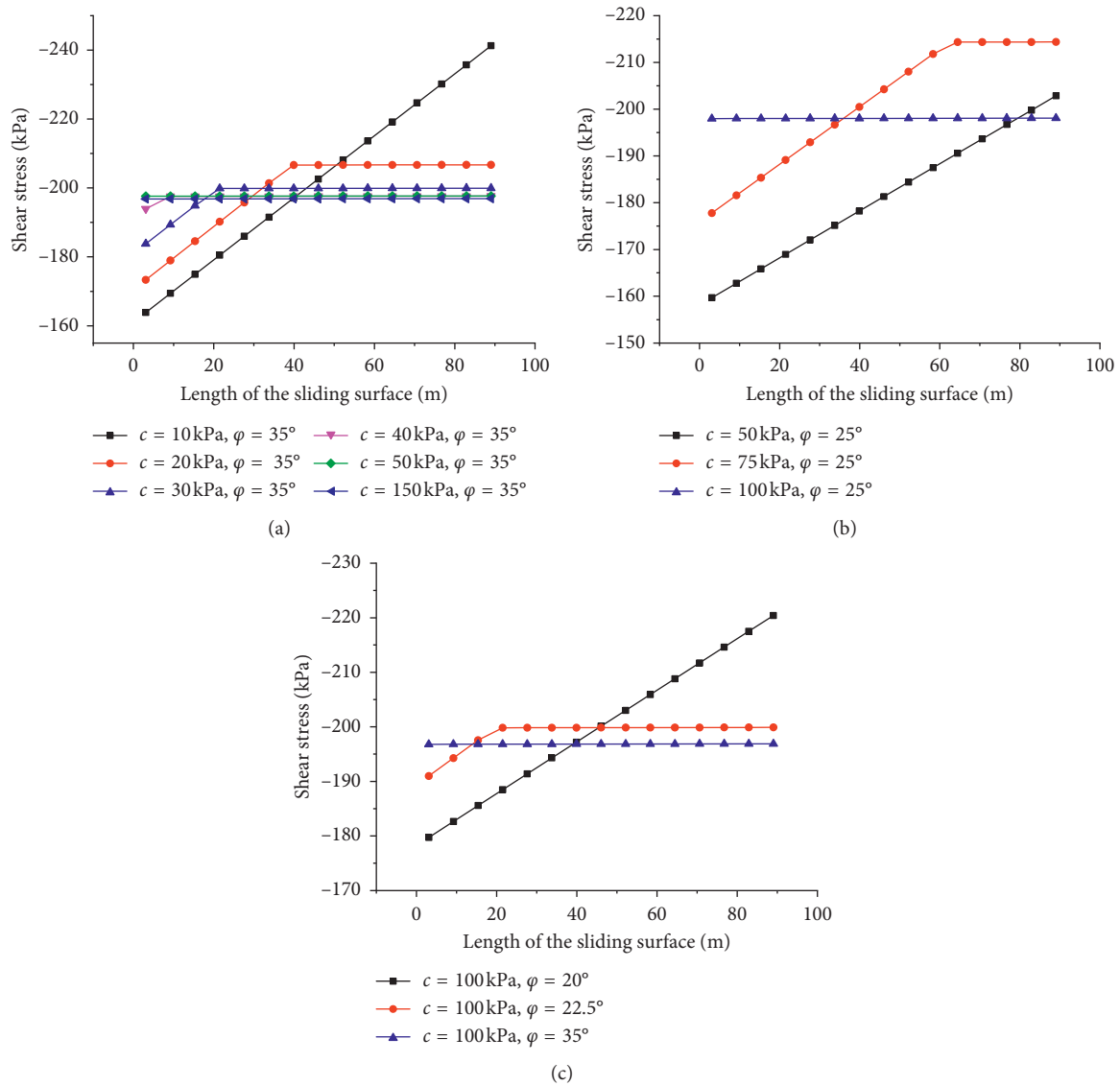


FIGURE 6: Shear stress distribution on the sliding surface with changes of  $c$  and  $\phi$ . (a)  $\phi = 35^\circ$ , with the change in value of  $c$ ; (b)  $\phi = 25^\circ$ , with the change in value of  $c$ ; (c)  $c = 100$  kPa, with the change in value of  $\phi$ .

TABLE 6: Influence of progressive failure on safety factors and error range.

Schemes	LE method	FE method	Error (%)
1	1.06	1.01	-5
2	1.12	1.03	-9
3	1.18	1.10	-7
4	1.24	1.16	-7
5	1.30	1.26	-3
6	1.92	1.76	-9
7	0.91	0.65	-40
8	1.12	0.81	-38
9	1.28	1.17	-9
10	1.13	0.60	-88
11	1.21	0.99	-22
12	1.61	1.50	-7

The effect of the sliding body elastic modulus on safety factors and errors is shown in Table 7. As the value of  $E$  decreases, the error of two methods decreases first and then increases. For stable slopes, the error reduces from 15% to 1% and then increases to 7%. For local failure slopes, the error drops from 49% to 2% and then increases to 17%. As the elastic modulus gradually approaches a general value of rocks and continues to soften, the error eventually drops to 4%.

The main reason for such a change is that when the sliding body begins to transform from rigid to elastic, its slight deformation properly relieves the plastic slip of each point on the sliding surface. However, as the sliding body continues to soften, the increasing deformation exacerbates the degree of plastic slip, and the expansion of damage zones in the slope

TABLE 7: Influence of sliding body elastic modulus on safety factors and error range.

Slope states	Schemes	Elastic modulus (GPa)	Poisson's ratio	LE method	FE method	Error (%)
Stable slope	1	15.0e6	0.25	1.44	1.25	-15
	2	15.0e4	0.25	1.44	1.45	1
	3	15.0e2	0.25	1.44	1.41	-2
	4	15.0	0.25	1.44	1.34	-7
	5	1.5	0.25	1.44	1.34	-7
	6	0.15	0.25	1.44	1.35	-7
Local failure slope	7	15.0e6	0.25	1.15	0.77	-49
	8	15.0e4	0.25	1.15	1.17	2
	9	15.0e2	0.25	1.15	0.98	-17
	10	15.0	0.25	1.15	1.04	-11
	11	1.5	0.25	1.15	1.06	-8
	12	0.15	0.25	1.15	1.11	-4

TABLE 8: Influence of sliding body Poisson's ratio on safety factors and error range.

Slope states	Schemes	Elastic modulus (GPa)	Poisson's ratio	LE method	FE method	Error (%)
Stable slope	1	15.0	0.01	1.44	1.31	-10
	2	15.0	0.05	1.44	1.33	-8
	3	15.0	0.1	1.44	1.34	-7
	4	15.0	0.2	1.44	1.34	-7
	5	15.0	0.3	1.44	1.35	-7
	6	15.0	0.4	1.44	1.36	-6
Local failure slope	7	15.0	0.01	1.15	0.96	-20
	8	15.0	0.05	1.15	0.98	-17
	9	15.0	0.1	1.15	1.01	-14
	10	15.0	0.2	1.15	1.04	-11
	11	15.0	0.3	1.15	1.02	-13
	12	15.0	0.4	1.15	0.86	-34

increases the calculation error. When the elastic modulus of the sliding body becomes much smaller than that of the sliding bed, the plastic slip of the sliding surface is restrained.

**4.4.3. Influence of Poisson's Ratio on Slope Stability.** As mentioned above, stress distribution properties of the sliding surface are determined by the elastic modulus of the sliding mass. However, when the elastic modulus is a constant, the position and magnitude of the maximum shear stress on the sliding surface are decided by Poisson's ratio. With the increase of Poisson's ratio, the shear stress on the upper part (slope crest) of the sliding surface decreases and on the lower part (slope toe) increases (Figure 8). The distribution of the maximum shear stress tends to shift toward the crest.

For stable slopes, the shear stress on the sliding surface shows a regular and equal proportion change. Failure zones of local instability slopes appear in the middle and upper parts of the sliding surface, and damage scopes gradually enlarge with the increase of Poisson's ratio.

Table 8 shows the influence of the sliding body Poisson's ratio on safety factors and errors. The FE results of all the schemes are less than the results of the planar sliding method. With the increase of  $\mu$ , the error of stable slopes changes little from 10% to 6%. The change in local failure slopes is not monotonic but first reduces from 19% to 10% and then rapidly increases to 31%. The reason for the phenomenon is the same as that of the elastic modulus, which is a result of the

interaction between elastic deformation of the sliding body and elastic-plastic deformation of the sliding surface. Relatively, the elastic modulus exhibits more sensitivity than Poisson's ratio in FE analysis; hence, the elastic modulus has a greater influence on coupling action.

#### 4.5. Influence of Sliding Bed

**4.5.1. Analysis Schemes.** According to Section 4.4, the effect of coordinate deformation between the sliding bed and sliding body on calculation results is further studied. The problem can be reflected by changing the elastic modulus and Poisson's ratio of the sliding bed so that it transforms from a rigid support to an elastic support. Parameters of the sliding body and sliding surface are shown in Table 8. Sliding bed parameters and schemes are shown in Table 9.

**4.5.2. Results Analysis.** Table 10 shows the effect of the sliding bed stiffness on safety factors and errors. For both stable and local failure slopes, calculation errors are gradually increasing and safety factors of the FE method are still less than those of the LE method. Moreover, the change in the sliding bed stiffness has great influence on the error. When the sliding bed is a rigid or an approximate rigid support, the error has little change between 7% and 11%. However, when the elastic parameter of the sliding bed is

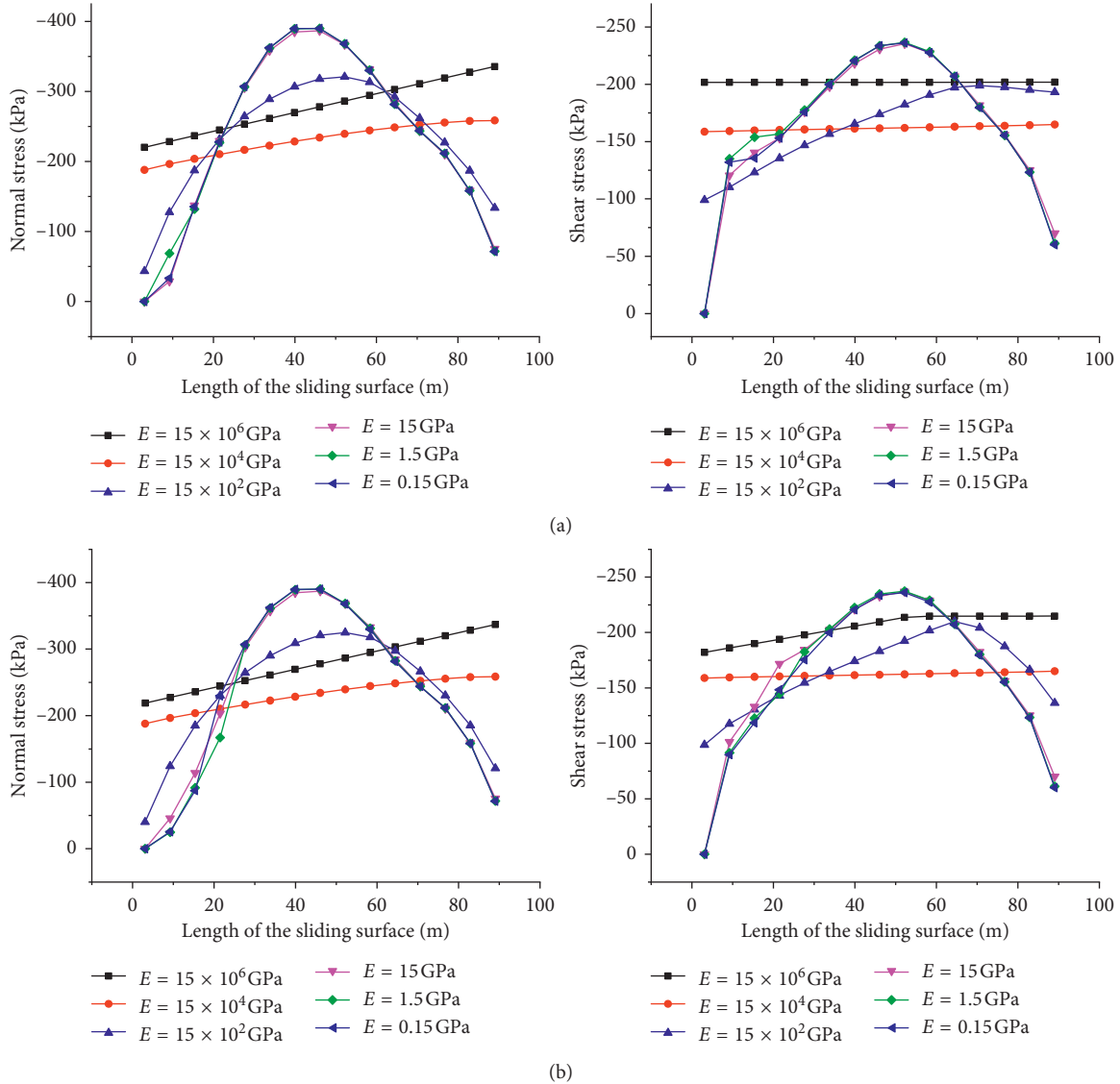


FIGURE 7: Effect of sliding body elastic modulus on stress distribution of the sliding surface: normal and shear stresses on the sliding surface of stable slopes (a) and unstable slopes (b).

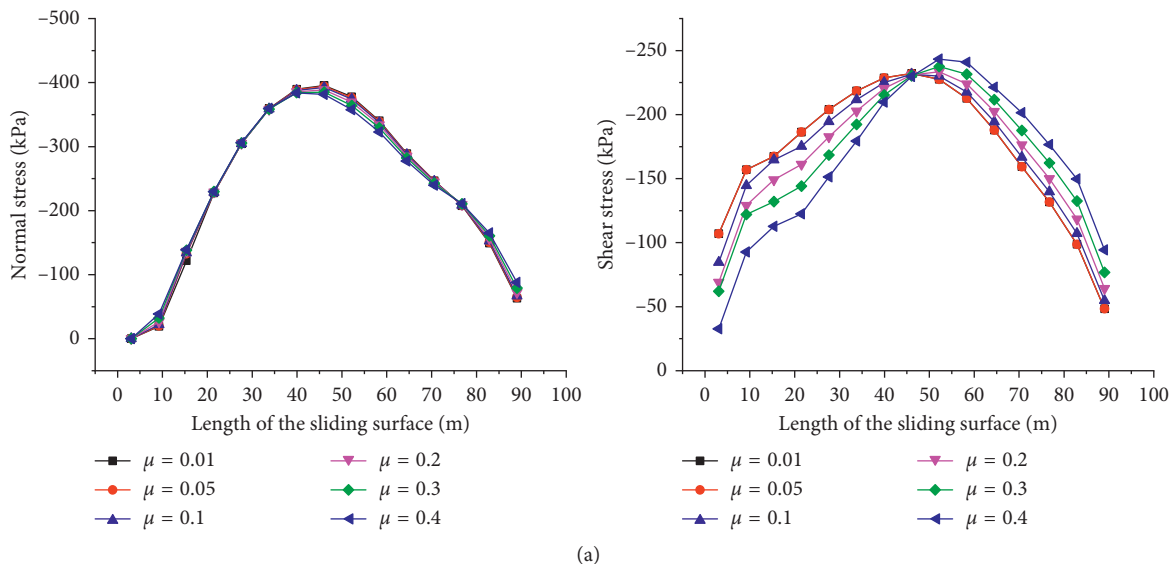


FIGURE 8: Continued.

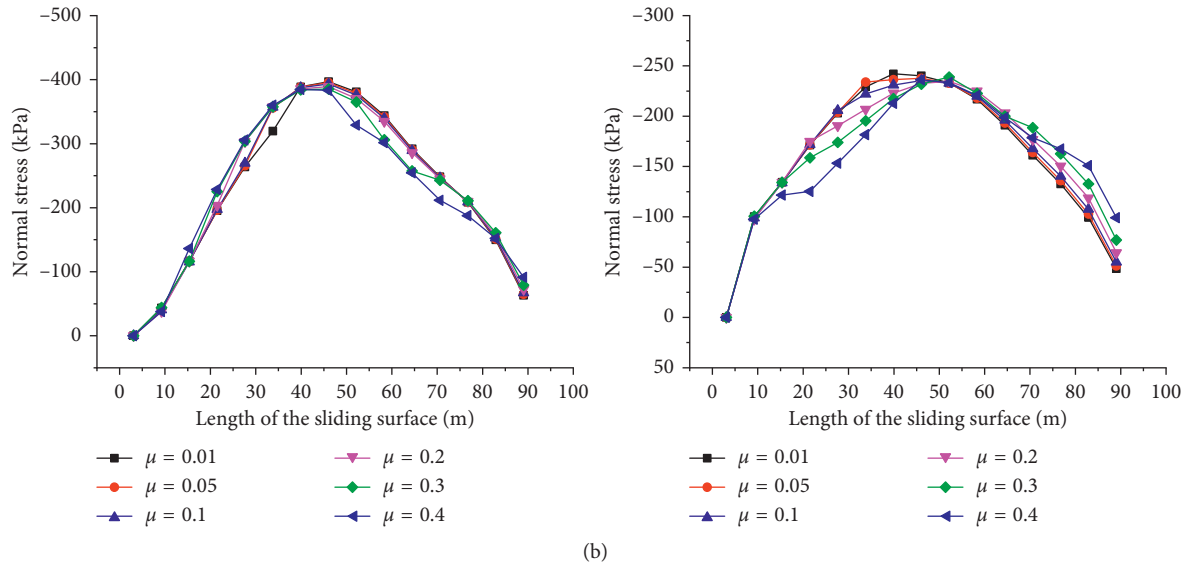


FIGURE 8: Influence of sliding body Poisson's ratio on stress distribution of the sliding surface: normal and shear stresses distribution of stable slopes (a) and unstable slopes (b).

TABLE 9: Calculation parameters of the sliding body and sliding surface.

Modes	Sliding body		Bulk density (kN/m <sup>3</sup> )	Sliding surface	
	Elastic modulus (GPa)	Poisson's ratio		Friction angle (°)	Cohesion (kPa)
Stable slope	15.0	0.25	23.0	20	150
Local failure slope	15.0	0.25	23.0	25	80

TABLE 10: Influence of elastic modulus and Poisson's ratio of the sliding bed on safety factors and error range.

Modes	Schemes	Elastic modulus (GPa)	Poisson's ratio	LE method	FE method	Error range (%)
Stable slope	1	15.0e6	0.01	1.44	1.35	-7
	2	15.0e2	0.1	1.44	1.35	-7
	3	15.0	0.2	1.44	1.00	-44
	4	0.15	0.3	1.44	0.91	-58
	5	0.015	0.4	1.44	1.01	-43
Local failure slope	6	15.0e6	0.01	1.15	1.04	-11
	7	15.0e2	0.1	1.15	1.04	-11
	8	15.0	0.2	1.15	0.75	-53
	9	0.15	0.3	1.15	0.66	-74
	10	0.015	0.4	1.15	0.69	-66

gradually close to that of the sliding body, the safety factor calculated by the FE is greatly reduced and the error rapidly increases to over 50%. As the sliding bed is further softened, the error continues to increase, but the growth rate slows down significantly.

**4.6. Influence of Excavation Stress Release.** In this section, we study the effect of excavation stress release on calculation results when the geometric parameters (slope shape and dip angle of sliding surfaces) of slopes are determined.

**4.6.1. Analysis Schemes.** Most of the excavated slopes have no large tectonic stress; thus, an initial stress field is dominated by the gravity stress. A main factor that influences the

magnitude of the gravity stress is the bulk density  $\gamma$  of rock mass. The larger value of  $\gamma$  indicates that the more tectonic stress the rock mass gathered before excavation. In this study, the initial stress changes are simulated by altering the bulk density of the sliding body and sliding bed. Calculation errors are explored under the cases considering and without considering in situ stress release, and the relevant schemes are shown in Table 11.

**4.6.2. Results Analysis.** As shown in Figure 9, after excavation and in situ stress release, the normal stress and shear stress on the sliding surface tend to transfer to the bottom of the slope, especially the shear stress changes more significantly. Under the same bulk density, stresses on the sliding surface obtained

TABLE 11: Calculation schemes for influence of excavation stress release on slope stability.

Schemes	Bulk density (kN/m <sup>3</sup> )	Sliding bed		Sliding body		Sliding surface	
		Elastic modulus (GPa)	Poisson's ratio	Elastic modulus (GPa)	Poisson's ratio	Friction angle (°)	Cohesion (kPa)
1	27.0	15.0	0.25	1.5	0.35	20	150
2	23.0	15.0	0.25	1.5	0.35	20	150
3	19.0	15.0	0.25	1.5	0.35	20	150

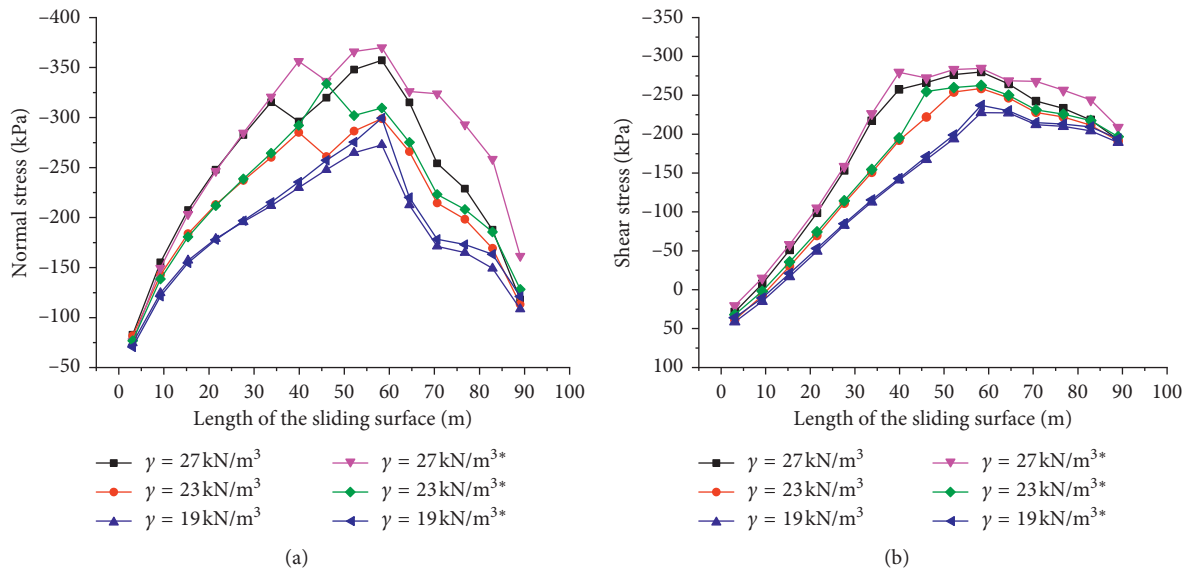


FIGURE 9: Influence of in situ stress release on stress distribution of the sliding surface: (a) normal stress distribution; (b) shear stress distribution. Note: \* represents the consideration of in situ stress release.

TABLE 12: Influence of in situ stress release on safety factors and error range.

Schemes	LE method	FE method		Error 1 (%)	Error 2 (%)
		Without considering stress release	Considering stress release		
1	1.30	1.15	0.84	-13	-54
2	1.44	1.38	1.01	-4	-42
3	1.63	1.57	1.25	-4	-30

Note: Error 1 is the error that does not consider stress release, while Error 2 considers stress release.

by considering excavation schemes are larger than those without considering. In the case of the largest amount of in situ stress release (Scheme 1), local instability occurs in the slope.

Stability analysis of actual slopes should consider the stress release caused by excavation, and the resulting error is difficult to be neglected. Table 12 shows the safety factors and error range for slopes with and without considering in situ stress release. It is obvious that the in situ stress release is very unfavorable to slope stability. Calculation errors of the slopes without considering stress release are between 4% and 13%. However, safety factors reduce rapidly with the increase of in situ stress release, and the calculation error reaches more than 30%. In particular, the error of local damage slopes is as high as 54%.

It should be noted that the comparative analysis in this section is conducted after slope excavation. This is different

from the concept of “cutting slope and reducing load” to achieve stabilization because the latter is to study the impact of excavation on slope stability, that is, to compare the slope states before and after excavation.

### 5. Discussion

This study only discusses the error source and error range of LE methods when the sliding surface is planar. Further research is needed for biplanar and circular sliding slopes. The following are some preliminary understandings of these two types of landslides:

- (i) The stability of a biplanar landslide depends not only on the occurrence and mechanical index of sliding surfaces but also on the interaction of the two sliding

surfaces. For example, retrogressive and thrust-type landslides are different in sliding forms and failure mechanisms. Safety factors of the biplanar landslide cannot be simply calculated by scalar quantity of the upper and lower sliding surface results, and an overall stability of the slope needs to be evaluated.

- (ii) In numerical modelling, we need to determine the critical sliding surface of a circular sliding slope by LE methods. Combined with the FE evaluation method proposed in this study, the safety factor is defined as the ratio of the total antisliding moment and sliding moment on the surface, and it is solved by means of moment balance.

## 6. Conclusions

- (i) For a planar landslide, safety factors obtained by the FE method without considering residual strength are close to those obtained by the LE method, and the error is within 10%. The FE evaluation method considering residual strength proposed in this study is more practical. For slope stability, the results are generally more dangerous than the results of the LE method.
- (ii) The influence of progressive failure makes the calculation error of stable slopes within 10%; the error of local failure slopes is between 6% and 35%, and the error of overall failure is above 38%. Error values are closely related to the damage range of sliding surfaces and the selection of strength parameters. Because LE methods assume that the strength of sliding surfaces is reduced simultaneously, an unrealistic stress distribution is obtained.
- (iii) As the elastic deformation of the sliding body increases, the calculation error of stable slopes is between 5% and 15%. For local failure slopes, the error is first reduced and then increased. The reason is that the energy of the sliding body can be firstly sustained by its coordinated deformation, thereby alleviating the plastic slip of the sliding surface, but the continuous softening of the sliding body further aggravates the sliding state. When the sliding body parameters are close to those of general rock mass, the error grows to 10%–30%. The elastic modulus of the sliding body has a greater effect on calculated results than Poisson's ratio.
- (iv) The sliding bed rigidity has the same influence on stable and local failure slopes. When the sliding bed is a rigid support, the error is between 7% and 10%. When elastic parameters of the sliding bed are close to those of the sliding body, the error rapidly grows to 50% and beyond. Further softening of the sliding bed continues to increase the error, but the growth rate slows down.
- (v) In situ stress release has a significant impact on the stability of excavated slopes, and calculation errors are proportional to the magnitude of the release. For

a rock slope with a height of 80 m under self-weight stress, the release of in situ stress caused by stepped excavation can reduce safety factors by more than 30%.

## Data Availability

The finite-element program used to support the findings of this study was supplied by Prof. Ning Li under license and so cannot be made freely available. Requests for access to these data should be made to the corresponding author.

## Conflicts of Interest

The authors declare no conflicts of interest.

## Acknowledgments

This research was funded by the National Natural Science Foundation of China (Nos. 11572246, 51779207, and 41372295). Besides, we would like to thank Dr. Gao Lv for his guidance on research ideas and Miss Qi's help in English writing.

## References

- [1] D. V. Griffiths, "Slope stability analysis by finite elements," *Geotechnique*, vol. 49, no. 3, pp. 387–403, 1999.
- [2] D. Q. Li, T. Xiao, Z. J. Cao et al., "Efficient and consistent reliability analysis of soil slope stability using both limit equilibrium analysis and finite element analysis," *International Journal of Geomechanics*, vol. 17, no. 4, pp. 1–12, 2017.
- [3] G. S. Sun, W. Jiang, S. G. Cheng et al., "Optimization model for determining safety factor and thrust line in landslide assessments," *Applied Mathematical Modelling*, vol. 40, pp. 5216–5229, 2016.
- [4] E. Eberhardt, D. Stead, and J. S. Coggan, "Numerical analysis of initiation and progressive failure in natural rock slopes—the 1991 Randa rockslide," *International Journal of Rock Mechanics and Mining Sciences*, vol. 41, no. 1, pp. 69–87, 2004.
- [5] S. W. Sloan, "Geotechnical stability analysis," *Geotechnique*, vol. 63, no. 7, pp. 531–572, 2013.
- [6] D. Stead, E. Eberhardt, J. Coggan et al., "Advanced numerical techniques in rock slope stability analysis – applications and limitations," in *Proceedings of International Conference on Landslides—Causes, Impacts and Countermeasures*, pp. 615–624, Davos, Switzerland, June 2001.
- [7] J. M. Duncan, "State of the art: limit equilibrium and finite element analysis of slopes," *Journal of Geotechnical and Geoenvironmental Engineering*, vol. 122, no. 7, pp. 577–596, 1996.
- [8] S. Y. Liu, L. T. Shao, and H. J. Li, "Slope stability analysis using the limit equilibrium method and two finite element methods," *Computers and Geotechnics*, vol. 63, no. 1, pp. 291–298, 2015.
- [9] H. S. Yu, R. Salgado, S. W. Sloan, and J. M. Kim, "Limit analysis versus equilibrium for slope stability," *Journal of Geotechnical and Geoenvironmental Engineering*, vol. 124, no. 1, pp. 1–11, 1998.
- [10] M. H. Huang and H. Ding, "Some assumption condition of limit equilibrium method," *Chinese Journal of Rock Mechanics and Engineering*, vol. 25, no. 12, pp. 2529–2536, 2006.

- [11] H. Zheng, C. G. Li, and C. F. LI, "Finite element method for solving the factor of safety," *Chinese Journal of Geotechnical Engineering*, vol. 24, no. 5, pp. 626–628, 2002.
- [12] P. A. Lane and D. V. Griffiths, "Assessment of stability of slopes under drawdown conditions," *Journal of Geotechnical and Geoenvironmental Engineering*, vol. 126, no. 5, pp. 443–450, 2000.
- [13] N. A. Hammouri, A. I. H. Malkawi, and M. M. A. Yamin, "Stability analysis of slopes using the finite element method and limiting equilibrium approach," *Bulletin of Engineering Geology and the Environment*, vol. 67, no. 4, pp. 471–478, 2008.
- [14] S. L. Zhang, Z. H. Zhu, S. C. Qi et al., "Deformation process and mechanism analyses for a planar sliding in the Mayanpo massive bedding rock slope at the Xiangjiaba Hydropower Station," *Landslides*, vol. 15, no. 10, pp. 2061–2073, 2018.
- [15] D. C. Wyllie, *Rock Slope Engineering: Civil Applications*, CRC Press, Boca Raton, 5th edition, 2018.
- [16] Y. L. Tu, X. R. Liu, Z. L. Zhong, and Y. Li, "New criteria for defining slope failure using the strength reduction method," *Engineering Geology*, vol. 212, pp. 63–71, 2016.
- [17] H. Zheng, L. G. Tham, and D. F. Liu, "On two definitions of the factor of safety commonly used in the finite element slope stability analysis," *Computers and Geotechnics*, vol. 33, no. 3, pp. 188–195, 2006.
- [18] A. W. Skempton, "Long term stability of clay slopes," *Geotechnique*, vol. 14, no. 2, pp. 77–102, 1964.
- [19] P. Xin, S. R. Wu, J. S. Shi et al., "Structural characteristics of soft-rock slip zone and experimental study of its formation mechanism in Boji mountain large-scale old landslide," *Chinese Journal of Rock Mechanics and Engineering*, vol. 32, no. 7, pp. 1382–1391, 2013.
- [20] R. E. Goodman, R. L. Taylor, and T. L. Brekke, "A model for the mechanics of jointed rock," *Journal of Soil Mechanics and Foundations Division*, vol. 94, pp. 637–660, 1968.
- [21] X. H. Xue, X. G. Yang, and E. L. Liu, "Application of the modified Goodman model in soil nailing," *International Journal of Geomechanics*, vol. 13, no. 1, pp. 41–48, 2013.
- [22] M. G. Katona, "A simple contact–friction interface element with applications to buried culverts," *International Journal for Numerical and Analytical Methods in Geomechanics*, vol. 7, no. 3, pp. 371–384, 1983.
- [23] G. Swoboda and M. Marenc, "Numerical modelling of rock bolts in intersection with fault system," in *Proceeding of Numerical Models in Geomechanics, NUMOG*, pp. 729–738, Swansea, UK, August 1992.
- [24] Z. Q. Zhang, F. F. Chen, N. Li et al., "Influence of fault on the surrounding rock stability of a tunnel: location and thickness," *Tunnelling and Underground Space Technology*, vol. 61, pp. 1–11, 2017.
- [25] X. Y. Lei, G. Swoboda, and Q. H. Du, "Theory and application of contact-friction interface element," *Chinese Journal of Geotechnical Engineering*, vol. 16, no. 3, pp. 23–32, 1994.
- [26] P. Zhang, "Research on the error-mechanism and error-range of the rigid limited equilibrium method in the stability of rock and soil slope," Master thesis, Xi'an University of Technology, Xi'an, China, 2003.

## Research Article

# Landslide Susceptibility Mapping in Darjeeling Himalayas, India

**Amit Chawla** <sup>1</sup>, **Sowmiya Chawla**,<sup>1</sup> **Srinivas Pasupuleti** <sup>1</sup>, **A. C. S. Rao**,<sup>2</sup>  
**Kripamoy Sarkar**,<sup>3</sup> and **Rajesh Dwivedi**<sup>4</sup>

<sup>1</sup>Department of Civil Engineering, IIT(ISM) Dhanbad, Jharkhand, India

<sup>2</sup>Department of Computer Science & Engineering, IIT(ISM) Dhanbad, Jharkhand, India

<sup>3</sup>Department of Applied Geology, IIT(ISM) Dhanbad, Jharkhand, India

<sup>4</sup>Department of Computer Science & Engineering, Vignana's Foundation for Science, Technology & Research, Andhra Pradesh, India

Correspondence should be addressed to Amit Chawla; [amit84\\_cha@yahoo.co.in](mailto:amit84_cha@yahoo.co.in)

Received 30 March 2018; Revised 12 June 2018; Accepted 11 July 2018; Published 16 September 2018

Academic Editor: Haiyun Shi

Copyright © 2018 Amit Chawla et al. This is an open access article distributed under the Creative Commons Attribution License, which permits unrestricted use, distribution, and reproduction in any medium, provided the original work is properly cited.

Landslide susceptibility map aids decision makers and planners for the prevention and mitigation of landslide hazard. This study presents a methodology for the generation of landslide susceptibility mapping using remote sensing data and Geographic Information System technique for the part of the Darjeeling district, Eastern Himalaya, in India. Topographic, earthquake, and remote sensing data and published geology, soil, and rainfall maps were collected and processed using Geographic Information System. Landslide influencing factors in the study area are drainage, lineament, slope, rainfall, earthquake, lithology, land use/land cover, fault, valley, soil, relief, and aspect. These factors were evaluated for the generation of thematic data layers. Numerical weight and rating for each factor was assigned using the overlay analysis method for the generation of landslide susceptibility map in the Geographic Information System environment. The resulting landslide susceptibility zonation map demarcated the study area into four different susceptibility classes: very high, high, moderate, and low. Particle Swarm Optimization-Support Vector Machine technique was used for the prediction and classification of landslide susceptibility classes, and Genetic Programming method was used to generate models and to predict landslide susceptibility classes in conjunction with Geographic Information System output, respectively. Genetic Programming and Particle Swarm Optimization-Support Vector Machine have performed well with respect to overall prediction accuracy and validated the landslide susceptibility model generated in the Geographic Information System environment. The efficiency of the landslide susceptibility zonation map was also confirmed by correlating the landslide frequency between different susceptible classes.

## 1. Introduction

Landslides are momentary and instantaneously happening vandalize natural hazard in mountains; however, it turns in to a disaster due to immature geology coupled with external temporal triggering factors causing landscape changes and direct and indirect losses. Landslide happens when the slope changes from a steady to an unsteady state. The influence of gravity is the key operating force for the landslide to happen. It is a motion of mass of rock, earth, or debris along the slope [1]. More than 15% of total land area in India is considered to be affected by landslides [2]. Globally awareness has been drawn on the study of landslides mostly because of growing pressure of urbanization and its socioeconomic effects on the

terrain habitats [3]. This trend of landslides is expected to continue in the time to come due to sustained deforestation, increment of haphazard urbanization, and changing climatic patterns in the landslide-prone areas [4, 5]. Landslide risk cannot be utterly averted; however, the impact of its acuteness and intensity may be reduced by identifying and predicting the problems in advance. Despite advances in science and technology, landslides continue to result in economic, human, and environmental losses worldwide [6]. The external and temporal triggering factors like rainfall and earthquakes, if happening individually or in combination with some considerable time and magnitude, are directly accountable for inducing the landslides [7]. Rainfall is an inevitable triggering factor which could contribute to the

occurrence of landslides [8]. The landslide susceptibility is the probability of spatial phenomenon of slope failures [9]. Remote sensing can play a role in the generation of landslide inventory map and thematic maps related to landslide occurrences [10]. Remote sensing (RS) data in conjunction with data from other sources in digital form and their analysis in Geographic Information System (GIS) environment have made possible to generate different thematic data layers corresponding to the contributing factors accountable for the occurrence of landslides [11–13]. Geomatics by taking advantage of modern tools, such as remote sensing and GIS, provides a perfect opportunity for usage, validation, and comparison of different methods to produce a landslide susceptibility map [14]. For the creation of the LSZ map in the GIS environment, the integration of various thematic data layers with weights was assigned with respect to their relative significance [15–18]. Production of the landslide susceptibility map describes the prone area where landslides may occur in the future [19]. The landslide susceptibility analysis has been applied for the purpose of assessing the degree of risk in landslide-prone areas [20]. Landslide susceptibility mapping is an important step prior to landslide assessment planning, management, and disaster mitigation [21]. Landslide susceptibility zonation (LSZ) maps are helpful in identifying the landslide vulnerable zone in advance, planning the future development projects and mitigation programs. Hence, for effective and efficient disaster management, there is an urgent requirement of recognizing unstable slopes and mitigating its effects, which may be attained with the assistance of LSZ mapping.

The objective of Particle Swarm Optimization (PSO)-Support Vector Machine (SVM) approach used in landslide susceptibility mapping is to generate an accurate landslide susceptibility map through classification technique [22]. Particle Swarm Optimization is a computational technique that optimizes an issue towards iterative attempt to move forward a particle solution with respect to a provided measure about quality [23]. The advantages of PSO over other soft computing models are as follows: PSO provides more range and exploration for the population and the movements of particles allows the fast convergence of greater diversity in the search space. The principle behind the Support Vector Machine classifier is setting a boundary to an area of points which all are the same types.

Genetic Programming (GP) is an evolutionary computing technique that is used to solve a variety of complex problems. Koza [24] developed the Genetic Programming approach, and since then, it has been widely used in science and engineering applications. GP is a very popular method with diverse applications. In the field of geosciences, GP has been used by Litschert [25] to map landslide hazard zones in California locations. In another study by Nourani et al. [26], landslide susceptibility mapping was performed using GP for Zonouz plain in Iran.

This study presents a methodology for the generation of landslide susceptibility mapping using remote sensing data and Geographic Information System technique for the part of the Darjeeling district, Eastern Himalaya, in India.

The performance of this GIS output was evaluated by using PSO-SVM and GP techniques, which aims to predict the accuracy of landslide susceptibility classes. The study also aims to determine the usefulness of remote sensing and GIS, and an attempt was made to generate the landslide susceptibility map for effective and efficient disaster management for the future.

## 2. Study Area

In India, about 12.6% of Indian landmass are in the Himalayan terrain region and are landslide susceptible regions [2]. This study focused on a part of Darjeeling hills, West Bengal, Eastern Himalaya, in India, which lies within the latitude  $26^{\circ}49' 31.910''$  to  $26^{\circ}56' 38.366''$  N and longitude  $88^{\circ}13'3.706''$  to  $88^{\circ}22'31.818''$  E and reports an area of about 201 sq. km (Figure 1). This study belongs to the steep and rugged mountainous terrain, which falls at the alluvial plains of north extreme of West Bengal, India, and is highly prone to landslide. During monsoon, these regions observed regular land sliding incidents activated by rainfall. The study area also belongs to the high damage risk and severe earthquake intensity zone in India, that is, Zone IV [27], and is thus prone to earthquake-induced landslides. As per 2011 census, the study area has an inhabitant's density of 586 inhabitants per square kilometer, and its inhabitant expansion rate over the decade 2001–2011 was 14.77%. The study area is dominated with the factors mostly favorable for occurrence of landslide areas like slope of degree  $>45^{\circ}$ , highly dissected hill slopes, barren land, high rainfall, high earthquake-prone areas, and relief  $>2000$  m. The study area has a history of land sliding events which resulted in loss of life and infrastructure. In the past, the study area experiences earthquakes of high intensity. From the history of landslide events in the Darjeeling Himalayas, it is concluded that the study area is vulnerable to landslides, and hence, the landslide susceptibility zonation map for the study area is required to be analyzed.

## 3. Data

In this study, the statistics utilized were IRS-RESOURCE-SAT-II LISS-IV, CARTOSAT-I PAN satellite data (Table 1) of the National Remote Sensing Centre, India; topographic maps of the Survey of India (1 : 50,000 scale); earthquake data of the National Centre for Seismology, India; and information from the published geology, soil, and rainfall maps. Integration of LISS-IV and PAN data was attempted to have the benefit of both high spatial and high spectral resolution in a sole image. Figure 2 shows the satellite image of the study area.

## 4. Methodology

The methodology adopted in this study (Figure 3) for the generation of LSZ map in the GIS environment, involves the selection of various factors, creation of various thematic layers, assigning numerical rating to factors, blending of data

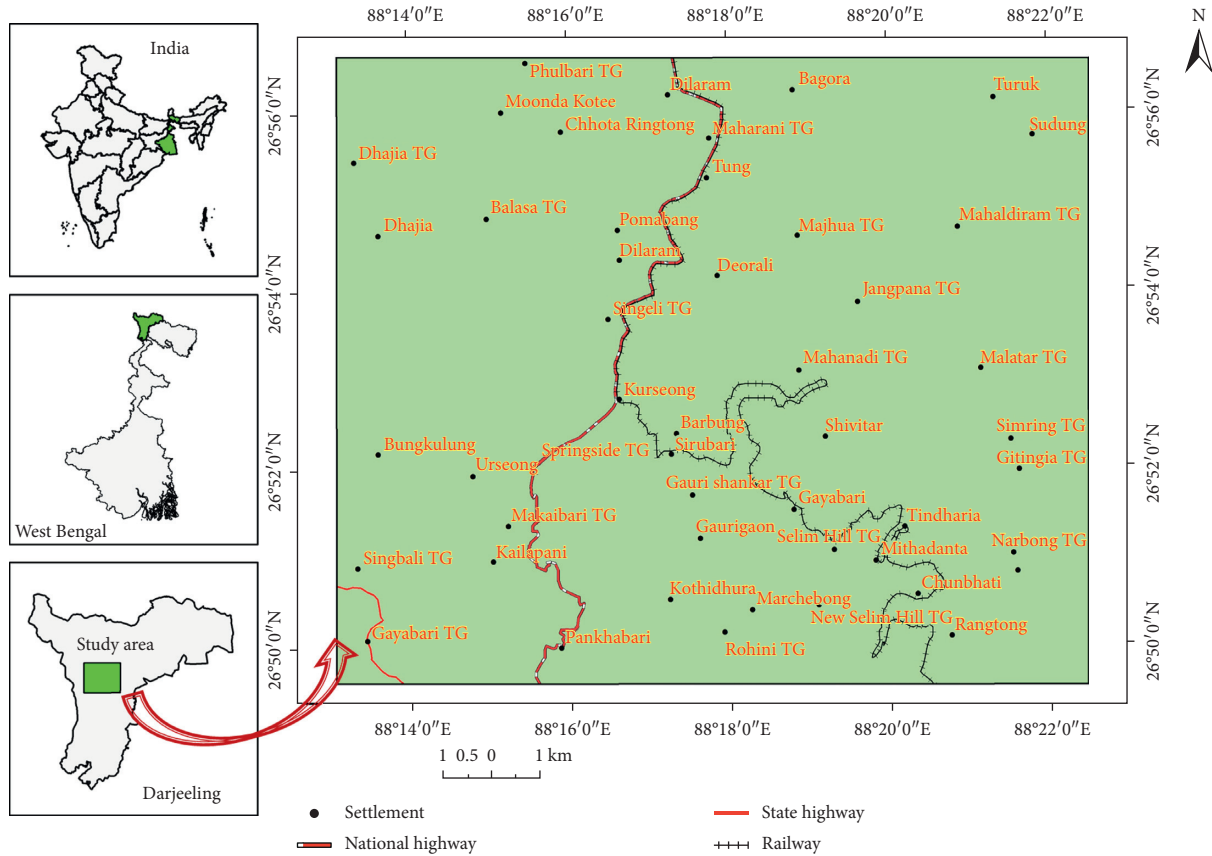


FIGURE 1: Location map of the study area.

TABLE 1: Details of satellite statistics used in this study.

Name of satellite	Sensor	Product ID	Path/row	Product type	Resolution	Date of satellite image
IRS-RESOURCESAT-II	L4FX	174047811	Path-107 Row-52	Orthorectified	5.0 m	15th Jan 2015
CARTOSAT-I	PAN_FORE	174047741	Path-0584 Row-0273	Standard geocorrected	2.5 m	19th Dec 2010
CARTOSAT-I	PAN_FORE	174047751	Path-0584 Row-0274	Standard geocorrected	2.5 m	19th Dec 2010

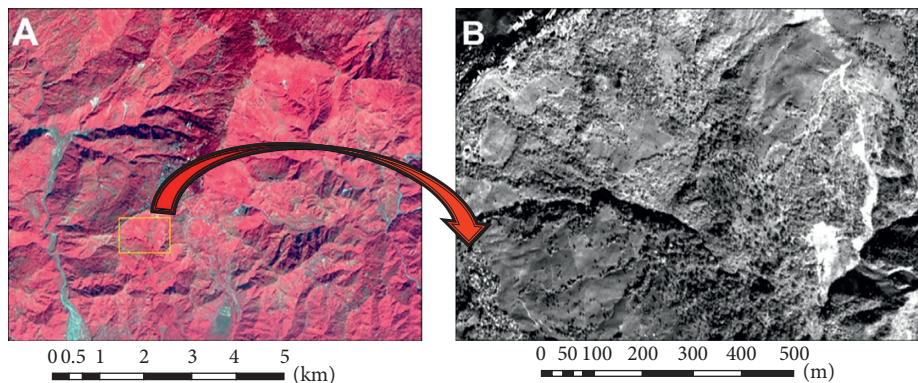


FIGURE 2: (A) RESOURCESAT-II LISS-IV satellite image of the study area. (B) Illustration of the CARTOSAT-I PAN image of the rectangular area marked in (A).

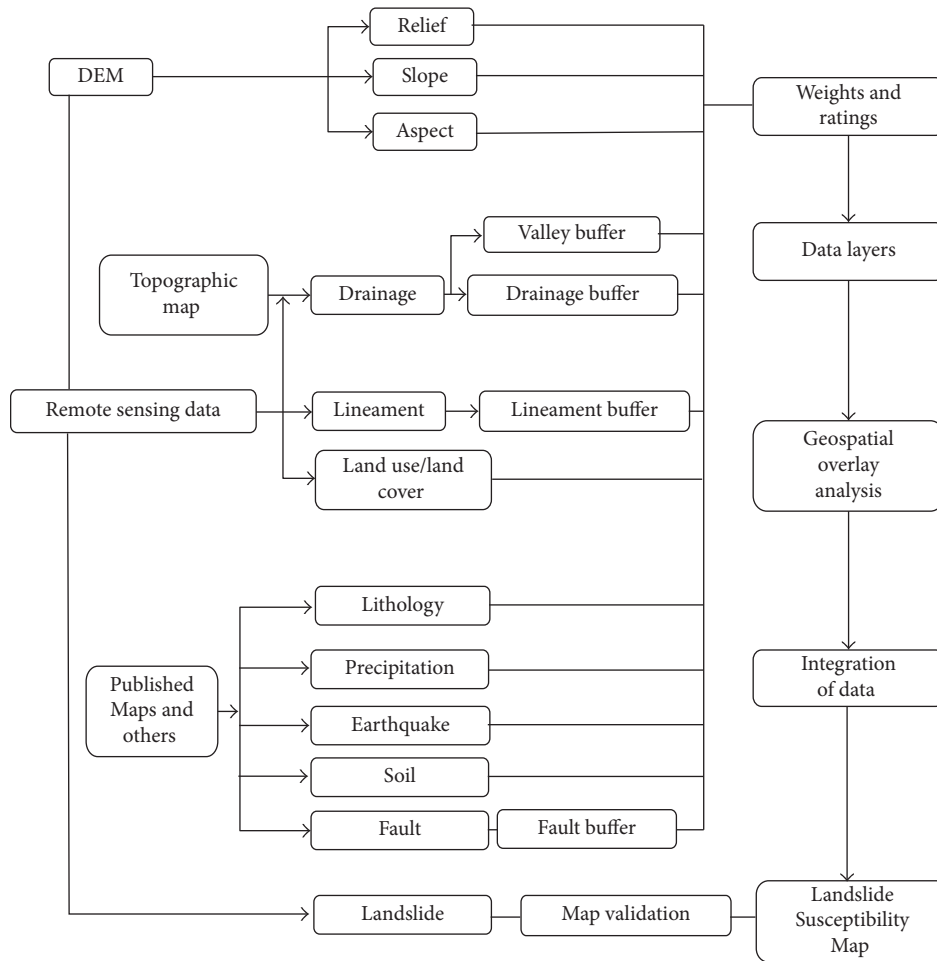


FIGURE 3: Flow diagram showing different steps involved in the preparation of landslide susceptibility mapping.

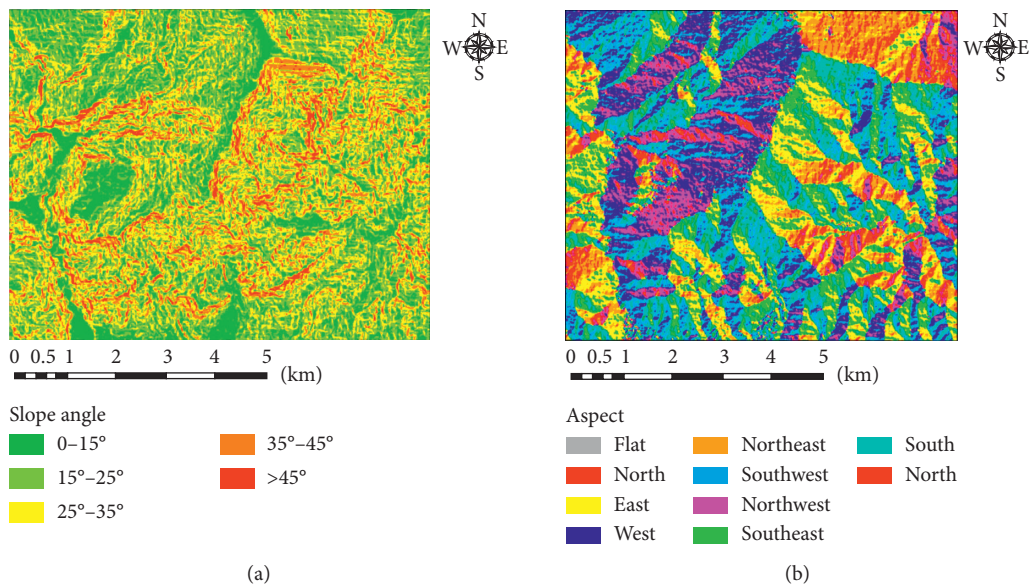
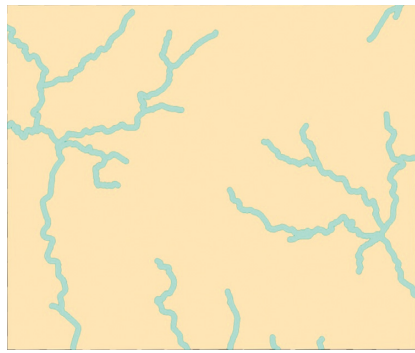


FIGURE 4: Continued.



0 0.5 1 2 3 4 5 (km)

Valley buffer  
 0-100 m  
 >100 m

(c)



0 0.5 1 2 3 4 5 (km)

Land use  
 Agriculture land  
 Barren land  
 Built up area  
 Scrub land  
 Sparse forest  
 Tea plantation  
 Thick forest  
 Water body

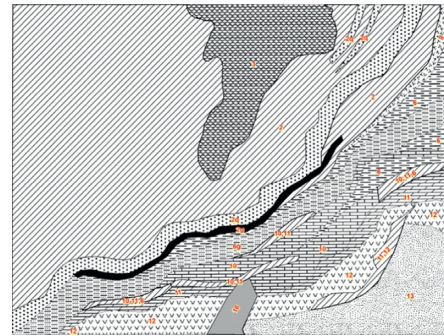
(d)



0 0.5 1 2 3 4 5 (km)

Soil type  
 Coarse loamy  
 Fine loamy  
 Loamy skeletal

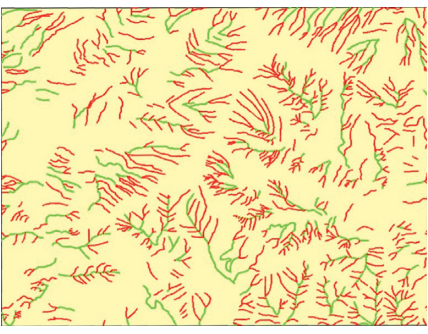
(e)



0 0.5 1 2 3 4 5 (km)

Lithology  
 Darjeeling gneiss  
 Geabdat sandstone  
 Chunabati formation  
 Damuda formation  
 Quartzite key beds  
 Quaternary and recent sediments  
 Rangit pebble slate  
 Gorubathan formation  
 Feldspathic greywacke  
 Graphite schist/gneiss  
 Lingtse granite gneiss  
 Paro-subgroup (parogneiss)

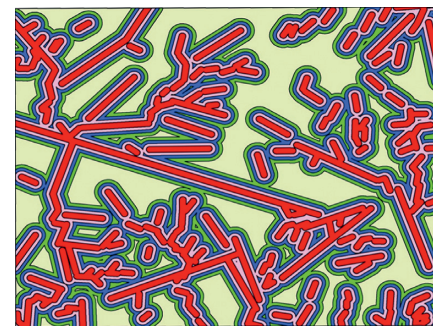
(f)



0 0.5 1 2 3 4 5 (km)

Drainage buffer  
 1st order  
 2nd order

(g)



0 0.5 1 2 3 4 5 (km)

Lineament buffer  
 0-125 m  
 125-250 m  
 250-375 m  
 375-500 m  
 >500 m

(h)

FIGURE 4: Continued.

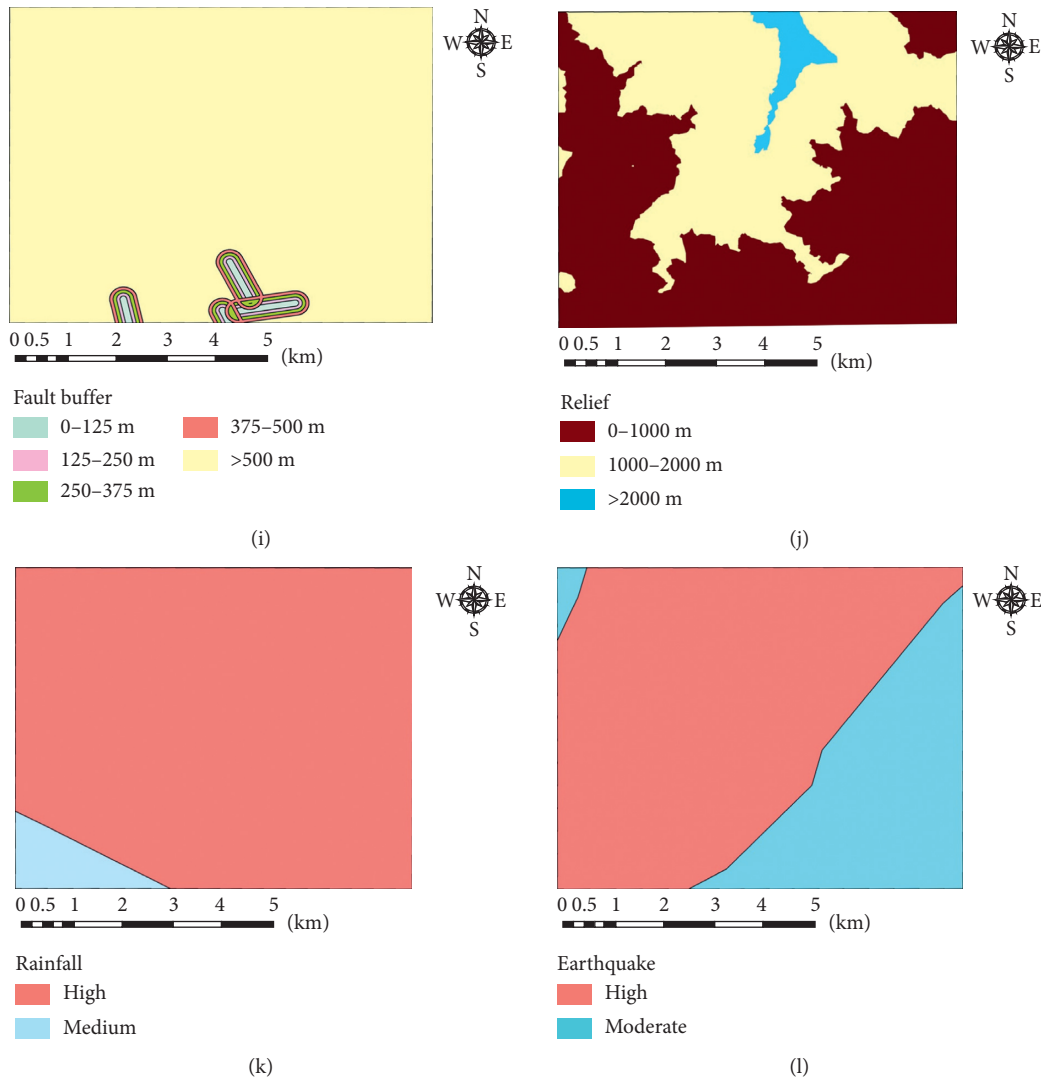


FIGURE 4: (a) Slope, (b) aspect, (c) valley buffer, (d) land use/land cover, (e) soil, (f) lithology, (g) drainage buffer, (h) lineament buffer, (i) fault buffer, (j) relief, (k) rainfall, and (l) earthquake maps of the study area.

in GIS environment, calculating landslide potential index, and classifying and validating landslide susceptibility map.

In this study, twelve different factors were assessed for the generation of landslide susceptibility mapping in the GIS environment. In this study, overlay analysis technique was adopted in the GIS environment for the generation of thematic data layers. For the study area, on the basis of field knowledge, experience, and available literature, weight values were allocated to the data layers/factors on a 1 to 10 numerical scale in series of their significance towards slope instability, whereas the rating values were allocated to the classes of the layers on a 0 to 9 numerical scale, in which higher rating reflects greater influence on landslide event compared to lower one. The numerical values adopted for weights and ratings were allotted to the different factors. Thematic data layers were created by mathematically multiplying the weight of the layer with the ratings of the correlating class of the individual layer. The outcome of the final LSZ map was classified into various discrete

susceptibility classes. Validation of the landslide susceptibility map was attempted with the help of landslide distribution map and data of landslides. Twelve prime parameters and the landslide potential index obtained from the parameters were involved as an input to PSO-SVM and GP model.

## 5. Thematic Data Layers

For the preparation of the LSZ map, generation of various thematic data layers is required, and the factors selected were both preparatory and triggering. The layers were produced in the GIS environment. CARTOSAT-1 DEM at a resolution of pixel size  $25 \times 25$  m was utilized to extract information on slope, relief, and aspect layers.

**5.1. Slope.** The slope instability is directly proportional to the angle of the slope. The slope map (Figure 4(a)) was derived

from the surface tool (spatial analysis) of DEM using GIS software. Slope statistics of the study area computed were 23.66%, 32.21%, 26.91%, 13.31%, and 3.91% for the degree of slope 0–15°, 15°–25°, 25°–35°, 35°–45°, and >45°, respectively.

**5.2. Aspect.** Generally, the south-facing slopes have lesser vegetation density as compared to the north-facing slopes [28]. With respect to the landslide distribution, south- and east-facing slopes are further susceptible to landslides [29]. The aspect map (Figure 4(b)) is derived from the surface (spatial analysis) tool of DEM using GIS software. Aspect statistics of the study area computed were 0%, 7.76%, 9.66%, 14.17%, 11%, 15.24%, 13.73%, 13.34%, and 15.09% for the flat, north, northeast, east, southeast, south, southwest, west, and northwest directions, respectively.

**5.3. Valley Buffer.** A valley buffer of 100 meter was considered for the study area along the major streams, that is, 3rd and higher-order drainages, and accordingly, the valley buffer map was generated (Figure 4(c)). Valley buffer statistics of the study area computed were 92.18% and 7.82%, for the valley buffer >100 m and <100 m, respectively.

**5.4. Land Use/Land Cover.** Land use is an indirect measure for the strength of the slope, as it commands the rate of weathering and erosion. In this study, the LU/LC map (Figure 4(d)) was generated by utilizing the IRS-RESOURCESAT-II LISS-IV image with four bands along with the CARTOSAT-I PAN image. The interpreted land use/land cover has been digitized, and after that it was rasterized on 25 × 25 m pixel size. Land use/land cover statistics of the study area computed were 0.36%, 0.94%, 6.48%, 1.84%, 63.47%, 10.39%, 13.77%, and 2.75%, for the land use class agriculture land, barren land, built-up area, scrub land, sparse forest, tea plantation, thick forest, and waterbody, respectively.

**5.5. Soil.** Top soil cover on a slope has an influence on the occurrence of landslides [17]. The soil map (Figure 4(e)) was extracted from a regional soil map published by National Bureau of Soil Survey and Land use planning using the GIS environment. Soil statistics of the study area computed were 45.16%, 16.46%, and 38.38%, for the soil unit coarse loamy, fine loamy, and loamy skeletal, respectively.

**5.6. Lithology.** In contrast to the weaker rocks, the stronger rocks give more resistance to the driving forces and consequently are less susceptible to landslides and vice versa [30]. The lithology is a representation of the physical characteristics of rock or soil. The lithology map (Figure 4(f)) was generated from the geological map [31] of the Darjeeling area in GIS environment. Lithology statistics of the study area computed was 6.34%, 0.94%, 0.93%, 0.93%, 3.27%, 8.24%, 6.57%, 7.46%, 4.44%, 1.22%, 1.12%, 46.20%, 6.12%, 1.05%, and 5.17% for the rock Chunabati formation, composite of Damuda formation and Chunabati formation, composite of Rangit pebble slate

and Damuda formation, composite of Rangit pebble slate, Damuda formation and Gorubathan formation, Damuda formation, Darjeeling gneiss, feldspathic greywacke, geabdat sandstone, Gorubathan formation, graphite schist/gneiss, lingtse granite gneiss, paro subgroup (paro gneiss), quartzite key beds (paro quartzite), quaternary and recent sediments, and Rangit pebble slate, respectively.

**5.7. Drainage.** Most common cause for landslide in terrain region is soil erosion due to drainage activity. Increase of pore water pressure and decrease in the shear strength due to water infiltration will result in instability to the slope. Methodology for generating the drainage buffer by correlating with the landslide distribution has been suggested by Kanungo et al. [30], to map the landslide hazard zones in the Darjeeling Himalayas. From the topographic sheets of Survey of India in the scale of 1:50,000, most of the drainage layers were produced by digitization of the drainages and subsequently they were updated with the aid of the PAN image and LISS-IV image in the GIS environment. For all the drainage orders, a 25 m buffer zone on both sides of the drainages was created. After the spatial association of landslide distribution, it was observed that most of the landslide pixels fall in the 1st- and 2nd-order drainage buffers only. Accordingly, a drainage buffer map (Figure 4(g)) was generated in the GIS environment by taking into account the 1st- and 2nd-order streams only with 25 m buffer zones around these drainages. Drainage statistics of the study area computed were 8.62%, 3.57%, and 87.81% for the drainage buffers 1st order, 2nd order, and for the rest of the area, respectively.

**5.8. Lineaments.** Landslides are more prone in the jointed, fractured, and faulted areas. Methodology for generating the lineament buffer layers with equal interval buffer zones has been suggested by Kanungo et al. [30], to map the landslide hazard zones in the Darjeeling Himalayas. PAN and LISSIV satellite images are used for the interpretation of lineaments. Interpreted lineaments were processed for the generation of lineament layers in the GIS environment. Lineament buffer regions were generated at 250 m distance, and then they were geospatially cross-tallied with the pixels of landslides. 84% of the pixels had befallen in the primary two buffer regions only. Hence, it has been evaluated to have five equal distance lineament buffer zones at 125 m distance, and with respect to these zones, the lineament buffer map (Figure 4(h)) was generated. The lineament statistics of the study area computed were 20.63%, 21.13%, 18.39%, 14.72%, and 25.13% for the lineament buffers <125 m, 125–250 m, 250–375 m, 375–500 m, and >500 m, respectively.

**5.9. Fault Buffer.** Huge jointed area displaying offsets of chain of hills are faults. The faults were obtained from the geological map [31] of the Darjeeling area by using GIS software. Hence for the study area, it has been considered to have five equal distance buffer zones at 125 m distance for the generation of the fault buffer map (Figure 4(i)), to study the effect of faults on the landslide occurrence. The fault

buffer statistics of the study area computed were 0.73%, 0.88%, 0.98%, 1.14%, and 96.27% for the fault buffers <125 m, 125–250 m, 250–375 m, 375–500 m, and >500 m, respectively.

**5.10. Relief.** Relief represents the difference in altitude between two points. The lesser relief value nominates a mature topography, whereas the higher relief value nominates immature topography. The relief map (Figure 4(j)) was extracted from DEM in the GIS environment. The relief statistics of the study area computed were 56.10%, 41.07%, and 2.83% for the reliefs 0–1000 m, 1000–2000 m, and >2000 m, respectively.

**5.11. Rainfall.** Rainfall plays a critical part in the unforeseen events like landslides. It is an external temporal triggering factor, and excess of it may make the slope become heavy due to increase in pore water pressure and shall result in slope slips. The rainfall map (Figure 4(k)) of the study area was generated by digitizing the polygons from the rainfall map of National Atlas and Thematic Mapping Organisation, Kolkata, India, in a vector layer. The rainfall map was rasterized at 25 m × 25 m spatial resolution. The rainfall statistics of the study area computed were 4.84% and 95.16% for the rainfall classes medium and high, respectively.

**5.12. Earthquake.** Both the destructive natural disasters, that is, earthquakes and landslides, are common in one sense that both are scary and destructive in nature. The tremors produced by the earthquakes do not only activate currently developed landslides but also revive the older ones. The earthquake map for the study area has been prepared by using the point data of more than last 200 years, and these point data were explained with the magnitude and epicenter location. The data collected were obtained from National Centre for Seismology, New Delhi, India. The earthquake map (Figure 4(l)) has been generated by interpolation technique utilizing the Inverse Distance Weighted (IDW) tool in GIS environment; in which, the IDW tool forms a surface with respect to the value of point data. The earthquake map was subcategorized into two categories of moderate- and high-prone zones with respect to the reference of past history of earthquake magnitudes ranging from 3 to 5 (moderate) and above 5 (high) measured in the Richter scale, respectively. Earthquake statistics of the study area computed were 69.59% and 30.41% for the earthquake classes high and moderate, respectively.

**5.13. Landslide Distribution.** The principal features for locating the landslides by using satellite images are spectral attributes, size, shape, contrast, and so on; the landslides are mostly bare of vegetation, and they showed high reflectance [17]. In the past, for the detection of landslides, SPOT PAN and ATM high-resolution satellite images of 10 m and 7.5 m resolution, respectively, were used by Mason et al. [32]. For the study area, landslides were detected by using the IRS-RESOURCESAT-II LISS-IV and CARTOSAT-I PAN high-

resolution satellite images of 5 m and 2.5 m resolution, respectively. Some of the extracted landslides from the satellite images were crosschecked, and the landslide distribution map (Figure 5) was modified accordingly. The mapping of prevailing landslides is necessary to study the association between the landslide distribution and the causative factors [30]. History of landslide inventory of the study area was prepared from the Special Publication Number 94, Geological Survey of India. According to this landslide inventory, 17 major landslides were falling in our study area. When these 17 landslide locations were correlated with the landslide distribution map and field verification, it was observed that most of these major historical landslide locations are still falling in the landslide distribution map of the study area. The landslide distribution map contains 91 landslides which were scattered over the complete study area. Most of the landslides falling are in the varying span from 500 sq. m to 3000 sq. m.

In the study area, ground truth verification for some of the significant landslides was carried out by using the global positioning system (GPS) device. Four significant landslide sites were selected within the study area (Figure 5), for explaining the information on actual occurrence and type of landslides with the help of field survey and Google Earth satellite image (Figure 6). In location Site 1, the type of landslide observed was translational debris slide, and the state of this slide was enlarging and multiple. For Site 2, the type of landslide observed was translational rock-cum-debris slide, and the state of this slide was successive. For Site 3, the type of landslide observed was translational debris slide, and the state of this slide was enlarging and single. However, for Site 4, the type of landslide observed was complex slide, where the slide is partly translational grading to earthflow at toe, and the state of this slide was single.

**5.14. Landslide Susceptibility Mapping.** Identification of potential landslide area can be achieved by developing a rating scheme in which the factors and their classes were assigned numerical values based on the associated causative factors [17]. In this study, an attempt was made to generate a grading system in which the factors and their classes have been allocated numerical values. The thematic data layers have been generated in the GIS environment. The weights and ratings allotted to each factor and their classes are given in Table 2. In this study, twelve thematic data layers were generated, and they were overlaid and mathematically added by using (1) for generating the landslide potential index (LPI) in the GIS environment for each cell:

$$\begin{aligned} \text{LPI} = & \text{Dr} + \text{Li} + \text{Sl} + \text{Pr} + \text{Ea} + \text{Lith} \\ & + \text{Fb} + \text{Vb} + \text{La} + \text{So} + \text{Re} + \text{As}, \end{aligned} \quad (1)$$

where Dr, Li, Sl, Pr, Ea, Lith, Fb, Vb, La, So, Re, and As are the representative symbols for the thematic weighted layers for drainage buffer, lineament buffer, slope, precipitation, earthquake, lithology, fault buffer, valley buffer, land use/land cover, soil, relief, and aspect, respectively. The range for LPI adjudged was between 171 and 502, which was later on categorized to generate landslide susceptibility classes. For

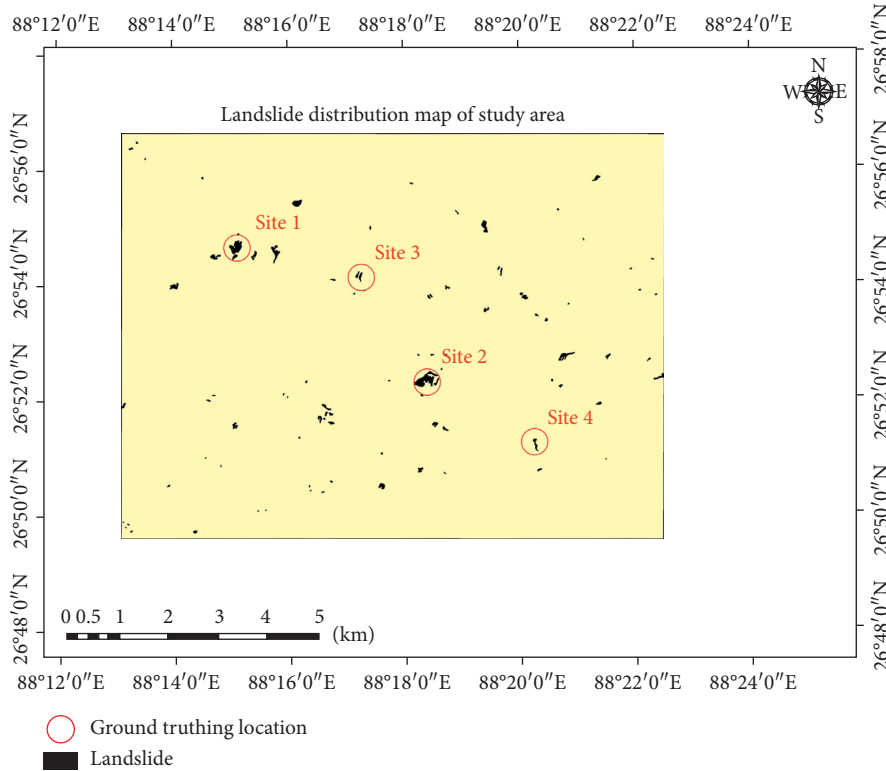


FIGURE 5: Landslide distribution map.

such classifications, a judicious way is to look for values of sudden abrupt alterations [33]. Boundaries for different susceptible classes were drawn at significant changes in gradient [17]. Hence, a graph was plotted with LPI-frequency values, emerging many swings. In this graph (Figure 7), motion mean with the mean window lengths of 3, 7, and 11 was utilized for smoothening the curve and finer classification. To acquire respective susceptibility zones for different categories, the borders were drawn at abrupt alteration in gradient of the slope at the LPI values of 212, 302, and 381 (Table 3). The LSZ map (Figure 8) was generated by using the LPI-class boundaries in the GIS environment.

**5.15. Classification and Prediction Using PSO-SVM Approach Based on LPI.** In PSO, the framework is started with a populace of random solutions and scans for optima by refreshing generations. In this approach, the potential arrangements, called particles, fly through the issue space by following the present ideal particles.

**5.16. The Algorithm for PSO-SVM.** PSO is introduced with a gathering of random particles (solution) and afterward looks for optima by refreshing generations. In each generation, every molecule is modified by following two “best” parameters. The first is the best solution (fitness) it has accomplished so far (fitness parameter is additionally put away). This value is called pbest. Another “best” parameter that is followed by the particle swarm analyzer is the best

value, got so far by any particle in the populace. This best value is a global best and called gbest. The movements of the particles are directed by the values pbest and gbest. At the point when enhanced positions are being found, these values will then come to direct the movements of the swarm. The particle performs movement by updating its velocity and positions by using (2) and (3), respectively. Figure 9 describes the optimization of particles using PSO algorithm.

Formula (2) is for velocity update operation:

$$v_i^{t+1} = v_i^t + c_1 \text{rand}_1(p_{\text{best } i}^t - x_i^t) + c_2 \text{rand}_2(g_{\text{best}}^t - x_i^t). \quad (2)$$

Formula (3) is for position update according to velocity:

$$x_i^{t+1} = x_i^t + v_i^{t+1}, \quad (3)$$

where  $v_i^t$  and  $x_i^t$  denote the velocity and position of  $i$ th particle,  $p_{\text{best } i}^t$  denotes individual best known position of  $i$ th particle,  $g_{\text{best}}^t$  denotes the entire swarm best known position, and  $\text{rand}_1$  and  $\text{rand}_2$  are the two random variables, whereas  $c_1$  and  $c_2$  are the learning parameters.

The flowchart presented in Figure 9 describes that for every particle, if the calculated fitness value is superior than the best fitness value calculated in the past, make the present fitness value as new pbest. After that the gbest value is calculated by assigning best particle’s pbest value to gbest.

**5.17. Procedure for PSO-SVM.** The flowchart describing the working of PSO is shown in Figure 10. For the classification task, optimal LPI values are identified using PSO according to the minimum and maximum ranges for all

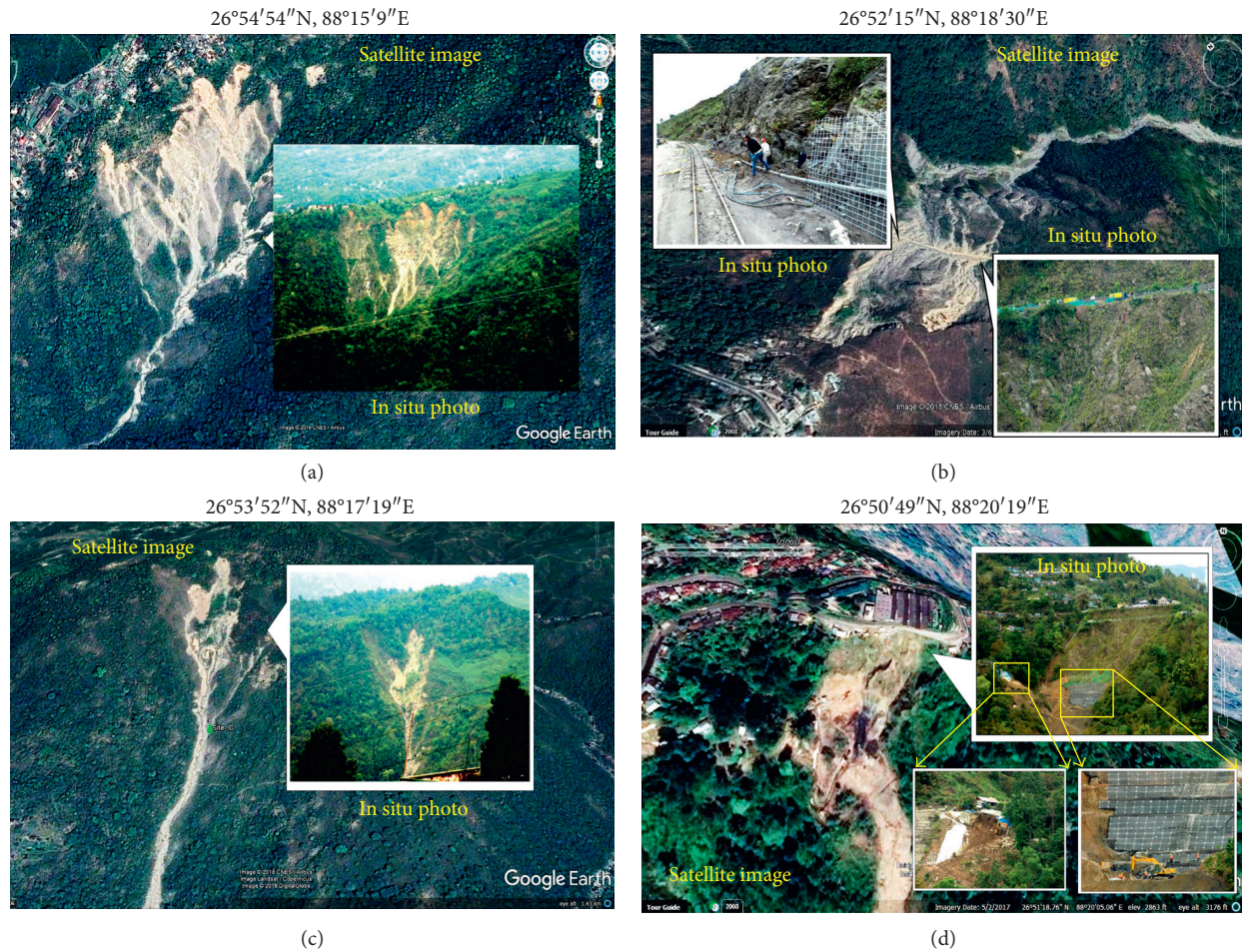


FIGURE 6: Field photographs, Google Earth images, and types of some of the major landslide events in the study area. (a) Site 1: translational debris slide. (b) Site 2: translational rock-cum-debris slide. (c) Site 3: translational debris slide. (d) Site 4: complex slide.

the 12 parameters by considering the numerical value of weights and ratings as given in Table 2. This work started with an initial population of “50” particles and processed up to “500” maximum iterations (generation). The procedure for classification are as follows. Step 1: describe the LPI function as fitness function and also initialize “population” and “max generation”; Step 2: set the minimum and maximum limits for each parameter used in LPI function according to Table 2; Step 3: record the movements of every particle in each generation in the vector format containing the LPI value along with the corresponding parameter values. In each generation, population moves from one place to suitable place and generates the new fitness values.

**5.18. Classification System for PSO-SVM.** In the classification, data are loaded from the database and divided into 70% training set and 30% testing set. In the data set, the parameter values corresponding to fitness values are treated as a feature vector. SVM looks generally advantageous hyperplanes that give the maximum profit. Input: training set, class labels, and testing set. Step 1: perform training of the SVM classifier with

training set and class labels. Step 2: perform testing with testing set to test the accuracy of prediction.

**5.19. Discussion for PSO-SVM Study.** The PSO-SVM study was carried out by taking selected “800” LPI values (200 for each class) along with the corresponding parameters that cover the entire range of classification for each class. Training is carried by taking 600 LPIs (150 from each class), and testing is performed using 200 LPIs (50 from each class).

The test accuracy described by the confusion matrix is presented in Figure 11(a), and a comparison between classifications based on LPI values and predicted classification based on the SVM classifier the same as the confusion matrix is presented in Figure 11(b). The confusion matrix is used to explain the classification performance model on a set of testing data for which the original labels are known. Each row of the matrix represents the instances in a predicted class, while each column represents the instances in an actual class (or vice versa). In Figure 11(a), there are 5 columns and 5 rows, but classification in this task is limited to only 4 classes, and the fifth column and fifth row are filled with all zeros. The first, second, third, and fourth columns and rows

TABLE 2: Weights and ratings for various factors and their classes.

Factors	Classes	Weights	Ratings
Drainage buffer	1st order	10	9
	2nd order		5
Lineament buffer	0–125 m	9	9
	125–250 m		7
	250–375 m		5
	375–500 m		3
	>500 m		1
Slope	0°–15°	8	1
	15°–25°		3
	25°–35°		5
	35°–45°		7
	>45°		9
Rainfall	Moderate	7	6
	High		9
Earthquake	Moderate	7	6
	High		9
Lithology	Paro-subgroup (parogneiss)	6	4
	Darjeeling gneiss		6
	Gorubathan formation		7
	Feldspathic greywacke		2
	Graphite schist/gneiss		7
	Quartzite key beds (paroquartzite)		1
	Lingtse granite gneiss		8
	Rangit pebble slate		8
	Damuda formation		4
	Geabdat sandstone		3
	Chunabati formation		6
	Quaternary and recent sediments		9
	Composite of Rangit pebble slate and Damuda formation		6
	Composite of Rangit pebble slate, Damuda formation, and Gorubathan formation		7
	Composite of Damuda formation and Chunabati formation		5
Land use/land cover	Agriculture land	5	5
	Barren land		9
	Built-up area		2
	Scrub land		7
	Sparse forest		6
	Tea plantation		3
	Thick forest		1
	Waterbody		0
Fault buffer	0–125 m	5	9
	125–250 m		7
	250–375 m		5
	375–500 m		3
	>500 m		1
Valley buffer	0–100 m	4	6
	>100 m		0
Soil	Fine loamy	3	3
	Coarse loamy		6
	Loamy skeletal		9
Relief	<1000 m	3	3
	1000–2000 m		6
	>2000 m		9

TABLE 2: Continued.

Factors	Classes	Weights	Ratings
Aspect	Flat	1	0
	North		1
	Northeast		4
	East		7
	Southeast		8
	South		9
	Southwest		6
	West		3
Northwest	2		

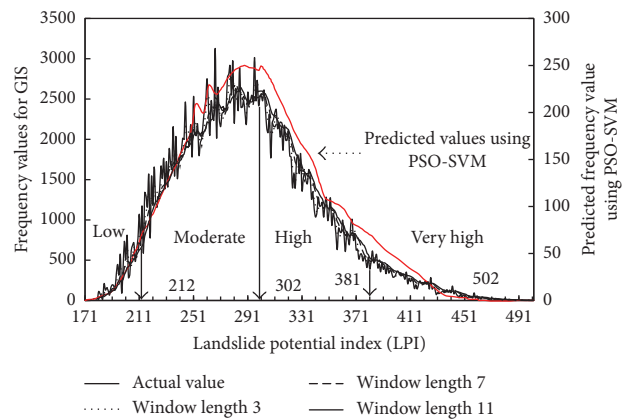


FIGURE 7: Frequency division of landslide potential index and predicted frequency using PSO-SVM.

TABLE 3: Distribution of landslide susceptibility zones and landslide potential index of the study area.

Susceptibility zone	Area (sq. km)	LPI
Low	7.267	171 to 212
Moderate	117.736	213 to 302
High	65.787	303 to 381
Very high	10.97	382 to 502

correspond to low, moderate, high, and very high classes, respectively. Each column related to these classes will have a sum of 50 LPIs; that is, the testing is done by 200 LPIs, by taking 50 LPIs from each class, which is the target class (actual classification based on LPI values), and predicted classification by the SVM classifier is represented by rows. In the first row, a sum of 50 LPIs are presented that means out of 50 low-class LPIs, and the system predicted that all are the low class LPIs. In the second, third, and fourth rows, a sum of 52, 51, and 47 is present that means out of 50 moderate, 50 high, and 50 very high-class LPIs, the system predicted that 52 belongs to moderate, 51 belongs to high, and 47 belongs to very high. The prediction accuracy is also written in the sixth row corresponding to each class. A comparison of the measured LPI values generated by GIS and the predicted

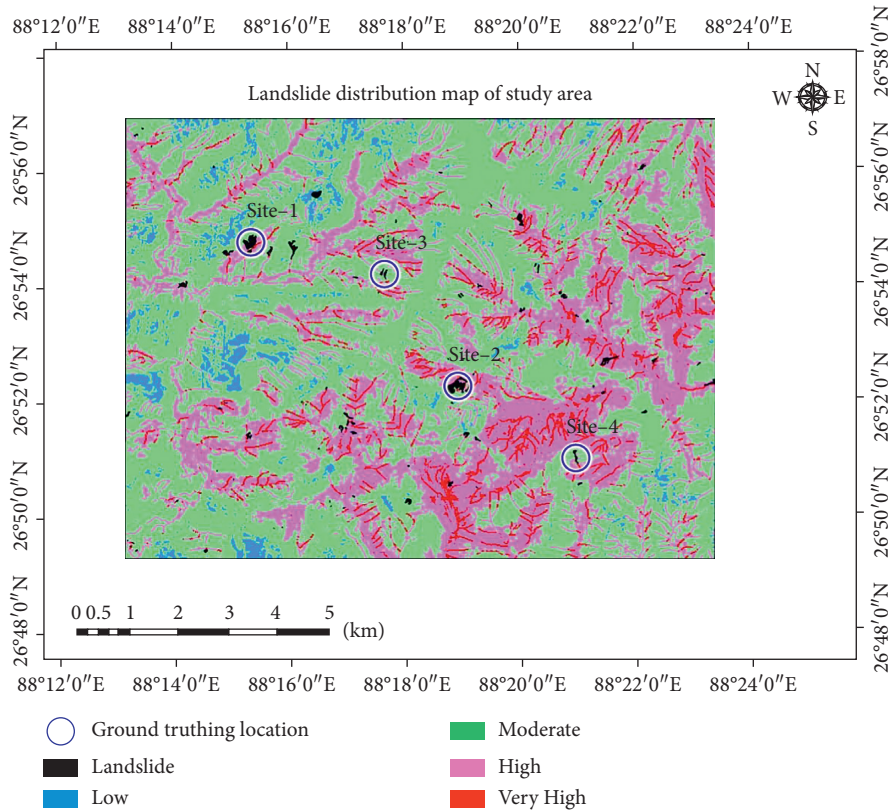


FIGURE 8: Landslide susceptibility map of the study area.

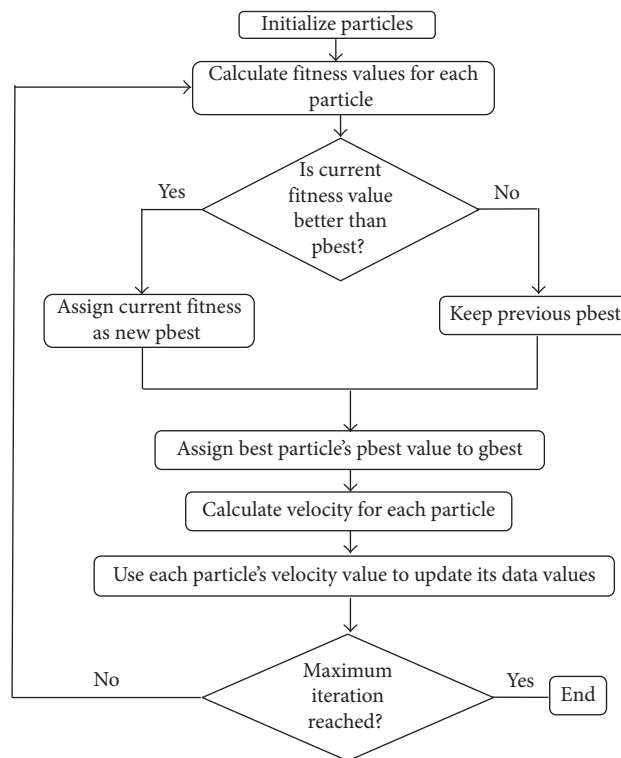


FIGURE 9: Flowchart for optimization of particles using PSO algorithm.

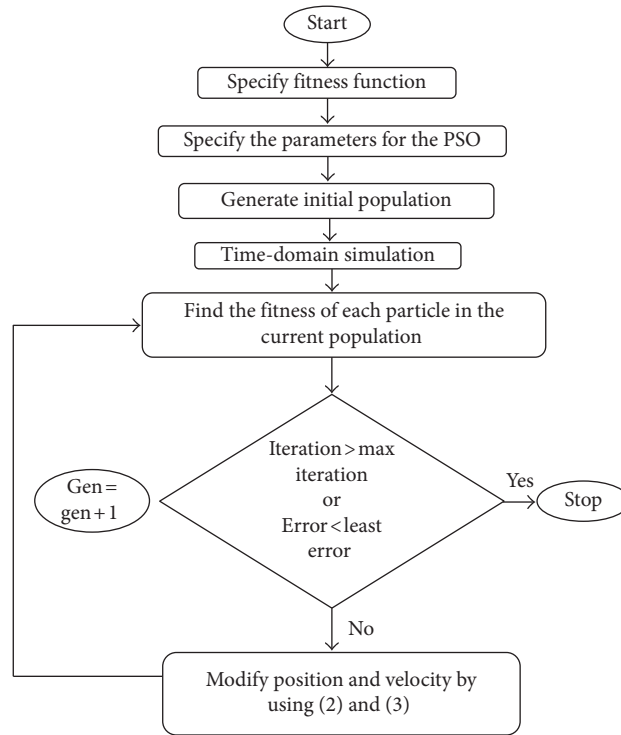


FIGURE 10: Flowchart describing the working of PSO.

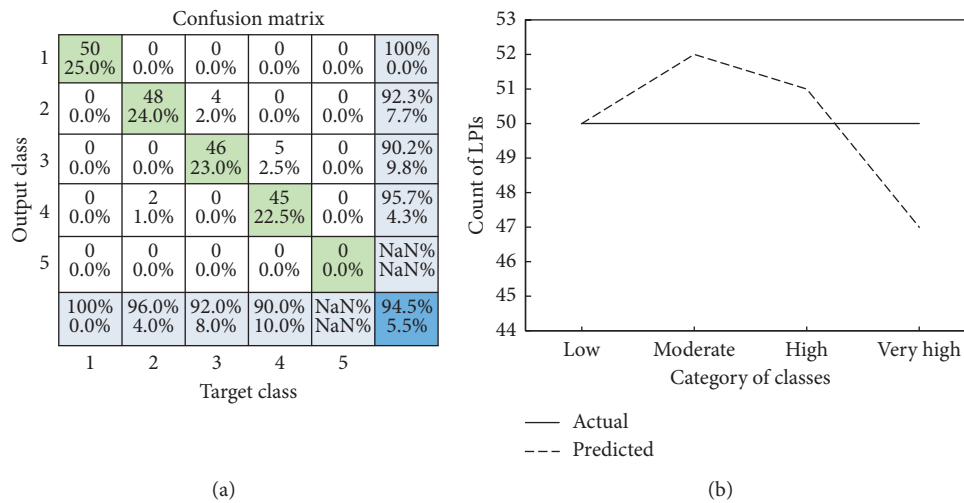


FIGURE 11: Confusion matrix (a) and graph (b) describing the accuracy.

values generated by PSO-SVM in terms of frequency division is shown in Figure 7.

5.20. Classification and Prediction Using Genetic Programming Approach Based on LPI. Genetic Programming (GP) is based on Darwin’s theory of evolution. It uses the principle of natural selection and genetic recombination. This method transforms units that define a given problem,

and with the progress of number of iterations, they familiarize themselves to their surroundings. A GP model consists of variables and functions represented in a tree structure. The leaf nodes of the tree are the variables that are user defined like soil type and slope and interior nodes are the functions like +, −, sine, and cosine.

The basic steps involved in the operation of GP are the creation of random set of population for the given variables and functions which are then evaluated for fitness. The fittest

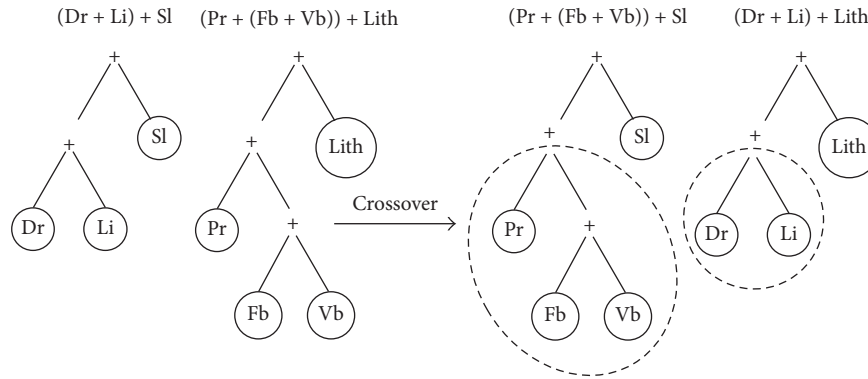


FIGURE 12: Illustration of crossover operation.

TABLE 4: Genetic Programming run results.

Run number	Population size	Number of generations	Training accuracy <sup>#</sup>	Test accuracy <sup>#</sup>	Function
1	500	2	0.9043	0.9016	+, -, sine, square
2	500	3	0.9100	0.9089	+, sine, square
3	500	4	0.9693	0.9700	+, square,
4	500	5	0.9557	0.9560	+, square, -, cosine
5	500	10	0.9707	0.9709	+, -, cosine
6	500	20	0.9939	0.9942	+, square
7	500	30	1.0000	1.0000	+
8	500	40	1.0000	1.0000	+, square
9	500	50	1.0000	1.0000	+
10	1000	500*	1.0000	1.0000	+, -, sine, square

Note. <sup>#</sup>The accuracy is measured in terms of coefficient of correlation ( $R$ ). \*The iteration achieved best fitness before reaching 200th generation.

populations are passed on the next generation after applying genetic operators like crossover, mutation, and duplication and further checked for fitness. An illustration for crossover operation is shown in Figure 12. As the number of generation increases, the possibility of more fit models enhances. The GP tends to attain a model of 100% accuracy by iterating for few numbers of generations or otherwise gives a model of fairly high accuracy having reached the specified number of generation or the time limit.

**5.21. Genetic Programming Procedure.** In this study, a computer program code for GP was run in MATLAB programming language. Before the run, training and testing data sets as inputs to the GP code were created. The input data sets were based on the variables and functions that formed the original LPI equation given by the GIS method. In this equation, the value for each variable to create the data set was randomly chosen within the limits as mentioned in Table 2. Out of the total number of data sets, 70% was used as the training set and remaining 30% as the testing set.

To begin with, the number of generations was kept very low as to check the accuracy that it attains at low generation values. Gradually the number of generations was increased and at 30th generation, the accuracy was found to be 100%, but the complexity of the model obtained was fairly high. On increasing further, the number of generations at 50th

generation, the model equation obtained was the simplest, while maintaining the same accuracy of 100%. This equation obtained was the closest match to the original LPI equation given by the GIS method with a value of 0.000224 added at the end. The run results for the various numbers of generations are shown in Table 4 below.

The equations obtained for each iteration are shown in Table 5. A comparison of the measured LPI values generated by GIS and the predicted values generated by GP in terms of frequency division is shown in Figure 13.

The total number of data points is different for LPI values of GIS and PSO-SVM methods (Figure 7) and GIS and GP methods (Figure 13) of analysis. A particular LPI value has a different number of occurrences while comparing the performance of GIS and PSO-SVM methods and GIS and GP methods; however, by comparing the trend at a suitable scale in the frequency axis of the comparison chart, an overall matching trend shall be observed. Hence, to compare the LPI-frequency trend of both the methods (PSO-SVM and GP) with the LPI-frequency trend using GIS (Figures 7 and 13), the scales of the frequency axes have been kept different in left and right ordinates.

**5.22. Map Validation.** Computation of landslide frequency for each class is the dominant factor for evaluating the quality of LSZ map [34]. The landslide susceptibility zones reflect the existing field instability conditions [17]. While

TABLE 5: Prediction equations by GP.

Number of generation	Functions used	Model equations (for LPI)
2	+, -, sine, square	$1.239Dr + 1.22As + 0.9052Li + 0.9627Sl - 0.2843 \sin(\sin(Sl)) + 0.01915 \text{ square}(Ea) + 0.04053SoPr + 110.9$
3	+, sine, square	$1.189So + 0.0234Re + 0.8868Li + 0.9452Sl + 1.595Pr + 1.189 \sin(La) + 0.0003481 \text{ square}(x1) + 0.0234Dr Ea + 104.3$
4	+, square,	$0.867Li + 1.043Sl + 2.03Ea + 0.8899Fb + 1.043La + 0.007235 \text{ square}(Dr + Lith) + 0.02292Li Vb + 68.67$
5	+, square, -, cosine	$0.9824Sl + 1.315Pr + 1.629Ea + 1.315Vb + 0.01981 \text{ square}(Lith) + 0.02173Dr Fb + 0.03422La(Li - \cos(La)) + 82.18$
10	+, -, cosine	$1.164Dr + 1.001Li + 1.021Sl + 1.869Ea + 1.07Lith + 1.164La - 1.021 \cos(\cos(Re)) + 0.06572Re Fb + 34.1$
20	+, square	$0.4065Dr + 1.005So + 1.001Li + 1.024Ea + 1.024Lith + 1.005La + 0.007404 \text{ square}(Sl + Fb + Vb + 5.73168) + 0.01453Dr Pr + 0.01453Re Pr + 72.64$
30	+	$Dr + So + Re + As + Li + Sl + Pr + Ea + Lith + Fb + Vb + La + 1.044 \times 10^{-10}$
40	+, square	$Dr + So + As + Li + Sl + Pr + Lith + Fb + Vb + La + 2.458 \text{ square}(0.6379)(Re + Ea) + 2.598 \times 10^{-10}$
50	+	<b><math>Dr + So + Re + As + Li + Sl + Pr + Ea + Lith + Fb + Vb + La + 0.000224</math></b>
500	+, -, sine, square	$Dr + So + Re + As + Li + Sl + 0.9998Pr + Ea + Lith + Fb + Vb + La - 9.609 \sin(Pr + Lith) \times 10^{-14} - \text{square}(1.285362) - 3.783 (2Li - \sin(Vb))(2Lith - Pr + Vb) \times 10^{-15} + 1.652$

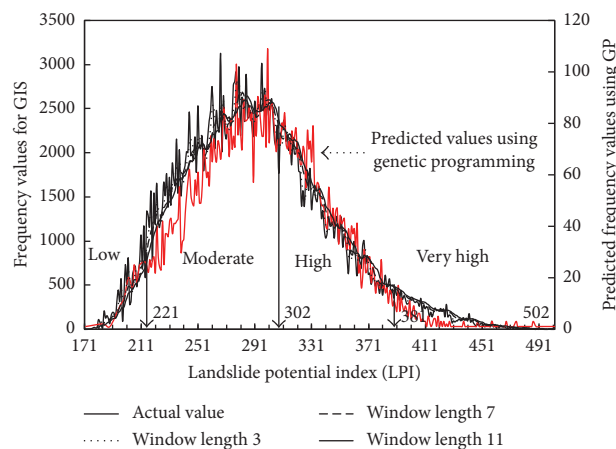


FIGURE 13: Frequency division of landslide potential index and predicted frequency using GP.

verifying the LSZ map, very high and high susceptible zones show signs of soil erosion, slope instability, and so on. For evaluating the effectiveness of the LSZ map, it is significant to calculate the landslide frequency for each zone. The study area has been classified into four zones, namely, low susceptibility zone, moderate susceptibility zone, high susceptibility zone, and very high susceptibility zone, and the

number of landslides and frequency per susceptible zone have been computed (Table 6).

## 6. Conclusions

Based on the studies described above, the following conclusions are drawn:

TABLE 6: Details of landslides and frequency in different susceptible zones.

Landslide susceptible zone	Area (sq. km)	Area (%) of total area	Number of landslides	Landslide area occupied per zone (sq. km)	Landslide area occupied per zone (%)	Frequency (per sq. km)
Low	7.267	3.6	1	0.003	0.34	0.14
Moderate	117.736	58.35	22	0.126	14.35	0.19
High	65.787	32.61	48	0.296	33.71	0.73
Very high	10.97	5.44	20	0.453	51.60	1.82

- (1) The entire study area was divided in to four respective susceptibility zones, that is, low (3.6%), moderate (58.35%), high (32.61%), and very high (5.44%) susceptibility zones, and landslide areas occupied per zone are 0.34%, 14.35%, 33.71%, and 51.60% for low, moderate, high, and very high susceptible zones, respectively; hence, this outcome was validated on the reasoning of landslide distribution, Genetic Programming method and Particle Swarm Optimization (PSO)-Support Vector Machine (SVM) technique.
- (2) Landslide frequency for the very high susceptibility zone (1.82/sq. km) was significantly higher as compared with that for high (0.73/sq. km), moderate (0.19/sq. km), and low (0.14/sq. km) susceptibility zones, and it was concluded that there is a gradual increment and substantial detachment of landslide frequency numerical values in between the susceptibility classes. Hence due to prevailing field unreliable conditions, the area falling in very high and high susceptible zones shall be treated as the potential landslide-prone zone, and it is highly recommended to avoid those zones, and if not possible, then immediate remedial measures may be taken to diminish the impact of landslide events.
- (3) The frequency division obtained by Particle Swarm Optimization-Support Vector Machine technique was a close match to the measured GIS values, and PSO-SVM technique has performed well with overall prediction accuracy of 94.5%, by considering accuracy average for each class.
- (4) The Genetic Programming method has also performed well with a nearly accuracy of 100% and suggested a model equation which is very close to the original equation given in the GIS environment. The frequency division obtained by GP was also a close match to the measured GIS values, thus suggesting the same susceptibility zones as suggested by the GIS model.
- (5) It is high time that a diligent landslide hazard study of very high and high susceptibility zones of the study area should be executed, especially in suggesting the geotechnical remedies for mitigating the slope instability. The LSZ map of the study area shall help planners in making decisions for future development of projects and disaster mitigation measures.

## Data Availability

The data like earthquake, satellite image, and toposheets used to support the findings of this study were supplied by the National Centre for Seismology, New Delhi, India; National Remote Sensing Centre, Hyderabad, India; and Survey of India, Kolkata, and cannot be made freely available due to defence restricted area. The request for access to these data should be made to the National Centre for Seismology, New Delhi, India; National Remote Sensing Centre, Hyderabad, India; and Survey of India, Kolkata.

## Conflicts of Interest

The authors declare that they have no conflicts of interest.

## Acknowledgments

The authors thank the National Remote Sensing Centre, Hyderabad, India; National Centre for Seismology, New Delhi, India; Survey of India, Kolkata, India; Geological Survey of India, Kolkata, India; National Atlas and Thematic Mapping Organisation, Kolkata, India; and National Bureau of Soil Survey and Land Use Planning, Kolkata, India, for providing various data used in this study. The authors are grateful to Dr. Shanatanu Sarkar, CBRI, Roorkee, India; Dr. V.V. Govind Kumar, IIT(ISM) Dhanbad, India; and Mr. Harish Sinha, CHiPS, India, for their valuable suggestions. Support from the Indian Institute of Technology (Indian School of Mines) Dhanbad, Jharkhand, India; Public Works Department, Delhi, India; and Central Public Works Department, Delhi, India, is also acknowledged.

## References

- [1] D. M. Cruden, "A simple definition of a landslide," *Bulletin of the International Association of Engineering Geology*, vol. 43, no. 1, pp. 27–29, 1991.
- [2] NDMA, *Management of Landslides and Snow Avalanches*, National Disaster Management Authority (NDMA), Government of India, New Delhi, India, 2009.
- [3] P. Aleotti and R. Chowdhury, "Landslide hazard assessment: summary, review and new perspectives," *Bulletin of Engineering Geology and the Environment*, vol. 58, no. 1, pp. 21–44, 1999.
- [4] R. Schuster, "Socioeconomic significance of landslides," in *Landslides: Investigation and Mitigation: Special Report*,

- A. K. Turner and R. L. Schuster, Eds., Vol. 247, pp. 12–36, National Academic Press, Washington, DC, USA, 1996.
- [5] M. Ercanoglu and C. Gokceoglu, "Use of fuzzy relations to produce landslide susceptibility map of a landslide prone area (West Black Sea Region, Turkey)," *Engineering Geology*, vol. 75, no. 3-4, pp. 229–250, 2004.
- [6] C. Chalkias, M. Ferentinou, and C. Polykretis, "GIS based landslide susceptibility mapping on the Peloponnese, Peninsula, Greece," *Geosciences*, vol. 4, no. 3, pp. 176–190, 2014.
- [7] S. Chawla, A. Chawla, and S. Pasupuleti, "A feasible approach for landslide susceptibility map using GIS," in *Proceedings of Geo-Risk ASCE 2017*, pp. 101–110, Denver, CO, USA, June 2017.
- [8] S. N. L. Taib, O. S. Selaman, C. L. Chen, R. Lim, and D. S. Awang Ismail, "Landslide susceptibility in relation to correlation of groundwater development and ground condition," *Advances in Civil Engineering*, vol. 2017, Article ID 4320340, 7 pages, 2017.
- [9] F. Guzzetti, *Landslide hazard and risk assessment*, Ph.D. dissertation, University of Bonn, Bonn, Germany, 2005.
- [10] H. Shahabi and M. Hashim, "Landslide susceptibility mapping using GIS-based statistical models and remote sensing data in tropical environment," *Scientific Reports*, vol. 5, no. 1, pp. 1–14, 2015.
- [11] R. P. Gupta and B. C. Joshi, "Landslide hazard zonation using the GIS Approach-a case study from the Ramganga catchment, Himalayas," *Engineering Geology*, vol. 28, no. 1-2, pp. 119–131, 1990.
- [12] R. Nagarajan, A. Mukherjee, A. Roy, and M.V. Khire, "Temporal remote sensing data and GIS application in landslide hazard zonation of part of Western Ghat, India," *International Journal of Remote Sensing*, vol. 19, no. 4, pp. 573–585, 1998.
- [13] R. P. Gupta, *Remote Sensing Geology*, Springer-Verlag, Berlin, Germany, 2nd edition, 2003.
- [14] V. Vakhshoori and M. Zare, "Landslide susceptibility mapping by comparing weight of evidence, fuzzy logic, and frequency ratio methods," *Geomatics, Natural Hazards and Risk*, vol. 7, no. 5, pp. 1731–1752, 2016.
- [15] R. P. Gupta, A. K. Saha, M. K. Arora, and A. Kumar, "Landslide hazard zonation in a part of the Bhagirathi Valley, Garhwal Himalayas, using integrated remote sensing-GIS," *Himalayan Geology*, vol. 20, no. 2, pp. 71–85, 1999.
- [16] A. K. Saha, R. P. Gupta, and M. K. Arora, "GIS-based landslide hazard zonation in the Bhagirathi (Ganga) valley, Himalayas," *International Journal of Remote Sensing*, vol. 23, no. 2, pp. 357–369, 2002.
- [17] S. Sarkar and D. P. Kanungo, "An integrated approach for landslide susceptibility mapping using remote sensing and GIS," *Photogrammetric Engineering and Remote Sensing*, vol. 70, no. 5, pp. 617–625, 2004.
- [18] A. K. Saha, R. P. Gupta, I. Sarkar, M. K. Arora, and E. Csaplovics, "An approach for GIS-based statistical landslide susceptibility zonation-with a case study in the Himalayas," *Landslides*, vol. 2, no. 1, pp. 61–69, 2005.
- [19] M. Basharat, H. R. Shah, and N. Hameed, "Landslide susceptibility mapping using GIS and weighted overlay method: a case study from NW Himalayas, Pakistan," *Arabian Journal of Geosciences*, vol. 9, no. 4, 2016.
- [20] H. J. Oh, S. Lee, and S. M. Hong, "Landslide susceptibility assessment using frequency ratio technique with iterative random sampling," *Journal of Sensors*, vol. 2017, Article ID 3730913, 21 pages, 2017.
- [21] S. Kanwal, S. Atif, and M. Shafiq, "GIS based landslide susceptibility mapping of northern areas of Pakistan, a case study of Shigar and Shyok basins," *Geomatics, Natural Hazards and Risk*, vol. 8, no. 2, pp. 348–366, 2016.
- [22] C. Zhou, K. Yin, Y. Cao, and B. Ahmed, "Application of time series analysis and PSO-SVM model in predicting the Bazimen landslide in the Three Gorges Reservoir, China," *Engineering Geology*, vol. 204, pp. 108–120, 2016.
- [23] Y. Shi and R. C. Eberhart, "Empirical study of particle swarm optimization," in *Proceedings of 1999 Congress on Evolutionary Computation-CEC99*, vol. 3, pp. 1945–1950, Washington, DC, USA, July 1999.
- [24] J. R. Koza, *Genetic Programming: A Paradigm for Genetically Breeding Populations of Computer Programs to Solve Problems*, Stanford University, Department of Computer Science, Vol. 34, Stanford University, Department of Computer Science, Stanford, CA, USA, 1990.
- [25] S. Litschert, "Landslide hazard zoning using genetic programming," *Physical Geography*, vol. 25, no. 2, pp. 130–151, 2004.
- [26] V. Nourani, B. Pradhan, H. Ghaffari, and S. S. Sharifi, "Landslide susceptibility mapping at Zonouz Plain, Iran using genetic programming and comparison with frequency ratio, logistic regression, and artificial neural network models," *Natural Hazards*, vol. 71, no. 1, pp. 523–547, 2014.
- [27] BIS, *Criteria for Earthquake Resistant Design of Structures: General Provisions and Buildings*, Bureau of Indian Standards (BIS), IS 1893:2002, Part-1, New Delhi, India, 2002.
- [28] B. N. Sinha, R. S. Varma, and D. K. Paul, "Landslides in Darjeeling district (West Bengal) and adjacent areas," *Bulletin of the geological Survey of India Series*, vol. 36, pp. 1–45, 1975.
- [29] A. S. Dhakal, T. Amada, and M. Aniya, "Landslide hazard mapping and its evaluation using GIS: an investigation of sampling schemes for a grid-cell based quantitative method," *Photogrammetric Engineering and Remote Sensing*, vol. 66, no. 8, pp. 981–989, 2000.
- [30] D. P. Kanungo, M. K. Arora, S. Sarkar, and R. P. Gupta, "A comparative study of conventional, ANN black box, fuzzy and combined neural and fuzzy weighting procedures for landslide susceptibility zonation in Darjeeling Himalayas," *Engineering Geology*, vol. 85, pp. 347–366, 2006.
- [31] S. K. Acharya and K. K. Ray, *Daling Group and Related Rocks*, Special Publication No. 22, Geological Survey of India, Kolkata, India, 1989.
- [32] P. J. Mason, M. S. Rosenbaum, and J. M. Moore, "Digital image texture analysis for landslide hazard mapping," *Geological Society, London, Engineering Geology Special Publications*, vol. 15, no. 1, pp. 297–305, 1998.
- [33] J. C. Davis, *Statistics and Data Analysis in Geology*, John Wiley & Sons, New York, NY, USA, 1986.
- [34] S. Sarkar, *Landslide hazard zonation and slope stability assessment techniques: applications to Srinagar-Rudraprayag, Garhwal Himalaya*, Ph.D. thesis, University of Roorkee, Roorkee, India, 1996.

## Research Article

# Reproducing Field Measurements Using Scaled-Down Hydraulic Model Studies in a Laboratory

Seung Oh Lee<sup>1</sup> and Seung Ho Hong <sup>2</sup>

<sup>1</sup>*School of Urban and Civil Engineering, Hongik University, Seoul, Republic of Korea*

<sup>2</sup>*Department of Civil and Environmental Engineering, West Virginia University, Morgantown, WV 26505, USA*

Correspondence should be addressed to Seung Ho Hong; [sehong@mail.wvu.edu](mailto:sehong@mail.wvu.edu)

Received 3 May 2018; Revised 30 June 2018; Accepted 16 July 2018; Published 12 August 2018

Academic Editor: Haiyun Shi

Copyright © 2018 Seung Oh Lee and Seung Ho Hong. This is an open access article distributed under the Creative Commons Attribution License, which permits unrestricted use, distribution, and reproduction in any medium, provided the original work is properly cited.

Little efforts have been made to the value of laboratory model study in closing the gap between results from idealized laboratory experiments and those from field data. Thus, at first, three bridge sites were selected and equipped with fathometers to find the bed elevation change in the vicinity of bridge pier over time. After and during the flooding, the stream flow variables and their bathymetry were measured using current viable technologies at the field. Then, to develop and suggest a laboratory modeling techniques, full three-dimensional physical models including measured river bathymetry and bridge geometry were designed and fabricated in a laboratory based on the scale ratio except for the sediment size, and the laboratory results were compared with the field measurements. Size of uniform sediment was carefully selected and used in the laboratory to explore the scale effect caused by sediment size scaling. The comparisons between laboratory results and field measurements show that the physical models successfully reproduced the flow characteristics and the scour depth around bridge foundations. With respect to the location of the maximum scour depth, they are not consistent with the results as in the previous research. Instead of occurring at the nose of each pier, the maximum scour depths are located further downstream of each pier column in several experimental runs because of the combination of complex pier bent geometry and river bathymetry, and the resulting unique flow motions around the pier bent.

## 1. Introduction

General purposes of physical hydraulic modeling are reproduction and/or duplication of actual flow phenomena in a laboratory. Thus, with the help of successful physical hydraulic modeling, the effects of selected flow parameters around various hydraulic structures, such as different shape of orifices [1], T-shaped spur dike [2], bridge pier, and so on, can be examined using well-controlled laboratory experiment. This study is an experimental investigation of local pier scour throughout the reach of a bridge section under clear-water scour conditions using scale-down full bridge geometry and river bathymetry. Pier scour is analyzed with reference to its spatial and temporal distribution, and several experimental observations and conclusions are reported.

One thousand bridges have collapsed over the last 30 years in the United States, and 60 percent of those failures stem from hydraulic failure including bridge foundation

scour [3]. Thus, the topic of foundation of scour has been attracted by many researchers and scientist since the late 1950s. Although numerous studies for the prediction of bridge scour depths have been conducted using physical modeling in laboratory and also using numerical simulation [4, 5], the topic is still challengeable when the resultant scour depths are applied to large-scale prototype because most of the current scour prediction formula are based on laboratory experiments which have been implemented with simple channel and bridge geometry even though most of bridge foundations in the field have complex geometry and the channel shape is site specific. Even though the earliest laboratory experiment conducted by Durand-Claye [6] used three different shapes of pier (rectangular, round, and triangular) to find local pier scour, since then, most experimental investigations have been conducted with a single cylindrical pier in the laboratory [7–9]. Therefore, relations and estimations of the pier scour depth developed from

laboratory data show inaccurate results compared to the actual pier scour depths measured at field sites [10]. Furthermore, most of the predictive formulas presented in the literatures have not been verified by field data because there are few long-term stations that monitor the scour process at a specific bridge site including real-time velocity measurements [11].

Only a few studies [12–14] show results for scour around scaled model having the same shape as actual field bridge pier including river bathymetry. Prototype bridges usually have complex pier configurations including shapes other than cylindrical, multiple columns with variable spacing along the pier column, and multiple pier bents at variable flow depths across the river that may be skewed relative to the main flow direction. In addition, the measurements of scour depth at complex bridge piers in the field for the validation of lab results are tricky because of the safety and economical reason. Under these circumstances, scale-down physical modeling is suggested that can reproduce the prototype flow characteristics and scour patterns including location of the maximum scour depths, which may not be at the nose of the pier as in idealized laboratory studies.

In this study, laboratory pier scour experiments on particular bridges in Georgia, USA, were conducted and their hydraulic and geometrical conditions were reproduced in the laboratory by equating the Froude numbers in the model and prototype. Based on the Froude number similarity between the model and the prototype, all of the measured prototype data including discharge, stage, velocity distributions, and river bathymetry were reproduced in the laboratory except for the sediment size. The sediment size scaling, which is one of the important hydraulic modeling criteria, will be explained in more detail in the Physical Modeling Strategy. The USGS has been gauging stream flow at the chosen bridge sites for long periods, but detailed monitoring including continuous measurement (30-minute intervals) of pier scour using fathometers and velocity measurements using acoustic velocity meter has been underway since 2002 as part of a large scour study for the Georgia Department of Transportation (GDOT) [15]. The measured temporal variation of scour depth and velocity measurement around the bridge pier for specific flood events were analyzed and compared with laboratory experimental data, and the several experimental observations and conclusions are presented here.

## 2. Hydraulic Modeling Procedure

*2.1. Field Monitoring of Regional Bridge Sites in Georgia.* A standard USGS stage-discharge station is located at each of the three bridge sites (a bridge over the Flint River at Bainbridge, a bridge over the Chattahoochee River near Cornelia, and a bridge over the Ocmulgee River at Macon) chosen for modeling. In each bridge sites, bed sediment samples were collected both upstream and downstream of the bridge. Also, continuous velocity data were measured using a cross-channel acoustic Doppler velocity sensor which provided two-dimensional velocity components in the bridge approach section at 15-minute intervals. In addition, temporal

variations of channel bed elevations near the bridge pier bent were measured by several fathometers attached to the wall of the bridge piers. The horizontal locations of the bridge pier bents were determined by a kinematic differential Global Positioning System (GPS), which was also used to establish the horizontal positions where elevations and velocity were measured at each cross section. During large flood events, an acoustic Doppler current profiler (ADCP) and a digital fathometer were deployed in a boat to measure three-dimensional velocities and channel bathymetry in more detail [15].

The first bridge site for physical modeling is a bridge over the Flint River at Bainbridge, Georgia. This particular bridge was chosen partly because cross-sectional geometry and velocity data along the bridge deck were measured adequately by the USGS during tropical storm Alberto. Tropical storm Alberto produced peak flood discharges greater than 500-year events in July 1994 and caused numerous bridge failures in southern part of Georgia [16]. One other reason for the selection was the bridge was representative of the Georgia coastal plain. The width of the main channel is approximately 150 m, and there is a very wide and flat floodplain on both sides of main channel. The channel is straight for upstream and has a sharp bend about 150 m downstream of the bridge. The effect of backwater propagated from the Jim Woodruff Reservoir located 40 km downstream of the bridge exists at lower stages, but the backwater can be neglected at higher stages [15]. There are four bridge pier bents, two of which are situated in the main channel, while the other two are located on each bank. As shown in Figure 1, each pier bent has two square concrete pier columns having 1.83 m width and placed on large stepped square concrete footings. The median size of the bed material sample is approximately 0.4 mm, and the geometric standard deviation is 2.17.

The second bridge site is the Georgia Highway 384 (Duncan Bridge Road) bridge over the Chattahoochee River in the Piedmont physiographic province near Cornelia, Georgia. During the 2003 flooding, the USGS measured the bed elevations along the immediate upstream of the bridge deck and also presented mean velocities measured by the in situ acoustic velocity meter at the left side of the central pier. Based on the measurement in 2003, the USGS rated a peak discharge of 385 m<sup>3</sup>/s which corresponded with a bank-full flow and found approximately 1.8 m of local scour at the bridge foundation. The channel is fairly straight for several hundred meters upstream and downstream of the bridge. The bridge was supported by three bridge pier bents, and one of them is located in the main channel and the others on each side of left and right banks. As shown in Figure 2, each bridge pier bent consists of four rectangular concrete columns and rectangular concrete footings. Among the four pier columns, two inner pier columns were connected by a web, while two outer pier columns were newly added to widen original Georgia Highway 384 Bridge in 1988. The bridge piers were designed to be aligned with the flow and the width is 1.07 m. The median size of bed material around the center of the channel is about 0.7 mm, and the geometric standard deviation is 1.6.

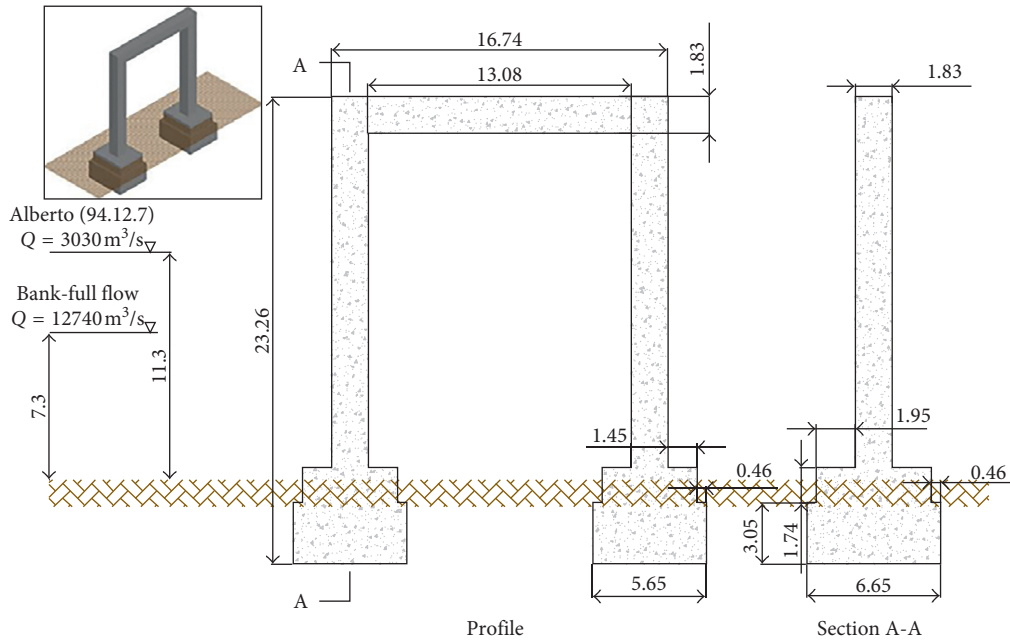


FIGURE 1: Dimensions of the bridge bent in Flint River at Bainbridge, GA (prototype dimensions in m).

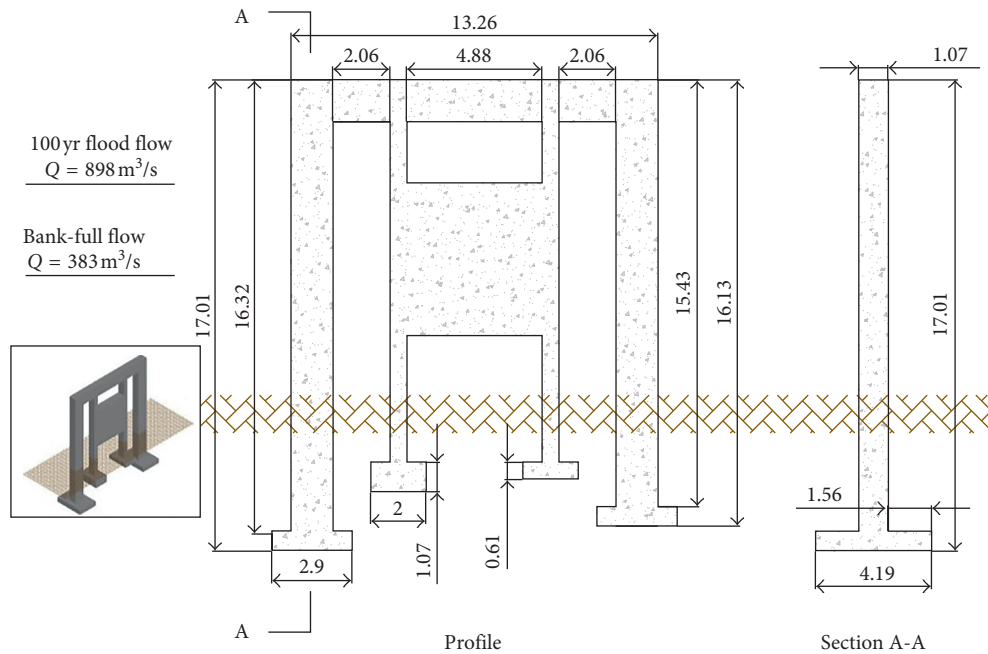


FIGURE 2: Dimensions of central pier bent in Chattahoochee River Bridge near Cornelia, GA (prototype dimensions in m).

The third bridge site was the Fifth Street Bridge over the Ocmulgee River at Macon, Georgia, located in the physiographic Fall Line region. The historical peak discharge at this site is  $1841 \text{ m}^3/\text{s}$  and measured in March 1998 along with approximately 3.3 m of total scour depth caused by both contraction scour as well as local scour on the upstream side of the bridge pier bent located in the main channel [15, 17]. As shown in Figure 3, the bridge pier bents consist of four circular cylinders each having a diameter of 1.83 m placed on rectangular concrete footings. The median size of bed material is about 0.8 mm, and the geometric standard deviation is 2.13.

As explained in the previous paragraph, temporal variations of bed elevations as well as continuous velocity data were collected for each site. Figure 4 shows example plot of the fathometer data collected for bed elevations during the period of March 25, 2005, to April 14, 2005, on the nose of the front pier columns at a bridge over Flint River, May 5, 2003, to May 12, 2003, on the nose of central pier bent in Chattahoochee River, and February 15, 2003, to March 2, 2003, on the left side of pier bent in Ocmulgee River, respectively. During this time record, the continuous fathometer measurements of scour depth illustrate the

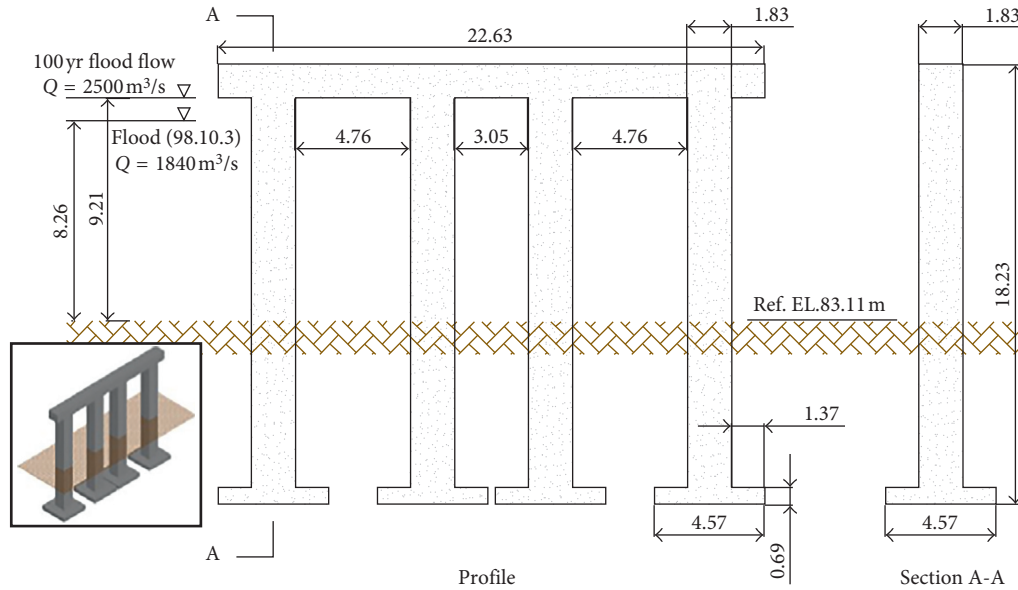


FIGURE 3: Dimensions of the central bridge pier bent in Ocmulgee River at Macon, Georgia (prototype dimensions in m).

dynamic nature of scour process. For example, Figure 4(a) shows that the fathometer measured almost 0.8 m of scour at the peak discharge of 1,800 m<sup>3</sup>/s, but the local pier scour holes alternately filled and scoured back out, even in similar magnitude of the peak discharge amount during a week period (April 1, 2005, to April 7, 2005). A cross section was also surveyed during the flooding event across the bridge for the comparison with laboratory data.

**2.2. Physical Modeling Strategy.** The local scour around a bridge pier is often governed by multiple parameters as given in the following equation [13, 18, 19]:

$$\frac{d_s}{b} = f\left(K_s, K_\theta, \frac{y_1}{b}, \frac{b}{d_{50}}, \frac{V_1}{V_c}, Fr_1 \text{ or } Fr_b, R_1 \text{ or } R_b\right), \quad (1)$$

where  $d_s$  is the scour depth;  $b$  is the width (diameter) of bridge pier;  $K_s$  is the shape factor;  $K_\theta$  is the pier alignment factor;  $d_{50}$  is the median sediment size;  $y_1$  and  $V_1$  are approach depth and velocity, respectively;  $V_c$  is the velocity for initiation of motion of sediment;  $Fr_1$  is the approach Froude number ( $V_1/\sqrt{gy_1}$ );  $Fr_b$  is the approach pier Froude number ( $V_1/\sqrt{gb}$ );  $R_1$  is the approach Reynolds number ( $V_1 y_1/\nu$ ), and  $R_b$  is the pier Reynolds number ( $V_1 b/\nu$ ). Firstly, one of the challenging parts in the laboratory modeling is that it is almost impossible to satisfy all requisite similarity criteria simultaneously. The sediment size, for instance, cannot be scaled using same geometric scale ratio in the laboratory because very small model sediment sizes exhibit interparticle forces that are not present in prototype sand-bed streams. Hence, a physically reasonable model strategy is required to predict the prototype behavior effectively.

Second challenging work is “How to reproduce/mimic field scour regime (live-bed scour) in a laboratory?” and “If we cannot reproduce/mimic field scour regime, is there any way of surrogate?” Keulegan’s equation for fully rough turbulent flow was used to evaluate the critical velocities of

sediment in the field and laboratory [20]. Then, the value of  $V_1/V_c$  confirmed that scour regime in the field was certainly live-bed scour. It is difficult to reproduce live-bed scour conditions in a laboratory due to the physical and economic constraints, even though a large scale is selected in a large flume. As a result, a surrogate method of finding maximum scour depth using clear-water scour experiment should be suggested instead of conducting experiment in live-bed conditions.

Among the nondimensional variables in (1), local scour depth relative to the pier width,  $d_s/b$ , relative flow depth,  $y_1/b$ , nondimensionalized by pier width, and the ratio of pier width to median sediment size,  $b/d_{50}$ , are meaningful nondimensional parameters. The effect of Reynolds number can be negligible because the flow around the pier is fully turbulent [8, 21]. Thus, the Froude number similarity can be utilized as a dynamic similarity, and the length scale ratio can be determined based on the constructability of a physical model. The Froude number governs open-channel flow through the bridge and hence the pressure gradient in the vicinity of the piers. Geometric similarity is maintained in terms of  $y_1/b$  in order to preserve the relative size and strength of the horseshoe vortex. While maintaining the Froude number similarity and geometric similarity ( $y_1/b$ ) in between field and laboratory, the sediment size in the laboratory can be selected to produce a value of  $V_1/V_c < 1.0$  (clear-water scour condition) as a surrogate to model live-bed scour in a laboratory and concurrently to compensate for the reduction in dimensionless scour depth,  $d_s/b$ , at large values of  $b/d_{50}$  (maximum scour depth occurs for  $V_1/V_c = 1.0$ ). The laboratory model was constructed using an undistorted scale from the Froude number similarity with equality of  $y_1/b$ .

The scale for laboratory models was determined based on the measured field extent versus physical horizontal flume space. Then, discharge, water depth, and velocity were calculated to match Froude numbers between field and laboratory. Finally, possible experimental runs were selected

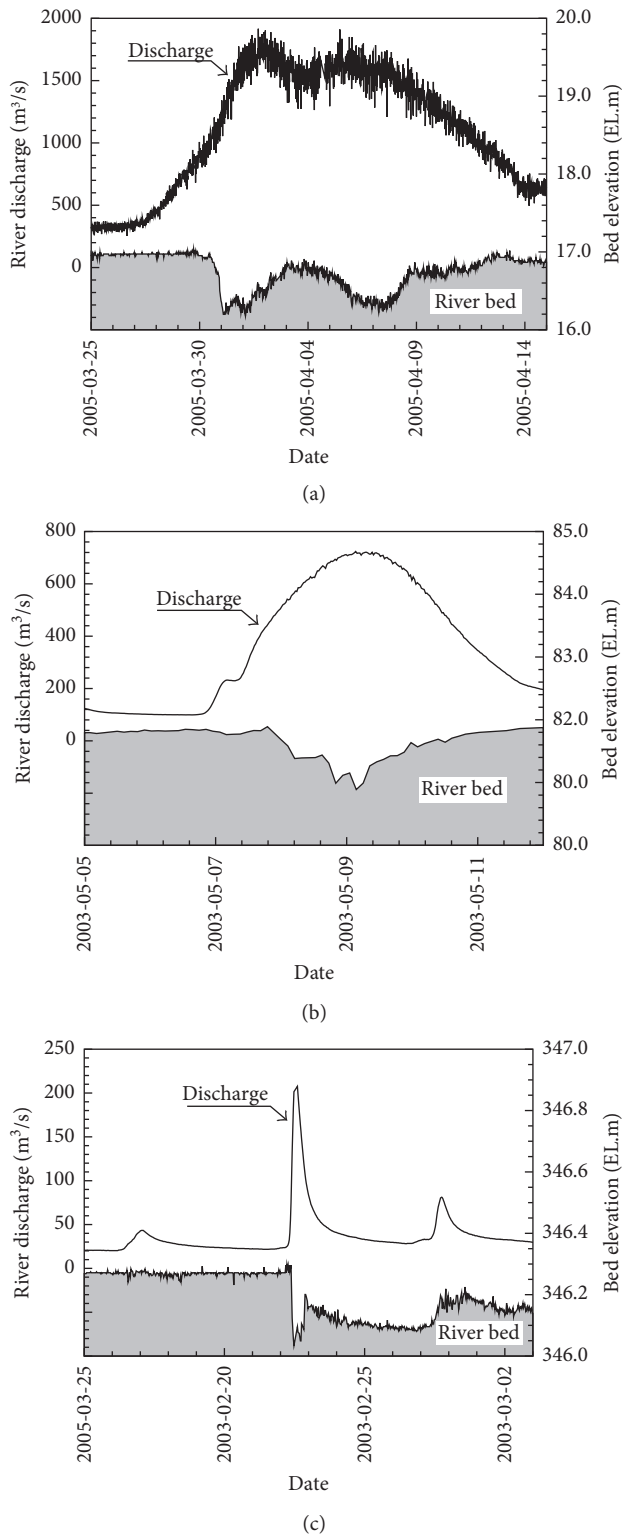


FIGURE 4: Temporal variation of bed elevation around bridge pier bent with corresponding discharge in (a) Flint River, (b) Chattahoochee River, and (c) Ocmulgee River.

up to where the approach velocity in the laboratory model became close to the critical velocity calculated by Keulegan’s equation to conduct the experiment in clear-water scour regime.

2.3. *Laboratory Experiments.* All of laboratory experiments were conducted in a 4.3 m wide, 24.4 m long, and 0.6 m deep open-channel flume with test section where the models of bridge piers and embankments were built. The templates for cross sections were made of plywood with scaled elevations, and the vertical wooden templates corresponding to the scaled river bathymetry were placed in the flume based on the coordinates determined by a Global Positioning System (GPS). This GPS information was used not only to locate the cross sections and the bridge appurtenances but also to establish corresponding positions where the scour results from the experiments were compared with field measurements.

The test section for the scour in which the bridge pier, embankment, and abutment were placed began at 7.3 m, 7.9 m, and 9.4 m from the inlet of flume for Chattahoochee River model, Flint River model, and Ocmulgee River model, respectively, to create fully developed turbulent flow in the approach section. The approach section (7.3 m long, 7.9 m long, and 9.4 m long) for each model was filled with a sediment having a median grain size of 3.3 mm and a geometric standard deviation of  $\sigma_g = 1.3$ . The moveable bed test section and the sediment trap section were leveled carefully by hand to match the templates manufactured by thin aluminum panels based on the measured river bathymetry, and the aluminum panels were removed after the bed was shaped for scour experiment. In the test section, the full depth was filled with 1.1 mm sand to measure the bed deformation by scour. Finally, the sediment trap section was filled with 3.3 mm of sand and the surface layer was fixed with spraying polyurethane to trap the sediment transported out of the moveable test section.

The water flows into the head box of the flume vertically from a 0.305 m diameter supply pipe, and the maximum flow rate is up to 0.283 m<sup>3</sup>/s. Turbulence at the entrance of the flume is reduced by a flow diffuser, overflow weir, and baffles, and those device produced stilling of the inflow and a uniform flume inlet velocity distribution. A flap tailgate is located at the downstream end of the flume to control the water elevation. Water was recurred through the laboratory sump from which two pumps continuously provided overflow to the constant-head tank. In the supply pipe, discharge was measured by a magnetic flow meter with an uncertainty of  $\pm 0.0003$  m<sup>3</sup>/s.

An acoustic Doppler velocimeter (ADV), which is used for measuring instantaneous point velocities and turbulence quantities, is mounted on the carriage and can be moved in three dimensions freely. Three different types of ADV probes, 3D down-looking, 3D side-looking, and 2D side-looking, were used for measurements. When velocity measurements were needed at points close to the free surface and at shallow water depths, the 2D and 3D side-looking ADV probes were used. The ADV with 3D down-looking probe gives the distance from the sampling volume to the bed which can be converted into elevation relative to the datum by reading the point gage vertical scale to which the ADV is attached. The temporal variation of scour depth in front of a bridge pier was measured periodically using the ADV temporarily positioned for a moment above the point of scouring. Each experiment was ended when the local

scour depth reached the equilibrium state at which there are negligible changes in bed elevation with time as guided in literatures [9, 13], but it was never less than 48 hours. Scour depth was measured with a point gage having a  $\pm 0.3$  mm scale error and an ADV having a  $\pm 1$  mm scale error.

### 3. Results and Discussion

Experimental flow conditions and results for each river model are presented in Table 1 including field measurements from the USGS. One of the interesting findings from these experimental studies is that the scour contours show non-symmetrical pattern relative to the bridge pier bent centerline. Experimental results from several other researchers show that the location of maximum local scour depth was in front of the first pier in many cases. However, as shown in Figure 5, the maximum scour depth occurred at the nose of the third pier, not at the first pier, and the footing of the third pier was almost exposed as measured as in the Chattahoochee River Bridge because of the site-specific river bathymetry, angle of attack, and alignment of the bridge pier bent in the main channel. These findings will be discussed in the following sections in more detail.

*3.1. Comparison of Velocity Distribution.* As shown in Figure 6, the laboratory velocities were compared with available field measurements to examine our laboratory modeling regime which is Froude number similitude. In Figure 6(a), the streamwise, depth-averaged velocity distribution along the bridge deck (FR1 in Table 1) was compared with corresponding field data (FF in Table 1) in Flint River Bridge measured during tropical storm Alberto occurred in 1994. Even though there is some discrepancy in the velocities near the right bank (around station 200) and at the nose of the bridge pier in the main channel, the velocity distribution measured in the laboratory is in good agreement overall with field measurements. For the Chattahoochee River case as shown in Figure 6(b), flow velocities in the field were measured with an acoustic Doppler velocity meter mounted at the side of the upstream pier and pointed in the cross-stream direction during the 2003 flood events. There were three data points at different distances from the side wall of the bridge pier located in the main channel. The velocity comparison shows also good agreement in Figure 6(b). Finally, Figure 6(c) shows the velocity comparison for the case in Ocmulgee River Bridge. Because measurement activities during the flooding are too dangerous in the field, the velocities were measured at a short time after the peak discharge of  $1,841 \text{ m}^3/\text{s}$ . Thus, the actual discharge during the measurements was  $1,388 \text{ m}^3/\text{s}$ . Therefore, the magnitude of each velocity measured by the USGS was slightly smaller than that of laboratory measurement. However, the shape of the velocity distribution for each case is similar enough to verify the validity of the Froude number similitude [17].

*3.2. Comparisons of Bed Elevation Upstream of the Bridge Foundations.* When the bed elevations for physical modeling of Flint River Bridge were compared with the field data

measured during tropical storm Alberto, local pier scour depths upstream of each pier in the main channel were reproduced well in the laboratory model experiment as shown in Figure 7(a). However, the scour profiles in the constricted region between two bridge pier bents in the main channel (between the station 100 m and 150 m) did not agree well with the field cross section possibly because of the lack of sufficient time for full development of the contraction scour in the laboratory which develops more slowly than the local pier scour [17].

For the Chattahoochee River Bridge comparison as shown in Figure 7(b), the measurement across the upstream bridge for bank-full flow conditions that occurred in July 2003 with a peak discharge of  $385 \text{ m}^3/\text{s}$  was compared with the laboratory results. The maximum scour depth occurred at the nose of the upstream pier in both field and laboratory with a 2 percent relative error between the two measurements. It is also interesting to note that a flood of similar magnitude ( $371 \text{ m}^3/\text{s}$ ) as in July 2003 occurred in December of 1961 and the maximum scour depth is remarkably similar to the value after 2003 flooding with a difference of 0.06 %. The shapes of the scour holes are approximately the same and the maximum scour depths at the nose of the bridge pier despite the intervening time interval of 42 years during which many cycles of alternate scouring and filling occurred. There is some discrepancy between laboratory and field cross sections in the deposition region between the pier bents because the experiment was conducted under clear-water scour conditions while live-bed scour conditions occurred in the field. The measured cross sections upstream of the bridge in Ocmulgee River during the 1998 flood were compared with the experimental run OR1 in Figure 7(c). The pier scour depth showed a good agreement of the bed elevation with field data, while the scour depth between the central pier and pier on the right side (located around 100 m) did not seem to agree with the field data because of the similar reason as in Flint River Bridge through the flow contraction region.

*3.3. Comparison of Maximum Scour Depth Upstream of the Bridge Piers.* The scour depths measured at the nose of the upstream of pier for each physical model are compared with the commonly accepted scour prediction formulas in the United States, which are HEC-18 [22], Melville [23], and Sheppard et al. [24]. One of the important objectives of writing research paper is suggesting a design practice that determines how their design can best take their interest into account. That is the reason why those three equations are chosen because they are the mostly used equations for the hydraulic engineers. The effect of the flow intensity,  $V_1/V_c$ , on the dimensionless scour depth,  $d_s/b$ , is observed by comparison with scour prediction formulas having constant values of  $y_1/b$  and  $b/d_{50}$  for each comparison. The approach Froude number is given as a label on each data point in Figures 8–10.

It is found that the laboratory data for Flint River modeling with  $b/d_{50} = 18.8$  agree well with Melville's and Sheppard et al.'s formula, while HEC-18 overpredicts the scour depth for two small Froude numbers as shown in

TABLE 1: Summary of experimental results and field data for each river.

Name	Scale	$Q$ $m^3/s$	$b$ m	$y_1$ m	$V_1$ m/s	$d_s$ m	$Fr_1$	$V_1/V_c$	$y_1/b$	$b/d_{50}$	$d_s/b$
CR <sup>1</sup>	1/40	0.071	0.027	0.190	0.317	0.060	0.23	0.71	7.04	24.53	2.23
CR2	1/40	0.038	0.027	0.107	0.308	0.052	0.30	0.75	3.95	24.53	1.92
CR3	1/40	0.085	0.027	0.190	0.348	0.059	0.26	0.78	7.04	24.53	2.19
CR4	1/40	0.042	0.027	0.107	0.341	0.060	0.33	0.83	3.95	24.53	2.23
CR5	1/40	0.047	0.027	0.107	0.411	0.068	0.40	1.00	3.95	24.53	2.51
CF <sup>2</sup>	NA	385.0	1.067	4.279	2.140	2.003	0.33	4.39	4.01	1568	1.88
FR <sup>3</sup> 1	1/90	0.042	0.021	0.152	0.247	0.022	0.20	0.57	7.35	18.8	1.05
FR2	1/90	0.047	0.021	0.152	0.290	0.037	0.24	0.67	7.35	18.8	1.77
FR3	1/90	0.051	0.021	0.152	0.335	0.058	0.27	0.78	7.35	18.8	2.79
FF <sup>4</sup>	NA	3030	1.829	11.28	2.306	2.908	0.22	5.27	6.17	4813	1.59
OR <sup>5</sup> 1	1/45	0.136	0.041	0.181	0.312	0.050	0.23	0.70	4.45	36.9	2.05
OR2	1/45	0.165	0.041	0.191	0.336	0.053	0.25	0.75	4.69	36.9	2.20
OR3	1/45	0.184	0.041	0.203	0.350	0.084	0.25	0.78	4.99	36.9	2.19
OF <sup>6</sup>	NA	1841	1.829	8.230	2.094	0.032	0.23	3.73	4.50	2286	1.78

CR<sup>1</sup> = Chattahoochee River model experiment ( $d_{50} = 1.1$  mm), CF<sup>2</sup> = field data at Chattahoochee River ( $d_{50} = 0.68$  mm), FR<sup>3</sup> = Flint River model experiment ( $d_{50} = 1.1$  mm), FF<sup>4</sup> = field data at Flint River ( $d_{50} = 0.38$  mm), OR<sup>5</sup> = Ocmulgee River model experiment ( $d_{50} = 1.1$  mm), OF<sup>6</sup> = field data at Ocmulgee River ( $d_{50} = 0.8$  mm).

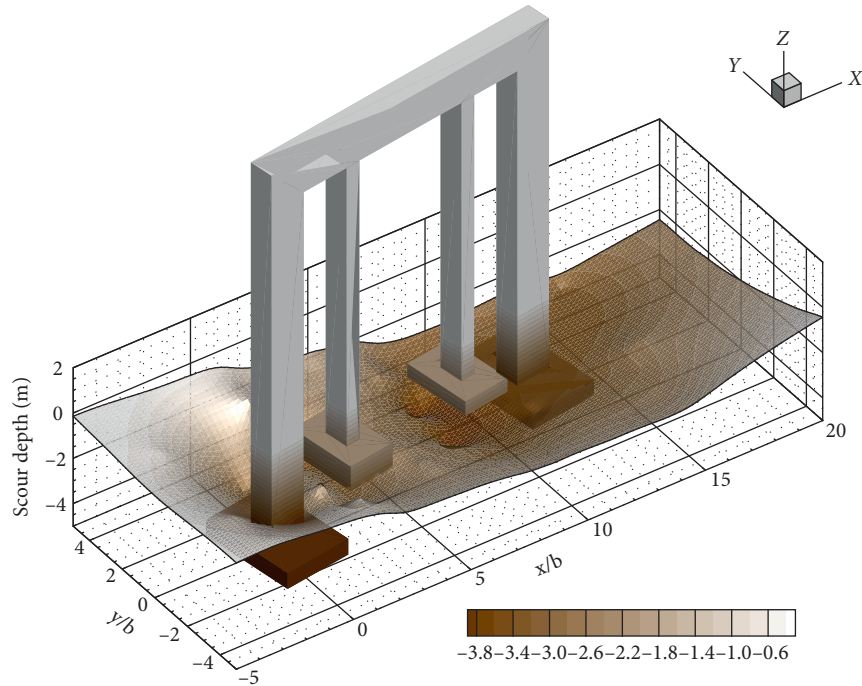
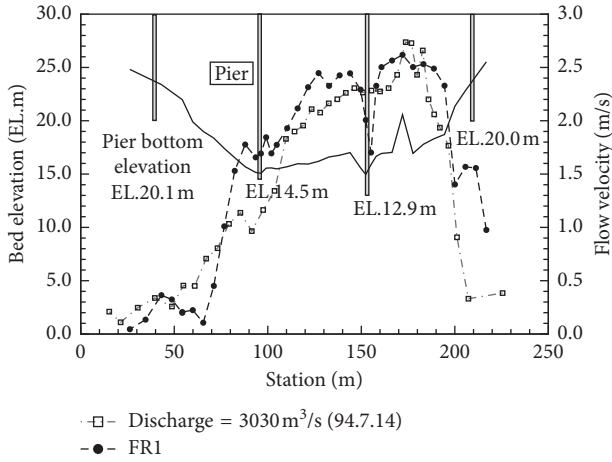


FIGURE 5: Scour depth contours for experimental run CR4.

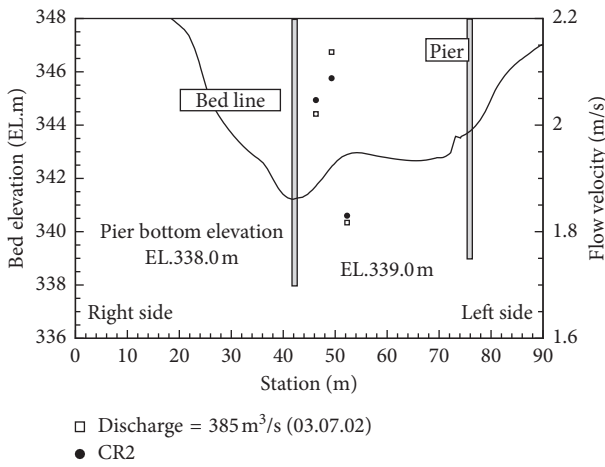
Figure 8. The HEC-18 formula includes the effect of the approach Froude number but does not include the parameter bearing the effect of  $V_1/V_c$ . Conversely, the other two formulas, the Melville and the Sheppard et al. formulas, include the effect of  $V_1/V_c$  but do not consider the approach Froude number. Also, the Melville and Sheppard et al. formulas include a reduction in  $d_s/b$  because the relative sediment size,  $b/d_{50}$ , is less than 25. The effect of the relative flow depth,  $y_1/b$ , has an effect only in the HEC-18 formula because the value of  $y_1/b$  is large enough that it has almost no influence in the Melville and Sheppard et al. formulas. The field data of Flint River are in the live-bed scour

condition with  $b/d_{50} = 1569$  ( $d_{50} = 0.38$  mm in the field). The dimensionless scour depths were overpredicted by the HEC-18 and Melville formula, while Sheppard et al.'s formula slightly underestimated the dimensionless scour depth.

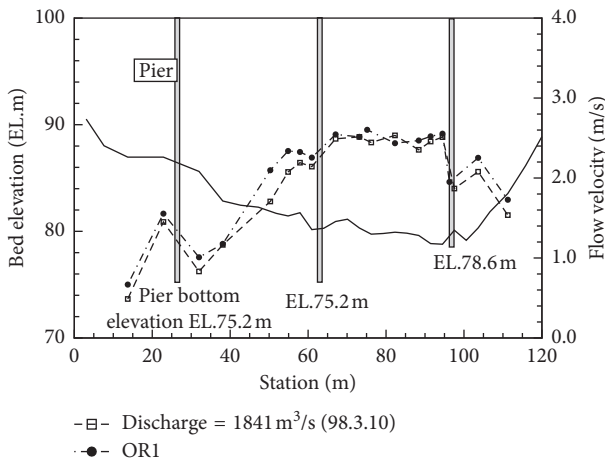
For Chattahoochee River modeling as shown in Figure 9, the laboratory data also agree relatively well with all three formulas even though HEC-18 slightly overpredicts the scour depth. With the field data, the Melville and HEC-18 formulas still overpredict the dimensionless scour depths with the value of  $b/d_{50} = 1569$  ( $d_{50} = 0.68$  mm in the field), while the Sheppard formula shows reasonably good agreement. Finally, as shown in Figure 10, for the Ocmulgee River



(a)



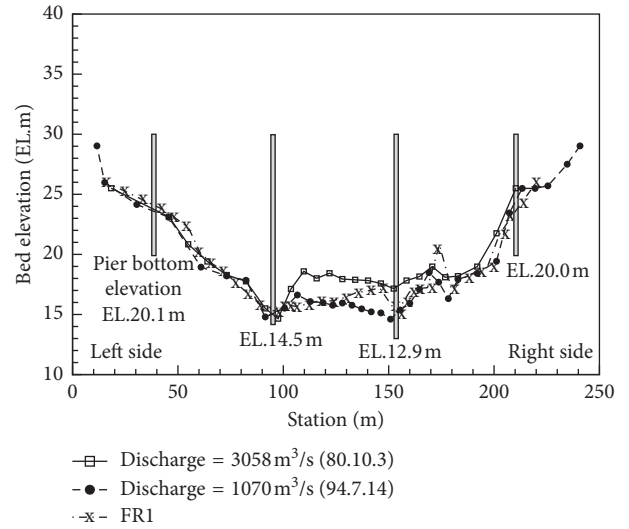
(b)



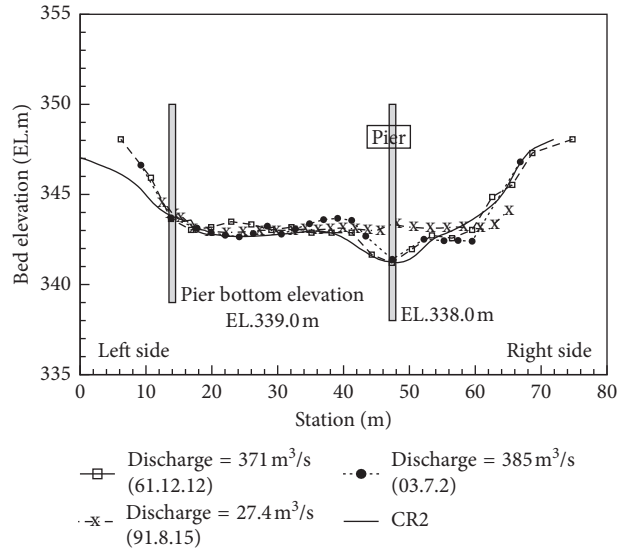
(c)

FIGURE 6: Velocity comparison between laboratory and field measurements for (a) FR1, (b) CR2, and (c) OR1.

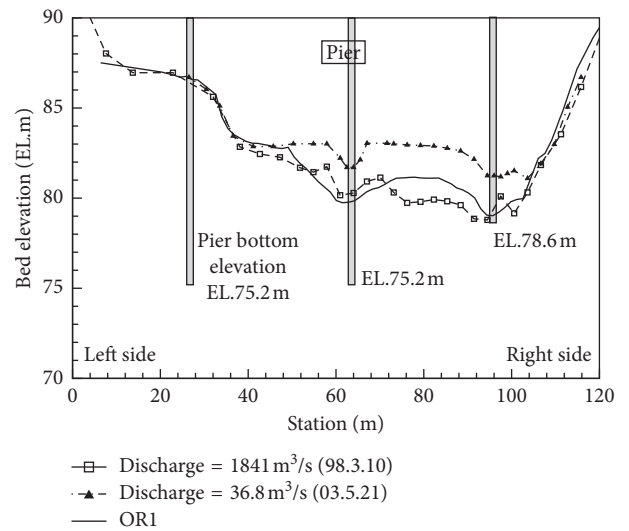
field data with the value of  $b/d_{50} = 2286$  ( $d_{50} = 0.8$  mm in the field), the Sheppard formula underpredicts the dimensionless scour, and the other two formulas shows overprediction even though it agrees relatively well with the laboratory data. These comparisons highlight that the field



(a)



(b)



(c)

FIGURE 7: Cross section comparison between laboratory and field measurements for (a) FR1, (b) CR2, and (c) OR1.

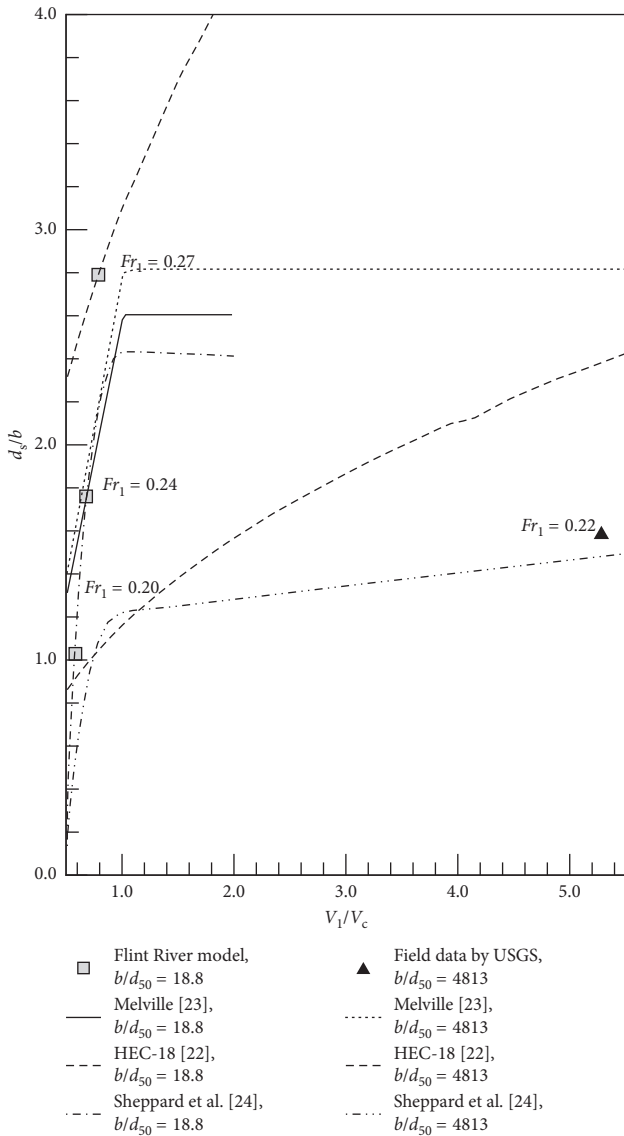


FIGURE 8: Comparison of field and laboratory measurements of scour depths and scour prediction formulas for Flint River Bridge.

engineers need to carefully select the scour formulas for their design because the current widely used scour formulas are only based on the idealized laboratory experiments, and sometimes, the results show somewhat unreliable answer.

#### 4. Summary and Conclusions

In this study, scaled physical models were constructed and conducted based on the actual field surveys, and the results have been compared with detailed field measurements of contraction scour and pier scour. Comparisons of velocity distributions for all river models showed good agreement with the field measurements. The shapes of the cross section and bed elevations along the bridge deck were well reproduced in laboratory experiments including the maximum pier scour depths in front of the pier. The close agreement between field and laboratory measurements appears to validate the modeling strategy presented in this study in

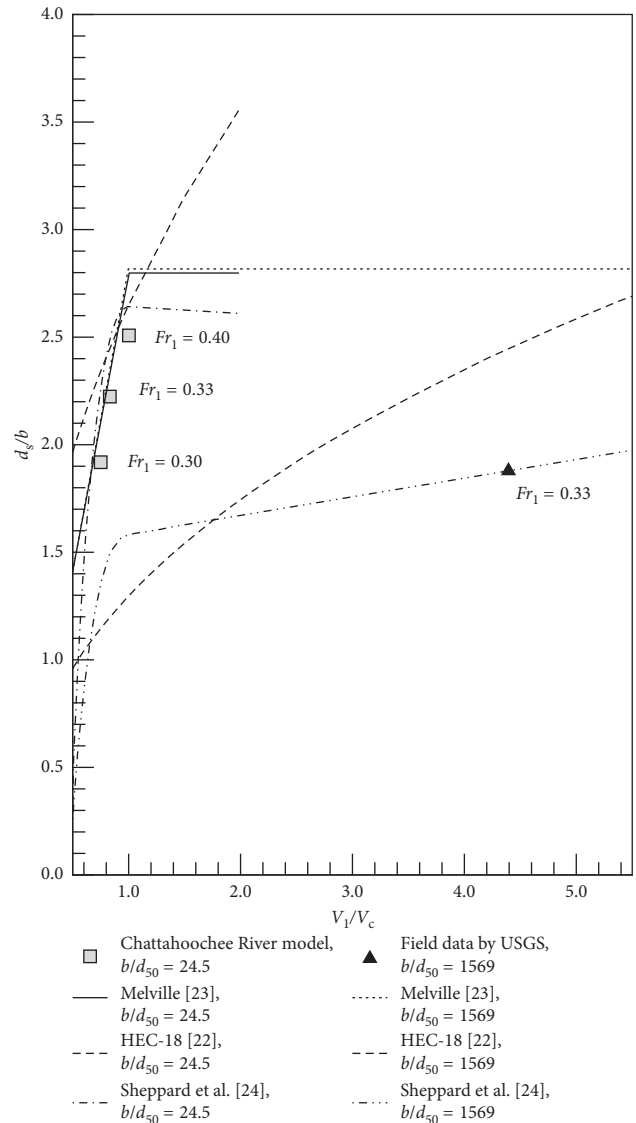


FIGURE 9: Comparison of field and laboratory measurements of scour depths and scour prediction formulas for Chattahoochee River Bridge.

which the Froude number similarity and the geometric similarity ( $y_1/b$ ) are maintained while choosing a sediment size in the laboratory that produces the ratio of pier size to sediment size,  $b/d_{50}$ , in the range of 25–50 where it has negligible influence on pier scour. Furthermore, the ratio of approach velocity to the critical velocity which concludes the condition of clear scour regime is also an important factor to choose sediment size. Values of  $b/d_{50}$  are quite large in the prototype and so they cannot be reproduced in the laboratory because the sediment size satisfied with scale ratio becomes so small that the innerparticle cohesive force acted important role, which do not exist in prototype sand-bed streams. In other words, live-bed scour depths in the prototype can be matched using clear-water scour in the laboratory by compensating for an observed decrease in scour depth due to large prototype values of  $b/d_{50}$  with a corresponding decrease in  $V_1/V_c$  to a value less than 1.0 at which

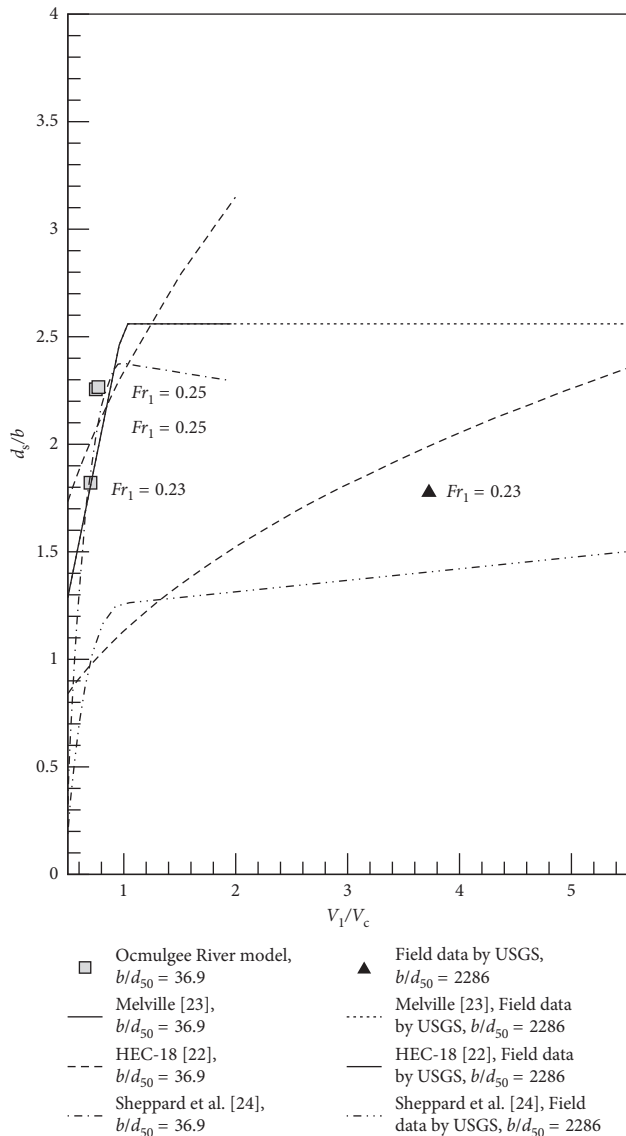


FIGURE 10: Comparison of field and laboratory measurements of scour depths and scour prediction formulas for Ocmulgee River Bridge.

maximum scour depth occurs. “How this good comparison was achieved?” is one of the important results of this research in that it provides a modeling methodology with scaling laws that can be used to design models of complex pier and bridge geometries, select the appropriate model sediment size, and then translate the results to the prototype. If the relationship for decreases in local scour depth with increasing values of  $b/d_{50}$  in prototype and decreasing value of  $V_1/V_c$  in laboratory clear-water scour is well known, then it can be used to evaluate the prototype local scour depth from the measured model value of local scour depth. So far, little effort has been made to the value of laboratory model study in closing the gap between results from idealized laboratory experiments and those from field data because of economical and practical reasons. However, the experimental results show that the location of the maximum scour depth around a complex pier is not consistent due to the

variability of the horseshoe vortex system and the complexity of bridge geometry and river bathymetry, which gives another essential reason for the need to conduct a physical model study of local scour depth, especially for large, expensive bridges.

The laboratory and field data were compared with several existing pier scour formulas to find their accuracy when the effect of  $b/d_{50}$  is included in their comparison. The results show that none of the accepted formulas provided a satisfactory estimate of scour depth because several cases show considerable underprediction as well as overprediction in many cases. These results emphasize the need for improvement in explaining and accounting for the effect of  $b/d_{50}$  in order to obtain more accurate scour predictions [25].

In this study, three prototype bridges in Georgia were modeled in the laboratory including the actual bridge and pier geometry as well as the river bathymetry using different geometric scale ratios. The laboratory results were compared with continuous field measurements to provide a more comprehensive collection of realistic local scour data than has been developed in the past.

## Data Availability

The data used to support the findings of this study are included within the article.

## Conflicts of Interest

The authors declare that they have no conflicts of interest.

## Acknowledgments

The authors would like to thank the GDOT for supporting this research study. This study was also supported by the National Research Foundation of Korea (NRF) grant funded by the Korean government (MSIT) (NRF-2017R1A2B2011990).

## References

- [1] H. Hajikandi, H. Vosoughi, and S. Jamali, “Comparing the scour upstream of circular and square orifices,” *International Journal of Civil Engineering*, pp. 1–12, 2017.
- [2] M. Mehraein, M. Ghodsian, M. Khosravi Mashizi, and M. Vaghefi, “Experimental study on flow pattern and scour hole dimensions around a T-shaped spur dike in a channel bend under emerged and submerged conditions,” *International Journal of Civil Engineering*, vol. 15, no. 7, pp. 1019–1034, 2017.
- [3] A. M. Shirole, “Planning for a comprehensive bridge safety assurance program,” *Transportation Research Record*, vol. 1290, pp. 137–142, 1991.
- [4] M. Alemi and R. Maia, “Numerical simulation of the flow and local scour process around single and complex bridge piers,” *International Journal of Civil Engineering*, vol. 16, no. 5, pp. 475–487, 2016.
- [5] M. Khan, H. M. Azamathulla, and M. Tufail, “Gene-expression programming to predict pier scour depth using laboratory data,” *Journal of Hydroinformatics*, vol. 14, no. 3, pp. 628–645, 2012.

- [6] A. Durand-Claye, "Hydraulique-Experiences sur les affouillements," *Annales des Ponts et Chaussées*, vol. 5, no. 29, pp. 467–483, 1873.
- [7] U. C. Kothiyari, R. J. Garde, and K. G. Ranga Raju, "Temporal variation of scour around circular bridge piers," *Journal of Hydraulic Engineering*, vol. 118, no. 8, pp. 1091–1106, 1992.
- [8] R. Ettema, B. W. Melville, and B. Barkdoll, "Scale effect in pier scour experiments," *Journal of Hydraulic Engineering*, vol. 124, no. 6, pp. 639–642, 1998.
- [9] B. W. Melville and Y. M. Chiew, "Time scale for local scour at bridge piers," *Journal of Hydraulic Engineering*, vol. 125, no. 1, p. 59, 1999.
- [10] M. N. Landers and D. S. Mueller, "Evaluation of selected pier-scour equations using field data," *Transportation Research Record: Journal of the Transportation Research Board*, vol. 1523, pp. 186–195, 1996.
- [11] D. S. Mueller and C. R. Wagner, *Field Observations and Evaluations of Streambed Scour at Bridges*, U.S. Department of Transportation, Federal Highway Administration, Research, Development, and Technology, Turner-Fairbank Highway Research Center, McLean, VA, USA, 2005.
- [12] D. M. Sheppard, J. J. Sterling, and O. Mufeed, "Local sediment scour model tests for the woodrow wilson bridge piers," in *Proceedings of 2000 Joint Conference on Water Resource Engineering and Water Resources Planning & Management*, Minneapolis, MN, USA, pp. 132–141, August 2000.
- [13] S. Lee and T. W. Sturm, "Effect of sediment size scaling on physical modeling of bridge pier scour," *Journal of Hydraulic Engineering*, vol. 135, no. 10, pp. 793–802, 2009.
- [14] S. H. Hong, T. W. Sturm, and T. Stoesser, "Clear-water abutment scour depth in compound channel for extreme hydrologic events," *Journal of Hydraulic Engineering*, vol. 141, no. 6, pp. 1–12, 2015.
- [15] T. W. Sturm, F. Sotiropoulos, M. N. Landers et al., *Laboratory and 3D Numerical Modeling with Field Monitoring of Regional Bridge Scour in Georgia*, Georgia Department of Transportation, Atlanta, GA, USA, 2004.
- [16] T. C. Stamey, *Summary of Data-Collection Activities and Effects of Flooding from Tropical Storm Alberto in Parts of Georgia, Alabama, and Florida, July 1994*, USGS, Reston, VA, USA, 1996.
- [17] S. Hong, "Interaction of bridge contraction scour and pier scour in a laboratory river model," M.Sc. thesis, Georgia Institute of Technology, Atlanta, GA, USA, 2005.
- [18] R. Ettema, *Scour at bridge piers*, Ph.D. thesis, University of Auckland, Auckland, New Zealand, 1980.
- [19] T. W. Sturm, *Open-Channel Hydraulics*, McGraw-Hill, Boston, MA, USA, 2nd edition, 2010.
- [20] S. H. Hong and I. Abid, "Physical model study of bridge contraction scour," *KSCE Journal of Civil Engineering*, vol. 20, no. 6, pp. 2578–2585, 2016.
- [21] T. W. Sturm, "Scour around bankline and setback abutments in compound channels," *Journal of Hydraulic Engineering*, vol. 132, no. 1, pp. 21–32, 2006.
- [22] E. V. Richardson and S. R. Davis, *Evaluating Scour at Bridges: Hydraulic Engineering Circular No. 18*, U.S. Federal Highway Administration, Washington, DC, USA, 4th edition, 2001.
- [23] B. W. Melville, "Pier and abutment scour: integrated approach," *Journal of Hydraulic Engineering*, vol. 123, no. 2, pp. 125–136, 1997.
- [24] D. M. Sheppard, M. Odeh, and T. Glasser, "Large scale clear-water local pier scour experiments," *Journal of Hydraulic Engineering*, vol. 130, no. 10, pp. 957–963, 2004.
- [25] S. O. Lee, *Physical modeling of local scour around complex bridge piers*, Ph.D. thesis, Georgia Institute of Technology, Atlanta, GA, USA, 2006.

## Research Article

# Heat Treatment and Ventilation Optimization in a Deep Mine

Xingxin Nie , Xiaobin Wei , Xiaochen Li, and Caiwu Lu 

*School of Management, Xi'an University of Architecture and Technology, Xi'an, Shaanxi 710055, China*

Correspondence should be addressed to Xingxin Nie; 670127529@qq.com and Xiaobin Wei; 1462658088@qq.com

Received 19 March 2018; Accepted 14 June 2018; Published 1 August 2018

Academic Editor: Hugo Rodrigues

Copyright © 2018 Xingxin Nie et al. This is an open access article distributed under the Creative Commons Attribution License, which permits unrestricted use, distribution, and reproduction in any medium, provided the original work is properly cited.

In order to address the issue of high temperatures and thermal damages in deep mines, the factors causing downhole heat damage at high temperatures were analyzed, the mine ventilation system was optimized and rebuilt, and a cooling system was established. The proposed cooling system uses mine water as the cooling source, and its features are based on the analysis of traditional cooling systems. The current ventilation system in the 1118 m deep pit of the Jinqu Gold Mine was evaluated, and the ventilation network, ventilation equipment, and ventilation structures near the underground working face were optimized. The low-temperature mine water stored in the middle section of the mine at 640 m depth was used as the cooling source, and a cooling system was established near the 440 m deep middle return well to alleviate the high-temperature and high-humidity conditions of the 280 m deep middle-western area. The results show that the effective air volume in the west wing at 280 m was 3.0 m<sup>3</sup>/s, the operating ambient temperature was 27.6°C, the relative humidity was reduced to 76%, and the temperature was reduced by 5–6°C after the optimization of the system.

## 1. Introduction

In an era of rapid development of the global economy, the energy dependence is increasing rapidly [1–4]. As the shallow mineral resources on Earth's surface have been depleted [5], countries worldwide have successively begun to mine deep resources. As the mining depth increases, the temperature of the rock increases, and the heat damage caused by the ground temperatures and other factors is amplified [6–11]. For example, at a depth of 900 m in a mine in Germany, the average temperature is 41°C and at the mining depth of 1712 m, the maximum temperature is 50°C. In gold mines in India, at a depth of 3000 m, the geothermal temperature is more than 60°C. The world's deepest underground mine is South Africa's Carletonville gold deposit: the mining depth is 4000 m and the ground temperatures is 70°C. At present, China is also encountering the problem of high temperatures in deep mines, as in the Shandong Sun Cun mine [12], the Tongling Shizhan copper mine [13], and the Fushun Hongtoushan copper mine [14] where the mining depth is more than 1000 m and the geothermal temperature is 45°C. The general distribution of high temperatures and heat damage

in deep mines in China is shown in Figure 1. The hot and humid working environment has seriously endangered the miners' health [15–18]; according to China's Technical Specification for Ventilation System of Metallic and Non-Metallic Underground Mine, the air temperature in downhole operation sites shall not exceed 28°C [19]; therefore, it is very important and of practical significance to minimize the heat damage in underground high-temperature and heat damage-prone working environments. The high-temperature, high-humidity, and low-velocity work environment on the working surface in deep mines will cause the central nervous system to be inhibited by workers working underground for a long period of time. The symptoms include mental retardation, lack of concentration, and decreased ability to work. At the same time, the environment is hot and humid. Working for a long time will also make the workers feel uncomfortable, irritated, and have eczema and other diseases that will seriously affect the safety production efficiency of the mine. Solving the problem of ventilation difficulties and high-temperature heat damage in deep mines can not only protect the physical and mental health of underground miners, but also help improve the

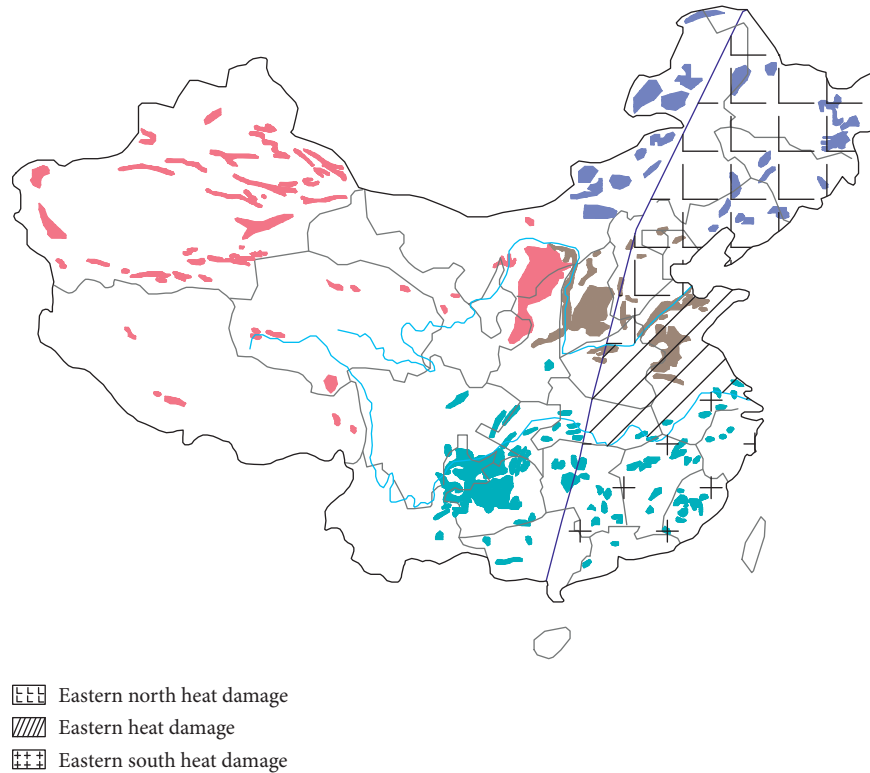


FIGURE 1: Distribution map of high-temperature mine in deep mining in China.

production efficiency of deep mine operating surfaces and contribute to the exploitation of mineral resources rich in the depth of the Earth.

High-temperature thermal damage in underground mines can be minimized by nonartificial refrigeration cooling and artificial refrigeration cooling. Common non-artificial refrigeration cooling methods include ventilation cooling, heat insulation, and personal protection. Common artificial cooling methods include water cooling, ice cooling, and thermoelectric cooling combined with cogeneration. However, nonartificial refrigeration cooling methods cannot be applied in deep mines to minimize high temperatures due to the limitations in the cooling capacity. Yuan et al. [20] proposed a new coupled cooling method of Latent Heat Thermal Energy Storage (LHTES) combined with Pre-cooling of Envelope (PE). Guo and Chen [21] used the deep well return air as the cold source of the cooling system to achieve cooling and dehumidification on the working surface. Shi et al. [22] used liquid nitrogen to inject into the working face to achieve cooling effect. Guo et al. [23] used the heat of the bathing water on the surface and created a refrigeration unit to achieve a heat exchange between the chilled water and the high-temperature air on the working surface; the heat created by the condensation of the refrigeration unit was recovered and the thermal hazard of the high temperatures in the mine was converted into heat energy, thereby improving the energy efficiency. Wang et al. [24] optimized a ventilation system and increased the ventilation of a mine and the distribution of the air volume to accelerate the downhole airflow to achieve cooling.

Zou et al. [25] used the theories of fluid mechanics and heat transfer to develop heat insulation materials in the mine main ventilation tunnel to achieve heat insulation, heat removal, and cooling. Zhang [26] used combined heat and power cogeneration technology using steam lithium bromide chillers and centrifugal chillers for heating, power generation, and refrigeration to improve the energy utilization. In this study, we propose a downhole centralized cooling system using mine water as the cooling source with a focus on underground mines with inflow water or water seepage. The method is based on the principle of heat exchange between the cold mine water and the high air temperatures of the working area and minimizes the heat damage in the working area. The cooling system assisted by mine water source cooling is to reduce the output of refrigeration unit cooling capacity by using the cold energy hidden by the groundwater source to save the running cost of cooling and cooling system. In addition, the condensing heat discharged by the cooling and cooling system can be absorbed by the cold energy contained in the mine water source itself, reducing the emission of condensation heat and reducing the secondary thermal hazards generated underground.

## 2. Thermal Damage Analysis of High-Temperature Mine

The related research shows that the fundamental cause of the high-temperature heat damage near the working face of the mine is the concentration of the heat on the working surface

because the heat cannot be discharged from the well in time. This results in an increase in the ambient temperature of the working surface. Therefore, the main reasons for the high-temperature heat damage in deep wells are the heat release from underground heat sources and the poor air circulation.

## 2.1. High-Temperature Heat Release

**2.1.1. Heat Radiating from the Well Rock.** The original rock temperature shows a nonlinear increase with the increase in the depth of the stratum. The thermal physical properties of the stratum rock in deep mining have a great influence on the high-temperature thermal damage [5]. High-temperature underground rock releases heat through heat conduction and convection due to heat exchange with the air, resulting in increased enthalpy in the air, and in high air temperatures in the roadways. In engineering practice, the formula for calculating the heat transfer between a high-temperature wall rock and the air in the roadway is

$$Q_r = K_r UL(t_{rm} - t), \quad (1)$$

$$K_r = \frac{1.163}{(1/9.6v_B) + 0.0441}, \quad (2)$$

where  $Q_r$  is the heat transfer of the surrounding rock in the tunnel, kW;  $K_r$  is the unstable heat transfer coefficient between the surrounding rock and the airflow, kW/(m<sup>2</sup>·°C);  $U$  is the perimeter of the mine roadway, m;  $L$  is the length of well, m;  $t_{rm}$  is the average primary rock temperature, °C;  $t$  is the average temperature of the air in the mine shaft, °C;  $v_B$  is the average velocity of the airflow in the mine shaft, m/s.

However, in the real life, the wall surface of underground mine tunnel is not dry, and there is water seepage in the surrounding rock wall of the roadway. The evaporation of moisture will absorb part of the heat to generate heat and moisture exchange. Therefore, the latent heat exchange between the water and wind flow in the tunnel wall is calculated. It is required. The formula for calculating latent heat exchange between water and air is

$$Q_w = \beta F k_B (p_w - p_B), \quad (3)$$

$$\beta = 0.0846 + 0.0262v_B, \quad (4)$$

$$k_B = \frac{101.325}{B}, \quad (5)$$

where  $Q_w$  is the amount of latent heat exchange between water and winds, kW;  $\beta$  is latent heat exchange coefficient, J·s<sup>-1</sup>·N<sup>-1</sup>;  $F$  is the heat dissipation surface area of water, m<sup>2</sup>;  $k_B$  is the pressure correction factor;  $p_w$  is the saturated steam pressure at the water surface temperature, kPa;  $p_B$  is the partial pressure of water vapor in the air, kPa;  $B$  is the downhole atmospheric pressure, kPa.

**2.1.2. Electromechanical Equipment Is Exothermic.** With the continuous improvement in the mechanization of mine mining, the exothermic heat of the electromechanical

equipment in the downhole production process has become a major heat source for high-temperature thermal hazards downhole [27]. Mining equipment, wind turbines, transportation equipment, exploration equipment, and lighting are powered by electrical energy and release heat. The equation for heat generated by electromechanical equipment during the operation is

$$Q_d = \sum \varphi N_d, \quad (6)$$

where  $Q_d$  is the heating capacity of the electromechanical equipment to the downhole airflow, kW;  $\varphi$  is the heat dissipation coefficient of the electromechanical equipment; and  $N_d$  is the total power of the electromechanical equipment operating at the same time, kW.

The exothermic heat of electromechanical equipment is an important heat source for heat dissipation from the downhole heat source. The heat dissipation coefficient of the electromechanical equipment is an important factor affecting the heat dissipation of the equipment. The heat dissipation coefficient of the equipment is determined according to its own characteristics, so the heat dissipation coefficient of different equipment is different. In this paper, the heat dissipation coefficient of the downhole electromechanical equipment is determined according to the characteristics of the equipment itself and the on-site conditions.

**2.1.3. Heat Released during Ore Transportation.** The newly mined ore is exposed to the air, which increases the contact area with the downhole air and speeds up the cooling of the ore. The emitted heat is absorbed by the airflow in the transportation lane. The heat dissipation efficiency of the ore being mined is faster than that of unmined ore; therefore, the heat emitted by the ore during transport cannot be ignored. The equation of the exothermic reaction of the ore during transport is

$$Q_k = 0.0024L^{0.8}(t_r - t_{wm})mC_m, \quad (7)$$

where  $Q_k$  is the heat release of ore during transportation, kW;  $L$  is the distance of ore transportation, m;  $t_r$  is the average temperature of ore in transit, °C;  $t_{wm}$  is the average temperature of the air in the transportation lane, °C;  $m$  is the ore transport capacity, kg/s; and  $C_m$  is the specific heat capacity of the ore, kJ/(kg·°C).

**2.1.4. Heat Release from the Air due to Compression.** When fresh air flows from the outside to the well bottom surface, the air pressure increases with the increase in the depth. According to the principles of air compression and heat release, the air will release a certain amount of heat during the compression process. Under adiabatic conditions, the airflow will flow about 102 m vertically and its temperature increases about 1°C [28]. Under normal circumstances, there is a heat and moisture exchange between the wellbore and the airflow in the air intake tunnel. The heat balance equation for these conditions is

$$G(i_2 - i_1) - \frac{Z_1 - Z_2}{427} G - G \frac{\omega_2^2 - \omega_1^2}{2 \times 427} = Q_x + Q_q + Q_j - Q_1, \quad (8)$$

where  $Q_x$  is the sensible heat in the heat transfer from the borehole wall to the air, J/s;  $Q_q$  is the latent heat in the heat transfer from the borehole wall to the air, J/s;  $Q_j$  is the local heat release, J/s;  $Q_1$  is the heat that evaporates from the surface of a water droplet due to air absorption, J/s;  $G$  is the ventilation, kg/s; and  $1/427$  is the work heat equivalent, J/kgf·m.

Under normal circumstances, when there is little change in the wind speed, the wellbore can be defined as  $\omega_2 = \omega_1$ ; then (8) can be changed to

$$G(i_2 - i_1) = \frac{\Delta Z}{427} G + Q_x + Q_q - Q_1. \quad (9)$$

In the adiabatic state, the following is considered:

$$Q_x + Q_q - Q_1 = 0.$$

Therefore, only the adiabatic heat of compression is calculated here. The equation can be simplified as

$$Q_{\text{heating}} = \frac{\Delta Z}{427} G, \quad (10)$$

where  $\Delta Z$  is the height difference between the ground and the mining working face.

However, for mines that are mined in reality, the mine roadway is not adiabatic, and the sensible heat and latent heat in the mine will occur during the flow of air. Therefore, in actual mining wells, the heat generated by self-compression for every 100 m drop in air is insufficient due to the presence of heat exchange and its own temperature is increased by 1°C. Through experiments, it can be concluded that the temperature rises for every 100 m of air drop 0.4-0.5°C.

**2.2. Poor Ventilation of the Working Surface.** Mine ventilation systems are important for the safe operation of underground mines and provide fresh airflow and remove the contaminated air but also lower the heat and humidity of the working surface. Poor ventilation in the work area is one of the main causes of high temperatures and heat damage on the underground working surface. When the ventilation is poor, the high temperature can affect the physical and mental health and the work efficiency of mine employees.

**2.2.1. Ventilation Networks Are Complex and Changeable.** The layout of the ventilation network is a core component of the mine ventilation system and determines its efficiency. The underground environment is complex and variable as underground mining explorations increase. In many cases, the layout of the originally planned ventilation network undergoes tremendous changes as the mine expands. As a result, the underground ventilation network needs to be optimized to avoid ventilation problems. For example, the simultaneous mining of multiple middle segments results in problems such as changes in the working surface, difficulty in providing proper airflow, the continuous extension of

mine ventilation lines, the accumulation of waste rock in the ventilation tunnels, and the ventilation issues caused by the accumulation of wastewater. In addition, the airflow volume is affected by increased resistance, lack of planning for the extraction of a large number of goafs without timely filling and closing, and the increase in the number of crossroads lanes caused by wind, air leakage, and short circuits.

**2.2.2. Insufficient Power of Ventilation Equipment.** The volume of the airflow at the mining face and driving face of the underground mine depends on the capacity of the underground ventilation fans. In many mines, the ventilation capacity of the underground ventilation equipment is incompatible with the mine ventilation system, and this is a common problem in underground mining. As a result, the lack of fresh air affects the safety of the workers.

With the continuous expansion of underground mining, the number of downhole mining operations is also increasing; this requires an expansion of the ventilation requirements of the working surface and in many cases, the underground ventilation network is insufficient, which results in poor ventilation. The existing wind turbine equipment does not have the capacity to supply sufficient airflow and the increased temperatures and sewage gases seriously affect the physical and mental health of the staff. According to statistics [29], the average power consumption of mine ventilation equipment accounts for about 30% of the total electricity consumption of the mine. In order to ensure the economic and efficient operation of ventilation fans, the capacity of the ventilation equipment and the number and location of the fans have to be adjusted to the requirements to reduce the operating costs and ensure adequate airflow.

**2.2.3. Misalignment of Ventilation Structures.** The ventilation equipment, the ducts, barriers, and the adjustment of the ventilation equipment play important roles in the regulation of the airflow in the mine. Ventilation structures fall into two categories based on the airflow: The first type of ventilation structure allows the airflow to pass through and this structure includes an air inlet, an air deflector, and an air bridge. In the second type of structure, the airflow is not passing through the system and those components include dampers, air curtains, air walls, and wellhead closures [24]. The main function of ventilation structures in underground mines is to ensure the flow of fresh air so that all working surfaces in the underground wells are reached.

In many underground ventilation systems, the structures are installed improperly or components are missing, which affects the underground airflow negatively and results in difficulties in regulating the airflow and poor ventilation. Common problems encountered in mine ventilation systems include the low quality of ventilation structures, which lead to air leakage, short circuits, and a reduction in the airflow capacity. The structures are affected by the blasting vibration, transport equipment, and malfunctions. In some cases, daily maintenance of the facilities is not performed and the regulations are disregarded. Therefore, in order to ensure the stable operation of the underground mine ventilation

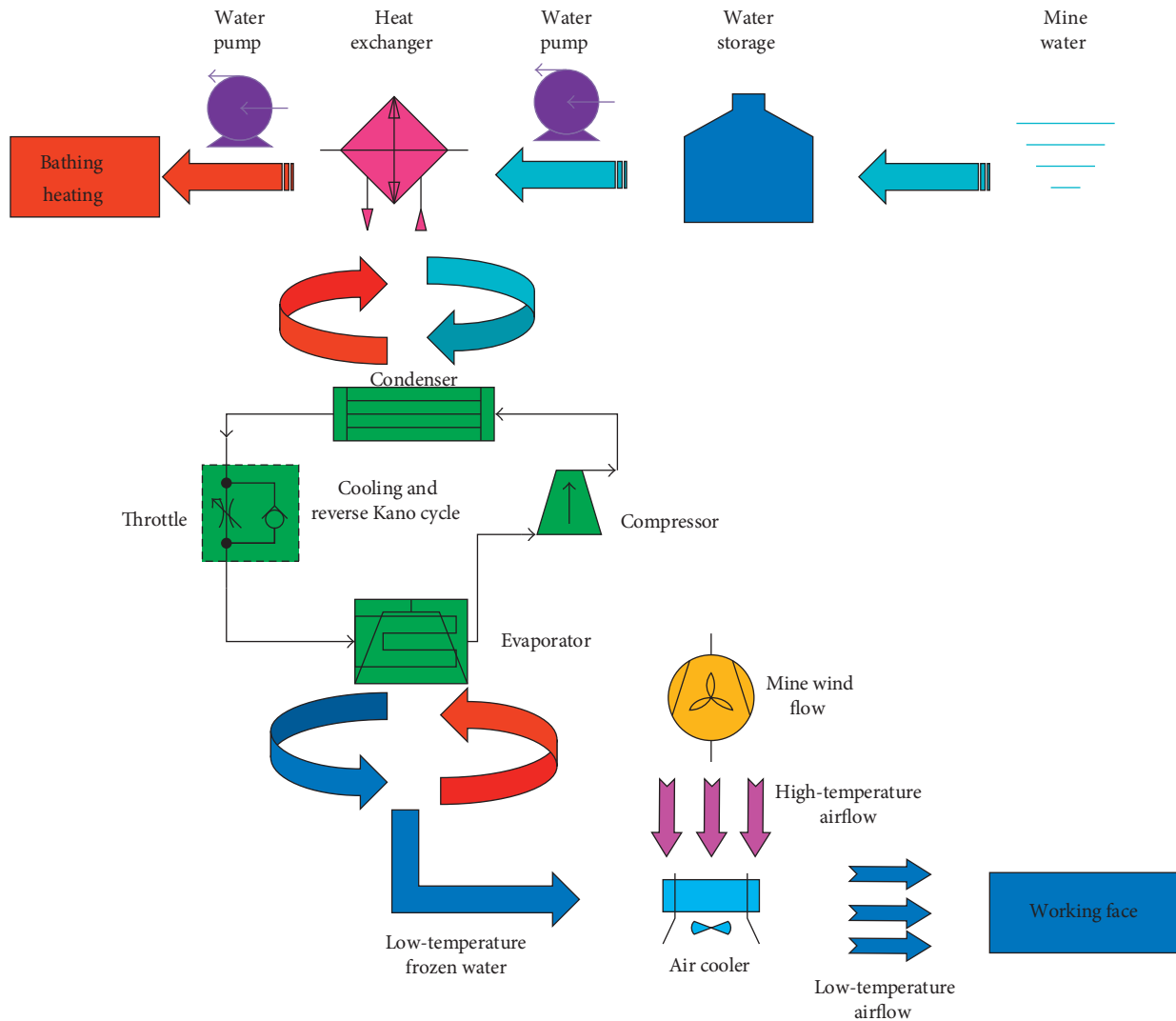


FIGURE 2: Cooling system of mine water as cold source.

system, the layout of the ventilation equipment should be well planned. The maintenance and management of the mine ventilation equipment should be regulated to ensure sufficient underground fresh airflow.

### 3. Refrigeration and Cooling System with Auxiliary Cooling of Mine Water Source

In the natural environment, water sources such as groundwater, surface water, and atmospheric precipitation cause water inflow or water seepage during the mining and production process in underground mines. Mine water influx exists in most underground mines. In order to make full use of the natural cold energy/heat energy contained in the underground water source, we can extract heat from deep well and high-temperature water [30] and extract cold energy from shallow low-temperature water [31, 32] to make use of it. The use of mine water for this purpose can be categorized based on the amount of the inflow water into high, medium, and low. The cooling principle is based on the

fact that the mine water is a source of cold energy that can be used in a downhole centralized cooling system. An example of an extraction system to extract the cold energy from the water and use the principle of heat exchange to reduce the high air temperatures on the operating surface is shown in Figure 2.

The cooling system that uses the mine inflow or seepage as the cold source includes three parts: the cooling source, refrigeration, and cooling. The core component is the cooling source, which provides a continuous cooling capacity for the refrigeration unit and for air conditioning. This technology can be used to produce chilled water in the air cooler to achieve a heat exchange and cool the operating surface.

The process of extracting cold from mine water: a water pump is used to pump the low-temperature water from the underground. Three filtration systems and a simple coarse filter are used to filter the corrosive water that is moved from the source to the cooling station, through three antiseptic systems from high pollution, high ore cooling, and corrosive mine water. At the same time, the initial high pressure of the

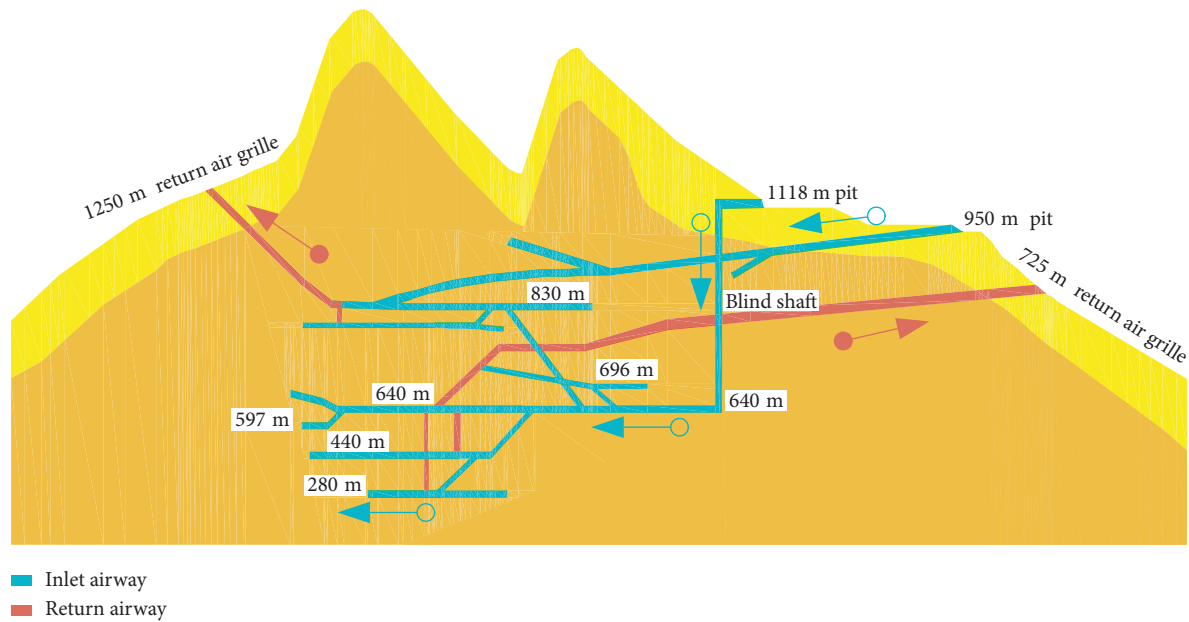


FIGURE 3: Current status of exploitation in Jinqu Gold Mine.

water is reduced when it enters the cooling system to reduce the damage to the system.

The process of producing cryogenic water: the refrigeration cooling system consists of a condenser, a throttle valve, an evaporator, and a four-part compressor. The cooling principle is based on the reverse Carnot cycle (Figure 2) and evaporation endothermic cooling. The reverse Carnot cycle consists of two isothermal processes and two isentropic processes. During the cycle, the cooling of the work surface is achieved by evaporation, heat absorption, and condensation of the refrigerant in the circuit, resulting in heat release. The detailed process of the circulation system is as follows: the refrigerant is condensed into a liquid state by using the cold mine water extracted from the underground storage tank. Then, the liquid refrigerant, whose pressure and temperature are lowered by the throttle valve device, flows into the evaporator. The evaporator absorbs the heat from the high-temperature mining operation surface and the water evaporates. During this process, the liquid refrigerant is vaporized from the high-temperature back-water on the working surface and releases the cold energy. The refrigerant is compressed, resulting in high temperature and high pressure of the vapor refrigerant. Finally, the steam refrigerant is liquefied by low-temperature mine water in the condenser. The high-temperature mine water can be used for underground bathing water and heating to improve the energy recycling.

The cooling process on the high-temperature working face is explained as follows: after the chilled water is transported to the air cooler on the working surface of the downhole by an insulated duct, the high-temperature air is transported to the air cooler by a blower for the heat exchange with the chilled water. On the high-temperature working surface, an air exchange occurs and reduces the temperature and humidity of the ambient air in the working environment.

## 4. Practical Application and Analysis

**4.1. Project Overview.** The study area is located in the western section of the Great Lakes Valley in Yangping Town, Lingbao City, Henan Province; the gold deposit is located in the northern part of the Laojiachac complex anticline in the Xiaoqinling Mountains. The syncline axis of the Xiyin-Leijia Pass runs through the northern part of the mining area. The terrain is comprised of low elevations in the south and high elevations in the north. The 1118 m deep pit mine at the Jinqu Gold Mine is currently under construction for exploration and infrastructure development. The pioneering method used in this mine pit excavation is the joint development of a blind shaft, a pit, and an incline; the area is dominated by excavation. The middle section of the 1118 m deep pit mine, which is currently being mined, consists of sections at the depths of 640 m, 830 m, 696 m, 597 m, 440 m, and 280 m. The midsections at 440 m and 280 m are the main open mining areas at this time [33]. The mining operation details are shown in Figure 3. The ventilation system of the 1118 m pit mine in Jinqu Gold Mine adopts single-wing diagonal extraction mechanical ventilation, and the local face of the tunnel is adopted with the local fan pressurization ventilation. At the 640 m level, a mine fan with model K40-4-14/90 and rated power of 90 kW is installed as the main fan of the ventilation system. The amount of airflow in the main ventilation shaft of the 1118 m underground pit ventilation system in Jinqu Gold Mine is shown in Table 1.

The depth of the 280 m middle working surface is as high as 838 m. The large depth of the underground mine results in high temperatures of the surrounding rocks in the excavation tunnel. This heats the air in the tunnel and creates a high-temperature working environment by long-distance heat conduction or convection. The large wind resistance generated by the ventilation line and the high airflow pressure causes low wind speeds in the ventilation ducts in

TABLE 1: Air volume of underground ventilation shaft in 1118 m pit of Jinqu Gold Mine.

Ventilation tunnel	Air volume (m <sup>3</sup> /s)	Air speed (m/s)
1118 m pithead inlat air tunnel	22.3	2.1
Blind shaft entry	21.5	2.4
640 m level main air tunnel	21.1	2.3
640 m level leading to the main return air tunnel	18.3	3.4
440 m inclined shaft airway	5.4	1.2
440 m level return air well	5.2	2.1
440 m level working face	0.2	0.07
280 m inclined shaft airway	0	0
280 m level return air well	0	0
280 m level working face	0.1	0.05

the middle section at 280 m. The seepage or inflow of water in the roadway accelerates the evaporation of the high-temperature environment and increases the humidity. The operational environment of high temperatures, high humidity, and low wind speeds in the middle section of the 280 m site has caused serious harm to the underground workers, and this problem has to be addressed.

#### 4.2. Calculation of Heat Dissipation and Cooling Load of Roadway

**4.2.1. Heat Release of Surrounding Rock in Well.** In the middle section of the 280 m pit, the surface temperature of the surrounding rock of the horizontal mining roadway is in the range of 35–39°C because this area is located at a depth of 838 m. The average wind speed is 2.8 m/s, the distance from the exit of the ventilation equipment to the work surface is 15 m–20 m, the cross section of the roadway is 7.5 m<sup>2</sup>, the perimeter of the roadway is 11.6 m, the average air temperature in the west wing roadway is 33.2°C, and the expected temperature after cooling is about 28°C. The heat exchange between the high-temperature surrounding rock and the air in the tunnel is the cause of the high temperature of the 280 m horizontal roadway. The roadway circumference was calculated using the relevant parameters of the 280 m horizontal roadway and (1) and (2). The heat dissipation of the rock is defined as follows:

$$Q_r = K_r UL(t_{rm} - t) = \frac{1.163}{((1/9.6 \times 2.8) + 0.0441)} \times 11.6 \times 18 \times \frac{(37 - 28)}{1000} = 26.88 \text{ (kW)}. \quad (11)$$

According to the relevant data from the mine pit monitoring at 1118 m of Jinqu Gold Mine and (3), (4), and (5), the heat absorbed by the latent heat in the mine airflow is 17.82 kW.

**4.2.2. Heat Dissipation of Electromechanical Equipment.** The degree of mechanization of the mining face at the 280 m level roadway tunnel is relatively high and the heat emitted

by the electromechanical equipment during normal operations accounts for a large part of the heat of the mining operation surface. The excavation work requires mechanical and electrical equipment, including three YT28 rock drilling machines with a power of 0.8 kW, a rake loader with a model of P-30 and power of 18.8 kW, one DBKJNO-6/2 × 15 kW counter-rotating local fan pressure inlet and withdrawable fan each, and transport equipment with a power of 40 kW. And mining equipment was calculated using the equipment specification and (6):

$$Q_d = \sum \varphi N_d = 3 \times 0.8 \times 0.6 + 18.8 \times 0.4 + 2 \times 15 \times 0.3 + 40 \times 0.2 = 25.96 \text{ (kW)}. \quad (12)$$

**4.2.3. Heat Dissipation of Ore in Transportation.** The transportation of the ore results in increases in the heat as the ore cools during transport and contributes to the high air temperatures in the roadway. According to existing records, the amount of ore transported per unit time is 8 kg/s. The length of the roadway for a single-head tunnel is 650 m. The initial rock temperature of the mining face is 37°C on average. The average wet-bulb temperature in the roadway is 33.3°C. According to (7), the heat dissipation of the transported ore is

$$Q_k = 0.0024L^{0.8}(t_r - t_{wm})mC_m = 0.0024 \times 650^{0.8} \times (37 - 33.3) \times 8 \times 0.97 = 12.26 \text{ (kW)}. \quad (13)$$

**4.2.4. Heat Energy Release due to Air Pressure Differences.** The vertical distance between the 1118 m deep pit and the 280 m horizontal working face in the Jinqu Gold Mine is 838 m. If we assume adiabatic conditions, the air temperature rises by about 1°C for every vertical downward flow of 102 m. The results show that the heat released due to the air pressure difference is significantly lower than that of the well. The warming of the air has a certain influence. As the air flows downward towards the working surface, the high temperature results in thermal expansion of the air and reduces the density of the air. Based on the given parameters, the mass flow rate  $G$  of the air is 2.7 kg/s. The heat released due to the air pressure differences can be obtained using (10):

$$Q_{\text{heating}} = \frac{\Delta Z}{427} G = \frac{838}{427} \times 0.5 \times 2.7 = 2.65 \text{ (kW)}. \quad (14)$$

**4.2.5. Calculation of Required Cooling Capacity.** The required cooling load for minimizing the thermal damage in underground mines usually refers to the required cooling capacity of the working areas such as the mining operation surface and the chamber. In this study, the 280 m horizontal west wing heading face is used as an example to calculate the required cooling capacity of the heading face; the mass flow rate of the air at the exit of the wind tunnel is 5.3 kg/s, and the flow rate is relatively stable. A wind turbine failure was ignored here. The required cooling capacity of the working area is calculated using the following equation:

$$Q_{\text{cooling}} \geq G(h_2 - h_1) + \sum Q_{\text{heating}}, \quad (15)$$

where  $Q_{\text{cooling}}$  is the required cooling capacity of the excavation work surface,  $G$  is the quality of the airflow at the cold location,  $h_2$  is the enthalpy of the wind at the cold location,  $h_1$  is the enthalpy of the wind at the cool-down destination, and  $\sum Q_{\text{heating}}$  is the total surface heat. The hottest dry-bulb temperature of the air at the 280 m horizontal heading face is 34.6°C, and the humidity is greater than 90%. If the dry-bulb temperature is 28°C, the unit mass enthalpy is 30.6 kW. However, in engineering practice, it is often necessary to increase the safety factor to prevent the loss of the cooling capacity during transportation. As a result, the cooling capacity of the work surface is insufficient and is generally about 1.2. Equation (15) is used to calculate the required cooling capacity of the working surface of the head:

$$Q_{\text{cooling}} \geq 1.2 \times [5.3 \times 30.6 + (2.65 + 12.26 + 25.96 + 26.88 + 17.82)] = 297.3 \text{ (kW)}. \quad (16)$$

Therefore, the required cooling capacity of the 280 m middle-end heading face is 297.3 kW.

### 4.3. Optimization of Underground Ventilation System and Effect Analysis

**4.3.1. Ventilation Network Optimization.** The current ventilation system in the 1118 m pit mine in the Jinqu Gold Mine is optimized with regard to the ventilation line, network layout, and broken area of ventilation tunnel and consists of the following improvements: (1) reasonably optimizing downhole ventilation line: expanding 280 m horizontal diameter 0.25 m air return guide hole diameter into 1.4 m air return well, form 280 m level and 640 m horizontal airflow loop and promoting natural wind circulation at 280 m level; (2) optimizing the effective flow section of airflow: clearing the waste rock and sewage accumulated in the ventilation tunnel in time, increasing the effective ventilation area of the ventilation tunnel, ensuring the smooth flow of the downhole, and reducing the ventilation resistance.

**4.3.2. Ventilation Equipment.** The fans are important components of the downhole ventilation system because they draw the air into the mine. The fans are important components of the downhole ventilation system because they draw the air into the mine. The following midsection fan optimization and improvement measures are implemented: (1) The existing two wind turbines with a power of 11 kW, which were used for supplying air to the mid-section of the 280 m section, are replaced with two wind turbines with a combined power of 21 kW to increase the blowing power. The radial distance between the blades of the fan is equipped with a special diffuser. (2) The size and material of the air duct are changed by replacing the unit with a diameter of 300 mm with a rigid air duct with the diameter of 500 mm to reduce the wind resistance. (3) In the middle of the 280 m section, a series-connected 11 kW

axial fan was added to pressurize the relay. It is worth noting that when adjusting the fan power, it must be ensured that the ingoing fan power is less than the outgoing fan power.

**4.3.3. Optimization of Ventilation Structure.** The optimization of the downhole ventilation structures consists of the following improvements: (1) A damper is installed at the opening of the ventilation roadway leading to the 830 m deep mining area in the middle section of the 640 m section to prevent the fresh airflow. (2) A controllable and adjustable mine ventilation window is installed in the 640 m middle section of the 640 m–440 m inclined shaft to allow a sufficient amount of fresh air to flow smoothly to the middle of the 440 m and 280 m middle sections.

**4.3.4. Analysis of Implementation Effect of Ventilation System Reform Project.** The 1118 m pit ventilation system of Jinqu Gold Mine has been rebuilt over a period of more than six months and the optimization of the ventilation system has basically been completed. Compared with the original ventilation system, the advantages of the existing ventilation system are mainly reflected in the following aspects: (1) The 280 m return air guide hole with a horizontal diameter of 0.25 m has become a 1.4 m diameter return air well, which promotes the circulation of 280 m horizontal natural wind currents. (2) The parameters of the main fan of the mine and the radial spacing of the blades have been optimized, which has increased the total intake air volume of the mine. (3) The air duct leading to the single-headed excavation work surface is replaced with a diameter of 300 mm. The rigid air duct made of a material reduces the ventilation resistance of the airflow. (4) Abandoned roadway of downhole ventilation system has been closed, which solved the phenomenon of downhole airflow short circuit and fresh airflow loss in the original ventilation system. (5) The installation of ventilation structures in the downhole ventilation system is added, the trend of the downhole air flow is reasonably adjusted, the air volume is allocated on every job surface in accordance with the demand, and the waste or shortage of fresh air flow in the underground is avoided. The results of the actual measurement of the air volume at each level and on the working surface after the optimization of the underground mine ventilation system are compared with those before the transformation are shown in Table 2.

**4.4. Thermal Damage Control Cooling Technology.** In this study, we designed a cooling system for the 640 m middle section using cold mine water as a source for the heat treatment of the 280 m horizontal working face of the 1118 m deep pit in the Jinqu Gold Mine. The details of the downhole centralized cooling system and the process are shown in Figure 4.

- (1) The water storage tank at the 640 m level is used as the cooling source of the downhole cooling system. A filtration system is used at the cooling water pump station to filter out the impurities in the gushing

TABLE 2: The measured air volume of main roadway before and after transformation of ventilation system.

Ventilation tunnel	Preoptimized air volume (m <sup>3</sup> /s)	Optimized air volume (m <sup>3</sup> /s)	Changing of air volume (m <sup>3</sup> /s)
1118 m pithead inlet air tunnel	22.3	37.0	+15.7
Blind shaft entry	21.5	36.3	+14.8
640 m level main air tunnel	21.1	35.1	14.2
640 m level leading to the main return air tunnel	18.3	12.1	-6.8
440 m inclined shaft airway	5.4	22.5	+17.4
440 m level return air well	5.2	10.2	+5.4
440 m level working face	0.2	2.9	+2.7
280 m inclined shaft airway	0	6.8	+6.8
280 m level return air well	0	6.2	+6.2
280 m level working face	0.1	3.0	+2.9

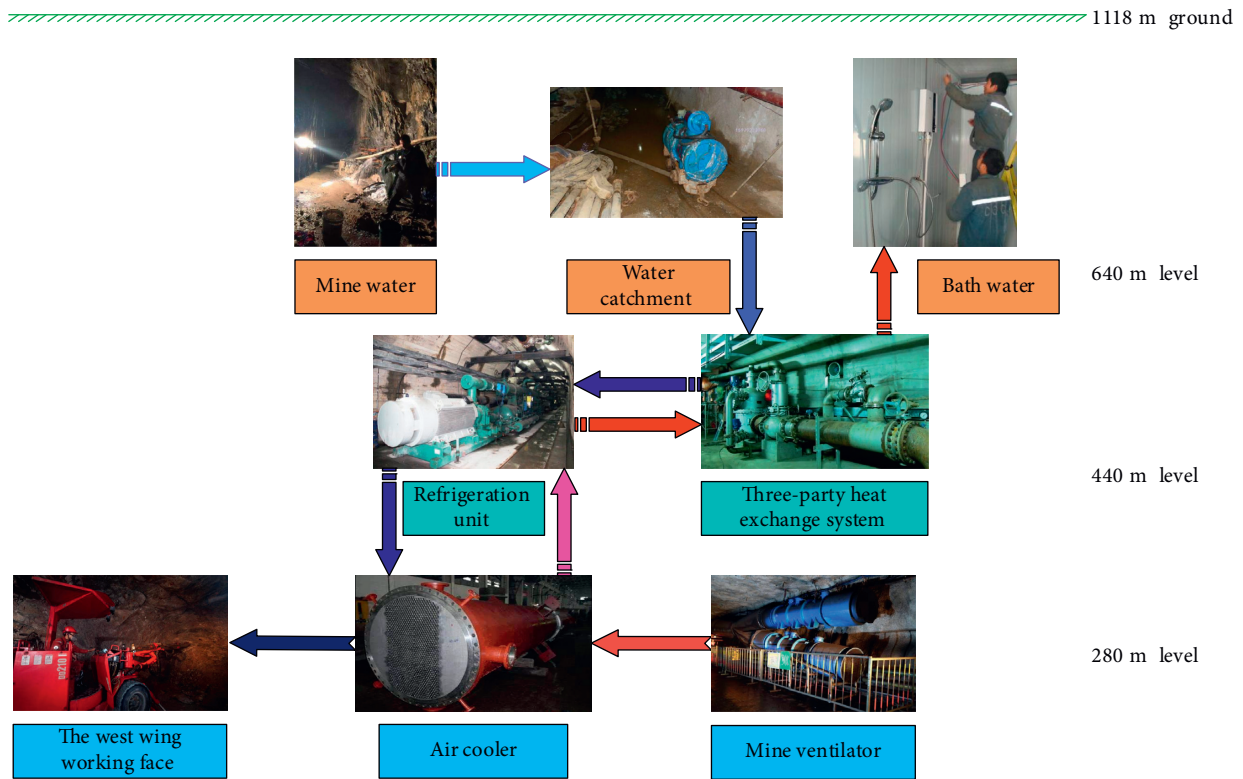


FIGURE 4: Design of cooling system for 1118 m pit in Jinqu Gold Mine.

- water and the cold water is then pumped to the 440 m level to the heat exchange station.
- (2) Three heat exchange systems are installed at the 440 m level to preliminarily purify the highly polluted and highly mineralized inflow water, extract the cold energy to be sent to the refrigeration unit, and convert the water pressure. The high water pressure caused by the difference in the height of the water source and destination is converted to low water pressure to reduce damages to the pipeline and the refrigeration unit.
  - (3) In the 440 m horizontal return-ventilation wells, cooling chillers are set up to further cool the chilled water, which is supplied to the air cooler at the 280 m horizontal mining surface.

- (4) The air cooler at the 280 m level precools the air flowing through the air cooler using the chilled water so that the low-temperature air flows to the work surface and exchanges the heat with the high-temperature air on the work surface to cool the work surface.

4.5. *Analysis of Practical Application.* After the implementation of the heat damage control and cooling measures at the 1118 m pit mouth and 280 m horizontal high-temperature working surface of the Jinqu Gold Mine, taking the 280 m horizontal west wing working surface as an example, the temperature and humidity of the underground 280 m level working environment were analyzed using the comparative analysis method. The layout of the monitoring

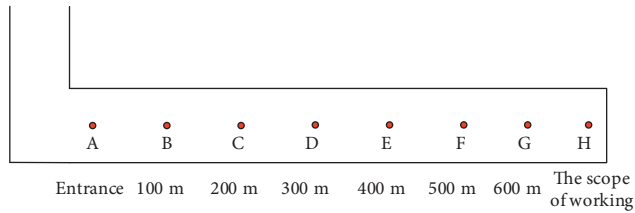


FIGURE 5: Layout of measuring points in the west tunnel of the middle section of 280 m.

TABLE 3: Temperature and humidity monitoring data before and after cooling.

Monitoring point	Temperature ( $^{\circ}\text{C}$ )		Relative humidity (%)	
	After cooling	Before cooling	After cooling	Before cooling
A	29.2	32.3	79	92
B	29.5	32.9	81	95
C	30.1	33.5	83	94
D	29.9	33.9	86	97
E	29.2	34.1	84	95
F	28.6	33.7	84	93
G	28.1	33.2	80	92
H	27.6	32.7	76	90

points is shown in Figure 5. The temperature and humidity of the air near the monitoring points are shown in Table 3.

Figure 6 shows the cooling effect at the monitoring points at the 280 m horizontal west wing driving head, through which the low-temperature airflow is directly sent to the working face of the driving head. The temperature of the working face is  $32.7^{\circ}\text{C}$  prior to cooling and  $27.6^{\circ}\text{C}$  after cooling with a cooling rate of  $5.1^{\circ}\text{C}$ . Prior to the implementation of the cooling measures, the relative humidity in this location was as high as 90%; after cooling, the relative humidity was 76% and the dehumidification amplitude is 14%.

## 5. Concluding Remarks

- (1) Based on the analysis of traditional cooling technology in underground mines, a downhole cooling system using mine water as the cooling source is proposed. By using the natural sources of low-temperature water infiltration or seepage in underground mines, the operating costs of the cooling system are reduced. In addition, the use of inflow water also solves the problem of heat condensation and cooling system emissions and reduces the occurrence of underground thermal damage.
- (2) The underground ventilation system and operating procedures were optimized, which improved the airflow and volume in the underground mining areas. The results of the optimization and reconstruction show that the effective air volume of the west wing in the 280 m midsection increased from  $0.9\text{ m}^3/\text{s}$  prior to the optimization to  $3.2\text{ m}^3/\text{s}$  after the optimization; this improved the working environment in this area.

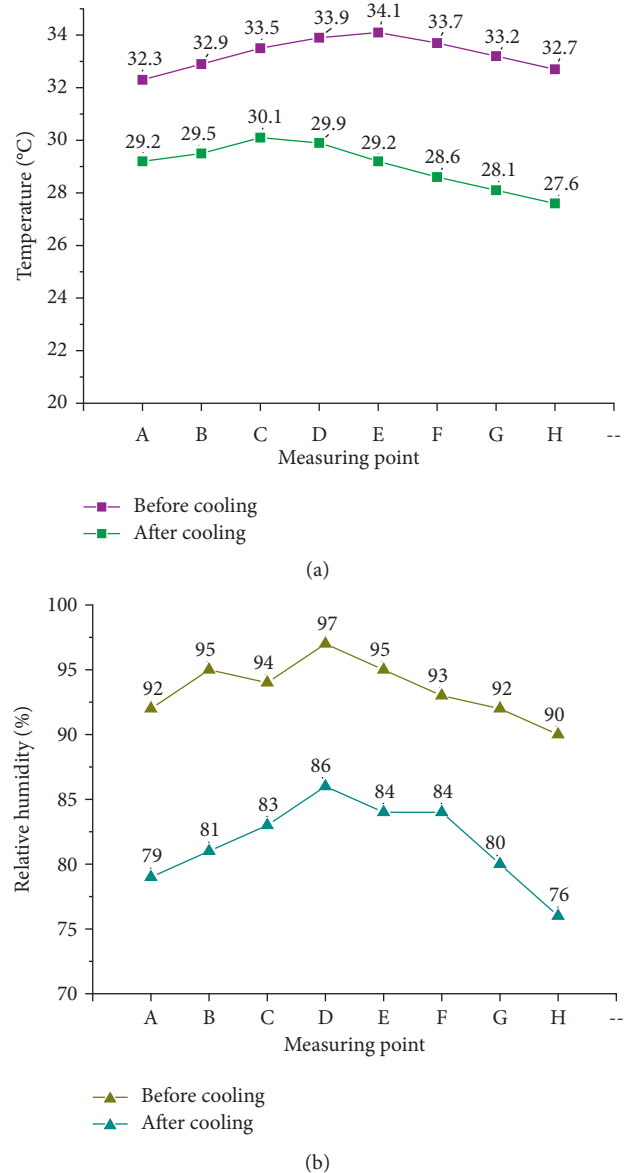


FIGURE 6: Comparison of temperature and humidity on the working face. (a) Before operation. (b) After operation.

- (3) A heating and cooling system using cold mine inflow water was built in the Jinqi Gold Mine. The 280 m middle working face was treated for thermal damage. The practical results showed that the temperature on the working face of the west wing target area was maintained at  $28^{\circ}\text{C}$ , the temperature of the heading face was reduced by  $5.4^{\circ}\text{C}$ , and the relative humidity on the working face was reduced by 15%. The results demonstrate the positive effects of the cooling system on the environmental conditions in the mine.

## Data Availability

The experimental data listed in this paper are measured and obtained from the Jinqi Gold Mine in Henan Province, China. The temperature, humidity, and wind speed of

various monitoring points are measured in the downhole working environment over a period of one month before/after the optimization of the ventilation and heat damage control. The optimization of ventilation and thermal hazard control techniques in the paper can be applied to underground mines with similar problems. The data used to support the findings of this study are available from the corresponding author upon request.

## Conflicts of Interest

The authors declare that there are no conflicts of interest regarding the publication of this paper.

## Acknowledgments

This work was supported by 15JK1414 (Special Scientific Research Project of Shaanxi Provincial Education Department, titled “Theoretical research on temporal and spatial 4D information model construction of open pit mine”) and 2016JM5088 (Foundation Project of Natural Science Foundation of Shaanxi Province, titled “Theoretical study on temporal and spatial deduction model of mining production information in open pit mine”).

## References

- [1] H. P. Xie, H. W. Zhou, D. J. Xue et al., “Research and consideration on deep coal mining and critical mining depth,” *Journal of China Coal Society*, vol. 37, no. 4, pp. 535–542, 2012.
- [2] J. X. Lai, X. L. Wang, J. L. Qiu, J. X. Xie, and Y. B. Luo, “A state-of-the-art review of sustainable energy based freeze proof technology for cold-region tunnels in China,” *Renewable and Sustainable Energy Reviews*, vol. 82, pp. 3554–3569, 2018.
- [3] J. X. Lai, X. L. Wang, J. L. Qiu et al., “Extreme deformation characteristics and countermeasures for a tunnel in difficult grounds in southern Shaanxi, China,” *Environmental Earth Sciences*, 2018, In press.
- [4] W. H. Zhou, H. Y. Qin, J. L. Qiu et al., “Building information modelling review with potential applications in tunnel engineering of China,” *Royal Society Open Science*, vol. 4, no. 8, pp. 170–174, 2017.
- [5] M. C. He and P. Y. Guo, “Deep rock mass thermodynamic effect and temperature control measures,” *Chinese Journal of Rock Mechanics and Engineering*, vol. 32, no. 12, pp. 2377–2393, 2013.
- [6] A. P. Sasmitho, J. C. Kurnia, E. Birgersson, and A. S. Mujumdar, “Computational evaluation of thermal management strategies in an underground mine,” *Applied Thermal Engineering*, vol. 90, pp. 1144–1150, 2015.
- [7] J. X. Lai, H. Zhou, K. Wang et al., “Shield-driven induced ground surface and Ming Dynasty city wall settlement of Xi’an metro,” *Tunnelling and Underground Space Technology*, 2018, In press.
- [8] J. L. Qiu, Y. L. Xie, H. B. Fan, Z. C. Wang, and Y. W. Zhang, “Centrifuge modelling of twin-tunnelling induced ground movements in loess strata,” *Arabian Journal of Geosciences*, vol. 10, no. 22, p. 493, 2017.
- [9] J. L. Qiu, X. L. Wang, S. Y. He, H. Q. Liu, J. X. Lai, and L. X. Wang, “The catastrophic landside in Maoxian County, Sichuan, SW China, on June 24,” *Natural Hazards*, vol. 89, no. 3, pp. 1485–1493, 2017.
- [10] J. X. Lai, S. Y. He, J. L. Qiu et al., “Characteristics of seismic disasters and aseismic measures of tunnels in Wenchuan earthquake,” *Environmental Earth Sciences*, vol. 76, no. 2, pp. 76–94, 2017.
- [11] J. X. Lai, S. Mao, J. L. Qiu et al., “Investigation progresses and applications of fractional derivative model in geotechnical engineering,” *Mathematical Problems in Engineering*, vol. 2016, Article ID 9183296, 15 pages, 2016.
- [12] S. R. Hu, J. C. Peng, C. Huang et al., “An overview of current status and progress in coal mining of the deep over a kilometer,” *China Mining Magazine*, vol. 20, no. 7, pp. 105–110, 2011.
- [13] H. Y. Qu, H. W. Liu, R. F. Pei et al., “Geochemical characteristic overview of the Shizishan ore-field at Tongling city, Anhui province, China,” *Contributions to Geology and Mineral Resources Research*, vol. 26, no. 3, pp. 239–248, 2011.
- [14] C. Q. Cheng, L. B. Dong, and S. D. Xu, “Simulation and optimization of deep stope mining sequence in hongtoushan copper mine,” *Metal Mine*, vol. 9, pp. 66–68, 2016.
- [15] M. Asghari, P. Nassiri, M. Reza Monazzam et al., “Weighting criteria and prioritizing of heat stress indices in surface mining using a Delphi technique and fuzzy AHP-TOPSIS method,” *Journal of Environmental Health Science and Engineering*, vol. 15, no. 1, pp. 1–11, 2017.
- [16] J. L. Qiu, X. L. Wang, J. X. Lai, Q. Zhang, and J. B. Wang, “Response characteristics and preventions for seismic subsidence of loess in Northwest China,” *Natural Hazards*, vol. 92, no. 3, pp. 1909–1935, 2018.
- [17] J. L. Qiu, H. Q. Liu, J. X. Lai et al., “Investigating the long term settlement of a tunnel built over improved loessial foundation soil using jet grouting technique,” *Journal of Performance of Constructed Facilities*, vol. 42, no. 5, pp. 112–134, 2018.
- [18] S. Mahdevari, K. Shahriar, and A. Esfahanipour, “Human health and safety risks management in underground coal mines using fuzzy TOPSIS,” *Science of the Total Environment*, vol. 488–489, pp. 85–99, 2014.
- [19] H. N. Wang, J. L. Peng, and Z. Cheng, “Analysis of ventilation and cooling in high temperature mine,” *Nonferrous Metals Engineering*, vol. 3, no. 3, pp. 34–37, 2013.
- [20] Y. P. Yuan, X. K. Gao, H. W. Wu et al., “Coupled cooling method and application of latent heat thermal energy storage combined with pre-cooling of envelope: method and model development,” *Energy*, vol. 119, pp. 817–833, 2017.
- [21] P. Y. Guo and C. Chen, “Field experimental study on the cooling effect of mine cooling system acquiring cold source from return air,” *International Journal of Mining Science and Technology*, vol. 23, no. 3, pp. 453–456, 2013.
- [22] B. B. Shi, L. J. Ma, W. Dong, and F. B. Zhou, “Application of a novel liquid nitrogen control technique for heat stress and fire prevention in underground mines,” *Journal of Occupational and Environmental Hygiene*, vol. 12, no. 8, pp. 168–177, 2015.
- [23] P. Y. Guo, M. C. He, L. G. Zheng, and N. Zhang, “A geothermal recycling system for cooling and heating in deep mines,” *Applied Thermal Engineering*, vol. 116, pp. 833–839, 2017.
- [24] H. N. Wang, B. Peng, J. L. Peng et al., “Analysis of commonly existing ventilation problems and the optimal approach to deal with them in large-size mines,” *Journal of Safety and Environment*, vol. 14, no. 3, pp. 24–27, 2014.
- [25] S. H. Zou, K. Q. Li, D. C. Zhang et al., “On the air-partition foe cooling with the heat-insulated plate,” *Journal of Safety and Environment*, vol. 16, no. 2, pp. 99–102, 2016.

- [26] Y. C. Zhang, "Research on treatment technology and cooling effect of thermal damage in Zhuji coal mine," *Safety in Coal Mines*, vol. 46, no. 10, pp. 157–159, 2015.
- [27] C. B. Wang, "Heat analysis and initial mining surface air temperature prediction research on Gaojiapu coal mine," *Coal Technology*, vol. 35, no. 11, pp. 210–212, 2016.
- [28] Z. X. Li, T. M. Wang, M. Q. Zhang et al., "Construction of air flow heat transfer coefficient and calculation of airflow temperature in mine wet roadway," *Journal of China Coal Society*, vol. 42, no. 12, pp. 3176–3181, 2017.
- [29] S. B. Yin, R. H. Shu, and M. L. Zhang, "Application of the mining ventilation system optimization by using equilibrium diagram adjustment method based on the principle of minimum energy," *Journal of Safety and Environment*, vol. 16, no. 5, pp. 120–124, 2016.
- [30] S. Jardón, A. Ordóñez, R. Álvarez, P. Cienfuegos, and J. Loredó, "Mine water for energy and water supply in the central coal basin of Asturias (Spain)," *Mine Water and the Environment*, vol. 32, no. 2, pp. 139–151, 2013.
- [31] A. P. Athresh, A. Al-Habaibeh, and K. Parker, "The design and evaluation of an open loop ground source heat pump operating in an ochre-rich coal mine water environment," *International Journal of Coal Geology*, vol. 164, pp. 69–76, 2016.
- [32] J. Sivret, D. L. Millar, and G. Lyle, "Conceptual overview and preliminary risk assessment of cryogen use in deep underground mine production," *IOP Conference Series: Materials Science and Engineering*, vol. 278, pp. 1–8, 2017.
- [33] X. X. Nie and X. B. Wei, "Optimization and practice on the reform schemes of ventilation system in the Jinqu Gold Mine," *Mining R&D*, vol. 37, no. 8, pp. 86–89, 2017.

## Research Article

# Probabilistic Analysis of Weathered Soil Slope in South Korea

Taeho Bong<sup>1</sup> and Younghwan Son <sup>2</sup>

<sup>1</sup>Oregon State University, 101 Kearney Hall, Corvallis, OR 97331, USA

<sup>2</sup>Department of Rural Systems Engineering and Research Institute for Agriculture and Life Sciences, Seoul National University, Seoul, Republic of Korea

Correspondence should be addressed to Younghwan Son; syh86@snu.ac.kr

Received 4 April 2018; Revised 25 May 2018; Accepted 25 June 2018; Published 18 July 2018

Academic Editor: Tiago Ferreira

Copyright © 2018 Taeho Bong and Younghwan Son. This is an open access article distributed under the Creative Commons Attribution License, which permits unrestricted use, distribution, and reproduction in any medium, provided the original work is properly cited.

Rainfall is a major trigger of shallow slope failures, and it is necessary to consider the spatial correlation of soil properties for probabilistic analysis of slope stability in heterogeneous soil. In this study, a case study of a weathered soil slope in Korea was performed to identify the rainfall-induced landslides considering the spatial variability of the soil properties and the probabilistic rainfall intensity depending on the return period and the rainfall duration. Various laboratory tests were performed to determine the physical properties of the site, and an electrical resistivity survey was carried out to understand the soil strata. Cohesion, friction angle, and permeability were considered as random variables considering the spatial variability, and the probabilistic rainfall intensities for return period of 2, 5, 10, 50, 100, and 200 years were used to consider the effects of rainfall infiltration. The results showed that a probabilistic framework can be used to efficiently consider the spatial variability of soil properties, and various slope failure patterns were identified according to the spatial variability of the soil properties and the probabilistic rainfall intensity.

## 1. Introduction

Shallow slope failure (typically 1–3 m deep) due to heavy rainfall during rainstorms and typhoons is common in mountain areas and take the form of translational slides, which form parallel to the original surface [1, 2]. Over the past decade, many studies on rainfall pattern changes due to climate change have been carried out, and climate change has resulted in changes in rainfall patterns that can cause less frequent, but more intense rainfall events [3, 4].

One of the main triggering factors for landslides is heavy rainfall [5–8], and the abnormal climate and localized heavy rainfall caused by climate change may lead to more frequent landslides [4, 8–12]. For this reason, the prediction of rainfall-induced landslides is becoming more important, and the infinite slope model is usually implemented for the stability analysis of natural slopes; this model is appropriate when the horizontal dimensions of the surface are relatively much larger than the vertical depth of the potential failure slope. In addition, physically-based models have frequently

been used in the framework of early warning systems devoted to rainfall-induced landslide hazard monitoring [13], and infinite slope model is commonly used to assess the factor of safety. However, the traditional infinite slope equation assumes homogeneous or averaged soil properties, and the potential failure surface is always fixed at the base of the slope [14] or wetting front depth (WFD). Although the uncertainties of the soil can be considered through the probabilistic analysis, the potential failure surface is still fixed and the probability of failure can be underestimated if the soil properties are treated as random variables without considering the spatial variability.

Geomorphological processes can lead to soil regions characterized by a degree of spatial heterogeneity [15], and the spatial variation can occur at various scales depending on the soil forming factors such as parent material, climate, topography, time, and so on. Describing and understanding the complexity of the interacting processes of soil formation has been a challenge, and geostatistics assumes that the variation of a property such as soil is continuous, which is

generally more realistic for soil [16]. If the spatial variability of soil properties is considered in the probabilistic analysis, the soil strength can vary depending on the depth considering the spatial correlation structure, and the potential failure surface can occur at various depths. Considering these features, some recent studies focused on the probabilistic analysis of slope stability in heterogeneous soil considering the spatial variability.

For example, Cho [17] identified the effect of spatial variability of unit weight and shear strength parameters using a limit equilibrium method, also, Griffiths et al. [18] investigated the effect of the spatial variability of shear strength parameters using the random finite-element method (RFEM), and Griffiths et al. [14] performed infinite slope analysis considering spatial variability of soil and showed that the potential failure surface can occur at various depths depending on spatial variability. Jiang et al. [19] identified the effect of spatial variability of shear strength parameters using a nonintrusive stochastic finite element method. Cho [20] discussed the effect of spatial variability of permeability on infinite slope stability and the distribution of failure depth due to rainfall infiltration. However, the saturated permeability is often depth-dependent, and Dou et al. [21] investigated the effect of spatial variability of permeability considering nonstationary random field of the saturated permeability as an extension of Cho's [20]. In a similar vein, Li et al. [22] conducted reliability analysis of an infinite slope considering the linear trend of shear strength parameters in a random field. Li et al. [23] also proposed a multiple response-surface method for efficient slope reliability analysis considering spatial variability, and Cai et al. [24] conducted a cross-correlation analysis to determine the impact of heterogeneity of permeability, soil cohesion, and soil friction angle on slope stability.

In previous studies, the random variables most frequently considered when analyzing spatial variability of the soil properties are shear strength parameters (cohesion,  $c$  and friction angle,  $\phi$ ), and the permeability has also been considered in slope stability analysis due to rainfall infiltration. In practice, other important factors for estimating the probability of landslides occurrence are the intensity of rainfall and duration time [25], which are climatic factors. Rainfall is a major cause of landslides, and it is known that spatial and temporal variability is very high [26]. Therefore, it is important to consider and evaluate the appropriate probabilistic rainfall intensity for predicting the actual probability of landslide occurrence. However, little is known about the role of spatial variability of soil properties in probabilistic analysis of slope stability considering the probability rainfall intensity.

The purpose of this study was to identify the probability of failure of rainfall-induced landslides considering the spatial variability of soil properties and probabilistic rainfall intensity. A case study of shallow slope failure of weathered residual soil slope in Jangheung, Korea, was performed to verify the probabilistic analysis framework. The soil strata of the slope were identified, and the site investigation point was selected through electrical resistivity survey. Then, the soil physical properties and infiltration characteristics of

unsaturated soil on natural slope were investigated, and two shear strength parameters ( $c$  and  $\phi$ ) and permeability were considered as random fields. A slope stability analysis was performed using an infinite slope model, and the probabilistic rainfall intensity for 2, 5, 10, 50, 100, and 200 years frequency for the study area was considered. A series of Latin hypercube sampling- (LHS-) [27] based Monte Carlo simulations was conducted to investigate the effect of the spatial variability of soil properties on the mechanism of slope failure during periods of rain infiltration. Consequently, the probability of slope failure according to the probabilistic rainfall intensity and spatial variability of soil properties was estimated. How soil properties and climatic factors affect slope stability were then discussed.

## 2. Random Field

Nearly all natural soils are highly variable in their properties, and their variability shows a spatial correlation. The spatial variability of soil properties can be effectively considered using random field theory, and probabilistic analyses that incorporate the spatial variability of soil properties as random fields are more appropriate to consider the uncertainty of soil than those considering soil properties as a single random variable.

*2.1. Spatial Variability of Soil.* Because of complex geological and environmental processes, soil is inherently heterogeneous, and its properties can be highly variable and spatially correlated in the vertical and horizontal directions. The spatial correlation of soil properties is known to influence the geotechnical response of soil, and it brings unavoidable uncertainty in design, leading to unexpected soil responses [15, 28]. These uncertain spatial properties can be characterized using random field theory [29, 30]. Vanmarcke [29] used a scale of fluctuation (SOF,  $\delta$ ) to describe the extent of how soil properties are spatially correlated. Various methods are available to estimate the SOF, and the simplest approach is to fit the theoretical autocorrelation function (ACF,  $\rho$ ) to the empirical ACF [31–34]. However, determining a theoretical ACF may not be easily implemented because a large amount of data is required. Therefore, some theoretical ACFs are usually used to characterize the spatial correlation of soil properties, and the single exponential ACF has been widely used to model the inherent spatial variability of soil properties in probabilistic analysis of slope stability [23]:

$$\rho(x_1, x_2) = \exp\left(-\frac{|x_1 - x_2|}{l}\right), \quad (1)$$

where  $l$  represents the autocorrelation distance and reflects the rate at which the correlation decays between two points ( $x_1, x_2$ ). The SOF implied by the single exponential autocorrelation function is equal to twice the value of the autocorrelation distance ( $\delta = 2l$ ).

*2.2. Random Fields.* In this study, the Karhunen–Loève expansion (KLE) was adopted to generate random fields because it is an efficient method for random field

discretization with a desired level of accuracy and provides the greatest accuracy when an exponential ACF is used [35].

The KLE of a random field with a mean value ( $\mu_\omega$ ) and a variance ( $\sigma_\omega^2$ ) is given by Spanos and Ghanem [36]:

$$\omega(x, \theta) = \mu_\omega(x) + \sum_{i=1}^{\infty} \sigma_\omega \sqrt{\lambda_i} f_i(x) \xi_i(\theta), \quad x \in \Omega, \quad (2)$$

where  $\lambda_i$  and  $f_i(x)$  are the eigenvalues and eigenfunctions of the covariance function, respectively, and  $\xi_i(\theta)$  represents the uncorrelated zero mean random variables. For practical implementation, the discretization of the random field  $\omega(x, \theta)$  is obtained by truncating the series expansion at the  $M$ th term:

$$\omega(x, \theta) = \mu_\omega(x) + \sum_{i=1}^M \sigma_\omega \sqrt{\lambda_i} f_i(x) \xi_i(\theta). \quad (3)$$

The accuracy of the represented random field depends on the number of terms used in the KLE expansion, and the number of required terms is determined according to the ratio of the correlation length and the domain size [37].

Normal random fields are often used for modeling uncertainties with spatial variability for mathematical convenience and due to a lack of available data, but they are not applicable in many situations where the random variable is always non-negative. Therefore, the assumption of a log-normal distribution is appropriate as the soil properties used in this study are always non-negative [38, 39]. In (3), if  $\mu_\omega$  is zero and  $\sigma_\omega$  is one, standard normal random fields are generated by KLE, and it can be transformed into log-normal random fields using (4) as follows:

$$\tilde{\omega}(x, \theta) = \exp\left(\mu_{\ln(x)} + \sigma_{\ln(x)} \sum_{i=1}^M \sqrt{\lambda_i} f_i(x) \xi_i(\theta)\right), \quad (4)$$

where  $\mu_{\ln(x)}$  and  $\sigma_{\ln(x)}$  are equal to the mean and standard deviation of  $\ln(x)$  of the underlying normal distribution.

### 3. Rainfall-Induced Landslide

In this section, the rainfall infiltration model and slope stability analysis model for unsaturated soils were described to assess the vulnerability of rainfall-induced landslides caused by rainfall, and then the probabilistic analysis procedure considering the spatial variability of soil properties was presented.

**3.1. Rainfall Infiltration.** In order to perform infiltration analysis considering spatial variability, the flow of water in multilayered soils should be considered, and this can be performed using differential equations that satisfy Darcy's law [20, 21, 24, 40]. Alternatively, semianalytical and areal-averaged infiltration models have been established to study field-scale infiltration over soils with the variability of permeability based on the Green-Ampt [41] model [42, 43]. Chu and Marino [44] present a modified Green-Ampt model considering infiltration in multilayered soils. This model is able to deal with unsteady and steady rainfall events as well as ponding and nonponding conditions. Therefore, in this study, the infiltration model by Chu and Marino [44]

was adopted to consider the spatial variability of permeability. Figure 1 shows infiltration of rainfall into an  $n$ -layered soil profile with permeability ( $k$ ) and initial volumetric water content ( $\theta_0$ ) for each layer.

When the wetting front is over layer  $n$  at location  $z$  ( $z_{n-1} < z \leq z_n$ ), the infiltration rate ( $i$ ) under an initially ponded condition can be expressed as

$$i_z = \frac{z + \Psi_{mn}}{\sum_{j=1}^{n-1} ((z_j - z_{j-1})/k_j) + ((z - z_{n-1})/k_n)}, \quad (5)$$

and cumulative infiltration ( $I$ ) is

$$\begin{aligned} I_z &= I_{z_{n-1}} + (z - z_{n-1})(\theta_{sn} - \theta_{0n}) \\ &= \sum_{j=1}^{n-1} (z_j - z_{j-1})\theta_{fj} + (z - z_{n-1})\theta_{fn}. \end{aligned} \quad (6)$$

The travel time to depth  $z$  can be expressed as

$$\begin{aligned} t_z &= t_{z_{n-1}} + \frac{\theta_{fn}}{k_n} (z - z_{n-1}) \\ &+ \theta_{fn} \left[ \sum_{j=1}^{n-1} z_j \left( \frac{1}{k_j} - \frac{1}{k_{j+1}} \right) - \frac{\Psi_{mn}}{k_n} \right] \ln \left( \frac{z + \Psi_{mn}}{z_{n-1} + \Psi_{mn}} \right), \end{aligned} \quad (7)$$

where  $\theta_s$  is the saturated volumetric water content ( $L^3/L^3$ ),  $\Psi_m$  is the pressure head (suction) (L),  $\theta_f$  is  $(\theta_s - \theta_0)$ , and the subscript  $n$  means the  $n$ -layer. In the case of nonponding, where the infiltration capacity of soil is greater than the rainfall intensity, all rainfall was assumed to infiltrate into the soil producing a piston flow. A detailed description of rainfall infiltration can be found in Chu and Marino [44].

**3.2. Slope Stability of Unsaturated Soils.** Rainfall-induced landslides usually have shallow surface failure depth, being the main cause of the reduction of negative pore water pressure in unsaturated soil due to rainfall infiltration [5, 45]. Fredlund et al. [46] extended the shear strength criteria to unsaturated soils considering the matric suction, being possible to calculate the factor of safety along the potential failure surface (Figure 2) as

$$F_s = \frac{c' + \sigma' \tan \phi' + (u_a - u_w) \tan \phi^b}{W \sin \beta \cos \beta}, \quad (8)$$

where  $c'$  is the effective cohesion,  $\sigma'$  is the effective normal stress,  $\phi'$  is the effective friction angle,  $u_a$  is the pore air pressure,  $u_w$  is the pore water pressure,  $W$  is the weight of the soil slice per unit base area,  $\beta$  is the slope angle, and  $\phi^b$  is the angle indicating the rate of increase of shear strength relative to increased matric suction.

The shear strength contribution due to matric suction of unsaturated soil can be expressed as described by Fredlund and Rahardjo [45]:

$$\tan \phi^b = \tan \phi' \left( \frac{\theta - \theta_r}{\theta_s - \theta_r} \right) = \tan \phi' \cdot \Theta, \quad (9)$$

where  $\theta$  is the volumetric water content at potential failure surface and  $\theta_s$  and  $\theta_r$  are the saturated and residual volumetric water content, respectively.  $\Theta$  is normalized volumetric water

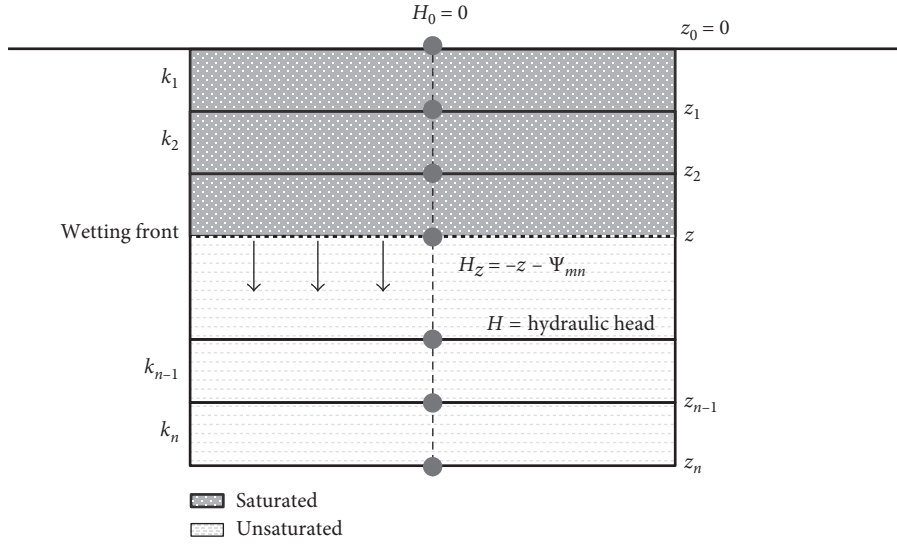


FIGURE 1: Infiltration into a layered soil profile under an initially ponded condition.

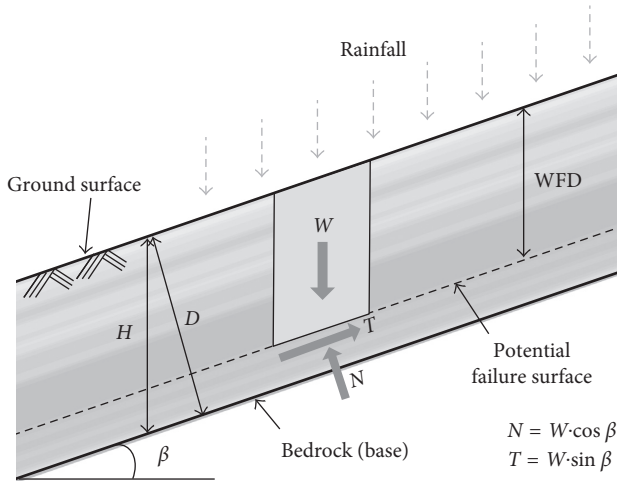


FIGURE 2: Infinite slope analysis model.

content, and the relationship between  $\Theta$  and the matric suction ( $\Psi$ ) was given by van Genuchten [47]:

$$\Theta = \frac{\theta - \theta_r}{\theta_s - \theta_r} = \left[ \frac{1}{1 + (\alpha\Psi)^n} \right]^m, \quad (10)$$

where  $\alpha$ ,  $n$ , and  $m$  are van Genuchten's soil-water characteristic curve (SWCC) parameters. Considering (9) and (10), (8) can be expressed as

$$F_s = \frac{c' + \sigma' \tan \phi' + (u_a - u_w) \tan \phi' [1/(1 + (\alpha\Psi)^n)]^m}{W \sin \beta \cos \beta}. \quad (11)$$

**3.3. Probabilistic Analysis.** The schematic view of the probabilistic slope analysis considering the spatial variability of soil properties and probabilistic rainfall intensity is shown in Figure 3. In order to consider the spatial variability of soil, random fields are generated for three soil properties ( $c$ ,  $\phi$ , and  $k_s$ ), which are mainly considered as random variables in the

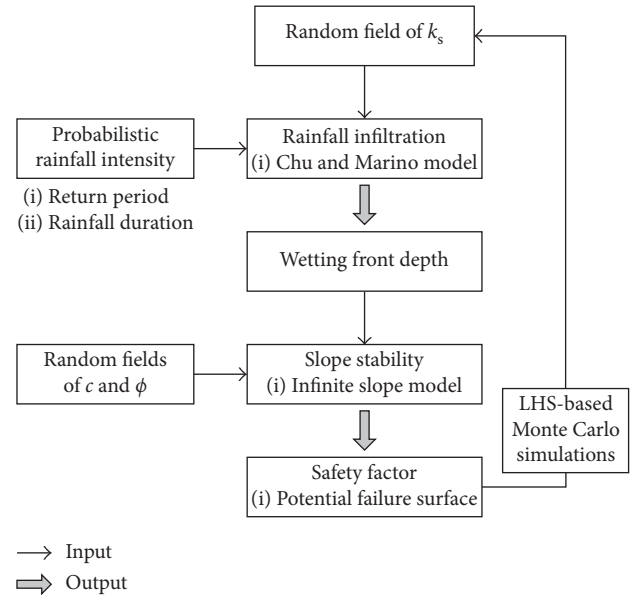


FIGURE 3: Flow chart for the probabilistic slope analysis.

existing studies on slope stability, and these are used as input values in the rainfall infiltration and slope stability analysis. The probability rainfall intensity depending on the return period and the rainfall duration is applied to consider rainfall characteristics for the site, and the WFD due to rainfall infiltration is estimated by Chu and Marino [44] model. Subsequently, the WFD is used for infinite slope stability analysis. As a result, the factor of safety for each depth and potential failure surface is estimated. This process is repeated to derive probabilistic results, and a series of LHS-based Monte Carlo simulations is conducted for efficient random sampling.

## 4. Study Area

**4.1. Soil Physical Properties.** The study area is located in Jangheung, Gyeonggi-do, South Korea ( $37^{\circ}45'03''N$ ,

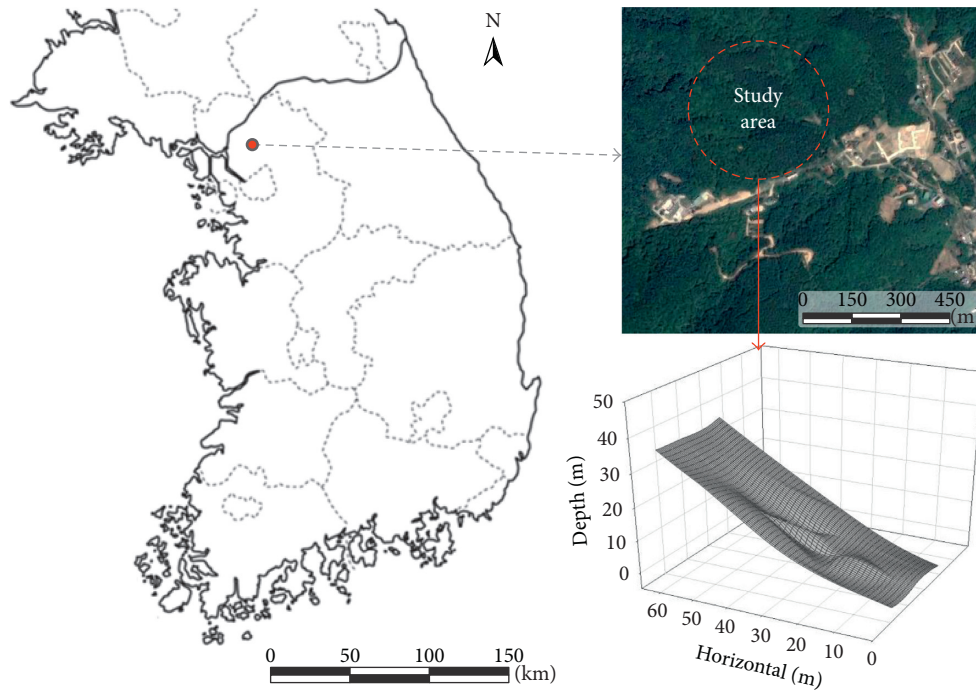


FIGURE 4: Location of the study area and surface plot.

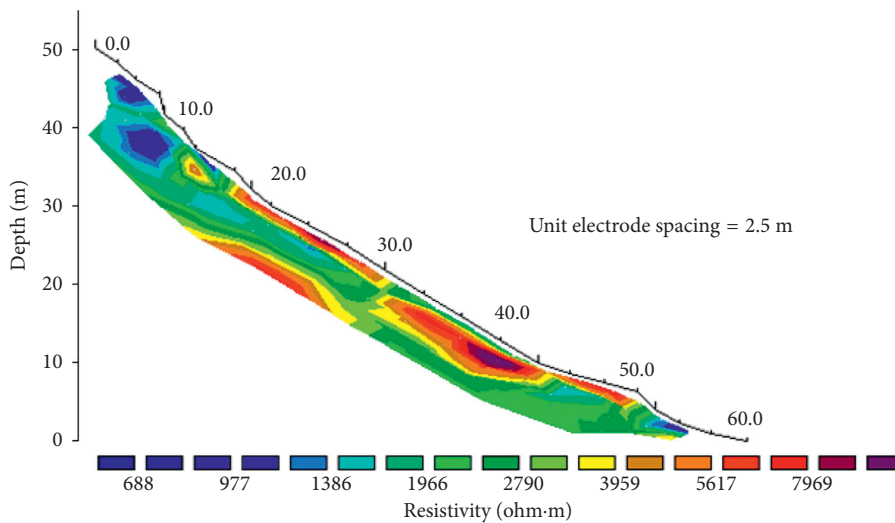


FIGURE 5: Resistivity tomography of the slope.

126°56'21"E). This area is underlain by a Gyeonggi gneiss complex that belongs to the Gyeonggi massif, and the bedrock is intensely weathered. The surface is covered by *Pinus koraiensis*, commonly known as the Korean pine. As a preliminary investigation, the slope length, depth, and gradient which seems to be vulnerable to landslides (with steep and long slope) was chosen as the study slope. A topographic survey was carried out to clarify the geometrical characteristics of the slope using electronic distance measurement (EDM), slope length and angle approximately being 50 m and 31°, respectively. Figure 4 shows the location and topographic surface of the study slope.

Electrical resistivity survey was carried out in order to identify soil strata from the resistivity distribution and to select the site investigation point. Resistar RS-100M equipment with multielectrode system ME-100 (Geofyzika A.s.) was used for a multielectrode survey using a Wenner–Schlumberger electrode array with electrode spacing of 2.5 m. Primary data were processed into resistivity cross sections by a 2-D inverse method using the software Res2DInv [48]. Figure 5 shows the resistivity tomography of the slope of the study area.

As shown in Figure 5, the direction of the soil strata can be regarded as parallel to the slope surface, and horizontal autocorrelation is higher than vertical autocorrelation for soil resistivity. Therefore, it is reasonable to generate

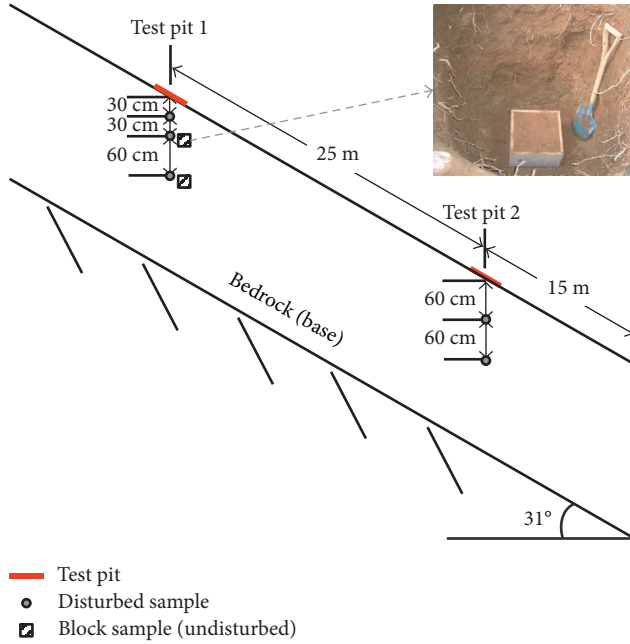


FIGURE 6: Location of sampling points.

a random field for the vertical direction on the slope surface. Blue (red) indicates low (high) electrical resistivity. The area with the highest electrical resistivity was in good agreement with the location of the exposed outcrop. The upper slope shows a relatively low resistance value, and it can be assumed that the water content is high [49] and the strength is relatively weak. Therefore, the cross section of the upper slope was selected as the analysis section. Hand auger borings were carried out primarily to identify soil depth and stratum, and two test pits with a size of 1 m × 1 m were dug. The test pits and soil sampling locations are depicted in Figure 6. The wet unit weight of each sampling depth was obtained by the sand replacement method, and three and two disturbed soil samples were obtained from the upper and lower slope test pits, respectively. The triaxial compression test and the constant head permeability test were carried out to determine the soil physical properties. In addition, the undisturbed samples were also obtained from the upper slope using block sampling and used for the SWCC test. The basic physical properties of soil and slope conditions are summarized in Table 1.

In accordance with the United Soil Classification System (USCS), the soil is classified as SM or SC, and the specific gravity ( $G_s$ ) of soil is 2.62. The shear strength test was carried out on soil with a depth of 30, 60, and 120 cm, and the average values for cohesion and friction angle were 14.7 kPa and 17.9°, respectively. The permeability test was also performed on the same depths, and the average saturated permeability ( $k_s$ ) was  $1.64 \times 10^{-6}$  m/s. The random variables selected for the stability analysis are two shear strength parameters ( $c'$  and  $\phi'$ ) and saturated permeability. However, the measured data were small, and there was a limit to identifying the statistical characteristics of soil properties by using measured data. Therefore, only the average values of the measured data for  $c$ ,  $\phi$ , and  $k_s$  were used, and their COV and PDF were assumed through the literatures [15, 30]. The

TABLE 1: Summary of basic soil properties and slope conditions.

	Parameter	Value
Soil property	Specific gravity, $G_s$	2.62
	Water content (%)	19.1
	Dry unit weight, $\gamma_d$ (kN/m <sup>3</sup> )	14.7
	Porosity (%)	43.1
	Plastic limit (%)	15.7
	USCS	SM, SC
Slope	Length (m)	50
	Angle (°)	31
	Depth (m)	2.8

soil properties vary based on the depositional and stress history of the deposit, and its distribution characteristics can be quantitatively reflected through the probability density function (PDF). The PDF type was assumed to be a log-normal distribution for all three parameters, and the coefficient of variation (COV) of  $c'$ ,  $\phi'$ , and  $k_s$ , was assumed equal to 30%, 20%, and 50%, respectively. Phoon and Kulhawy [30] summarized the SOFs and COVs of inherent spatial variability of various soil properties; however, information of soil strength SOF is insufficient. Therefore, the normalized SOFs ( $\delta/D$ ) were assumed to be 0.1, 0.2, 0.4, 0.8, 1.5, and 3.0 for vertical depth to slope surface ( $D$ ) in order to observe the effect of spatial variability. The statistical properties of the three parameters are summarized in Table 2.

Rainfall infiltration into the soil begins from unsaturated conditions, and it is necessary to identify the permeability characteristics under unsaturated conditions. Therefore, a laboratory test for SWCC was conducted, and parameters of the van Genuchten [47] model were estimated as  $\alpha = 0.0291$ ,  $m = 0.3473$ , and  $n = 1.532$ . The conditions of infiltration analysis are summarized in Table 3, and SWCC is shown in Figure 7.

**4.2. Probabilistic Rainfall Intensity.** Rainfall information on the study area is very important because rainfall has a high spatial and temporal variability, and its probabilistic characteristics are very different depending on the region. The information of probability rainfall intensity at the study area was obtained from the Korea precipitation frequency data server of the Ministry of Land, Infrastructure and Transport (MOLIT, <http://www.k-idf.re.kr>). Figure 8 shows intensity-duration-frequency (IDF) curves.

Rainfall intensity for the IDF curve increased as the return period increased, and the smaller the duration, the greater the difference in rainfall intensity. In this study, the probabilistic rainfall intensity for a return period ( $T_r$ ) of 2, 5, 10, 50, 100, and 200 years was considered. Rainfall events with durations of 1, 2, 3, 6, 9, 12, 15, 18, and 24 hours were chosen for slope analysis, and rainfall intensity is summarized in Table 4.

## 5. Results and Discussion

**5.1. Wetting Front Depth and the Factor of Safety.** Figure 9 shows the change of wetting front depth (WFD) and the factor of safety depending on rainfall duration. Soil

TABLE 2: Statistical properties of shear strength parameters.

Soil property	Mean	Standard deviation	COV (%)	PDF	Scale of fluctuation
Cohesion, $c$ (kPa)	14.7	4.41	30	Log-normal	0.1D, 0.2D
Friction angle, $\phi$ ( $^\circ$ )	17.9	3.58	20	Log-normal	0.4D, 0.8D
Permeability, $k_s$ (m/s)	$1.64 \times 10^{-6}$	$8.19 \times 10^{-7}$	50	Log-normal	1.5D, 3.0D

TABLE 3: Conditions of infiltration analysis.

$\theta_0$ (%)	$\theta_s$ (%)	Fitting parameters of van Genuchten's SWCC			$\Psi_{mf}$ (m)
		$\alpha$ (kPa $^{-1}$ )	$m$	$m$	
28.1	41.2	0.0286	0.3580	1.5576	0.89

$\theta_0$ : initial volumetric water content;  $\theta_s$ : saturated volumetric water content.

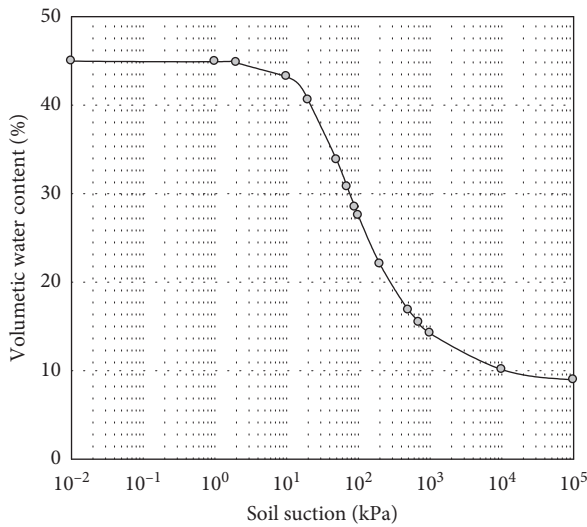


FIGURE 7: Soil-water characteristic curve.

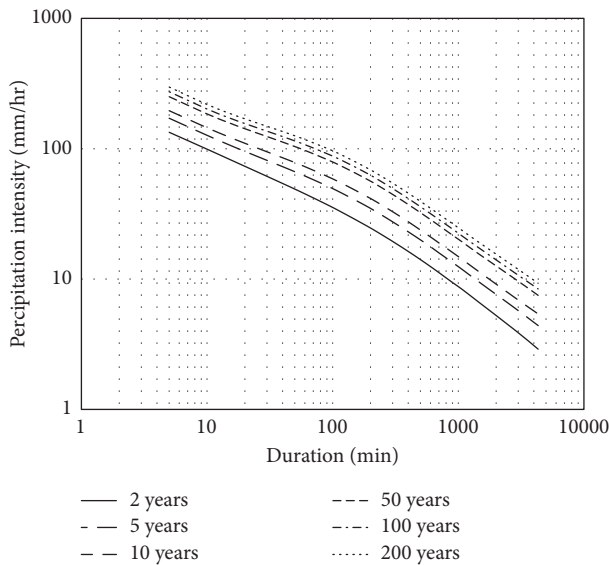


FIGURE 8: IDF curves for study site.

saturation occurs from the surface due to rainfall infiltration, and the WFD increased with the increase of rainfall duration. The deterministic approach using Chu and Marino [44]

TABLE 4: Probabilistic rainfall intensity (mm/h) of the study area.

Return period (year)	Duration time (hour)								
	1	2	3	6	9	12	15	18	24
2	45.1	32.3	26.1	17.4	13.4	11.0	9.4	8.3	6.7
5	61.8	45.3	36.9	24.6	19.0	15.6	13.4	11.8	9.6
10	72.9	53.9	43.9	29.4	22.6	18.6	16.0	14.1	11.5
50	97.2	72.8	59.6	39.9	30.7	25.3	21.7	19.2	15.7
100	107.5	80.8	66.2	44.3	34.1	28.1	24.2	21.3	17.5
200	117.7	88.8	72.7	48.7	37.5	30.9	26.6	23.5	19.3

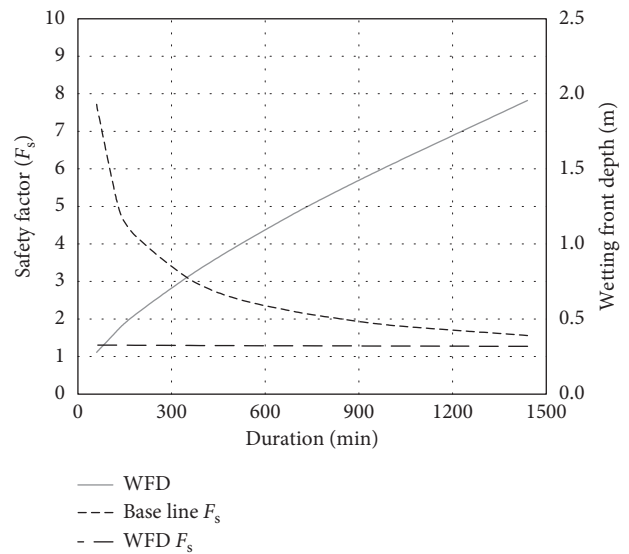


FIGURE 9: Change in wetting front depth and factor of safety depending on rainfall duration using a deterministic approach.

model was carried out to estimate the WFD and the factor of safety at the baseline and WFD according to the rainfall duration.

The gray line indicates the WDF changes and the dotted lines the changes of FS at the baseline and at the WFD. WFD increases approximately 2 m when rainfall duration is equal to 24 h, and the factor of safety at WFD was drastically reduced due to the dissipation of negative pore water pressure in unsaturated soil as the rainfall began to penetrate into the ground. The factor of safety at the baseline showed a very small reduction rate considering only an increase in unit weight due to the rainfall infiltration. In the deterministic approach, the factor of safety until a rainfall of 24 h was greater than 1. The change in the WFD with the rainfall duration and normalized SOF is shown in Figure 10.

The average WFD showed a significant increase with increasing rainfall duration, but it increased very slightly with normalized SOF. When the return period was low, the

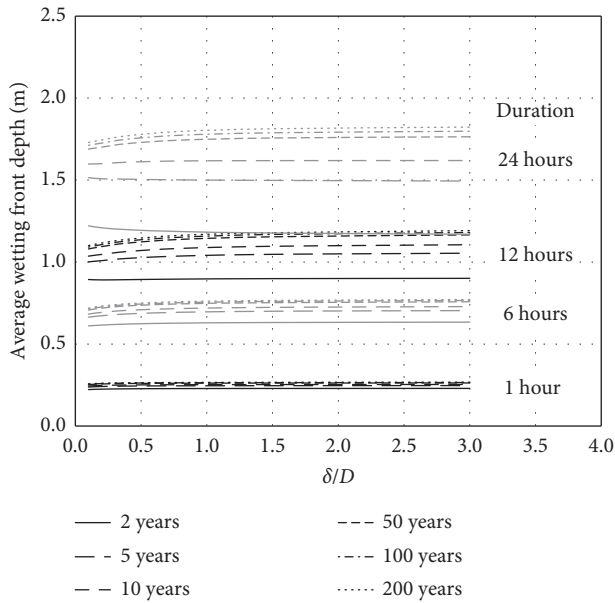


FIGURE 10: Change in wetting front depth depending on rainfall duration and normalized SOF.

difference in average WFD according to the return period was not significant even though there was a large difference in rainfall intensity, whereas the average WFD significantly changed with the return period for high rainfall durations. Although there was no significant difference in average WFD with normalized SOF, there was a large variation in standard deviation. The WFD appeared at various depths depending on the spatial variability of the permeability, and the distribution exhibited a wider range as the rainfall duration increased (Figure 11).

**5.2. Effect of Spatial Variability and Probabilistic Rainfall Intensity.** In this study, the potential failure surface was defined as the deepest depth with a factor of safety of less than 1, and if the factor of safety is less than 1 at any depth, the slope failure was considered to have occurred. The probability of failure is significantly affected by the return period and the rainfall duration as shown in Figure 12. The effect of the return period increases with rainfall duration because WFD shows a large difference as the rainfall duration increased. However, the effect of the return period decreased as the return period increased, and there was no significant difference in the probability of failure when the return period was over 100 years. This is because the surface runoff occurs when the rainfall intensity exceeds a certain level, and the infiltration is dominated by the infiltration capability of the soil after reaching the initial ponding condition. The spatial variability of soil properties was found to have a major influence. If spatial variability of soil is not considered, the normalized SOF is considered infinity ( $\delta/D = \infty$ ), and its results showed the lowest probability of failure. This is because the soil is considered to be homogeneous, and it does not take into account the potential failure surface at various depths as the failure surface is fixed to the WFD or the baseline. The impact of the return period

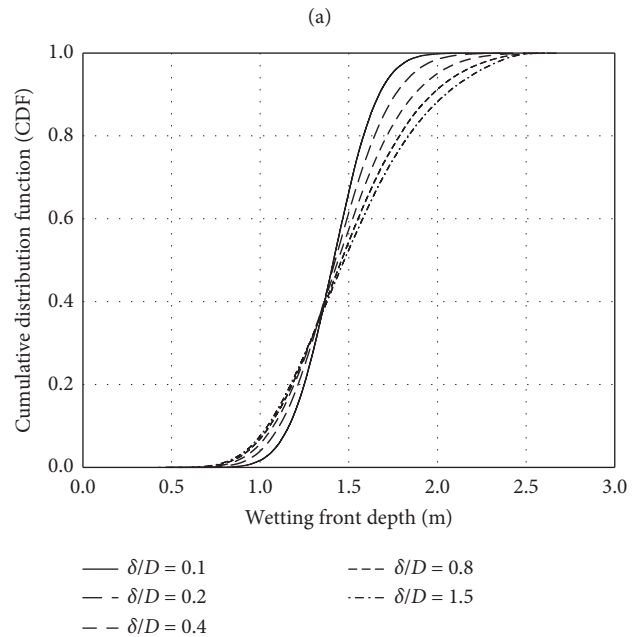
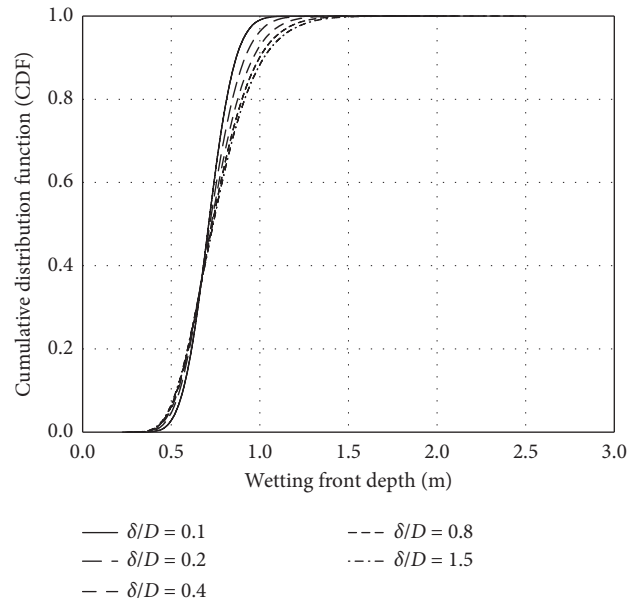


FIGURE 11: Distribution of WFD according to normalized SOF for rainfall duration of (a) 6 hours and (b) 18 hours.

and the rainfall duration on the probability of failure also varied depending on the spatial variability of soil properties, and the variation of the failure probability with the return period and the rainfall duration was larger as the normalized SOF decreased.

The variation of the probability of failure according to normalized SOF for the return period of 2 and 100 years is shown in Figure 13. The probability of failure decreased with increasing normalized SOF, and it rapidly decreased when the normalized SOF was less than approximately 1. As identified in various studies [14, 20, 22], the location of the potential failure surface appeared at various depths in

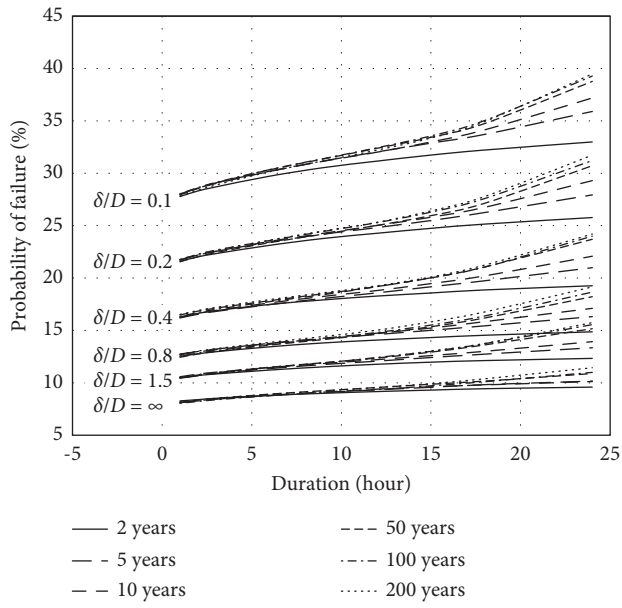
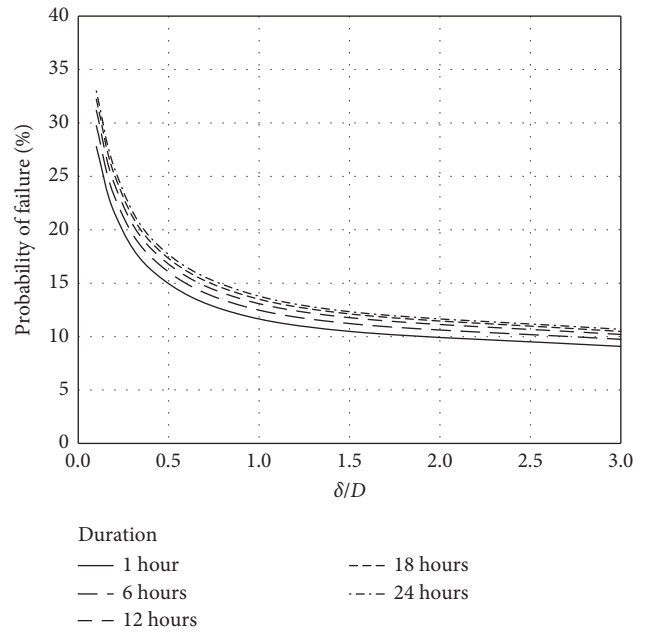


FIGURE 12: Change in the probability of failure depending on the return period and the rainfall duration.

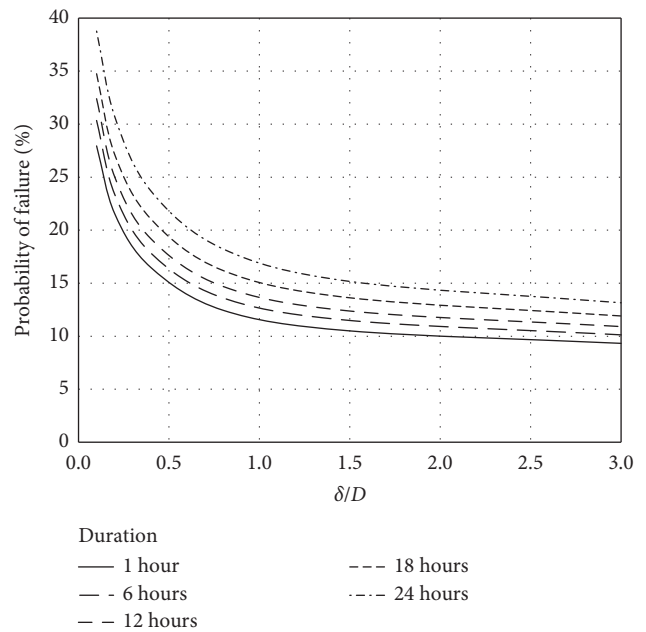
consideration of the spatial variability of soil properties, and the larger the normalized SOF, the lower the probability of failure because the failure occurs at a narrower range of depths. The difference in the probability of failure according to the rainfall duration for the return period of 2 years is smaller than that of the return period of 100 years. The reason is that although the probability of failure is almost the same regardless of the return period for low rainfall duration under the same normalized SOF, the probability of failure increased with the increase of rainfall duration, and its growth rate was larger as the return period is higher as shown in Figure 12.

Figure 14 shows an example of histograms for the frequency of the critical depth where the minimum factor of safety less than 1 occurs and the cumulative failure probability along the depth for 100-year return period and the rainfall duration of 18 hours. The left cumulative distribution and gray histogram are the results for the normalized SOF of 0.1, and the right cumulative distribution and black histogram are the results for the normalized SOF of 1.5. When the normalized SOF was 0.1, the failure frequency near the baseline was about 19%, whereas that of the normalized SOF of 1.5 was about 40%. The normalized SOF of 0.1 shows higher failure frequency at various depths than that of the normalized SOF of 1.5, and this is due to the effects of the shear strength parameter as found in the results of Griffiths et al. [14] and the distribution of WFD as shown in Figure 11.

The probability of failure according to the normalized SOF and the rainfall duration for 2 and 100 years return periods were compared with the case where the spatial variability of soil properties was not considered (i.e., homogeneous soil) for each return period, and the differences in probability of failure ( $\Delta p_f$ ) are shown in Figure 15. The difference of the failure probability is significantly influenced by the normalized SOF,



(a)



(b)

FIGURE 13: Change in the probability of failure depending on normalized SOF for (a)  $T_r = 2$  years and (b)  $T_r = 100$  years.

and the return period and the rainfall duration also have an effect on the difference in probability of failure when the normalized SOF is small. If the normalized SOF is small (i.e.,  $\delta/D = 0.1$ ), a probabilistic difference of approximately 24~30% can occur, while the spatial variability of soil properties has little effect on the normalized SOF of three or more. This difference in the probability of failure is influenced by the slope and rainfall conditions and the statistical characteristics of soil properties, and therefore it can be different depending on the target slope. However, it was shown that the

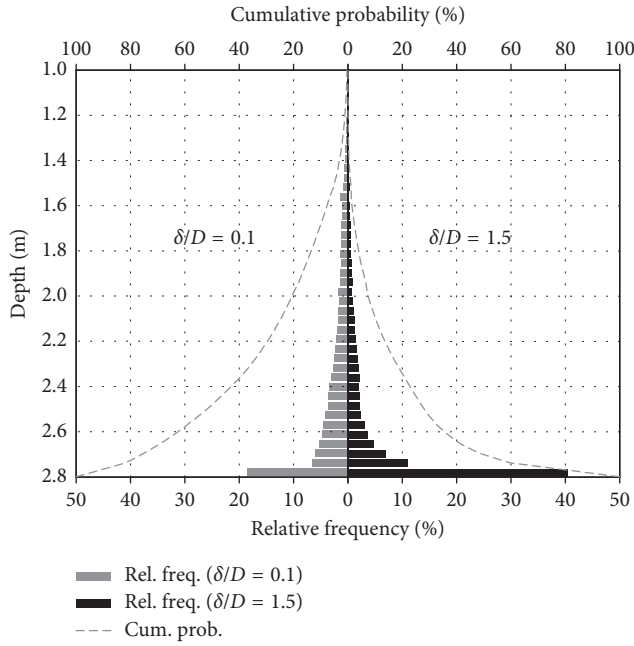


FIGURE 14: Histograms for the frequency of the critical depth and the cumulative failure probability along with the depth ( $T_r = 100$  years and 18 hours rainfall duration).

probabilistic results of the slope stability exhibit noticeable differences that vary with the spatial variability of soil properties, and it is a well-known fact that soil is heterogeneous. Therefore, there is a strong need to consider the spatial variability of soil in practice. In addition, rainfall is a major cause of landslides in South Korea, and the probability of failure of slopes is very different depending on the rainfall condition. Therefore, it is also important to consider the probability rainfall intensity reflecting local rainfall characteristics.

### 6. Conclusions

The purpose of this study was to identify the failure of rainfall-induced landslides considering the spatial variability of soil properties and the probabilistic rainfall intensity through a case study of a weathered soil slope in Korea. An electrical resistivity survey was performed to understand the stratum of the slope. Although the electrical resistivity survey has some inherent limitations as it cannot provide direct information such as shear strength, the distribution of soil strata can be confirmed with images, and information can be provided on soil survey location and direction of random field generation. Herein, three soil properties (i.e., cohesion, friction angle, and permeability) were considered as random fields, and the IDF curves with a 2-, 5-, 10-, 50-, 100-, and 200-year return period were applied to identify the effects of probabilistic rainfall intensity. An infinite slope equation for unsaturated soil and multilayer infiltration model by Chu and Marino [44] was used to analyze the slope stability affected by rainfall, and a series of LHS-based Monte Carlo simulations was conducted for probabilistic analysis.

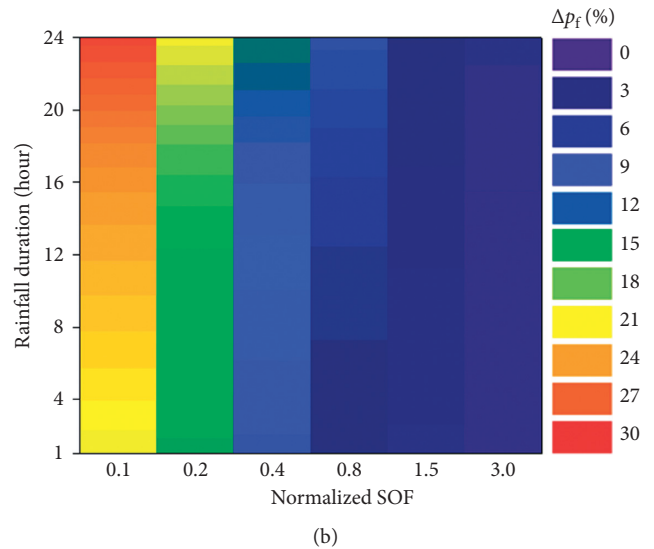
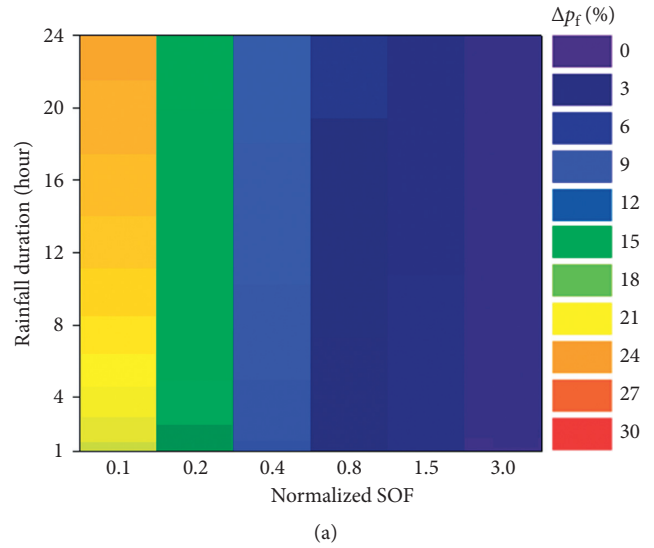


FIGURE 15: Difference in probability of failure with the results for homogeneous soil ( $\delta/D = \infty$ ) for (a)  $T_r = 2$  years and (b)  $T_r = 100$  years.

Probability of failure was significantly affected by the spatial variability of soil properties, and the results are similar to those of previous studies. The return period and rainfall duration also have a significant impact on slope stability due to the wetting front development. Although the rainfall conditions are the same, their effects on the slope stability were different according to the spatial variability of soil properties, and their effects were more sensitive with decreasing normalized SOF. The probability of failure increased as the return period and the rainfall duration increased. However, the increase rate of the probability of failure decreased as the return period increased, and there was no significant difference in probability of failure when the return period is over 100 years because rainfall infiltration is dominated by the infiltration capability of the soil.

Compared with the results of traditional probabilistic analysis without consideration of the spatial variability of soil properties, the difference in probability of failure was

found to be approximately 24~30% when the normalized SOF was small (i.e.,  $\delta/D=0.1$ ), and there was little effect of the spatial variability of soil properties for the normalized SOF more than 3. Naturally, the soil is inhomogeneous, and vertical spatial variability of soil properties is typically large. In addition, the probability of failure according to the probability rainfall intensity is greatly influenced by spatial variability of soil properties. Therefore, probabilistic analysis with consideration of spatial variability of soil properties is very important to obtain reasonable results. Although this study applied various SOFs and identified their effects, it is necessary to apply appropriate SOFs to the site in order to accurately estimate the probability of failure. It is well known that the spatial variability in the vertical direction is larger than that in the horizontal direction. This fact was confirmed herein indirectly through an electrical resistivity survey, and it was also confirmed that it is reasonable to generate a random field for the vertical direction on the slope surface. Additionally, this study used the IDF curve generated based on past rainfall data, but the impact of climate change was not reflected. Recently, however, a modified IDF curve has been proposed considering the climate change, and the impacts of climate change can be reflected by the modified IDF curve.

### Data Availability

The data used to support the findings of this study are included within the article.

### Conflicts of Interest

The authors declare that they have no conflicts of interest.

### Acknowledgments

The work of this research had been conducted in the Department of Rural System Engineering, Seoul National University, and the authors would like to thank them for their technical and laboratory support.

### References

- [1] A. B. Fourie, D. Rowe, and G. E. Blight, "The effect of infiltration on the stability of the slopes of a dry ash dump," *Geotechnique*, vol. 49, no. 1, pp. 1-13, 1999.
- [2] A. S. Muntohar and H. J. Liao, "Rainfall infiltration: infinite slope model for landslides triggering by rainstorm," *Natural Hazards*, vol. 54, no. 3, pp. 967-984, 2010.
- [3] A. M. Strauch, R. A. Mackenzie, C. P. Giardina, and G. L. Bruland, "Climate driven changes to rainfall and streamflow patterns in a model tropical island hydrological system," *Journal of Hydrology*, vol. 523, pp. 160-169, 2017.
- [4] J. D. Robinson, F. Vahedifard, and A. AghaKouchak, "Rainfall-triggered slope instabilities under a changing climate: comparative study using historical and projected precipitation extremes," *Canadian Geotechnical Journal*, vol. 54, no. 1, pp. 117-127, 2017.
- [5] C. W. W. Ng and Q. Shi, "A numerical investigation of the stability of unsaturated soil slopes subjected to transient seepage," *Computers and Geotechnics*, vol. 22, no. 1, pp. 1-28, 1998.
- [6] J. Kim, S. Jeong, S. Park, and J. Sharma, "Influence of rainfall-induced wetting on the stability of slopes in weathered soils," *Engineering Geology*, vol. 75, no. 3-4, pp. 251-262, 2004.
- [7] P. Frattini, G. Crosta, and R. Sosio, "Approaches for defining thresholds and return periods for rainfall-triggered shallow landslides," *Hydrological Processes*, vol. 23, no. 10, pp. 1444-1460, 2009.
- [8] H. An, T. T. Viet, G. Lee et al., "Development of time-variant landslide-prediction software considering three-dimensional subsurface unsaturated flow," *Environmental Modelling and Software*, vol. 85, pp. 172-183, 2006.
- [9] S. G. Evans and J. J. Clague, "Recent climatic change and catastrophic geomorphic processes in mountain environments," *Geomorphology*, vol. 10, no. 1-4, pp. 107-128, 1994.
- [10] V. Jomelli, D. Brunstein, D. Grancher, and P. Pech, "Is the response of hill slope debris flows to recent climate change univocal? A case study in the Massif des Ecrins (French Alps)," *Climatic Change*, vol. 85, no. 1-2, pp. 119-137, 2007.
- [11] L. Laloui, A. Ferrari, and J. Eichenberger, "Effect of climate change on landslide behaviour," *Geo-Strata*, pp. 36-41, October 2010.
- [12] M. Floris, A. D'Alpaos, C. Squarzone, R. Genevois, and M. Marani, "Recent changes in rainfall characteristics and their influence on thresholds for debris flow triggering in the Dolomitic area of Cortina d'Ampezzo, north-eastern Italian Alps," *Natural Hazards and Earth System Sciences*, vol. 10, no. 3, pp. 571-580, 2010.
- [13] L. Schilirò, L. Montrasio, and G. S. Mugnozza, "Prediction of shallow landslide occurrence: validation of a physically-based approach through a real case study," *Science of the Total Environment*, vol. 569-570, pp. 134-144, 2016.
- [14] D. V. Griffiths, J. Huang, and G. A. Fenton, "Probabilistic infinite slope analysis," *Computers and Geotechnics*, vol. 38, no. 4, pp. 577-584, 2011.
- [15] S. Lacasse and F. Nadim, "Uncertainties in characterizing soil properties," in *Uncertainty in the Geologic Environment (GSP 58)*, C. D. Shackelford, P. P. Nelson, and M. J. S. Roth, Eds., pp. 49-75, ASCE, New York, NY, USA, 1996.
- [16] R. Webster and M. A. Oliver, *Geostatistics for Environmental Scientists*, Wiley, Chichester, UK, 2nd edition, 2007.
- [17] S. E. Cho, "Effects of spatial variability of soil properties on slope stability," *Engineering Geology*, vol. 92, no. 3-4, pp. 97-109, 2007.
- [18] D. V. Griffiths, J. Huang, and G. A. Fenton, "Influence of spatial variability on slope reliability using 2-D random fields," *Journal of Geotechnical and Geoenvironmental Engineering*, vol. 135, no. 10, pp. 1367-1378, 2009.
- [19] S. H. Jiang, D. Q. Li, L. M. Zhang, and C. B. Zhou, "Slope reliability analysis considering spatially variable shear strength parameters using a non-intrusive stochastic finite element method," *Engineering Geology*, vol. 168, pp. 120-128, 2014.
- [20] S. E. Cho, "Probabilistic stability analysis of rainfall-induced landslides considering spatial variability of permeability," *Engineering Geology*, vol. 171, pp. 11-20, 2014.
- [21] H. Q. Dou, T. C. Han, X. N. Gong, Z. Y. Qiu, and Z. N. Li, "Effects of the spatial variability of permeability on rainfall-induced landslides," *Engineering Geology*, vol. 192, pp. 92-100, 2015.
- [22] D. Q. Li, X. H. Qi, K. K. Phoon, L. M. Zhang, and C. B. Zhou, "Effect of spatially variable shear strength parameters with

- linearly increasing mean trend on reliability of infinite slopes," *Structural Safety*, vol. 49, pp. 45–55, 2014.
- [23] D. Q. Li, S. H. Jiang, Z. J. Cao, W. Zhou, C. B. Zhou, and L. M. Zhang, "A multiple response-surface method for slope reliability analysis considering spatial variability of soil properties," *Engineering Geology*, vol. 187, pp. 60–72, 2015.
- [24] J. S. Cai, T. C. J. Yeh, E. C. Yan, Y. H. Hao, S. Y. Huang, and J. C. Wen, "Uncertainty of rainfall-induced landslides considering spatial variability of parameters," *Computers and Geotechnics*, vol. 87, pp. 149–162, 2017.
- [25] F. Guzzetti, S. Peruccacci, M. Rossi, and C. P. Stark, "The rainfall intensity–duration control of shallow landslides and debris flows: an update," *Landslides*, vol. 5, no. 1, pp. 3–17, 2008.
- [26] M. Kallache, M. Vrac, P. Naveau, and P. A. Michelangeli, "Nonstationary probabilistic downscaling of extreme precipitation," *Journal of Geophysical Research*, vol. 116, article D05113, 2011.
- [27] M. D. McKay, R. J. Beckman, and W. J. Conover, "A comparison of three methods for selecting values of input variables in analysis of output from a computer code," *Technometrics*, vol. 21, no. 2, pp. 239–245, 1979.
- [28] M. A. Hicks and C. Onisiphorou, "Stochastic evaluation of static liquefaction in a predominantly dilatative sand fill," *Géotechnique*, vol. 55, no. 2, pp. 123–133, 2005.
- [29] E. H. Vanmarcke, *Random Fields: Analysis and Synthesis*, MIT Press, Cambridge, MA, USA, 1983.
- [30] K. K. Phoon and F. H. Kulhawy, "Characterization of geotechnical variability," *Canadian Geotechnical Journal*, vol. 36, no. 4, pp. 612–624, 1999.
- [31] D. J. DeGroot and G. B. Baecher, "Estimating autocovariance of in-situ soil properties," *Journal of Geotechnical and Geoenvironmental Engineering*, vol. 119, no. 1, pp. 147–166, 1993.
- [32] G. A. Fenton, "Estimation for stochastic soil models," *Journal of Geotechnical and Geoenvironmental Engineering*, vol. 125, no. 6, pp. 470–485, 1999.
- [33] G. B. Baecher and J. T. Christian, *Reliability and Statistics in Geotechnical Engineering*, John Wiley & Sons, Hoboken, NJ, USA, 2003.
- [34] M. Uzielli, G. Vannucchi, and K. K. Phoon, "Random field characterisation of stress-normalised cone penetration testing parameters," *Géotechnique*, vol. 55, no. 1, pp. 3–20, 2005.
- [35] B. Sudret and A. Der Kiureghian, "Stochastic finite element methods and reliability: a state-of-the-art report," Tech. Rep. UCB/SEMM-2000/08, Department of Civil and Environmental Engineering, University of California (UC), Berkeley, CA, USA, 2000.
- [36] P. D. Spanos and R. G. Ghanem, "Stochastic finite element expansion for random media," *Journal of Engineering Mechanics*, vol. 115, no. 5, pp. 1035–1053, 1989.
- [37] D. Zhang and Z. Lu, "An efficient, high-order perturbation approach for flow in random porous media via Karhunen-Loeve and polynomial expansions," *Journal of Computational Physics*, vol. 194, no. 2, pp. 773–794, 2004.
- [38] J. Brejda, J. Moorman, T. B. Smith, J. L. Karlen, D. L. Allan, and T. H. Dao, "Distribution and variability of surface soil properties at a regional scale," *Soil Science Society of America Journal*, vol. 64, no. 3, pp. 974–982, 2000.
- [39] G. A. Fenton and D. V. Griffiths, "Bearing capacity prediction of spatially random  $c$ - $\phi$  soils," *Canadian Geotechnical Journal*, vol. 40, no. 1, pp. 54–65, 2003.
- [40] S. E. Cho and S. R. Lee, "Instability of unsaturated soil slopes due to infiltration," *Computers and Geotechnics*, vol. 28, no. 3, pp. 185–208, 2001.
- [41] W. H. Green and C. A. Ampt, "Studies on soil physics, part 1, the flow of air and water through soils," *Journal of Agricultural Science*, vol. 4, pp. 1–24, 1911.
- [42] Z. Chen, R. S. Govindaraju, and M. L. Kavvas, "Spatial averaging of unsaturated flow equations under infiltration conditions over areally heterogeneous fields: 1. Development of models," *Water Resources Research*, vol. 30, no. 2, pp. 523–533, 1994.
- [43] R. S. Govindaraju, C. Corradini, and R. Morbidelli, "A semi-analytical model of expected areal-average infiltration under spatial heterogeneity of rainfall and soil saturated hydraulic conductivity," *Journal of Hydrology*, vol. 316, no. 1–4, pp. 184–194, 2006.
- [44] X. Chu and M. A. Marino, "Determination of ponding condition and infiltration into layered soils under unsteady rainfall," *Journal of Hydrology*, vol. 313, no. 3–4, pp. 195–207, 2005.
- [45] D. G. Fredlund and H. Rahardjo, *Soil Mechanics for Unsaturated Soils*, John Wiley & Sons, New York, NY, USA, 1993.
- [46] D. G. Fredlund, N. R. Morgenstern, and R. A. Widger, "The shear strength of unsaturated soils," *Canadian Geotechnical Journal*, vol. 15, no. 3, pp. 313–321, 1978.
- [47] M. T. van Genuchten, "Closed-form equation for predicting the hydraulic conductivity of unsaturated soils," *Soil Science Society of America Journal*, vol. 44, no. 5, pp. 892–898, 1980.
- [48] M. H. Loke and R. D. Barker, "Least-squares deconvolution of apparent resistivity pseudosections," *Geophysics*, vol. 60, no. 6, pp. 1682–1690, 1995.
- [49] A. Samouëlian, I. Cousin, A. Tabbagh, A. Bruand, and G. Richard, "Electrical resistivity survey in soil science: a review," *Soil and Tillage Research*, vol. 83, no. 2, pp. 173–193, 2005.

## Research Article

# Beneficial and Detrimental Effects of Soil-Structure Interaction on Probabilistic Seismic Hazard and Risk of Nuclear Power Plant

Shinyoung Kwag,<sup>1</sup> BuSeog Ju ,<sup>2</sup> and Wooyoung Jung <sup>3</sup>

<sup>1</sup>Korea Atomic Energy Research Institute, Daejeon, Republic of Korea

<sup>2</sup>Department of Civil Engineering, Kyung Hee University, Yongin, Gyeonggi 17104, Republic of Korea

<sup>3</sup>Department of Civil Engineering, Gangneung-Wonju National University, Gangneung, Republic of Korea

Correspondence should be addressed to BuSeog Ju; [bju2@khu.ac.kr](mailto:bju2@khu.ac.kr)

Received 9 April 2018; Revised 14 May 2018; Accepted 4 June 2018; Published 3 July 2018

Academic Editor: Lars Abrahamczyk

Copyright © 2018 Shinyoung Kwag et al. This is an open access article distributed under the Creative Commons Attribution License, which permits unrestricted use, distribution, and reproduction in any medium, provided the original work is properly cited.

The purpose of this study is to investigate the soil-structure interaction (SSI) effect on the overall risk of a PWR containment building structure with respect to two failure modes: strength and displacement. The precise quantification of the risk within the seismic probabilistic risk assessment framework depends considerably on an accurate treatment of the seismic response analysis. The SSI effect is one of the critical factors to consider when accurately predicting structural responses in the event of an earthquake. Previous studies have been conducted by focusing more on the positive side of the SSI effects and the effects mainly on the seismic fragility result. Therefore, this paper presents the results of a study of the SSI effect on the overall risk. Also, the study relies on an emphasis on revealing a beneficial and a detrimental effect of the SSI by utilizing an example of the containment structure in three soil conditions and two main failure modes. As a result, the consideration of SSI shows a complete conflicting effect on the seismic fragility and risk results depending on two failure modes considered in this study. This has a positive effect regarding the strength failure mode, but this brings a negative effect regarding the displacement failure mode. The risk fluctuation width is particularly noticeable in the site having a considerable change in seismic hazard information such as Los Angeles on the western site of the US. Such results can be expected to be utilized in a future study for investigating the pros and cons of the SSI effect associated with various failure modes in diverse conditions.

## 1. Introduction

Historically, strong earthquakes are not uncommon near the current sites of nuclear power plants. Examples include but are not limited to the 1811-1812 New Madrid earthquake, the 1886 Charleston earthquake, and the 1994 Northridge earthquake in the US. The 2011 Tohoku earthquake occurred in Japan, and the subsequent accident at the Fukushima Daiichi nuclear power plants demonstrated the need to explore scenarios in which the possible seismic hazard exceeds the design basis earthquake levels. Accordingly, this accident has motivated nuclear regulatory organizations to reassess the safety of nuclear facilities and evaluate the seismic margins and risk levels of such facilities in the US, EU, and Korea [1–3]. Such a situation once again sheds new

light on the importance of seismic margin assessment (SMA) [4, 5] and seismic probabilistic risk assessment (SPRA) [6–9] practices after the individual plant examination of external events (IPEEE) for severe accidents [10]. The SMA is intended to estimate how much margin exists at a plant above a design basis earthquake event based on the seismic fragility information of major systems, structures, and components. The SPRA is a more complete framework than the SMA because it integrates the seismic fragility data and seismic hazard information. One factor in common regarding the two methodologies is that they rely fundamentally on an accurate seismic response analysis as part of a fragility evaluation [11].

The seismic responses of structures, as the basic seismic fragility analysis data, are greatly affected not only by the

dynamic characteristics of the structures but also by the supporting soil stratum. The seismic responses accounting for the supporting soil deposits form the end result of the earthquake source, the travel path effects, the local site effects, and the soil-structure interaction (SSI) effect [12]. The result of the first three of these factors is the free-field ground motion. The structural responses with regard to the free-field motion are influenced by the SSI effect. Thus, an accurate assessment of the seismic performance of a structure requires the appropriate estimation of the free-field motion acting on the foundation of the structure and a proper consideration of the SSI effect. There remains controversy regarding the role of SSI in the seismic performance of structures embedded in soft soil. Traditionally, taking into account the SSI effect has been considered as a beneficial factor in the seismic response [13]. The beneficial effect emerges with reductions in the internal force and drift in the structure as the soft soil in the entire soil-structure system causes an increased structural period owing to its flexibility and plays a significant role in amplifying the energy dissipation effect in the response.

However, the reality occasionally differs from the positive perspective of the SSI effect. It should be considered that the SSI can have a detrimental effect on a flexible secondary system attached to the primary soil-structure system because it filters out high-frequency contents but amplifies the low-frequency contents of motions in the secondary system. In addition, because the soft soil at the bottom of the structure serves as a flexible pad, it can bring about excessive displacement in the structure. This phenomenon has a negative impact on closely connected structures, for example, a nuclear power plant, by causing adjacent structures consisting of the nuclear power plant to crash into one another. In this context, the USNRC has increased the soil-condition acceptance criterion which can neglect the SSI effect. For structures founded on soils having a shear-wave velocity in a range between 1,070 m/s and 2,440 m/s under the entire surface of the foundation, a fixed-base assumption cannot be acceptable to the regulatory body, any more. This is because the USNRC modified such a limit criterion from 1,070 m/s to 2,440 m/s in the Standard Review Plan (SRP) 3.7.2. This indicates that the structure having the soil which has less than 2,440 m/s of shear-wave velocity cannot be regarded as a model supported in the fixed-base condition. This enhanced criterion is a result reflecting the outcome of current research works in which the soil originally considered as relatively stiff (i.e., 1,070 m/s–2,440 m/s) can possibly influence the structure responses, quite a lot [14].

The research exploring the SSI effects on the responses and probabilistic seismic vulnerabilities of the structure has been actively studied recently [15–17]. Especially, such studies were subsequently extended into such SSI studies on nuclear power plants (NPPs). The common features of these current studies have focused on the NPP containment building structure and attempted to associate the SSI effect with a seismic fragility analysis of the NPP [18, 19]. In addition, these studies were restricted to the positive effects of the SSI and focused on the SSI effect only on the seismic fragility information [20–23]. Given these circumstances,

the purpose of this study is to investigate both the positive and negative SSI roles and their effects on the fragility and total risk results related to the containment structure.

Specifically, this paper initially introduces the probabilistic seismic hazard analysis and seismic fragility analysis methodologies within the SPRA framework. The seismic fragility analyses are implemented via the factor of the safety method and the statistical approach of maximum likelihood estimation. In order to quantify the SSI effect from a total risk perspective, the seismic responses of a pressurized water reactor (PWR) containment building structure in three soil conditions, that is, fixed, hard, and soft, are analyzed, and then, these are utilized for the basic information in the SPRA. Two main failure modes, strength and displacement, are taken into account in the risk estimation. Finally, the beneficial and detrimental effects of the SSI on the risk outcomes are quantified, and the results are discussed.

## 2. Probabilistic Seismic Hazard Analysis

A probabilistic seismic hazard analysis (PSHA) is intended to conduct for exploring the potential intensity of an earthquake and what level of ground motions can be expected under uncertainties. Such uncertainties include the *aleatory* one inherent in the earthquake itself and the *epistemic* one in the associated earthquake modeling. Technically, the PSHA sets the goal of quantifying uncertainties about the sources, size, distance, and ground motion of future earthquakes, as well as integrating them to produce an explicit description of the distribution of how large ground motions can occur at a site of interest. Typically, the final output of the PSHA is represented by seismic hazard curves, where the annual rates of exceedance ( $\lambda$ ) are plotted against a seismic hazard intensity parameter.

A conceptual image of the five key steps in the PSHA is shown in Figure 1. A detailed explanation and a description of the PSHA are described in a publication by McGuire [24].

For the purpose of a structural risk assessment, Cornell et al. [25] proposed the following approximated hazard curve equation:

$$H(\text{PGA}) = k_0 \text{PGA}^{-k}, \quad (1)$$

where the terms  $k_0$  and  $k$  are constant parameters. Equation (1) describes a linear relationship on a log-log plot. Typical values of the log-log slope  $k$  are known to be from 1 to 4, and this is steeper at the western US sites than at the eastern US sites. The specific values of  $k$  and  $k_0$  can be identified according to the hazard information and the appropriate regression analysis. Specifically, the values of  $k$  and  $k_0$  are usually fitted to well represent the seismic hazard information at design basis earthquake (DBE) and maximum considered earthquake (MCE) intensity levels which have 10% ( $\lambda = 0.0021 \text{ yr}^{-1}$  meaning the mean return period  $T = 475 \text{ yr}$ ) and 2% probabilities of exceedance in 50 years ( $\lambda = 4.04e-4 \text{ yr}^{-1}$ ;  $T = 2475 \text{ yr}$ ) by using the appropriate regression analysis. Due to this characteristic, this equation tends to overpredict the seismic hazard information out of these ranges since the shape of the hazard curve typically has

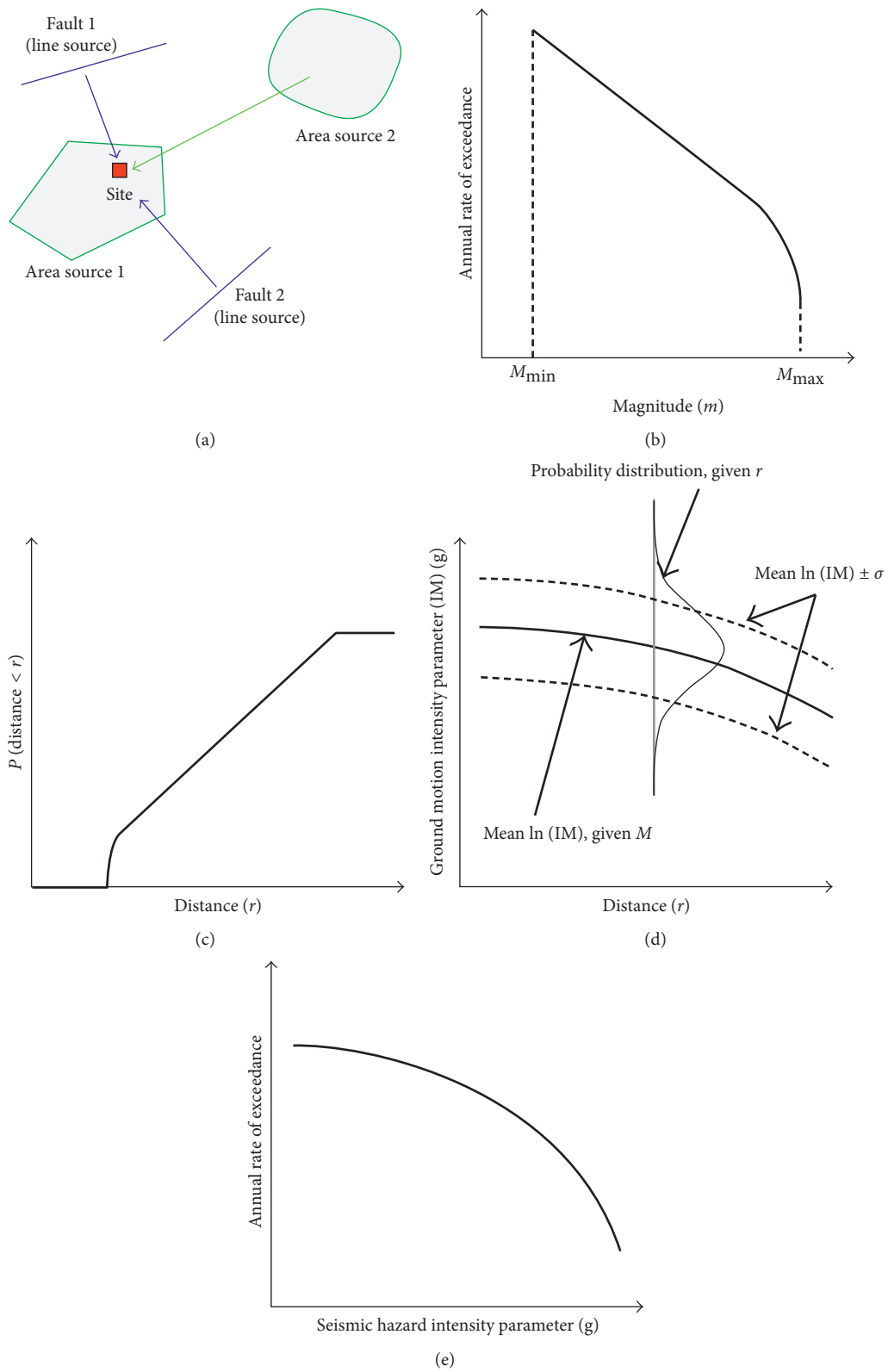


FIGURE 1: Conceptual image of the five key steps in a PSHA: (a) Step 1: identify the earthquake sources; (b) Step 2: define the distribution of the earthquake magnitude; (c) Step 3: define the distribution of earthquake distances; (d) Step 4: set the ground motion prediction model; (e) Step 5: annual rate of exceeding the seismic hazard intensity as determined by combining steps 1-4.

a “concave from below” global shape in the log-log scale [26]. But, in other words, because it is conservatively capable of estimating the seismic hazard, it can be quite useful to evaluate risks on the important structural systems such as nuclear power plants and high-rise buildings which highly demand a conservative risk evaluation.

### 3. Fragility Analysis

A seismic fragility analysis is done to determine the relationship between the seismic intensity parameter of an earthquake (PGA in this study) and the corresponding probability of a failure. Specifically, the seismic fragility of a structure, system, and component (SSC) is defined as the conditional failure probability to attain or exceed a specified performance function,  $G$ , under the given measure of the PGA. It can be stated as follows:

$$P_f = P(G < 0 \mid \text{PGA}), \quad (2)$$

where  $G$  is a function of the random variables representing the uncertainties of the material properties, modeling, and loading conditions of an SSC. This can be described in a very simplistic form as follows:

$$G = C - D, \quad (3)$$

where  $C$  denotes the “capacity” of the SSC corresponding to the specified loading condition and  $D$  represents the response “demand” corresponding to the given hazard intensity parameter. The capacity  $C$  is usually a representative value determined by the material properties, yield stress, ultimate stress, and other factors based on the design codes and standards. The response demand  $D$  is the structural response, as obtained from analyses considering numerical models, earthquake time histories, damping, frequency, coupling, soil-structure interaction, and other related factors, or experimental data, or field observation.

Various methods have been proposed for the fragility analysis of an SSC especially under the seismic intensity of an earthquake hazard based on empirical, experimental, and/or numerical simulation data. These can be broadly grouped according to the following classifications:

- (1) Factor of the safety method [9, 27–30]
- (2) Statistical inference approaches: maximum likelihood estimation (MLE) [31–33] and Bayesian approach [34–43]
- (3) Random vibration approach [44, 45]
- (4) Approaches based on Monte Carlo simulation [11, 46, 47]
- (5) Reliability-based method [48].

In this study, the factor of the safety method and the MLE-based statistical approach are utilized to evaluate the fragility curve of the NPP containment structure for a case study. The main reasons why we use these methods are as follows: (1) the factor of the safety method is simple and

appropriate for the strength-related fragility evaluations; (2) the MLE-based approach makes it possible to create the fragility curve with respect to the displacement-based performance limit; and (3) specifically, the strength failure is more like the stress-based limit problem, so this feature is easily implemented in a factor of the safety method setting. The displacement failure is close to the result of seismic performance; hence, this can be realized through a statistical approach based on the nonlinear seismic analysis results.

**3.1. Factor of the Safety Method.** The most widely adopted method to evaluate seismic fragilities is that proposed by Kennedy et al. [27]. In this method, the fragility is represented by a set of curves that express the probability of a failure versus ground motion levels at different confidence levels. This means that the seismic fragility illustrates the probabilistic capability of an SSC against ground motion causing structural damage. The probability of a failure of an SSC,  $P_f(\text{PGA})$ , at any nonexceedance probability level,  $Q$ , can be obtained from the following equation [28]:

$$P_f(\text{PGA}) = \Phi\left(\frac{\ln(\text{PGA}/A_m) + \beta_U \Phi^{-1}(Q)}{\beta_R}\right), \quad (4)$$

where  $\Phi(\cdot)$  is the standard Gaussian cumulative distribution function,  $A_m$  is the median seismic capacity,  $\Phi^{-1}(\cdot)$  is the inverse of the standard Gaussian cumulative distribution function, and  $\beta_R$  and  $\beta_U$  are the lognormal standard deviations. The two logarithmic standard deviations represent different types of uncertainties.  $\beta_R$ , referred to as the *aleatory* uncertainty, is a deviation of the inherent randomness which cannot be reduced by increasing knowledge.  $\beta_U$ , also known as the *epistemic* uncertainty, is a deviation of the uncertainty which represents a lack of complete knowledge.

The fragility parameters mentioned above are evaluated using an intermediate random variable termed “the factor of safety” [29]. The medium seismic capacity  $A_m$  is defined by (5). Here,  $A_{\text{DBE}}$  denotes the PGA values related to the design basis earthquake. The factor of safety  $F$  is defined in (6).  $F$  is expressed as a product of the capacity factor  $F_C$  and the response factor  $F_{\text{RS}}$ .  $F_C$  can be computed as a product of the strength factor  $F_S$ , which is represented as the ratio of the ultimate strength to the design-code-allowable stress level, and the inelastic energy absorption factor  $F_\mu$  in (7). In (8), the response factor  $F_{\text{RS}}$  can be computed as a product of the spectral shape factor  $F_{\text{SA}}$ , the damping factor  $F_\delta$ , the modeling factor  $F_M$ , the mode combination factor  $F_{\text{MC}}$ , the earthquake component factor  $F_{\text{EC}}$ , a factor which reflects the reduction of the seismic input with the depth  $F_{\text{SD}}$ , and a factor to account for the effect of the SSI  $F_{\text{SS}}$ . The logarithmic standard deviation of the factor of safety for the inherent randomness and knowledge uncertainty can be obtained by the square root of the sum of the squares of the individual logarithmic standard deviation of the capacity and response factors in (9) and (10). The subscript  $i$  in (9)

and (10) denotes the individual capacity and response factors in (7) and (8):

$$A_m = F \cdot A_{DBE}, \quad (5)$$

$$F = \frac{\text{actual seismic capacity of the component}}{\text{actual response due to DBE}} = F_C F_{RS}, \quad (6)$$

$$F_C = F_S \cdot F_\mu, \quad (7)$$

$$F_{RS} = F_{SA} \cdot F_\delta \cdot F_M \cdot F_{MC} \cdot F_{EC} \cdot F_{SD} \cdot F_{SS}, \quad (8)$$

$$\beta_R = \left( \sum \beta_{R_i}^2 \right)^{1/2}, \quad (9)$$

$$\beta_U = \left( \sum \beta_{U_i}^2 \right)^{1/2}. \quad (10)$$

The family of the fragility curves is usually expressed by a 95% confidence level fragility curve, a 50% confidence level fragility curve meaning the median curve, a 5% confidence level fragility curve using (4), and a mean fragility curve using the following equation:

$$P_f(\text{PGA}) = \Phi \left[ \frac{\ln(\text{PGA}/A_m)}{\sqrt{\beta_R^2 + \beta_U^2}} \right]. \quad (11)$$

The method typically depends on data from past studies and expert judgment regarding most factors, except for site-dependent factors. This study focuses on  $F_{SS}$  to investigate the effect of the SSI on the fragility and risk results.

**3.2. Statistical Inference Approach: Maximum Likelihood Estimation.** Without accounting for the *epistemic* uncertainty in the expression of (4), the fragility curve expression becomes

$$P_f(\text{PGA}) = \Phi \left[ \frac{\ln(\text{PGA}) - \ln(A_m)}{\beta_R} \right]. \quad (12)$$

Given discrete data from numerical simulations, experimental data, and field observations, the parameters of  $A_m$  and  $\beta_R$  can be identified by utilizing a statistical inference approach. This study adopts the maximum likelihood estimation- (MLE-) based statistical approach in order to determine the two parameters  $A_m$  and  $\beta_R$  in (12) by fitting the two parameters with the results from numerical simulation data.

The numerical simulation generates some number of failures out of a total number of ground motions at each PGA level. If assuming that the observation of a failure from each ground motion is independent of the observations from other ground motions, the probability of observing  $m_i$  failures out of  $n_i$  ground motions with  $\text{PGA} = x_i$  is given by the binomial distribution:

$$P(m_i \text{ failures in } n_i \text{ ground motions}) = \binom{n_i}{m_i} p_{f,i}^{m_i} \times (1 - p_{f,i})^{n_i - m_i}, \quad (13)$$

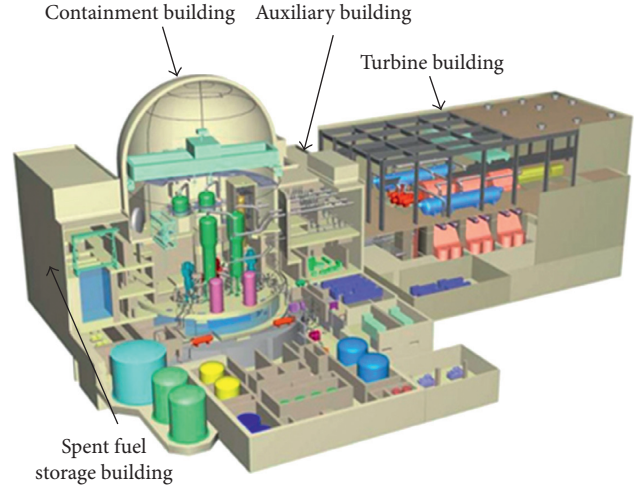


FIGURE 2: PWR nuclear power plant (KHNP).

where  $p_{f,i}$  denotes the probability that a ground motion with  $\text{PGA} = x_i$  will cause a failure of the structure according to (12). The MLE approach identifies the parameters of the fragility function of (12) which give the highest probability of having the observed failure data as obtained from the numerical simulation. If we have simulation data at multiple PGA levels, we take the product of the binomial probabilities of (13) at each PGA level to acquire the likelihood function  $L$  for all data sets:

$$L = \prod_{i=1}^j \binom{n_i}{m_i} p_{f,i}^{m_i} (1 - p_{f,i})^{n_i - m_i}, \quad (14)$$

where  $j$  is the number of PGA levels and  $\Pi$  denotes a product over all levels. Estimates of the two parameters are made by maximizing this likelihood function. Since it is easier to maximize the natural log of the likelihood function of (14), the numerical representation to find the optimal  $A_m$  and  $\beta_R$  is formulated as follows:

$$\arg \max_{A_m, \beta_R} \ln \left( \prod_{i=1}^k \binom{n_i}{m_i} p_{f,i}^{m_i} (1 - p_{f,i})^{n_i - m_i} \right). \quad (15)$$

The computation for solving (15) can be performed by implementing an appropriate optimization scheme. The MLE approach introduced in this section is applied to the structure in a case study to evaluate the seismic fragility regarding the displacement performance limit based upon the simulation data considering the SSI effect.

## 4. Case Study

A typical PWR NPP primarily consists of a containment building, an auxiliary building, a turbine building, and a spent fuel storage building. Figure 2 shows an advanced power reactor of a Korean NPP as an example. In this study, in order to show the SSI effect on the seismic fragility and risk of the NPP, the containment building structure is considered as an example structure. The NPP containment building is a cylindrical and prestressed reinforced concrete

structure that houses the nuclear reactor and various types of safety-related equipment.

The methods for the analysis of SSI can be mainly divided into two categories: direct approach and multistep approach (also called the substructure approach) [49]. Any of the two methods can be acknowledged by the regulatory organization (refer to SRP 3.7.2 of the USNRC) when analyzing the SSI problems. In the direct approach, the overall soil-foundation-structure system is modeled and analyzed in a single stage. The input motions are specified along soil boundaries. The use of the direct approach has a strong point to consider the SSI problem in one step and thus to easily deal with the nonlinearities of the soil and structure at the same time. But such an approach demands a large computational power to treat the nonlinear behavior of both the soil and structure simultaneously. In the multistep approach, it uses the principle of superposition to separate two major causes of the SSI: soil amplification effect (site response analysis) and the effect of the dynamic responses of the structure-foundation system on the movement of the supporting soil (seismic response analysis on the structure-foundation system). Due to these characteristics of the multistep approach, it should basically treat the problems as linear or equivalent linear. But it has some merits to relatively reduce the computational cost and also to aid in dividing and analyzing the two SSI effects separately. Given these pros and cons regarding the two approaches, the multistep approach is basically adopted in this study due to the need of multiple SSI analyses to achieve the probabilistic characteristic such as seismic fragility information, but within the structure-foundation response analysis domain, the nonlinearities of the structure are also taken into account. Specifically, the site response analyses are conducted by utilizing an equivalent linear analysis program like SHAKE [50], and the inelastic time-history analyses are performed using the MIDAS GEN [51] program to obtain the nonlinear responses of the structure. The purpose of the site response analysis is to investigate the soil/site amplification phenomenon at the surface due to the flexibility of soil strata. The results of the site response analyses are utilized as input earthquake motions to the soil-structure model in the MIDAS GEN. The detailed descriptions are represented in the following sections.

#### 4.1. Structure Model and Soil Profile

**4.1.1. Structure Model.** The selected containment building structure has a height of approximately 66 m, an outside diameter of about 40 m, a total mass of approximately 29,000 tons, and a fundamental frequency of 3.61 Hz. For efficient dynamic time-history analyses, the lumped-mass stick model of the building derived by calculating the point mass, area, effective shear area, moment of inertia, and other factors for a real shape is used. This model is essentially composed of a containment shell of prestressed concrete and an internal structure of reinforced concrete. For more complete information about the model, a previous study can be referred [52]. In contrast to the previous work, in this study, the stick (beam) element is defined as a nonlinear inelastic element in terms of the Takeda-type trilinear model

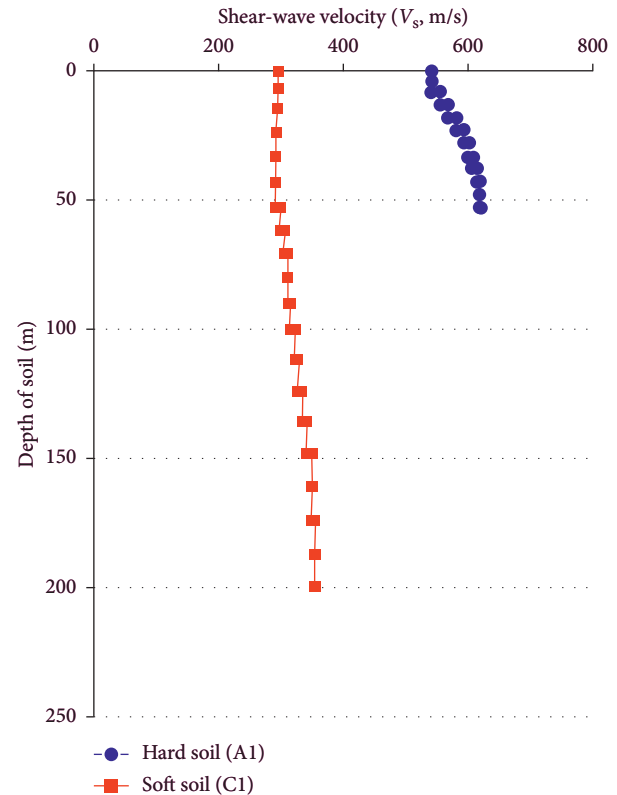


FIGURE 3: Soil profile: A1 and C1 conditions.

to describe the shear behavior of the containment building as it experiences the nonlinearity under strong-intensity ground motion. The curve for representing the nonlinear relationship between the shear stress and strain is determined according to the available technical guidelines [53].

**4.1.2. Soil Profile.** In the standard System 80+ design [54] with respect to the AP1000 and APR1400 models, the soil profiles are categorized mainly into conditions: A (A1), B (B1/B2/B3/B4), and C (C1/C2/C3). In the present study, soil conditions A1 and C1 are selected in order to represent hard and soft soil strata, respectively. Figure 3 shows and compares the shear-wave velocity ( $V_s$ ) of the two soil conditions of A1 and C1 along the depth. The corresponding soil layers and properties of A1 and C1 are summarized in Tables 1 and 2. The additional detailed information on the soil properties is represented in the standard system 80+ design [54].

**4.2. Seismic Excitation.** It is recommended that the site-specific earthquake ground motion be utilized for a design earthquake loading according to USNRC RG 1.208 [55]. However, in the site where the observed site-specific earthquake ground motions are rare, the design ground response spectrum (DGRS) defined by USNRC RG 1.60 [56] has been still utilized as a basic spectral shape for the earthquake loading in nuclear power plant design. The fundamental assumption behind this practice is that the DGRS is considered to well represent the rock-site response spectra. Such an assumption is reasonable and conservative because the

TABLE 1: Soil layers and properties of the condition A1.

Layer	Thickness (m)	$V_S$ (m/s)	$V_P$ (m/s)	Damping ratio for S-wave	Damping ratio for P-wave
1	1.22	541	1325	0.005	0.002
2	1.22	555	1359	0.009	0.003
3	1.52	568	1390	0.012	0.004
4	1.52	582	1426	0.013	0.004
5	1.52	594	1455	0.016	0.005
6	1.52	602	1475	0.018	0.006
7	1.52	608	1490	0.019	0.006
8	1.52	614	1504	0.021	0.007
9	1.52	617	1511	0.022	0.007
10	1.52	618	1515	0.024	0.008
11	1.52	618	1515	0.025	0.008
Base rock		1524	2489		

TABLE 2: Soil layers and properties of the condition C1.

Layer number	Thickness (m)	$V_S$ (m/s)	$V_P$ (m/s)	Damping ratio for S-wave	Damping ratio for P-wave
1	2.13	296	724	0.013	0.004
2	2.44	293	718	0.025	0.008
3	2.74	292	716	0.034	0.011
4	2.74	291	714	0.042	0.014
5	3.05	292	716	0.047	0.016
6	3.05	300	734	0.050	0.017
7	2.74	305	746	0.052	0.017
8	2.74	308	755	0.057	0.019
9	2.74	312	764	0.060	0.020
10	3.05	315	772	0.063	0.021
11	3.05	322	789	0.064	0.021
12	3.66	327	802	0.065	0.022
13	3.66	334	818	0.065	0.022
14	3.66	341	835	0.065	0.022
15	3.66	349	856	0.064	0.021
16	3.96	349	856	0.066	0.022
17	3.96	354	868	0.066	0.022
18	3.96	355	869	0.067	0.022
19	3.96	354	867	0.068	0.023
Base rock		1524	2489		

DGRS is utilized for the seismic design and risk assessment in nuclear plants. Hence, because this research does not focus on a specific site for design purposes but on the SSI effect according to uncertainties in the soil properties, probable earthquake ground motions are selected by taking various earthquake magnitudes, distances, intensity levels, and other measures into account. In addition, such earthquake ground motions are selected such that the overall response spectral shape of the selected ground motions follows the DGRS shape. Table 3 shows twenty sets of selected earthquake ground motions from the Pacific Earthquake Engineering Research (PEER) Center (URL: <http://peer.berkeley.edu/nga/>). Figure 4 plots the response spectra obtained from the seismic response analysis results of a 5% damped linear-elastic single-degree-of-freedom (SDOF) model subjected to each earthquake ground motion normalized to the PGA of 1g, in this case the mean response spectrum and the mean-plus-one-standard-deviation response spectrum.

**4.3. Site Response Analysis.** The soil deposit alters the ground surface motion compared to the original earthquake

motions occurring in bedrock. This is attributed to the fact that the seismic waves travel through the soil stratum, and accordingly, the soil plays a significant role in determining the characteristics of the ground surface motion. The influence of the local soil conditions on the earthquake motion can be quantified via a site response analysis. In this regard, site response analyses are performed for the A1 and C1 soil conditions, and these determine the input foundation motions to the NPP containment building structure. This study assumes the earthquake ground motions introduced in Section 4.2 as the motions occurring in the bedrock. The analyses are run on the assumption that the soil deposit is horizontally layered over a half space of rock, and the principle of one-dimensional propagation of seismic waves in a vertical direction is applied. Figure 5 shows the mean response spectra of the 5% damped linear-elastic SDOF model subjected to foundation input motions as determined from the site response analyses using 20 sets of earthquake ground motions (normalized to a PGA of 1g) as introduced in Section 4.2. This compares the mean response spectra of the bedrock, hard soil, and soft soil conditions. It is found

TABLE 3: Selected earthquake ground motions.

Number	Name	Year	Station name	*M	*Dis.	PGA (g)
1	Imperial Valley-06	1979	El Centro Array #5	6.53	3.95	0.375
2	Imperial Valley-06	1979	El Centro Array #6	6.53	1.35	0.442
3	Loma Prieta	1989	Gilroy-Gavilan College	6.93	9.96	0.294
4	Northridge-01	1994	Jensen Filter Plant	6.69	5.43	0.518
5	Northridge-01	1994	Sylmar Converter Station	6.69	5.35	0.594
6	Kobe, Japan	1995	KJMA	6.90	0.96	0.854
7	Kobe, Japan	1995	Takarazuka	6.90	0.27	0.645
8	Kocaeli, Turkey	1999	Gebze	7.51	10.92	0.241
9	Chi-Chi, Taiwan	1999	TCU052	7.62	0.66	0.375
10	Chi-Chi, Taiwan	1999	TCU068	7.62	0.32	0.564
11	Borrego Mtn	1968	San Onofre (South Carolina Edison)	6.63	129.1	0.045
12	Hector Mine	1999	Heart Bar State Park	7.13	61.21	0.070
13	Kern County	1952	LA-Hollywood Stor FF	7.36	114.6	0.058
14	Kocaeli, Turkey	1999	Botas	7.51	126	0.089
15	Lytle Creek	1970	Castaic (Old Ridge Route)	5.33	103.4	0.026
16	Anza-02	2001	San Jacinto CDF Fire Station 25	4.92	51.3	0.054
17	San Fernando	1971	Hemet Fire Station	6.61	139.1	0.047
18	Landers	1992	Yermo Fire Station	7.28	23.62	0.222
19	Denali, Alaska	2002	Carlo (temp)	7.9	50.94	0.087
20	Duzce, Turkey	1999	Mudurnu	7.14	34.3	0.114

\*Dis.: closest distance to a fault rupture (km); \*M: magnitude.

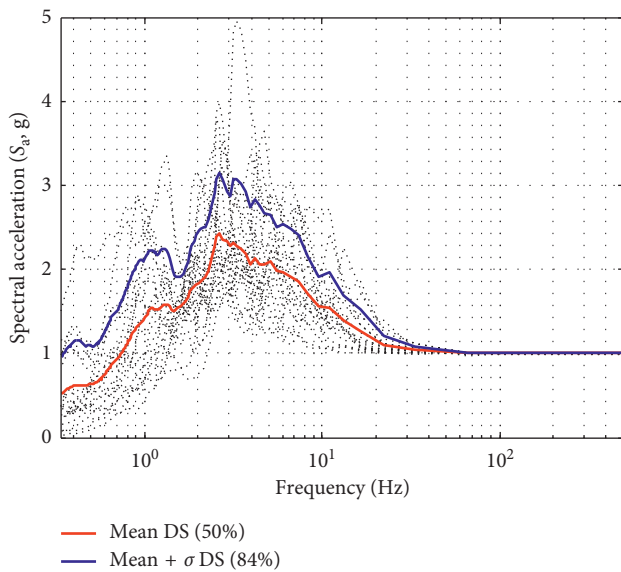


FIGURE 4: Response spectra under earthquake ground motions normalized to a PGA of 1.0 g.

that the motions in soft soil are more amplified than those in the hard soil and bedrock conditions. Specifically, the soft soil amplified the spectral accelerations over all frequencies, and the amplification was prominent in 1-2 Hz and 3-5 Hz. Such an observation comes from the fact that the fundamental frequency of the soft soil-structure system is shifted due to the increased flexibility of the soil. However, the hard soil did not make the site responses amplified relatively. Especially, the hard soil did not change the spectral acceleration in below 1.5 Hz at all. The reason for this is that the hard soil having the shear-wave velocity of about 600 m/s does not change the main dynamic characteristic of the

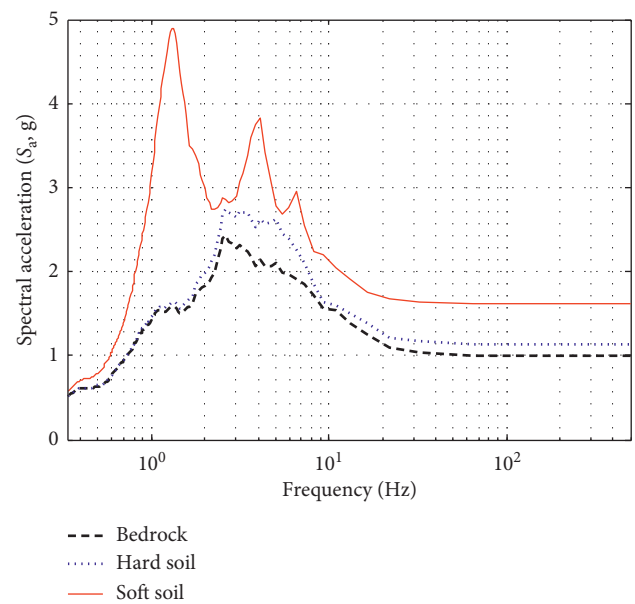


FIGURE 5: Mean response spectra obtained from site response analyses in bedrock, hard soil, and soft soil conditions.

structure, but relatively softer characteristics than the bed rock bring the amplification to the overall responses in the range greater than 1.5 Hz.

**4.4. Seismic Response Analysis.** A sufficiently accurate consideration of soil behavior can be obtained if the soil stiffness and damping coefficients of a circular massless foundation on the soil stratum are evaluated by the frequency independent expression. The stiffness and damping coefficients of the soil stratum are defined by

TABLE 4: Average soil dynamic properties of the different soil cases A1 and C1.

Properties of soil	Soil cases	
	Hard A1	Soft C1
Bulk modulus, $G$ (Pa)	3.2704e+009	2.1150e+008
Horizontal stiffness of the soil stratum, $K_h$ (N/m)	3.1349e+011	2.0273e+010
Rocking stiffness of the soil stratum, $K_r$ (N/m)	1.0418e+014	6.7375e+012
Vertical stiffness of the soil stratum, $K_v$ (N/m)	3.9186e+011	2.5342e+010
Horizontal damping coefficient, $C_h$ (Ns/m)	2.8167e+009	7.1629e+008
Rocking damping coefficient, $C_r$ (Ns/m)	2.4419e+011	6.2099e+010
Vertical damping coefficient, $C_v$ (Ns/m)	5.2047e+009	1.3236e+009

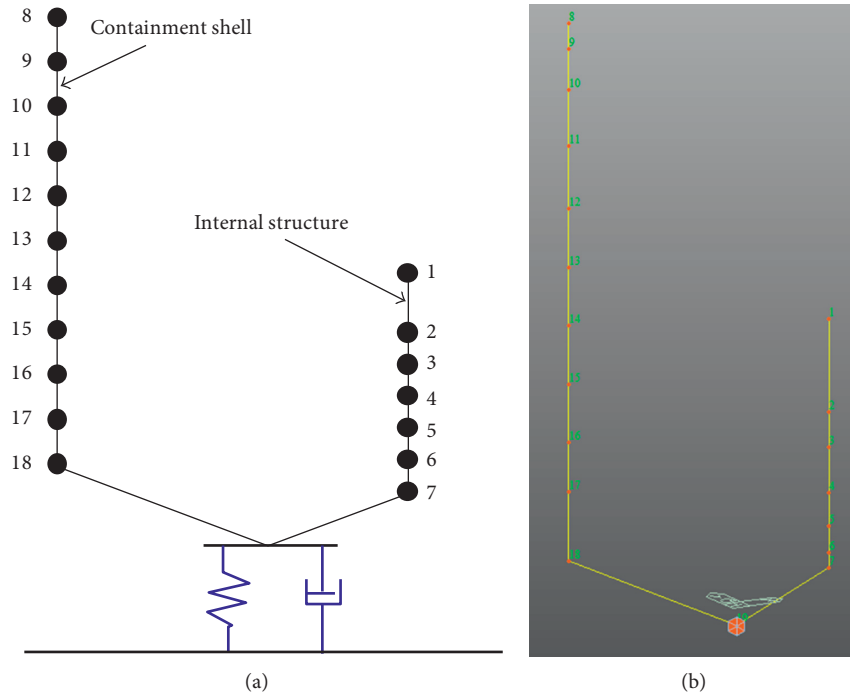


FIGURE 6: Lumped-mass stick model for the NPP containment building: (a) conceptual model; (b) numerical model in MIDAS GEN.

$$\begin{aligned}
 K_h &= \frac{8GR}{2-\nu}, \\
 K_r &= \frac{8GR^3}{3(1-\nu)}, \\
 K_v &= \frac{4GR}{1-\nu}, \\
 C_h &= \frac{4.6GR^2}{(2-\nu)V_s}, \\
 C_r &= \frac{0.4GR^4}{(1-\nu)V_s}, \\
 C_v &= \frac{3.4R^2}{1-\nu} \sqrt{G\rho},
 \end{aligned} \tag{16}$$

where  $K_h$ ,  $K_r$ , and  $K_v$  represent the horizontal, rocking, and vertical stiffness of the soil stratum, respectively;  $C_h$ ,  $C_r$ , and  $C_v$  represent the horizontal, rocking, and vertical viscous damping coefficients for the radiation soil damping, respectively;  $G$  is the soil shear modulus;  $V_s$  is the shear-wave velocity of the soil;  $R$  is the radius of circular footing;  $\nu$  is Poisson's ratio of the soil; and  $\rho$  is the density of the soil. The average shear-wave velocity representing the various soil layers can be computed as follows:

$$V_s = \frac{\sum_{i=1}^n d_i}{\sum_{i=1}^n (d_i/V_{si})}, \tag{17}$$

where  $d_i$  is the thickness of the soil layer,  $V_{si}$  is the shear-wave velocity of the corresponding soil layer, and  $n$  is the number of the soil layers. Table 4 represents the average soil dynamic properties of the two different soil cases A1 and C1.

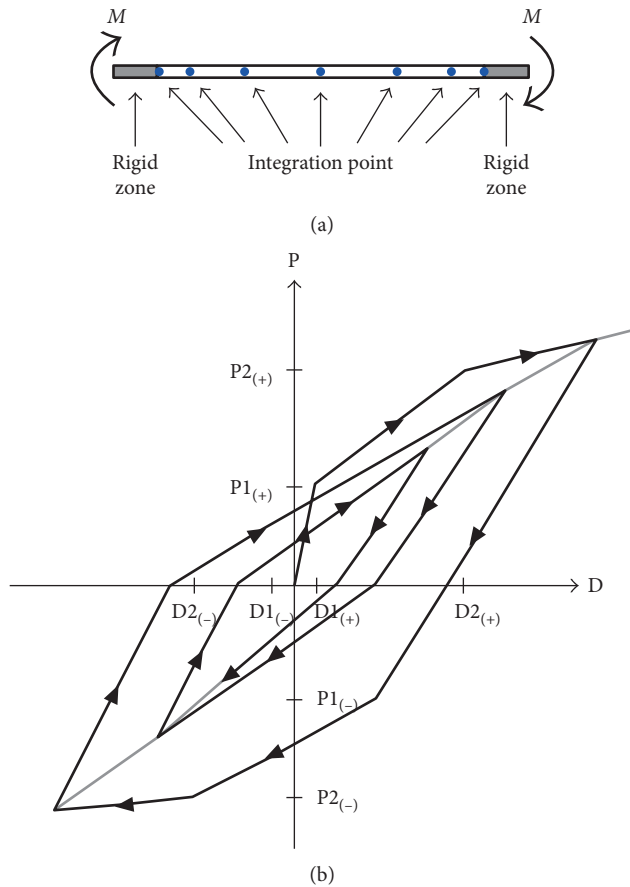


FIGURE 7: Takeda-type trilinear inelastic model for beam-column elements [51]: (a) distributed-type hinge model; (b) Takeda-type trilinear behavior.

These properties are utilized as spring and damper links at the bottom of the containment structure model.

Figure 6 shows the numerical model for the containment structure, constructed within a MIDAS GEN framework. The fundamental frequencies of such models with different soil conditions obtained from mode analyses are 3.33 Hz for A1 and 1.85 Hz for C1, respectively. The stick (beam) element is defined by a nonlinear inelastic element (in this study, Takeda-type trilinear model) for the shear behavior of the containment building since it experiences the nonlinearity in the strong intensity of motion. The turning points for the shear stress and strain relationship are decided according to the technical guidelines [53]. The distributed-type hinge model is used for the inelastic hinge properties of beam-column elements (Figure 7(a)). Specifically, we assume inelastic behavior throughout the member. The plastic hinge locations in the length direction of a member are defined as the integration points. The number of integration points can be between 3 and 20 in the MIDAS GEN. The flexibility matrix of a section, which represents the distribution of internal forces, is calculated through the integration points. The hinge behaviors can be expressed by force-deformation relationships in each axis direction, and the hinge hysteresis behavior of the flexural components can be expressed by the relationships of moment and angle of

rotation. Figure 7(b) shows the hysteresis rule of the Takeda-type trilinear model with regard to the force ( $P$ ) and displacement ( $D$ ) utilized in this study.  $P1$  and  $P2$  are the first and second yield strength, respectively.  $D1$  and  $D2$  are the first and second yield deformation, respectively.

The nonlinear seismic response analyses are conducted under the foundation input motions acquired from Section 4.3. These analyses consider three soil conditions: (1) rock (no SSI), (2) hard soil, and (3) soft soil. The rock condition is accomplished using the fixed boundary condition at the bottom of the structure. The hard soil and soft soil conditions are realized by formulating the soil impedance functions. Figure 8 shows the maximum displacements at the top of the NPP containment building structure with the three different soil conditions according to the 20 earthquake ground motions normalized to PGA values of 0.1 g to 2.0 g. The median, 25th percentiles, 75th percentiles, and the whiskers which extend to the most extreme points except for the outliers are presented based on the assumption that the obtained maximum displacements are normally distributed. It is observed that the responses and the effect of the nonlinearity of the containment building are much larger in the soft soil condition than in the other soil conditions. Specifically, the displacement at no SSI and hard soil conditions approximately has a similar pattern at 25th percentiles, median, and 75th percentiles, but the result on the soft soil is almost 5 to 10 times higher in all PGA ranges than the hard soil. The reason for this observation is that the soft soil condition plays a sort of a seismic isolator at the base of the NPP structure and accordingly induces the large displacement at the top of the structure. Also, the seismic energy dissipation occurs intensively in the soft soil layer, so the nonlinearity of the responses seems prominent in the soft soil condition compared to the other conditions.

Figure 9 illustrates the mean floor response spectra (FRS) at the top of the internal structure of the containment building in the three different soil conditions. This result shows that the secondary systems attached to the floor of the internal structure of the containment building such as the equipment and piping having low frequencies (0.5–2 Hz) are more vulnerable in the soft soil condition than in the hard soil or rock conditions. On the contrary, the secondary systems with the relatively high frequencies (i.e., more than 30 Hz) are more fragile in other soil conditions than in the soft soil condition. It is noteworthy that the maximum spectral response in the soft soil condition is less amplified than that in the other soil conditions. Consideration of the SSI effect shifts the dominant frequency range to the lower side because the soil acts as a flexible spring at the bottom of the structure and causes the fundamental period of the structure to become elongated. This also reduces the internal structural responses due to the effect of the energy dissipation mechanism of the soil. Owing to these characteristics, the SSI has a beneficial or detrimental effect on the seismic responses of structures. In the following sections, the quantitative SSI effect is investigated from the fragility and risk perspectives regarding the two major failure modes.

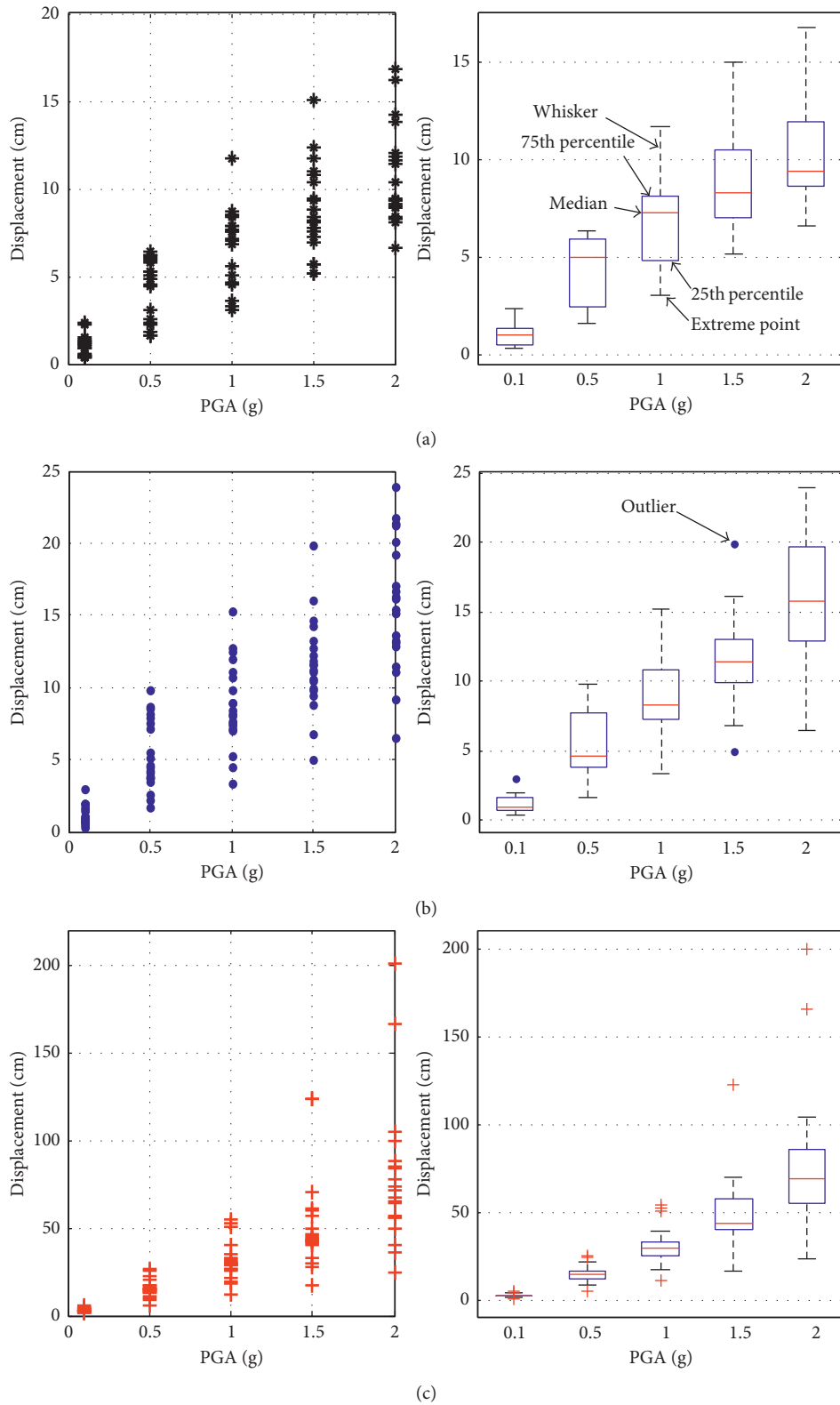


FIGURE 8: Maximum top displacement of the NPP containment building for three soil conditions under 20 earthquake ground motions normalized to PGA of 0.1g–2g: (a) no SSI; (b) hard soil; (c) soft soil.

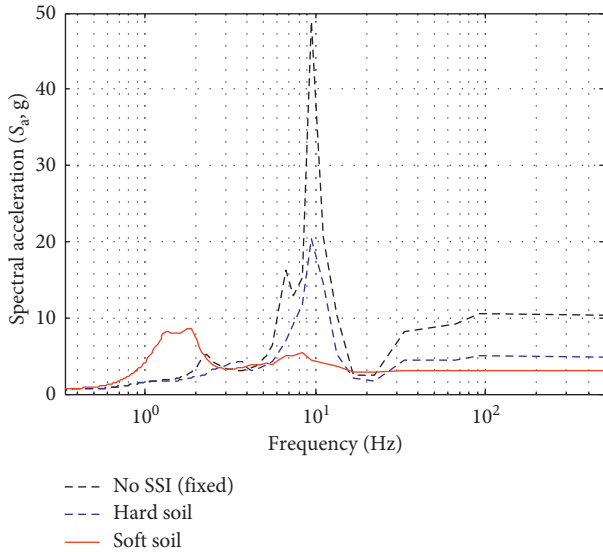
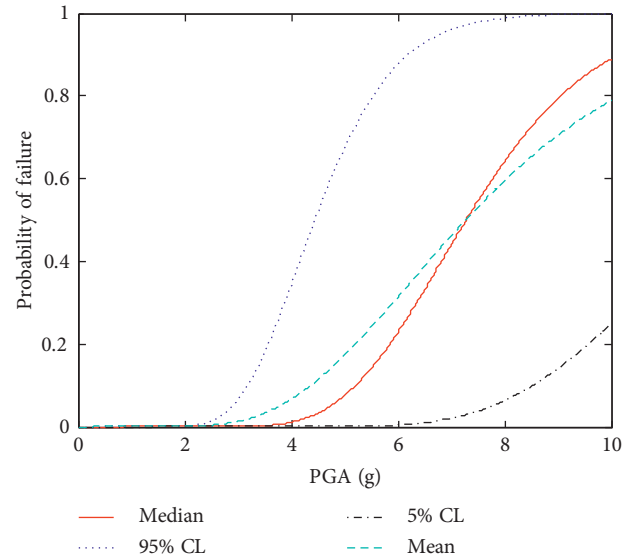


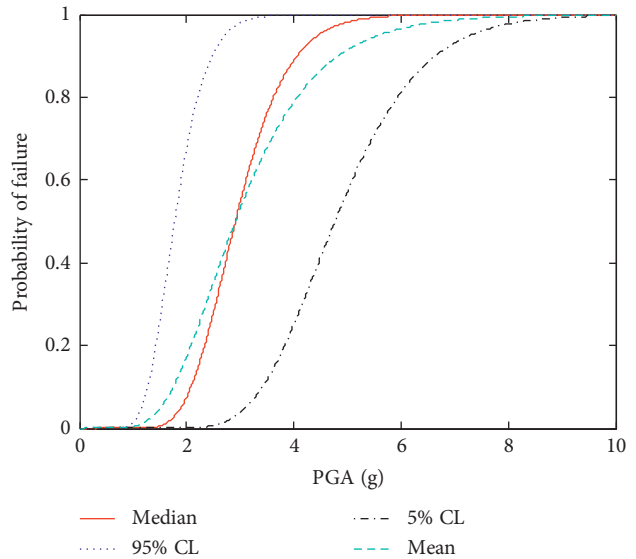
FIGURE 9: Mean floor response spectra at the top of the internal structure.

#### 4.5. Seismic Fragility Analysis regarding Two Major Failure Modes: Strength and Displacement

**4.5.1. Case 1: Strength Failure Mode.** To investigate the seismic fragility regarding the failure mode of the design strength, the factor of the safety method introduced in Section 3.1 is applied. In the factor of the safety method, the three key parameters  $A_m$ ,  $\beta_R$ , and  $\beta_U$  in (5), (9), and (10) need to be evaluated in order to develop the fragility curve. The value of  $A_m$  is calculated according to the product of the overall safety factor  $F$  and design basis earthquake  $A_{DBE}$ . The value of  $F$  is the end result obtained after the multiplication of various factors in (7) and (8). In this study, except for the SSI factor  $F_{SS}$ , other factors, including  $\beta_R$  and  $\beta_U$ , are derived from the generic data presented by numerous studies performed involving nearly 100 nuclear power plants [5, 57]. The value of  $F_{SS}$  is estimated by dividing the mean FRS of the fixed base by that of the SSI analysis [23]. The obtained values of  $F_C$  and  $F_{SA} \cdot F_{\delta} \cdot F_M \cdot F_{MC} \cdot F_{EC} \cdot F_{SD}$  are 2.2 and 1.8, respectively.  $\beta_R$  and  $\beta_U$  are determined to be 0.26 and 0.30 from generic data. The calculated value of  $F_{SS}$  is 6.13 for the soft soil condition and 2.45 for the hard soil condition.  $A_{DBE}$  is set to 0.3 g for this structure. Figure 10 shows the family of seismic fragility curves including the median, the 95% confidence level (CL), the 5% CL, and the mean in the soft soil and hard soil conditions. Figure 11 compares the median seismic hazard curves in the fixed, hard soil, and soft soil conditions. From these figures, consideration of the SSI has a beneficial influence on the results of the seismic fragility evaluation. This occurs due to the fact that the soft soil deposit increases the system damping effect, leading to a reduction of the induced internal forces. To be more specific, as mentioned previously, the soft soil condition acts like a seismic isolator at the base of the NPP containment structure. Therefore, such a phenomenon brought the excessive displacement at the top of the structure (Figure 8). But this causes the structure to perform rigid body motion



(a)



(b)

FIGURE 10: Seismic fragility curves: 5% confidence level, median, 95% confidence level, and mean (case 1). (a) Soft soil. (b) Hard soil.

and, accordingly, reduces acceleration responses (Figure 11) and internal deformation in the structure. These results are finally reflected in the strength failure mode for the structure, and these become main reasons to have its seismic fragility results, represented in Figure 11.

**4.5.2. Case 2: Displacement Failure Mode.** In the performance-based structural design, the displacement is an indicator which can represent whether a failure occurs or not in the structure. Because the containment building is in very close proximity to other utility buildings, a collision between the containment structure and other buildings, meaning its pounding to others, is a critical failure mode under an earthquake event. Thus, this study defines a failure in the containment building structure when excessive displacement

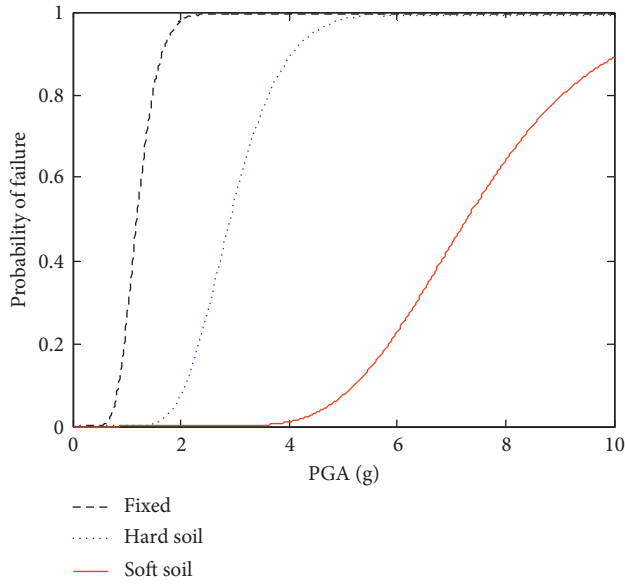


FIGURE 11: Comparison of median seismic hazard curves: fixed, hard soil, and soft soil conditions (case 1).

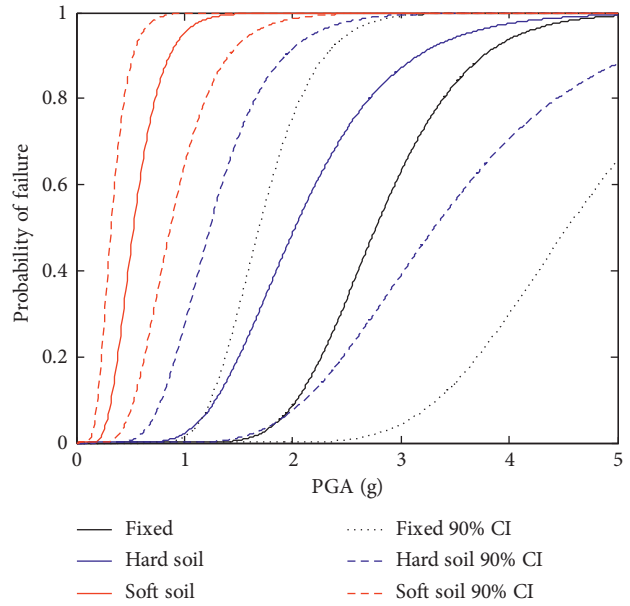


FIGURE 13: Seismic fragility curves of median and 90% CI: fixed, hard soil, and soft soil (case 2).

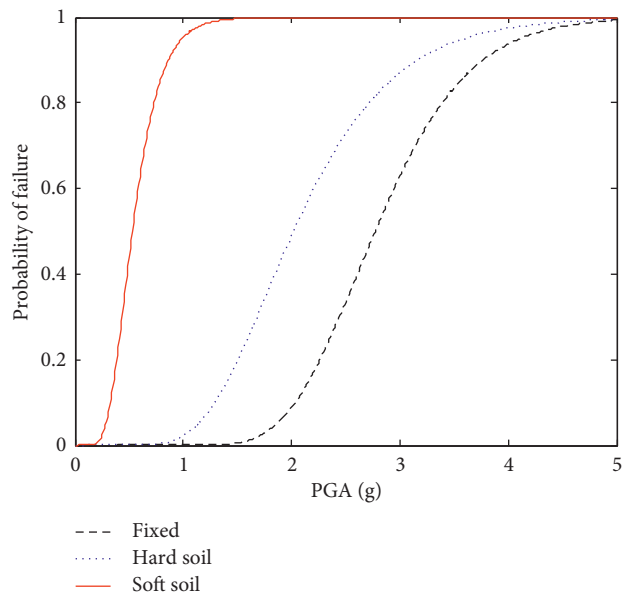


FIGURE 12: Median seismic fragility curves: fixed, hard soil, and soft soil (case 2).

takes place above the allowable seismic gap, that is, about 15 cm. Figure 12 shows the median seismic fragility curves for this failure mode by using the seismic response results of Section 4.4 and the MLE-based statistical approach in Section 3.2. Figure 13 illustrates the median and 90% confidence interval (CI) of the seismic fragility curves. From these results, we can see that considering the SSI effect in the failure mode in case 2 has a detrimental impact on the seismic fragility, unlike the strength failure mode of case 1. This occurs because the soft soil deposit brings flexibility to the bottom of the structure and induces large structural displacement at the top compared to the rock and hard soil conditions.

**4.6. Risk Analysis.** In this section, we investigate how the SSI effect changes the total risk in the specific seismic hazard information. Within the US, the US Geological Survey (USGS: <http://earthquake.usgs.gov/hazards/products/>) provides seismic hazard information at any place of interest. For example, Figure 14 shows the DBE- and MCE-level seismic hazard maps of the US. Therefore, based on the obtained hazard information of the USGS and on (1), the seismic hazard curve at any site of interest in the US can be developed by identifying the  $k_0$  and  $k$  values for seismic risk calculation purposes.

In this study, we consider the three representative sites Los Angeles in California ( $34.045^\circ, -118.247^\circ$ ), Memphis in Tennessee ( $35.145^\circ, -90.044^\circ$ ), and Charleston in South Carolina ( $32.790^\circ, -79.936^\circ$ ) to account for the different seismic characteristics throughout the US (for the graphical information on the locations, Figure 14). Specifically, the PGA-based seismic hazard information for these sites was extracted from the USGS seismic hazard database and is represented as blue circles in Figure 15. In addition, for the conservative seismic risk estimation, the log-log linear form of (1) was used to approximate the given discrete seismic hazard information. The values of the parameters  $k$  and  $k_0$  were identified from the least squares method such that the equation could well describe the hazard information in the DBE and MCE levels (i.e., the red dashed lines in Figure 15). The approximated log-log linear hazard curves finally obtained from such an approach are also represented along with the discrete hazard data. As shown in Figure 15, it is observed that the log-log linear seismic hazard curve could well predict the DBE- and MCE-level hazard information but overestimate outside of these ranges. Such a characteristic of the log-log linear hazard curve can enable the conservative evaluation of CDF.

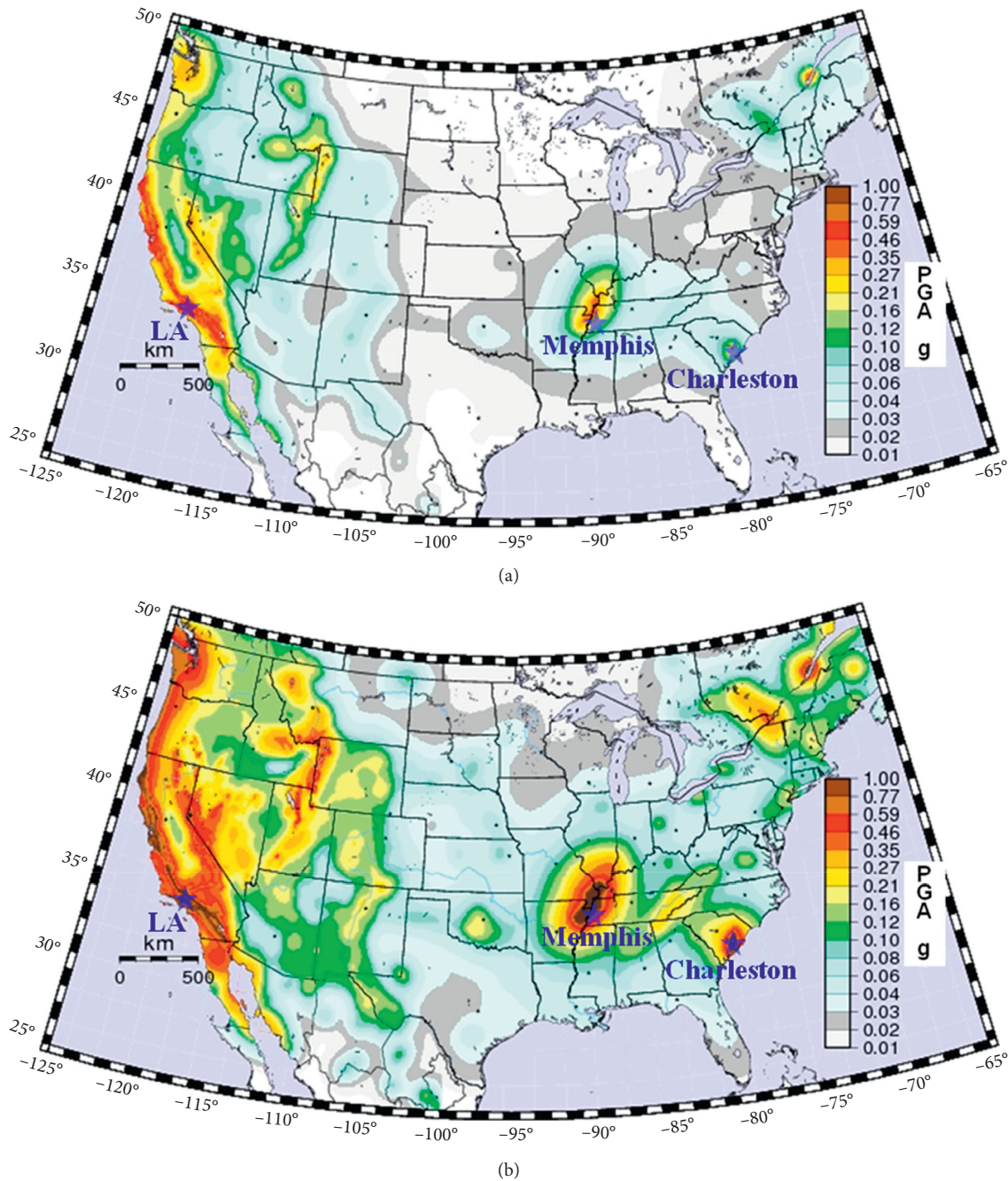


FIGURE 14: Seismic hazard maps for the US [58]: (a) 10% probability of exceedance in 50 years map of PGA; (b) 2% probability of exceedance in 50 years map of PGA.

Finally, Figure 16 shows the risk (i.e., annual CDF) of case 1 and case 2 in Los Angeles, Memphis, and Charleston. These are estimated using the convolution of the mean seismic fragility curve of each case and the log-log linear seismic hazard curves of Figure 15. The following are the observed findings:

(i) In case 1 (strength failure mode), the risk is reduced by 69.5 and 8.6 times for Los Angeles, 15.8 and 4.1 times for Memphis, and 9.6 and 3.2 times for Charleston due to the SSI effect.

(ii) However, in case 2 (displacement failure mode), the risk is increased by 60.3 and 2.5 times for Los Angeles, by 13.3 and 1.7 times for Memphis, and by 8.0 and 1.6 times for Charleston because of the SSI effect.

(iii) Regardless of the sites considered, a significant deviation in the risk results is observed to arise from the SSI effect.

The risk spread is particularly noticeable in Los Angeles on the western site of the US, which indicates that this site is

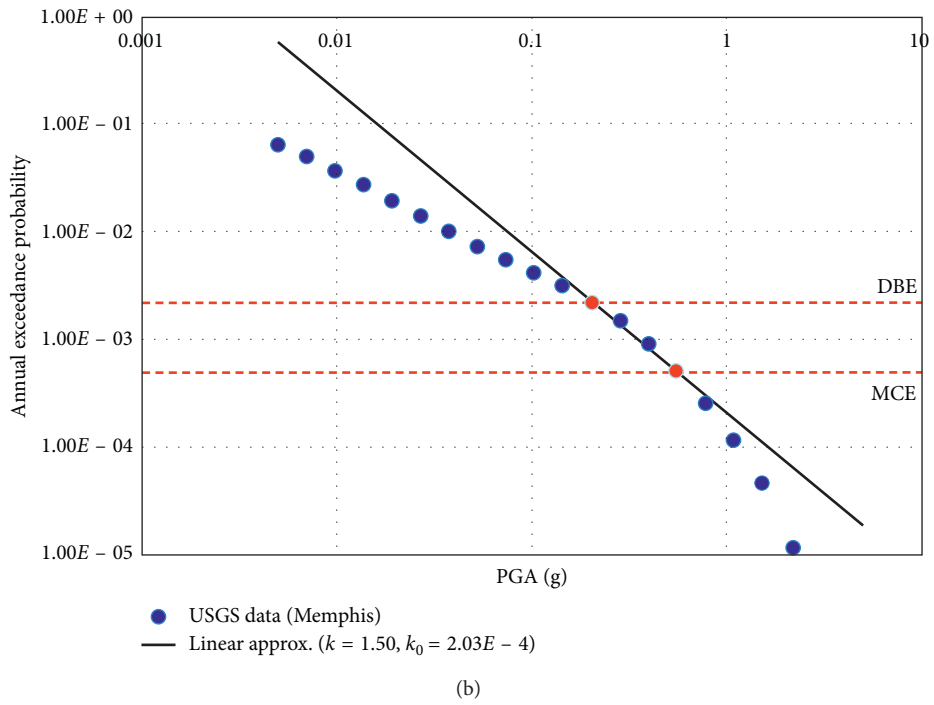
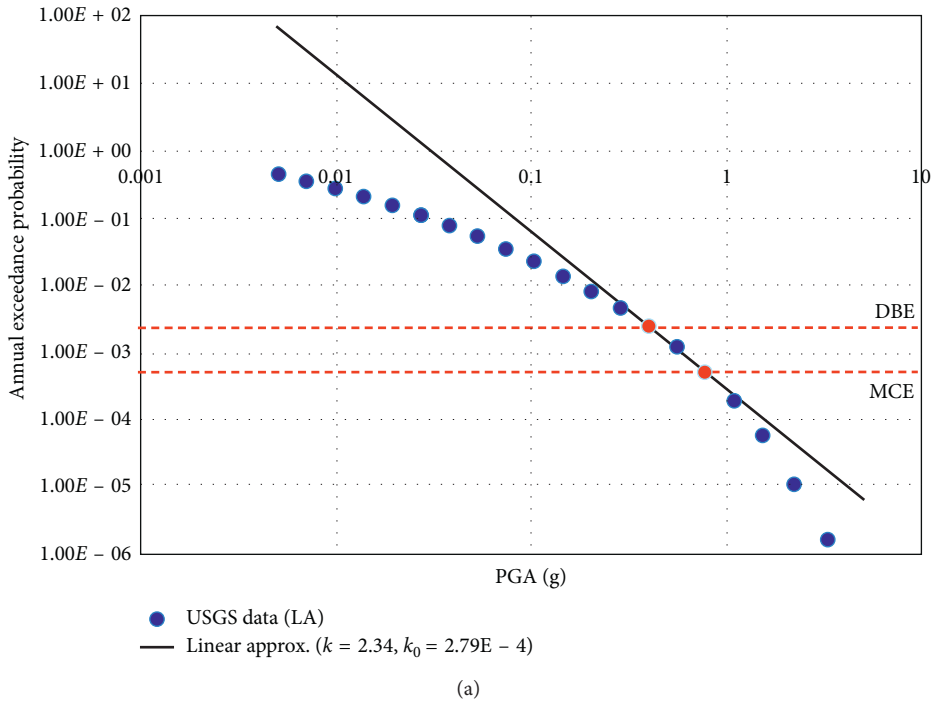


FIGURE 15: Continued.

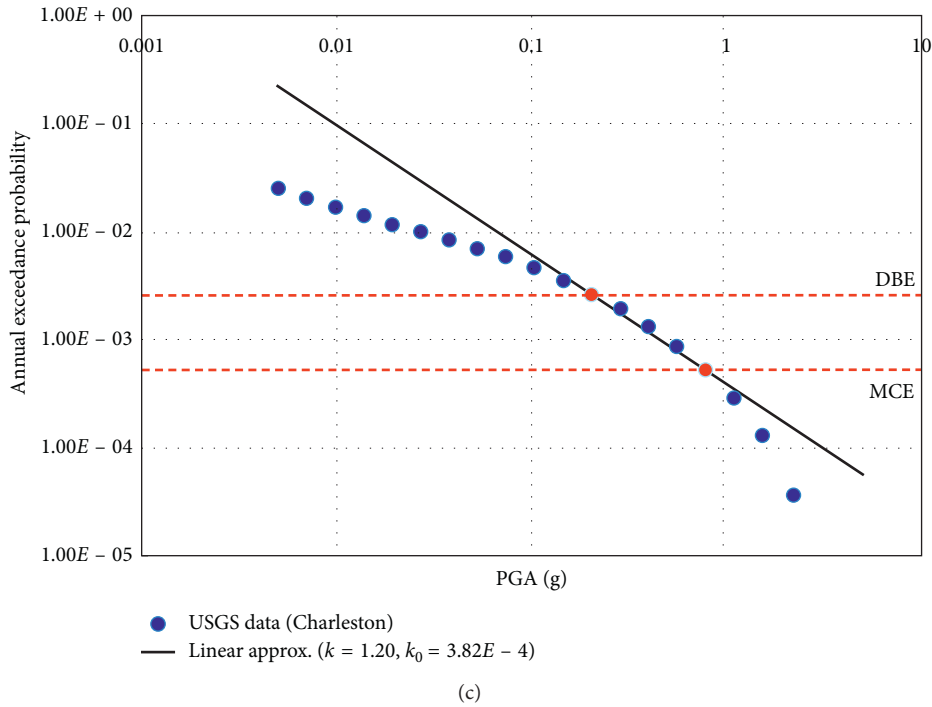


FIGURE 15: Seismic hazard curves for (a) Los Angeles, (b) Memphis, and (c) Charleston.

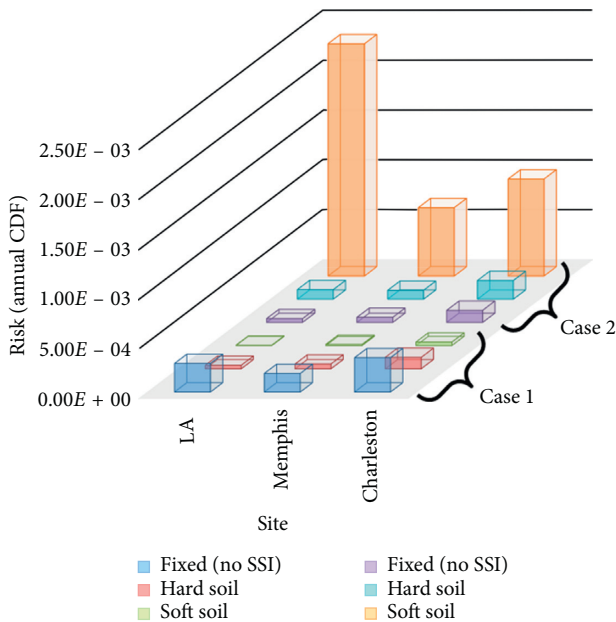


FIGURE 16: Comparison of the annual core damage frequencies.

the most risk-sensitive area out of the three sites. The reason for this risk result is attributable to the fact that the slope ( $k$ ) of the seismic hazard curve of Los Angeles is rather steep compared to those of Memphis and Charleston. Finally, it is noteworthy that consideration of the SSI has a complete conflicting effect on the risk depending on the failure modes of interest. If the SSI is associated with the strength failure mode of case 1, it has the positive effect on the risk. On the

contrary, if the SSI is related to the displacement failure mode of case 2, it has the negative effect on the total risk. This observation shows a similar context represented in Figures 11 and 12. Such findings ultimately support the core argument of this study.

### 5. Summary and Conclusion

This study explores the SSI effect on the overall risk of a PWR containment building structure with respect to two failure modes: strength and displacement. Such an exploration is based on the current SPRA framework which integrates seismic hazard and fragility information. For the fragility analysis purpose, the factor of the safety method and the MLE-based statistical approach are employed. The seismic responses of the containment structure supported on the three soil conditions: fixed, hard, and soft, are obtained by using site response analyses and inelastic time-history analyses, and such results are then utilized for basic information in the fragility quantification. The discrete seismic hazard information in the site of interest and the log-log linear approximation are utilized for the conservative risk assessment. Finally, the seismic fragility and risk results in the three different soil conditions are compared for each failure mode.

In conclusion, the main findings of this study are as follows.

- (i) The soft soil amplifies the spectral accelerations over all frequencies, and the amplification is prominent in 1-2 Hz and 3-5 Hz. However, the hard soil does not make the site responses amplified relatively.

- (ii) The displacement responses at no SSI and hard soil conditions approximately have a similar pattern at the top of the containment structure. But the result on the soft soil is almost 5 to 10 times higher in all PGA ranges than the hard soil.
- (iii) The consideration of SSI shows a complete conflicting effect on the seismic fragility and risk depending on the two failure modes. This has a positive effect regarding the strength failure mode, but this brings a negative effect regarding the displacement failure mode.
- (iv) The risk fluctuation width is particularly noticeable in the site having a considerable change in seismic hazard information (i.e., steep slope in the log-log seismic hazard curve) such as Los Angeles on the western site of the US.

All these results are because the soft soil condition acts like a seismic isolator at the base of the containment structure. Such a feature induces the excessive displacement at the top of the structure but causes the structure to perform rigid body motion and, accordingly, reduces internal deformation in the structure. These particular findings have a clear limitation because this study is based on a certain containment structure model, three general soil conditions, and two limited failure modes. Thus, the future work in this direction needs to include various failure modes and investigate the pros and cons of the SSI effect associated with these failure modes in diverse conditions.

## Data Availability

The data that support the findings of this study are available from the corresponding author upon reasonable request.

## Conflicts of Interest

The authors declare that there are no conflicts of interest regarding the publication of this paper.

## Acknowledgments

This work was supported by a National Research Foundation of Korea (NRF) Grant funded by the Korean government (Ministry of Science and ICT) (NRF-2017R1C1B1002855).

## References

- [1] ESNRG, *Stress Tests Specifications*, European Nuclear Safety Regulatory Group-European Commission, European Council, Europa building, Brussels, 2011.
- [2] USNRC, *Japan Lessons-Learned Project Directorate: Guidance on Performing a Seismic Margin Assessment in Response to the March 2012 Request for Information Letter, JLD-ISG-2012-04, Revision 0, 2012a*, 2012.
- [3] KINS, *Stress Test Performance Specification*, Korea Institute of Nuclear Safety, Daejeon, Republic of Korea, 2013.
- [4] R. J. Budnitz, P. J. Amico, C. A. Cornell et al., "Approach to the quantification of seismic margins in nuclear power plants," TNUREG/CR-4334, UCID-20444, Lawrence Livermore National Lab., Livermore, CA, USA, 1985.
- [5] EPRI, "A methodology for assessment of nuclear power plant seismic margin," NP-6041-SLR1, Electric Power Research Institute, Palo Alto, CA, USA, 1991.
- [6] USNRC, "Reactor safety study," WASH-1400, NUREG 73/041, US Nuclear Regulatory Commission, Rockville, MD, USA, 1975.
- [7] USNRC, "PRA procedure guide. A guide to the performance of probabilistic risk assessments for nuclear power plants," NUREG/CR-2300, US Nuclear Regulatory Commission, Rockville, MD, USA, 1983.
- [8] IAEA, *Procedures for Conducting Probabilistic Safety Assessments of Nuclear Power Plants (Level 1), Safety Series No. 50-P-4*, International Atomic Energy Agency, Vienna, Austria, 1992.
- [9] EPRI, "Methodology for developing seismic fragilities," TR-103959, Electric Power Research Institute, Palo Alto, CA, USA, 1994.
- [10] USNRC, "Procedural and submittal guidance for the individual plant examination of external events (IPEEE) for severe accident vulnerabilities," NUREG-1407, US Nuclear Regulatory Commission, Rockville, MD, USA, 1991.
- [11] S. Kwag, J. Oh, J.-M. Lee, and J.-S. Ryu, "Bayesian-based seismic margin assessment approach: application to research reactor," *Earthquakes and Structures*, vol. 12, no. 6, pp. 653–663, 2017.
- [12] P. J. Stewart, G. L. Fenves, and R. B. Seed, "Seismic soil-structure interaction in buildings. I: analytical methods," *Journal of Geotechnical and Geoenvironmental Engineering*, vol. 125, no. 1, pp. 26–37, 1999.
- [13] G. Mylonakis and G. Gazetas, "Seismic soil-structure interaction: beneficial or detrimental?," *Journal of Earthquake Engineering*, vol. 4, no. 3, pp. 277–301, 2000.
- [14] USNRC, *Standard Review Plan (SRP) Sec. 3.7.2: Seismic Design Parameters, NUREG0800 Revision 4*, 2012.
- [15] J. Coleman, "Demonstration of nonlinear seismic soil structure interaction and applicability to new system fragility seismic curves," INL/EXT-14-33222, Idaho National Lab (INL), Idaho Falls, ID, USA, 2014.
- [16] F. Behnamfar and M. Banizadeh, "Effects of soil-structure interaction on distribution of seismic vulnerability in RC structures," *Soil Dynamics and Earthquake Engineering*, vol. 80, pp. 73–86, 2016.
- [17] F. Mirzaie, M. Mahsuli, and M. A. Ghannad, "Probabilistic analysis of soil-structure interaction effects on the seismic performance of structures," *Earthquake Engineering and Structural Dynamics*, vol. 46, no. 4, pp. 641–660, 2017.
- [18] Z. Zhou and X. Wei, "Seismic soil-structure interaction analysis of isolated nuclear power plants in frequency domain," *Shock and Vibration*, vol. 2016, Article ID 6127895, 15 pages, 2016.
- [19] S. El-Bahey, Y. Alzeni, and K. Oikonomou, "Effect of soil-structure interaction on the seismic fragility of a nuclear reactor building," *Journal of Nuclear Engineering and Radiation Science*, vol. 4, no. 2, p. 020912, 2018.
- [20] D. M. Ghiocel, P. R. Wilson, G. G. Thomas, and J. D. Stevenson, "Seismic response and fragility evaluation for an Eastern US NPP including soil-structure interaction effects," *Reliability Engineering and System Safety*, vol. 62, no. 3, pp. 197–214, 1998.
- [21] M. Vermaut, P. Monette, P. Shah, and R. D. Campbell, "Methodology and results of the seismic probabilistic safety assessment of Krško nuclear power plant," *Nuclear engineering and design*, vol. 182, no. 1, pp. 59–72, 1998.
- [22] S. H. Eem, H. J. Jung, M. K. Kim, and I. K. Choi, "Seismic fragility evaluation of isolated NPP containment structure

- considering soil-structure interaction effect,” *Journal of the Earthquake Engineering Society of Korea*, vol. 17, no. 2, pp. 53–59, 2013.
- [23] S. M. Hoseyni, F. Yousefpour, A. A. Araei, K. Karimi, and S. M. Hoseyni, “Effects of soil-structure interaction on fragility and seismic risk; a case study of power plant containment,” *Journal of Loss Prevention in the Process Industries*, vol. 32, pp. 276–285, 2014.
- [24] R. K. McGuire, “Probabilistic seismic hazard analysis and design earthquakes: closing the loop,” *Bulletin of the Seismological Society of America*, vol. 85, no. 5, pp. 1275–1284, 1995.
- [25] C. A. Cornell, F. Jalayer, R. O. Hamburger, and D. A. Foutch, “Probabilistic basis for 2000 SAC Federal Emergency Management Agency steel moment frame guidelines,” *Journal of Structural Engineering*, vol. 128, no. 4, pp. 526–533, 2002.
- [26] B. A. Bradley, R. P. Dhakal, M. Cubrinovski, J. B. Mander, and G. A. MacRae, “Improved seismic hazard model with application to probabilistic seismic demand analysis,” *Earthquake Engineering and Structural Dynamics*, vol. 36, no. 14, pp. 2211–25, 2007.
- [27] R. P. Kennedy, C. A. Cornell, R. D. Campbell, S. Kaplan, and H. F. Perla, “Probabilistic seismic safety study of an existing nuclear power plant,” *Nuclear Engineering and Design*, vol. 59, no. 2, pp. 315–338, 1980.
- [28] R. P. Kennedy and M. K. Ravindra, “Seismic fragilities for nuclear power plant risk studies,” *Nuclear Engineering and Design*, vol. 79, no. 1, pp. 47–68, 1984.
- [29] S. Kwag, J. M. Lee, J. Oh, and J. S. Ryu, “Development of system design and seismic performance evaluation for reactor pool working platform of a research reactor,” *Nuclear Engineering and Design*, vol. 266, pp. 199–213, 2014.
- [30] J. Oh, S. Kwag, and J. M. Lee, “A new design concept and seismic margin assessment for a spent fuel storage system,” *Nuclear Engineering and Design*, vol. 326, pp. 150–161, 2018.
- [31] M. Shinozuka, M. Q. Feng, J. Lee, and T. Naganuma, “Statistical analysis of fragility curves,” *Journal of engineering mechanics*, vol. 126, no. 12, pp. 1224–1231, 2000.
- [32] J. W. Baker and C. A. Cornell, “Vector-valued ground motion intensity measures for probabilistic seismic demand analysis,” Report No. 150, Blume Earthquake Engineering Center, Stanford, CA, USA, 2005.
- [33] J. Rice, *Mathematical Statistics and Data Analysis*, Nelson Education, Toronto, QC, Canada, 2006.
- [34] A. Moseleh and G. Apostolakis, “The assessment of probability distributions from expert opinions with an application to seismic fragility curves,” *Risk Analysis*, vol. 6, no. 4, pp. 447–461, 1986.
- [35] A. Singhal and A. S. Kiremidjian, “Bayesian updating of fragilities with application to RC frames,” *Journal of structural Engineering*, vol. 124, no. 8, pp. 922–929, 1998.
- [36] M. Sasani and A. D. Kiureghian, “Seismic fragility of RC structural walls: displacement approach,” *Journal of Structural Engineering*, vol. 127, no. 2, pp. 219–228, 2001.
- [37] P. Gardoni, A. Der Kiureghian, and K. M. Mosalam, “Probabilistic capacity models and fragility estimates for reinforced concrete columns based on experimental observations,” *Journal of Engineering Mechanics*, vol. 128, no. 10, pp. 1024–1038, 2002.
- [38] D. Straub and A. Der Kiureghian, “Improved seismic fragility modeling from empirical data,” *Structural Safety*, vol. 30, no. 4, pp. 320–336, 2008.
- [39] P. S. Koutsourelakis, “Assessing structural vulnerability against earthquakes using multi-dimensional fragility surfaces: a Bayesian framework,” *Probabilistic Engineering Mechanics*, vol. 25, no. 1, pp. 49–60, 2010.
- [40] S. Kwag and A. Gupta, “Bayesian network technique in probabilistic risk assessment for multiple hazards,” in *Proceedings of 24th International Conference on Nuclear Engineering (ICONE 24)*, Charlotte, NC, USA, 2016.
- [41] S. Kwag and A. Gupta, “Probabilistic risk assessment framework for structural systems under multiple hazards using Bayesian statistics,” *Nuclear Engineering and Design*, vol. 315, no. 4, pp. 20–34, 2017.
- [42] S. Kwag, A. Gupta, and N. Dinh, “Probabilistic risk assessment based model validation method using Bayesian network,” *Reliability Engineering and System Safety*, vol. 169, pp. 380–393, 2018.
- [43] S. Kwag and A. Gupta, “Computationally efficient fragility assessment using equivalent elastic limit state and Bayesian updating,” *Computers and Structures*, 2018, In press.
- [44] H. Hwang, B. Ellingwood, M. Shinozuka, and M. Reich, “Probability-based design criteria for nuclear plant structures,” *Journal of structural engineering*, vol. 113, no. 5, pp. 925–942, 1987.
- [45] S. Kwag and S.-Y. Ok, “Robust design of seismic isolation system using constrained multi-objective optimization technique,” *KSCE Journal of Civil Engineering*, vol. 17, no. 5, pp. 1051–1063, 2013.
- [46] P. D. Smith, R. G. Dong, D. L. Bernreuter et al., “Seismic safety margins research program. Phase I, final report—overview,” NUREG/CR-2015-Vol. 1, UCRL-53021-Vol. 1, Lawrence Livermore National Lab., Livermore, CA, USA, 1987.
- [47] B. S. Ju and A. Gupta, “Seismic fragility of threaded Tee-joint connections in piping systems,” *International Journal of Pressure Vessels and Piping*, vol. 132, pp. 106–118, 2015.
- [48] Y. J. Lee and D. S. Moon, “A new methodology of the development of seismic fragility curves,” *Smart Structures and Systems*, vol. 14, no. 5, pp. 847–867, 2014.
- [49] S. L. Kramer, *Geotechnical Earthquake Engineering*, Prentice Hall, Inc., Upper Saddle River, NJ, USA, 1996.
- [50] P. B. Schnabel, “SHAKE: a computer program for earthquake response analysis of horizontally layered sites,” EERC Report, University of California, Berkeley, CA, USA, 1972.
- [51] MIDAS IT, *MIDAS GEN Structural Analysis Program Version 795*, MIDAS IT, Navi Mumbai, Maharashtra, 2016.
- [52] J. S. Ryu, C. G. Seo, J. M. Kim, and C. B. Yun, “Seismic response analysis of soil-structure interactive system using a coupled three-dimensional FE-IE method,” *Nuclear Engineering and Design*, vol. 240, no. 8, pp. 1949–1966, 2010.
- [53] Y. J. Park and C. H. Hofmayer, “Technical guidelines for aseismic design of nuclear power plants,” NUREG/CR-6241, Nuclear Regulatory Commission, Rockville, MD, USA, 1994.
- [54] Combustion Engineering, *System 80+ Standard Design*, US DOE, New York, NY, USA, 1990.
- [55] US Nuclear Regulatory Commission, *A Performance-Based Approach to Define the Site-Specific Earthquake Ground Motion, Regulatory Guide Version 1.208*, US Nuclear Regulatory Commission, Rockville, MD, USA, 2007.
- [56] US Nuclear Regulatory Commission, *Design Response Spectra for Seismic Design of Nuclear Power Plants, Regulatory Guide Version 1.60*, US Nuclear Regulatory Commission, Rockville, MD, USA, 2014.
- [57] USNRC, *Risk Assessment of Operational Events in External Events*, Vol. 2, US Nuclear Regulatory Commission, Rockville, MD, USA, 2008.
- [58] M. D. Petersen, M. P. Moschetti, P. M. Powers et al., *Documentation for the 2008 update of the United States national seismic hazard maps (No. 2008-1128)*, US Geological Survey, Reston, VA, USA, 2008.

## Review Article

# Can Repetitive Small Magnitude-Induced Seismic Events Actually Cause Damage?

Oliver-Denzil S. Taylor <sup>1</sup>, Alanna P. Lester,<sup>1</sup> Theodore A. Lee III,<sup>2</sup> and Mihan H. McKenna<sup>1</sup>

<sup>1</sup>U.S. Army Corps of Engineers, Engineer Research and Development Center, Geotechnical and Structures Laboratory, Vicksburg, MS 39180, USA

<sup>2</sup>U.S. Army Corps of Engineers, Engineer Research and Development Center, USACE Reachback Operations Center, Mobile, AL 36602, USA

Correspondence should be addressed to Oliver-Denzil S. Taylor; [oliver.d.taylor@usace.army.mil](mailto:oliver.d.taylor@usace.army.mil)

Received 12 January 2018; Accepted 10 April 2018; Published 8 May 2018

Academic Editor: Tiago Miguel Ferreira

Copyright © 2018 Oliver-Denzil S. Taylor et al. This is an open access article distributed under the Creative Commons Attribution License, which permits unrestricted use, distribution, and reproduction in any medium, provided the original work is properly cited.

Geoengineering activities such as reservoir impoundment, mining, wastewater injection, geothermal systems, and CO<sub>2</sub> capture have been linked directly to induced seismicity. With the industrial boom in natural shale gas production regions previously aseismic areas have seen an exponential growth in the frequency of small magnitude events, with multiple events observed in close proximity within a 24-hour time period. While the overwhelming majority of induced seismic research has focused on the causality, the potential risk posed to critical federal infrastructure has escaped scrutiny. This proposes the question, “Can repetitive small magnitude-induced seismic events actually cause damage?” A review of the potential risk is presented herein, concluding that a simplistic definitive statement of whether single or multiple small magnitude-induced seismic events do or do not cause damage to critical infrastructure cannot be justified, and warrants additional study. However, recent observations and research suggest the likelihood that these geoengineering-induced events can and do cause detrimental degradation of the subsurface (damaging the overlying structure) is not insignificant.

## 1. Introduction

Recent induced seismic research has shown that the current standard of practice for risk assessment for infrastructure is not applicable for the UHP-induced seismic hazard in historically aseismic continental regions [1, 2] but is critically important for understanding the immediate impact potential to USACE-owned dams and levees throughout the Central and southwest central United States (CeUS). Engineering, economic, social, and political decision-making matrices must therefore, include the questions of “What is the largest expected induced seismic event?” and “What is the probability of an induced seismic event generating a potentially damaging ground motion?” The answers to these questions are currently the focus of emerging research [1–4].

Intraplate regions are primed to be susceptible to induced earthquakes, as the geological stress states are already at critical stress conditions: the geological structure is in a quasistatic equilibrium state [3, 5–7]. Recent advances in

fluid-based geoengineering activities, hydraulic fracturing/enhanced recovery technology, population growth, and worldwide energy consumption rates are suspected of contributing to the exponential increase in seismic activity within these historically aseismic regions by altering deep lithology effective stress states, which result in subsurface shear failure [1–3, 5, 6, 8–20]. Seismologists and earthquake engineers have recently issued concerns about fluid-based geoengineering activities being the genesis of moderate induced seismicity [1, 2, 4, 19–21], yet the topic of damage potential of geoengineering-induced seismicity remains relatively unexplored.

## 2. Geoengineering-Induced Seismicity

The exponential rise in induced seismicity in the CeUS since 2008 is correlated with an increase in Modified Mercalli Intensities (MMI) from small, relatively shallow events [1, 2, 5, 22]. Common geophysical practice adheres to the

premise that seismicity below M5.0 is not significant for generating damaging ground motions and, thus, is not considered a substantial hazard to critical infrastructure [1, 2, 4]. Increased MMI combined with encroaching spatiotemporal proximity to critical infrastructure begs the question, “Could future small magnitude-induced events affect federal flood control structures and critical infrastructure?” This is particularly important to the aging infrastructure within the United States where some critical structures are beyond design life spans and/or designed without any seismic considerations [23].

This recent rise in seismicity within the CeUS appears to be different from what has been historically observed as these events are more shallow (typically between 2 and 5 km in depth as opposed to 10+ km for historically tectonic events), are smaller in magnitude, are persistent, and occur in previously essentially aseismic areas [3, 24–27]. It must be noted that the spatial location and average depth of recent events are loosely constrained due to instrument coverage and limitations within location algorithms, and some regions; for example, Oklahoma, have default depths of 5 km for shallow events, for events whose location accuracies are uncertain. However, the recent events reported are predominately occurring within the upper 5 km of the crust [24–27]. More important is the temporal frequency of these events. Recent research on the spatial-temporal behavior of geoen지니어ing-induced seismicity shows that these events can be highly concentrated; for example, a single region in Arkansas exhibited 6.5 events per km<sup>2</sup> at a rate of about 146 events per year between 2004 and 2013 [1, 2]. Some regions in the CeUS average over two events daily.

### 3. Damage Potential of Geoen지니어ing-Induced Seismicity

Small magnitude (between M3 and M5), shallow (2–5 km), geoen지니어ing-induced seismic events have demonstrated damage to many types of structures. Nowhere is this more apparent than in aseismic intraplate regions wherein damage is observed from both single and repeated small, shallow events. A series of shallow events in Alberta, Canada (largest event M4.0), caused some minor building damage [19, 28]. Residential damage has been observed within the Central United States, for example, the 2012 Timpson, Texas sequence (largest event of  $M_{W-RMT}$  4.8) [29] and the 2013 Azel, Texas sequence (largest event M3.7) [30]. In Cherokee, Oklahoma, there were several events on February 5, 2015 (largest event of M4.2) wherein interior walls were damaged in the Alfalfa County Courthouse [30–32]. In November 2014, an M4.9 event occurred in the vicinity of Milan, KS, with damage to the Harper County courthouse as well as to surrounding churches and residences; events continued through the spring of 2015 wherein new cracks generated and existing building cracks enlarged [9, 33–35]. On May 2, 2015, an M4.2 event occurred in Michigan with residential and commercial damage, for example, cracks in walls [36, 37]. This by no means an all-inclusive list; however, it is typical of the seemingly inconsequential damage documented from induced seismicity. Could future small

magnitude-induced events affect larger and heavier structures? Quinn and Taylor [38] showed fatigue failure potential from induced strains in earthen structures subjected to minor ground accelerations while under normal to slightly elevated service load and not necessarily limited to sudden catastrophic failure from a single large event. More importantly these damage reports indicate potentially more problematic hazards: (1) repetitive loading and (2) subsurface fatigue.

### 4. Single-Event Failure versus Multievent Fatigue

The repetitious nature of these events may generate cumulative damage effects, or fatigue, well in excess of the initial structural design. Moreover, these seemingly inconsequential dynamic loading scenarios are often dismissed as potentially damaging in favor of a single isolated event; that is, if a structure can withstand a much larger extreme event, then a minor event poses no significant threat. This would be a safe assumption provided that the occurrence frequency of the smaller events was not significant. For example, in Rhode Island, there have been numerous cases wherein vibrations caused by pile driving have resulted in detrimental settlement of adjacent structures (similar to the damage correlated with induced seismicity), leading to the demolition of some historic structures [39]. These vibrations were caused by impact hammers operating at low strike frequencies wherein each pile strike generated seismic velocities well below construction thresholds for even the most sensitive structures. Therefore, the question of damage potential becomes a source scaling issue.

Dynamic responses decay as a function of distance from an energy source. Finite seismic sources, for example, single induced events, in a bounded elastic media have a geometric amplitude decay of

$$A_2 = A_1 \left( \frac{r_1}{r_2} \right)^n, \quad (1)$$

where  $r_1$  is the radial distance from the source to a known amplitude,  $A_1$ ;  $r_2$  is the radial distance to an unknown amplitude,  $A_2$ ; and  $n$  is the exponent of decay depending on the seismic wave type. Small magnitude events, M5–, at a shallow depth can yield surface ground motions well in excess of much larger, M7+, tectonic earthquakes simply due to a significantly reduced  $r_2$ . Thus, simply negating damage potential based strictly on magnitude determinations is both mathematically and physically incorrect. New ground motion prediction equations are required for these events [4, 40]. Induced events have much shorter duration and higher frequency contents [19, 29]. For structures of low natural frequencies, single high-frequency peak acceleration would have little effect to the physical structure [41]. Therefore, it is unlikely that an induced event would cause significant damage to a large nonearthen structure. However, if we associate these induced events as an impulse force, that is, single-cycle large amplitude loading, the primary driver for damage potential is not the cyclic or frequency

effects to the physical structure, rather the damage potential is the subsurface yield that can cause detrimental settlement and structural damage.

Engineers and geophysicists often consider the crustal pore space, regardless of air/water make-up, to be initially static. This assumption is valid for tectonic cases where earthquakes are years to decades apart. In regions of frequent induced seismicity, where events are hours to days apart, pore pressures are not necessarily static at the onset of subsequent induced events [1, 2]. In terms of ground response for liquefiable cohesionless soils, excess pore pressure generation is relatively independent of loading frequency with dissipation being a function of permeability [39, 42]. Moreover, excess pore pressure ratios do not need to achieve unity to cause significant strains within a cohesionless continuum; strains as low as 0.3% can indicate the onset of uncontrolled degradation within the subsurface [39]. This degradation, or strength reduction, may cause differential settlement beneath a structure leading to foundation damage or failures even though the physical structure would be negligibly affected by the induced seismic waveform. For example, a loose liquefiable nonplastic silt has a cyclic resistance ratio, CRR, of 0.187 at the onset of significant straining, Figure 1 (a M7.5 tectonic event corresponds to 15 equivalent loading cycles [43]); the CRR increases to approximately 0.294 for a single cycle equivalent. Thus, based on Seed and Idriss [44] and Seed et al. [45], the smaller magnitude-induced event would have to yield approximately 1.5 times increase in peak acceleration to initiate significant subsurface straining. For tectonic events, such acceleration is not achieved with a decrease in earthquake magnitude. However, for induced seismicity, (1) illustrates that such an increase in acceleration with a decrease in earthquake magnitude is possible due to the shallow hypocenter.

A typical earthen structure may have a minimum threshold equivalent acceleration of approximately 0.2g before the onset of straining (damage) is believed to occur, typically referenced as 15 equivalent loading cycles. Therefore, in the case of loose liquefiable nonplastic silt lens, a single-cycle equivalent event, that is, induced seismic event, would require an acceleration of approximately 0.30g to have the same damage potential. Peak accelerations in excess of this example have been observed in induced events, for example,  $m_{BLg}$  4.1 Timpson, Texas, with peak accelerations of up to 0.62g [29]. If the induced seismic event equivalent loading cycles increase to four, then the required acceleration to achieve the same 0.2g threshold remains relatively unchanged at 0.27g, thus justifying a single induced event as impulse load. Repetitive induced events can then be treated as a low frequency loading equivalents with a sinusoidal maximum equivalent to the impulse.

Effects on smaller structures from high frequencies (both temporal and spectral), not the amplitude of the acceleration, can be observed at a significant distance from the epicenter and would observationally manifest in intensity reports. While aftershocks from tectonic events decrease in magnitude, induced seismicity magnitudes remain relatively constant for each subsequent event making the impulse load relatively constant with each event [1, 2]. Thus, it is

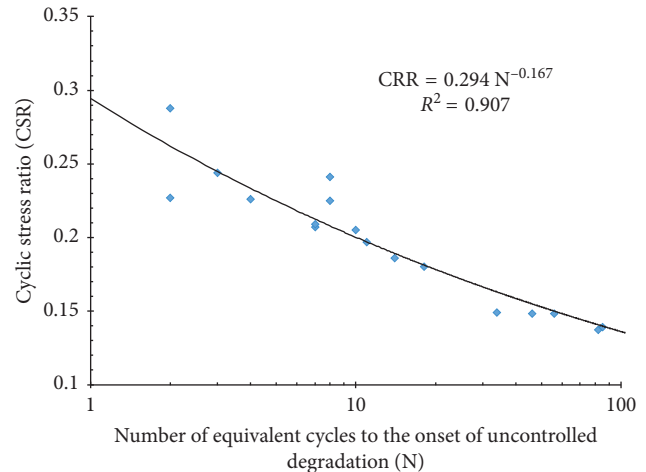


FIGURE 1: The cyclic resistance, to the onset of uncontrolled degradation, of a loose to medium dense nonplastic Rhode Island silt (after 40).

misleading to compare tectonic earthquakes and induced seismicity without accounting explicitly for variance in loading mechanisms. In regions of frequent induced seismicity, structures subjected to repetitive impulse loadings do not consider soil fatigue states. Such conditions are explicitly accounted in for other aspects of civil engineering, for example, traffic vibration in bridge design, in either design, or assessment processes and should be included in discussions of the subsurface damage potential for induced seismicity, due to the risk to the overall stability.

There are unknown effects that may increase the damage potential from induced seismicity, for example, the large vertical acceleration component as observed in Timpson, Texas [29]. Our understanding of seismic loading is based on tectonic events that manifest as large horizontal ground motions with minimal influence from the vertical component, which is often ignored. This change in loading direction alters the shearing axis and therefore the soil's capacity to resist the imparted load. Further, an applied shear load propagating vertically from the subsurface is more representative of an extension type loading; this is the weakest axis for soil resistance and warrants further study.

## 5. Hazard and Risk

Induced seismic events do not carry the same hazard as large tectonic equivalents. In tectonic events, the radial extent of large ground motions exceeds that of what has been observed in shallow induced seismicity. Therefore, the associative risk to critical infrastructure, of a single induced seismic event, would decrease in comparison, based on how risk is calculated [46]:

$$\text{Seismic Risk} = \text{Seismic Hazard} \otimes \text{Vulnerability}. \quad (2)$$

The *Vulnerability* of any structure is a function of exposure (within the proximity of the seismic event such that it may potentially be affected), fragility (susceptibility of the structure to the ground intensities), and consequence (socioeconomic impact should failure occur) [22]. In (2), the

*Seismic Hazard*, or probability of exceedance of a specified ground motion intensity, for tectonic events (the PGA, PGV, spectral content, etc.) can readily exceed that of induced events [1, 2] on a per event basis. However, the close spatial proximity and repetitious nature of induced events actually increase the exposure or the chance that an induced epicenter will occur within sufficient proximity to exceed a threshold acceleration by increasing the probability of an event occurrence, shown in the *b*-value for induced events [1, 2].

Quinn and Taylor [38] illustrated that in the case of earthen dams, normal to slight increases in one hazard (e.g., the impounded water head) can reduce the required seismic hazard threshold for exceedance. In this scenario, the *Seismic Risk* would be a joint probability function of the *Seismic Hazard* and the secondary hazard (e.g., flood event). It is then possible that repetitive low magnitude-induced events combined with a secondary hazard result in a higher *Seismic Risk*, or failure potential, than a larger tectonic event. This may yield a situation where the structural design is insufficient and the probability of occurrence is greater for the joint-induced seismic-secondary hazard event despite the structure being designed for a larger single tectonic event.

## 6. Conclusions

The answer to “Can repetitive small magnitude-induced seismic events actually cause damage?” requires a better understanding of the extent of failure modes (classic failure versus soil fatigue) and threshold limits within the seismic hazard, and vulnerability of structures ill-equipped to withstand seismic loading. Further, complicating the quantification of the *Seismic Hazard* for geoengineering-induced events is that the full extent of the hazard is not fully known and varies with changes in geoengineering activities, locations, and technologies [2]. Thus, making induced seismic hazard maps and other measures is currently more subjective than quantitative. Furthermore, the *Vulnerability* is complicated by the age of the infrastructure, for example, dams, locks, levee, and so on. For example, the US Army Corps of Engineers oversees maintains or operates over 700 dams, 14,500 miles of levees, and 220 locks [23]. Most of these are aging facilities in need of constant repair and rehabilitation; eleven of these locks are in excess of 100 years old [23]. Such conditions lower the exceedance threshold within the *Seismic Hazard* and increase the fragility within the *Vulnerability* thereby, generating even greater *Seismic Risk* for small magnitude events, both on single-event and multiple event bases. Thus, a simplistic definitive statement of whether single or multiple small magnitude-induced seismic events do or do not cause damage to critical infrastructure cannot be justified on the basis of comparative magnitudes between induced and tectonic events and warrants additional study, especially in respect to soil fatigue. However, recent observations and research suggest the likelihood that these geoengineering-induced events can and do cause detrimental degradation of the subsurface (damaging the overlying structure) is not insignificant.

## Conflicts of Interest

The authors declare that they have no conflicts of interest.

## Acknowledgments

The research was funded through the Assistant Secretary of the Army, Acquisition, Logistics and Technology (ASAALT) Military Engineering Direct Research program AT40 “Remote Assessment of Critical Infrastructure”. Director, Geotechnical and Structures Laboratory, U.S. Army Engineer Research & Development Center, granted permission to publish this research with unlimited distribution.

## References

- [1] O.-D. S. Taylor, A. P. Lester, and T. A. Lee, “Hazard and risk potential of unconventional hydrocarbon development-induced seismicity within the central United States,” *Natural Hazards Review*, vol. 16, no. 4, p. 04015008, 2015.
- [2] O.-D. S. Taylor, A. P. Lester, and T. A. Lee, *Unconventional Hydrocarbon Development Hazards within the Central United States: Report 1: Overview and Potential Risk To Infrastructure*, ERDC/GSL TR-15-26, U.S. Army Engineer Research and Development Center, Vicksburg, MS, USA, 2015.
- [3] A. McGarr, “Maximum magnitude earthquakes induced by fluid injection,” *Journal of Geophysical Research: Solid Earth*, vol. 119, no. 2, pp. 1008–1019, 2014.
- [4] G. M. Atkinson, “Ground-motion prediction equation for small-to-moderate events at short hypocentral distances, with application to induced-seismicity hazards,” *Bulletin of the Seismological Society of America*, vol. 105, no. 2A, pp. 981–992, 2015.
- [5] W. L. Ellsworth, “Injection-induced earthquakes,” *Science*, vol. 341, no. 6142, p. 1225942, 2013.
- [6] T. R. Harper, “Effective stress history and the potential for seismicity associated with hydraulic fracturing of shale reservoirs,” *Journal of the Geological Society*, vol. 171, no. 4, pp. 481–492, 2014.
- [7] S. E. Hough, L. Seeber, and J. G. Armbruster, “Intraplate triggered earthquakes: observations and interpretations,” *Bulletin of the Seismological Society of America*, vol. 93, no. 5, pp. 2212–2221, 2003.
- [8] E. Brodsky and L. Lajoie, “Anthropogenic seismicity rates and operational parameters at the Salton Sea Geothermal Field,” *Science*, vol. 341, no. 6145, pp. 543–546, 2013.
- [9] H. Davis, *KWCH12 News: Earthquakes Take Toll on Harper County Courthouse*, June 2015, <http://www.kwch.com/news/local-news/earthquakes-take-toll-on-harper-county-courthouse/31183754>.
- [10] C. Frohlich, C. Hayward, B. Stump, and E. Potter, “The Dallas-Fort Worth earthquake sequence: October 2008 through May 2009,” *Bulletin of the Seismological Society of America*, vol. 101, no. 1, pp. 327–340, 2011.
- [11] C. Frohlich, “Two-year survey comparing earthquake activity and injection-well locations in the Barnett Shale, Texas,” *Proceedings of the National Academy of Sciences: Earth, Planetary and Atmospheric Sciences*, vol. 109, no. 35, pp. 13934–13938, 2012.
- [12] C. Frohlich and M. Brunt, “Two-year survey of earthquakes and injection/production wells in the Eagle Ford Shale, Texas, prior to the Mw4.8 20 October 2011 earthquake,” *Earth and Planetary Science Letters*, vol. 379, pp. 56–63, 2013.
- [13] S. Horton, “Disposal of hydrofracking waste fluid by injection into subsurface aquifers triggers earthquake warm in Central

- Arkansas with potential for damaging earthquake,” *Seismological Research Letters*, vol. 83, no. 2, pp. 250–260, 2012.
- [14] W. Y. Kim, “Induced seismicity associated with fluid injection into a deep well in Youngstown, Ohio,” *Journal of Geophysical Research: Solid Earth*, vol. 118, no. 7, pp. 3506–3518, 2013.
- [15] C. D. Klose, “Human-riggered earthquakes and their impacts on human security, achieving environmental security: ecosystem services and human welfare,” in *NATO Science for Peace and Security Series-: Human and Societal Dynamics* vol. 69, pp. 13–19, P. H. Liotta Ed., IOS Press, Amsterdam, Netherlands, 2010.
- [16] L. Seeber, J. G. Armbruster, and W. Y. Kim, “A fluid-injection-triggered earthquake sequence in Ashtabula, Ohio: implications for seismogenesis in stable continental regions,” *Bulletin of the Seismological Society of America*, vol. 94, no. 1, pp. 76–87, 2004.
- [17] J. H. Healy, W. W. Rubey, D. T. Griggs, and C. B. Raleigh, “The Denver earthquakes,” *Science*, vol. 161, no. 3848, pp. 1301–1310, 1968.
- [18] C. B. Raleigh, J. H. Healy, and J. D. Bredehoeft, “An experiment in earthquake control at Rangely, Colorado,” *Science*, vol. 191, no. 4233, pp. 1230–1237, 1976.
- [19] G. Atkinson, K. Assatourians, B. Cheadle, and W. Greig, “Ground motions for three recent earthquakes in Western Alberta and Northeastern British Columbia and their implications for induced-seismicity hazard in eastern regions,” *Seismological Research Letters*, vol. 86, no. 3, pp. 1022–1031, 2015.
- [20] G. Atkinson, H. Ghofrani, and K. Assatourians, “Impact of induced seismicity on the evaluation of seismic hazard: Some preliminary considerations,” *Seismological Research Letters*, vol. 86, no. 3, pp. 1009–1021, 2015.
- [21] Christian Science Monitor, *Scientists: “Fracking” Should Be Part of Assessing Earthquake Hazards*, October 2014, <http://www.csmonitor.com/Environment/2014/0501/Scientists-Fracking-should-be-part-of-assessing-earthquake-hazards>.
- [22] J. K. Mitchell and R. A. Green, “Some induced seismicity considerations in geo-energy resource development,” *Geomechanics for Energy and the Environment*, vol. 10, pp. 3–11, 2017.
- [23] E. P. Chamberlayne, *Risky Buisness: “Fracking” and U.S. Army Infrastructure, Civilian Research Project*, Army War College Fellow, United States Army War College, Carlisle, PA, USA, 2015.
- [24] R. R. Burchett, K. V. Luza, O. J. Van Eck, and F. W. Wilson, *Seismicity and Tectonic Relationships of the Nemaha Uplift and Midcontinent Geophysical Anomaly (Final Project Summary)*. Vol. 4, Special Publication 85-2, Oklahoma Geological Survey, Norman, OK, USA, 1985.
- [25] K. M. Keranen, H. M. Savage, G. A. Abers, and E. S. Cochran, “Potentially induced earthquakes in Oklahoma, USA: links between wastewater injection and the 2011 Mw 5.7 earthquake sequence,” *Geology*, vol. 41, no. 6, pp. 699–702, 2013.
- [26] K. M. Keranen, M. Weingarten, G. Abers, B. Bekins, and S. Ge, “Sharp increase in central Oklahoma seismicity since 2008 induced by massive wastewater injection,” *Science*, vol. 345, no. 6195, pp. 448–451, 2014.
- [27] B. Oskin, *Fracking-Linked Earthquakes May Strike Far From Wells*, Live Science, May 2014, <http://www.livescience.com/45322-fracking-wastewater-farther-earthquakes.html>.
- [28] C. Ramsay, *4.3 Magnitude Earthquake Hits Near Rocky Mountain House*, Global News, August 2014, <http://globalnews.ca/news/1501147/earthquake-hits-northeast-of-rocky-mountain-house-power-outages-reported/>.
- [29] C. Frolich, W. Ellsworth, W. Brown et al., “The 17 May 2012 M 4.8 earthquake near Timpson, East Texas: an event possibly triggered by fluid injection,” *Journal of Geophysical Research: Solid Earth*, vol. 119, no. 1, pp. 581–593, 2014.
- [30] J. Malewitz, *After Surprise Quakes, North Texans Speak of Impact*, The Texas Tribune, Austin, TX, USA, June 2014, <http://www.texastribune.org/2014/01/03/texans-see-answers-drillings-link-earthquakes/>.
- [31] USGS—U.S. Geologic Survey, *Cherokee Oklahoma Earthquake Did You Feel It Archive Page*, U.S. Geological Survey, Reston, VA, USA, June 2015, <http://earthquake.usgs.gov/earthquakes/dyfi/events/us/c000tmeb/us/index.html>.
- [32] Associated Press, *Quake Slightly Damages Alfalfa County Courthouse*, Muskogee Phoenix, June 2015, [http://www.muskogeejournal.com/news/oklahoma\\_news/quake-slightly-damages-alfalfa-county-courthouse/article\\_e199f496-adc4-11e4-884a-978d3fa3aa8a.html](http://www.muskogeejournal.com/news/oklahoma_news/quake-slightly-damages-alfalfa-county-courthouse/article_e199f496-adc4-11e4-884a-978d3fa3aa8a.html).
- [33] D. Lefler, *The Wichita Eagle 2014: Kansans Clean up after Magnitude-4.8 Earthquake Shakes Wichita, Southern Part of State*, November 2014, <http://www.kansas.com/news/local/article3847222.html>.
- [34] A. Bickel, *Age, Quakes Escalate Damage at Harper Co. Courthouse at More Than \$1.1M*, Kansas Agland, June 2015, [http://www.kansasagland.com/news/stateagnews/age-quakes-escalate-damage-at-harper-co-courthouse-at-more/article\\_7d0f1168-4832-56a5-8236-2fe1f538590a.html](http://www.kansasagland.com/news/stateagnews/age-quakes-escalate-damage-at-harper-co-courthouse-at-more/article_7d0f1168-4832-56a5-8236-2fe1f538590a.html).
- [35] USGS—U.S. Geologic Survey, *Kansas 4.9 Earthquake*, U.S. Geological Survey, Reston, VA, USA, June 2015, [http://earthquake.usgs.gov/earthquakes/eventpage/usc000swru#general\\_summary](http://earthquake.usgs.gov/earthquakes/eventpage/usc000swru#general_summary).
- [36] J. Mack, *Michigan Earthquake Causes Minor Building Damage Near Galesburg Epicenter*, Mlive, June 2015, [http://www.mlive.com/news/kalamazoo/index.ssf/2015/05/michigan\\_earthquake\\_causes\\_min.html](http://www.mlive.com/news/kalamazoo/index.ssf/2015/05/michigan_earthquake_causes_min.html).
- [37] USGS—U.S. Geologic Survey, *M4.2—8 km S of Galesburg*, U.S. Geological Survey, Lansing, MI, USA, June 2015, [http://earthquake.usgs.gov/earthquakes/eventpage/us20002avh#scientific\\_summary](http://earthquake.usgs.gov/earthquakes/eventpage/us20002avh#scientific_summary).
- [38] M. C. L. Quinn and O.-D. S. Taylor, “Hazard topography: visual approach for identifying critical failure combinations for infrastructure,” *Natural Hazards Review*, vol. 15, no. 4, p. 04014012, 2014.
- [39] O.-D. S. Taylor, “Use of an energy-based liquefaction approach to predict deformation in silts due to pile driving,” Ph.D. dissertation, University of Rhode Island, Kingston, RI, USA, 2011.
- [40] J. J. Bommer, B. Dost, B. Edwards et al., “Developing an application-specific ground-motion model for induced seismicity,” *Bulletin of the Seismological Society of America*, vol. 106, no. 1, pp. 158–173, 2016.
- [41] D. E. Hudson, *Reading and Interpreting Strong Motion Accelerograms*, Earthquake Engineering Research Institute, Berkeley, CA, USA, 1979.
- [42] M. F. Riemer, W. B. Gookin, J. D. Bray, and I. Arango, *Effects of Loading Frequency and Control on the Liquefaction Behavior of Clean Sands*, Geotechnical Engineering Rep. UCB/GT/94-07, University of California, Berkeley, CA, USA, 1994.
- [43] R. Green and G. Terri, “Number of equivalent cycles concept for liquefaction evaluations—revisited,” *Journal Geotechnical and Geoenvironmental Engineering*, vol. 131, no. 4, pp. 477–488, 2005.
- [44] H. B. Seed and I. M. Idriss, “Simplified procedure for evaluating soil liquefaction potential,” *Journal of the Soil Mechanics and Foundations Division*, vol. 97, no. SM9, pp. 1249–1273, 1971.
- [45] H. B. Seed, I. M. Idriss, F. Makdisi, and N. Banerjee, *Representation of Irregular Stress Time Histories by Equivalent Uniform Stress Series in Liquefaction Analysis*, Tech. Rep. EERC 75–29, Earthquake Engineering Research Center, College of Engineering, University of California, Berkeley, CA, USA, 1975.
- [46] Z. Wang, “Seismic hazard assessment: issues and alternatives,” *Pure and Applied Geophysics*, vol. 168, no. 1-2, pp. 11–25, 2010.

## Research Article

# Seismic Response of Tunnel Lining for Shallow-Bias Tunnel with a Small Clear Distance under Wenchuan Earthquake

Yang Hui <sup>1,2</sup>, Jiang Xueliang,<sup>1,2</sup> and Lian Pengyuan<sup>1</sup>

<sup>1</sup>College of Civil Engineering, Central South University of Forestry and Technology, Changsha, Hunan 410018, China

<sup>2</sup>Rock and Soil Engineering Research Institute, Central South University of Forestry and Technology, Changsha, Hunan 410018, China

Correspondence should be addressed to Yang Hui; yanghui-dd@163.com

Received 25 December 2017; Revised 10 March 2018; Accepted 1 April 2018; Published 2 May 2018

Academic Editor: Hugo Rodrigues

Copyright © 2018 Yang Hui et al. This is an open access article distributed under the Creative Commons Attribution License, which permits unrestricted use, distribution, and reproduction in any medium, provided the original work is properly cited.

In order to study the internal force characteristics of shallow-bias tunnel with a small clear distance in earthquake, a large-scale shaking table slope model test was designed, and the geometric scale was 1 : 10. In the model test, the Wenchuan (WC) seismic wave was used as the excitation wave. Then, the three-dimensional numerical model was established by using MIDAS-NX, and the reliability of the numerical model was verified by comparing the acceleration of the test results. The axial force, bending moment, and shear force of the tunnel cross section and longitudinal direction were calculated by the numerical model under different excitation directions included the horizontal direction ( $X$ ), the vertical direction ( $Z$ ), and the horizontal and vertical direction ( $XZ$ ). The results show the following. (1) The internal force of right arch foot of left hole and the left arch foot of right hole is larger than other part of the tunnels because the distance between the two tunnels is smaller and they interact with each other. (2) The loading direction of single direction loading method is different and the variation trend of tunnel force are different, so the loading direction of seismic wave has a significant influence on the seismic force response of the tunnel. (3) All of the internal force values of tunnel lining under the seismic wave action in bidirection are larger than those in single direction. The value is not a simple superposition of two directions and has some coupling effect. The influence of the vertical seismic wave cannot be ignored in dynamic response research. These results improve the understanding of the rock slope with small spacing tunnel under seismic action.

## 1. Introduction

As an important form of traffic structure, the unsymmetrical loading tunnels usually appear when building roads and railways in hilly, mountainous, sloping areas. Compared with the general tunnel, the bias tunnel has the following characteristics: thin covering rock and soil, asymmetric pressure of surrounding rock, and poor dynamic stability of the whole tunnel. In recent years, earthquakes occur frequently in our country. In Wenchuan earthquake, many tunnels were damaged which including bias tunnels. In all the influence factors of tunnel damage [1], the buried depth is one of the main factors. The tunnel will be constrained greater by surrounding rock with the increase of its depth and will be suffered less damage in earthquake. But in

practical engineering, there are many shallow-buried bias tunnels due to topographic conditions, route planning, project cost, and environmental influence. In this condition, the distance between the two tunnels cannot conform to the standard requirements and the pressure on tunnel lining is not even, so many unsymmetrical loading neighborhood tunnels with shallow depth were constructed and, they would be damaged more serious in earthquake.

The dynamic response of tunnels against earthquake has been a subject of intense study after the Wenchuan earthquake and the research, mainly focusing on the experiment and numerical simulation. The shaking table test can simulate the process of earthquake well; it is the most direct and effective method to study the seismic response and failure mechanism of tunnel structure in the laboratory and is one

of the important methods in earthquake research. In recent years, many scholars have studied the response of the tunnel under earthquake action by model tests and obtained some valuable results [2–13]. The longitudinal distances of 100 m in the portal section of Galongla tunnel were selected as the prototype to conduct large-scale shaking table test by Shuping et al. [4]; the results showed that the tunnel vibrates synchronously with the surrounding soil and do not show the natural vibration frequency of itself. In order to research the tunnel structure, seismic responses, and the tunnel-surrounding rock interaction, a large-scale 3D shaking table model test was carried out by Hua et al. [5]. Lianjin et al. [6] researched the dynamic response in the portal section of the mountain tunnel with different gradients of upward slope based on large-scale shaking table test. The analysis results showed that an amplified effect of acceleration and displacements of tunnel structures exist at the entrance of the tunnel and there is not much difference in the law of the amplification effect for different gradients of upward slope. In the paper by Feng et al., [7] shaking table tests for seismic response of tunnels were conducted which considering that the tunnel diseases caused by earthquake are different in various depths. In the work of Dong et al., [8] a large-scale shaking table model test is conducted to study the dynamic behavior of entrance slope and its interaction with lining structure of mountain tunnel under earthquake loading. Test results showed that the acceleration response of tunnel entrance slope exhibits obvious amplification effect and surface effect along both vertical and axial directions.

In addition, many scholars also have studied the seismic response of tunnel by numerical simulation. Based on the ABAQUS, Yong [14] studied the effects of tunnel depth, tunnel space, lining stiffness, the properties of surrounding rock, seismic wave incident angle, and seismic intensity on the seismic response of shallow double-hole tunnels. In the paper by Jinsong [15], based on the background of Chongqing Shuangbei tunnel, the three-dimensional numerical model of large section tunnel hole body complex lining was build to research the seismic response calculation and analysis under earthquake. Kunpeng [16] analyzed the seismic dynamic response of unsymmetrically loaded tunnel with the numerical simulation method; it suggested that the unsymmetrical load can increase the entrance length, and the asymmetry of the dynamic response of the tunnel decreased with the increase of the slope soil thickness. The results of numerical calculation are a supplement to the experimental research [16–21].

Although numerous investigation and studies on dynamic response of tunnels have been thoroughly accomplished by many researchers, a few studies have been performed about the internal force of shallow-bias tunnel under seismic actions. In this paper, in order to obtain the internal force of shallow-buried tunnels with small distance under seismic action, a shaking table test was carried out. A three-dimensional numerical model was established by using MIDAS-NX, and the reliability of the numerical model was verified by comparing the acceleration of the test results. This numerical model was used for analyzing the change rule of the internal force of tunnel lining.



FIGURE 1: Model box.

## 2. Shaking Table Test

**2.1. Test Model.** In this test, the rigid model box (Figure 1) was used, and its internal dimensions was 3.5 m (length)  $\times$  1.5 m (width)  $\times$  2.1 m (height). The perspex plates were installed on both sides of the box. The box was opened at one end for filling material, installing sensor, and observing experimental process.

In order to reducing the reflection of seismic waves and the friction on the contact surface of the model and the model box [22, 23], the polystyrene foam board was pasted on the inner wall of the left and right sides of the model box, and a layer of PVC film was pasted on the polystyrene foam board. The middle sand and crushed stone were used at the bottom of the model box to increase the friction of the cement mortar and the bottom plate and also reduce the relative slip during the vibration.

**2.2. Similarity Relation Design.** According to the purpose of this test, the geometric similarity ratio, the acceleration similarity ratio, and the density similarity ratio were used as the main control parameters of the model. The table size, maximum weight capacity, boundary effect of the vibration, and the effect of model material were also comprehensively considered. According to similarity theory, the geometric similarity ratio was 1 : 10, the acceleration similarity ratio was 1 : 1, and the density similarity ratio was 1 : 1; other main similarity constants were deduced by similarity theory and dimensional analysis method.

In this test, it was assumed that the tunnel bias was caused by topographic factors and the gradient of rock slope at the top of tunnel was 1 : 1.5. The rock mass from top to bottom were Weak-weathered rock, Poor rock, and Hard rock, respectively. The rock mass was made of cement mortar which physical and mechanical properties was similar. The mixed proportion from top to bottom is 1 : 6.30 : 1.17 (cement : sand : water) of M7.5 mortar, 1 : 7.25 : 1.35 (cement : sand : water) of M5 mortar, and 1 : 5.58 : 1.04 (cement : sand : water) of M10 mortar, respectively. The tunnel size was designed to be a net height of 60 cm and a net width of 70 cm; the buried depth was 0.9 m and thickness of the middle partition wall was 0.4 m (Figure 2).

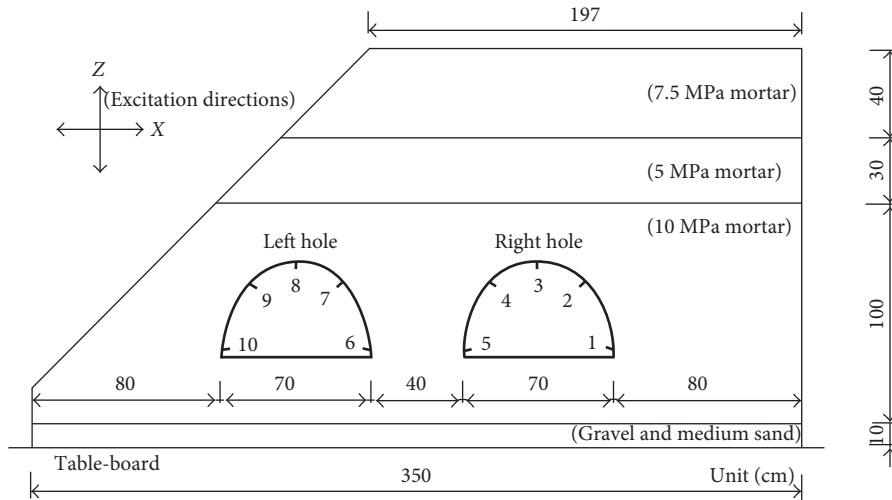


FIGURE 2: Slope model and locations of transducers.

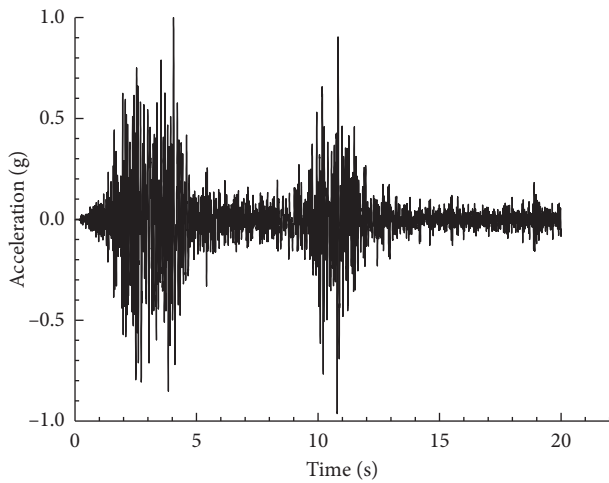


FIGURE 3: Acceleration time-history of Wenchuan seismic wave.

TABLE 1: Loading rule of shaking table test.

Serial number	Working condition	Acceleration peak (g)	
		X	Z
1	WN-1	—	—
2	WC-X-1	0.1	—
3	WC-Z-1	—	0.067
4	WC-XZ-1	0.1	0.067
5	WN-2	—	—
6	WC-X-2	0.2	—
7	WC-Z-2	—	0.133
8	WC-XZ-2	0.2	0.133
9	WN-3	—	—
10	WC-X-3	0.4	—
11	WC-Z-3	—	0.267
12	WC-XZ-3	0.4	0.267
13	WN-4	—	—
14	WC-X-4	0.6	—
15	WC-Z-4	—	0.4
16	WC-XZ-4	0.6	0.4
17	WN-5	—	—

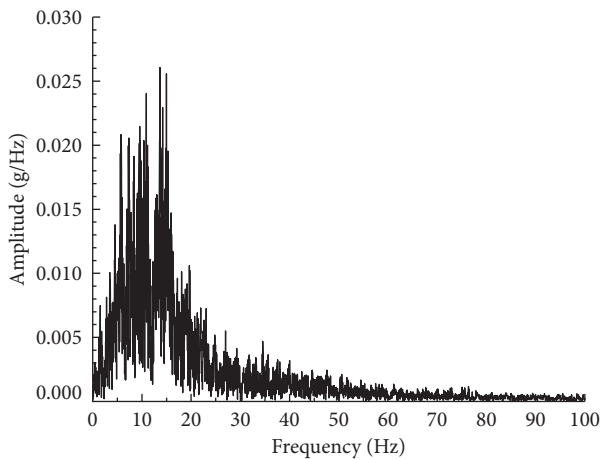


FIGURE 4: Fourier spectrum of Wenchuan seismic wave.

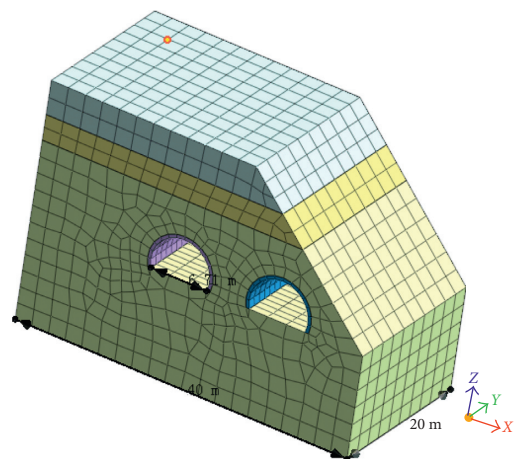


FIGURE 5: Numerical model.

The tunnel lining was made of microconcrete which was similar to the physical properties of concrete. Steel bar was simulated with galvanized iron wire. According to the similarity constant, the thickness of tunnel lining was 4 cm. After several times of proportioning test, the optimum tunnel lining material ratio was 1:6.9:1.3 (cement:sand:water). The strength of lining was converted to 5 MPa in accordance with stress similitude ratio.

The data which included acceleration, dynamic strain, and displacement were collected in the test. Its type was 1221L-002, the range was  $\pm 20 \text{ m}\cdot\text{s}^{-2}$ , and sensitivity was 2000 mv/g. A total of 20 accelerometer sensors, and 30 strain gauges were arranged in the test. The sensors were arranged on the inner wall of each tunnel lining, separately in the arch foot, arch spandrel, arch vault, because they were the key parts of maximum stress and maximum deformation, as shown in Figure 2. The measuring point number is 1–5 for the right hole and 6–10 for the left hole.

**2.3. Seismic Wave Loading.** The test was performed in High Speed Railway Construction Technology in Central South University. The vibrating table system consists of one fixed platform and three mobile platforms and these four vibrating tables are in the same line. All of the platforms have six degrees of freedom and the dimensions are 4.0 m (length)  $\times$  4.0 m (width); the working frequency of those test systems is 0.1–50 Hz. The maximum displacement of X, Y, Z direction is 250 mm, 250 mm, 160 mm, the maximum acceleration in each direction is  $\pm 1.0 \text{ g}$ , and the maximum seismic vibration velocity is 1000 mm/s.

The Wenchuan artificial wave was input to simulate earthquake. The main frequency was around 5–25 Hz, and each loading time was 20 s, as shown in Figures 3 and 4. Table 1 shows the loading scheme in the test. Seismic wave was applied with peak accelerations of 0.1 g, 0.2 g, 0.4 g, and 0.6 g in X direction and 2/3 of the X direction in Z direction. The white noise input peak wave was applied before seismic wave loading.

### 3. Numerical Simulation Analysis

**3.1. Numerical Simulation Model.** In this paper, MIDAX/NX software is used to analyze the dynamic response of the tunnel. The main parameters of the numerical model are as follows: the total length is 40 m; the height is 17 m; the length of tunnel is 15 m; and the thickness of tunnel lining is 0.4 m. The surrounding rocks and linings are modeled using three-dimensional solid elements, and the total number of units is 75,979 according to the results, as shown in Figure 5. Physical and mechanical parameters of surrounding rocks and linings are shown in Tables 2 and 3. In numerical calculation, the mechanical behavior of elements obeyed elastic-plastic constitutive relation and Mohr–Coulomb yield criterion.

**3.2. Verification of Numerical Calculation Model.** If MIDAX/NX numerical model is used to analyze the dynamic response of the tunnel, it must be verified that this model can match the experimental model well. So the

TABLE 2: Rock material parameters.

Materials	III-fair rock	IV-poor rock	III-hard rock
$E$ (MPa)	6000	1300	18,900
$\mu$	0.3	0.25	0.3
$\Phi$ ( $^\circ$ )	37	30	50
$C$ (kPa)	700	200	1500
$\gamma$ ( $\text{kN}\cdot\text{m}^{-3}$ )	23	20	25
$\sigma_c$ (MPa)	75	50	100
Thickness (m)	5	3	13

TABLE 3: Lining calculation parameters.

$E$ (GPa)	$\mu$	$\gamma$ ( $\text{kN}\cdot\text{m}^{-3}$ )	Thickness (m)
34.5	0.167	24	0.4

TABLE 4: Comparison of acceleration response peak value in the vertical direction (unit:  $\text{m}\cdot\text{s}^{-2}$ ).

Measuring points	0.2 g		0.4 g	
	Shaking table test	Numerical simulation	Shaking table test	Numerical simulation
1	1.75	1.38	3.48	3.04
2	0.88	0.42	1.72	1.51
3	1.76	1.41	3.22	2.85
4	0.86	0.78	1.73	1.62
5	1.69	1.38	3.21	2.54

TABLE 5: Comparison of acceleration response peak value in the horizontal direction (unit:  $\text{m}\cdot\text{s}^{-2}$ ).

Measuring points	0.2 g		0.4 g	
	Shaking table test	Numerical simulation	Shaking table test	Numerical simulation
1	1.95	2.11	3.45	3.79
2	1.05	1.17	1.91	1.56
3	2.09	1.95	3.84	3.45
4	1.96	1.68	3.7	3.3
5	1.93	1.91	3.53	3.65
6	0.94	0.89	1.88	2.18
7	2.1	1.85	3.85	3.71
8	1.05	1.22	1.94	1.56
9	2.08	1.79	3.75	3.51
10	3.12	2.76	5.75	5.29

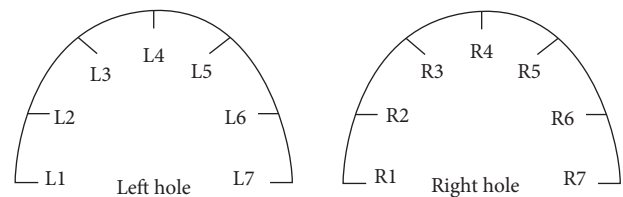


FIGURE 6: Numerical calculation points.

seismic wave input is same as the test. After calculation, the peak acceleration at same position of lining is compared. Comparison of acceleration response peak value under WC–Z seismic wave and WC–X seismic wave is shown in Tables 4 and 5, respectively.

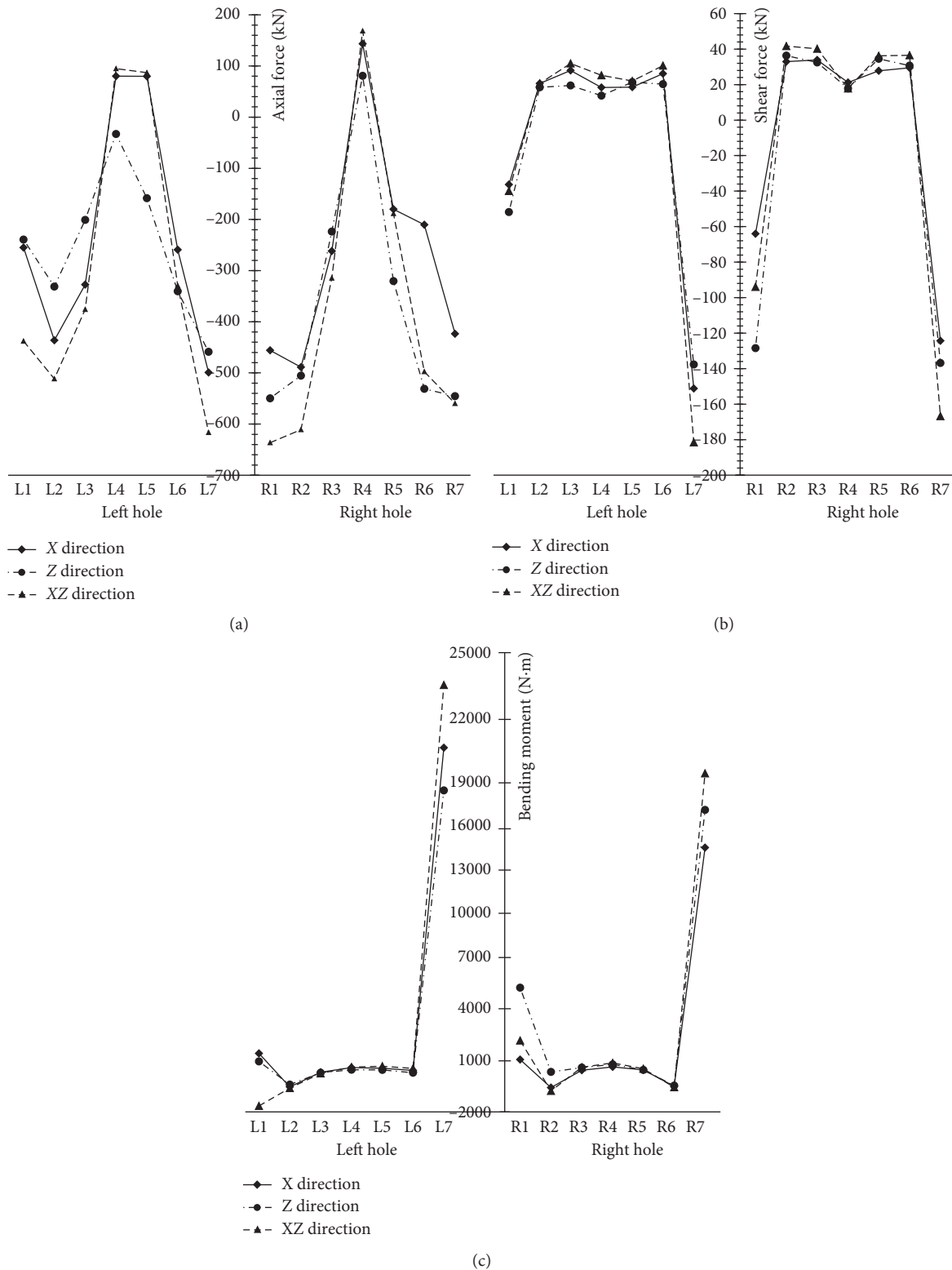


FIGURE 7: The internal force of lining cross section. (a) Axial force. (b) Shear force. (c) Bending moment.

The analysis shows that the trend of change for peak acceleration is basically the same and the error is within a reasonable range. The numerical model can be used to calculate and analyze the dynamic response of tunnel under many complex conditions when the experiment cannot be simulated in practical.

3.3. *Internal Force Analysis of Tunnel Lining Cross Section.* According to the test results and numerical analysis, the acceleration and strain reach the maximum at the peak of seismic wave, so the internal force analysis in this paper refers to the tunnel lining at the peak time of the seismic

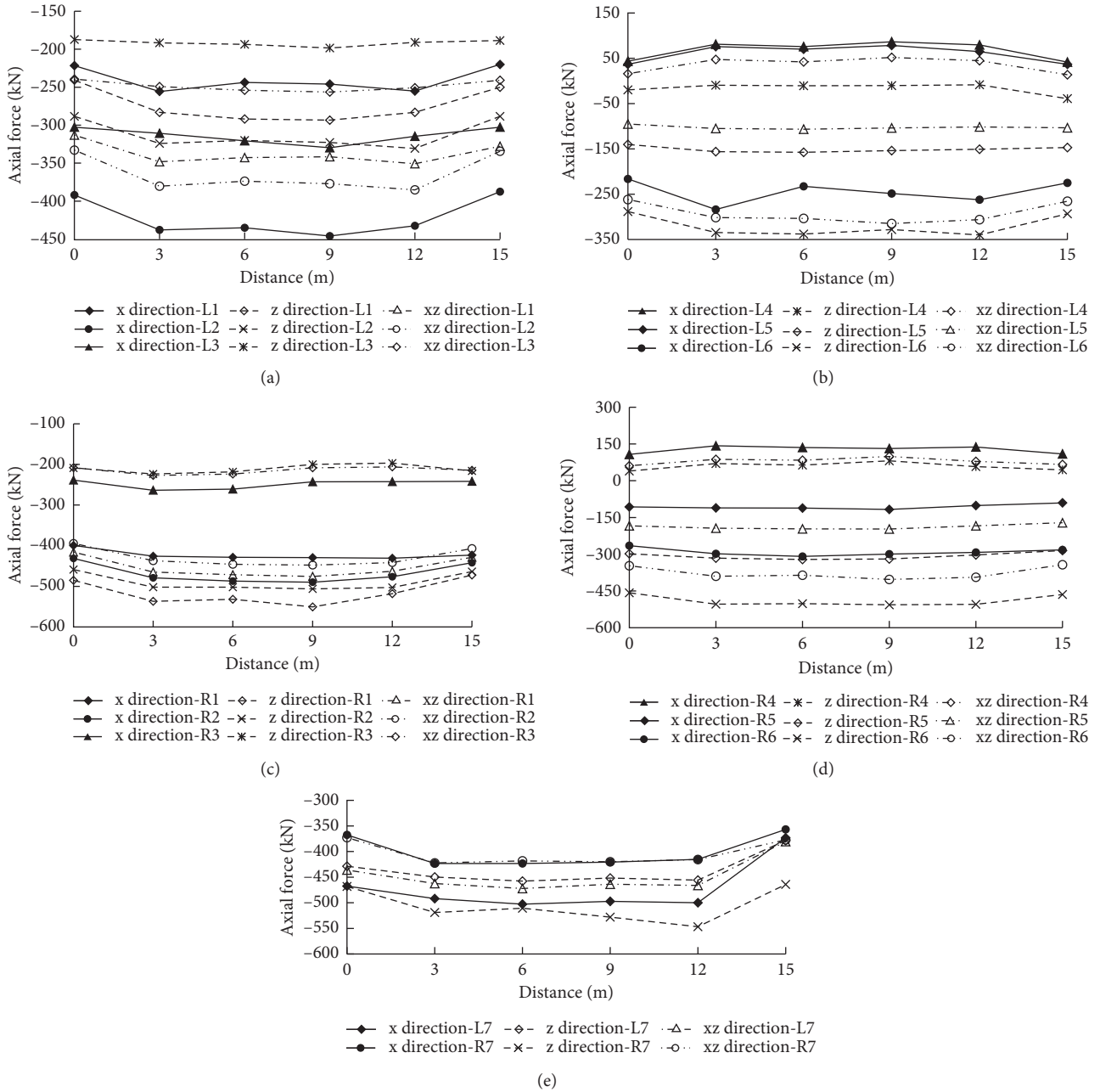


FIGURE 8: The axial force of tunnel lining along longitudinal direction.

wave. In the following paper, the number of measuring points is L1~L7 in the left hole and R1~R7 in the right hole; the detailed measuring points are shown in Figure 6.

Figure 7, under the action of horizontal seismic waves, to the left tunnel, the vault and right spandrel are tensiled and the others are compressed. The maximum pressure is on the right arch foot and its value is 499.3 kN. To the right tunnel, the vault is tensiled and the others are compressed; the maximum pressure is on the left arch waist and its value is 488.8 kN. The change of shear force is similar for both linings, the maximum shear force is on the right arch foot, and the value is -151.2 kN for the left hole and 124.3 kN for the right hole. Sign “±” indicates different direction of force. The maximum bending moment is also on the right arch

foot; the value is 20,204.6 N·m for left hole, and 14,117.8 N·m for right hole.

Under the action of vertical seismic waves, the axial force of left tunnel lining is pressure, the maximum pressure is on the right arch foot, and its value is 458.8 kN. This is different from the horizontal seismic waves. The change of shear force and bending moment is not obvious; the maximum shear force is 137.7 kN and bending moment is 17,600 N·m. To the right hole, the axial force and shear force have similar variation trend as the tunnel lining in the horizontal seismic wave action. But the bending moment of left arch waist changes direction and the inside part is changed to the outside part. The maximum is also on right arch foot and the value is 16,410 N·m.

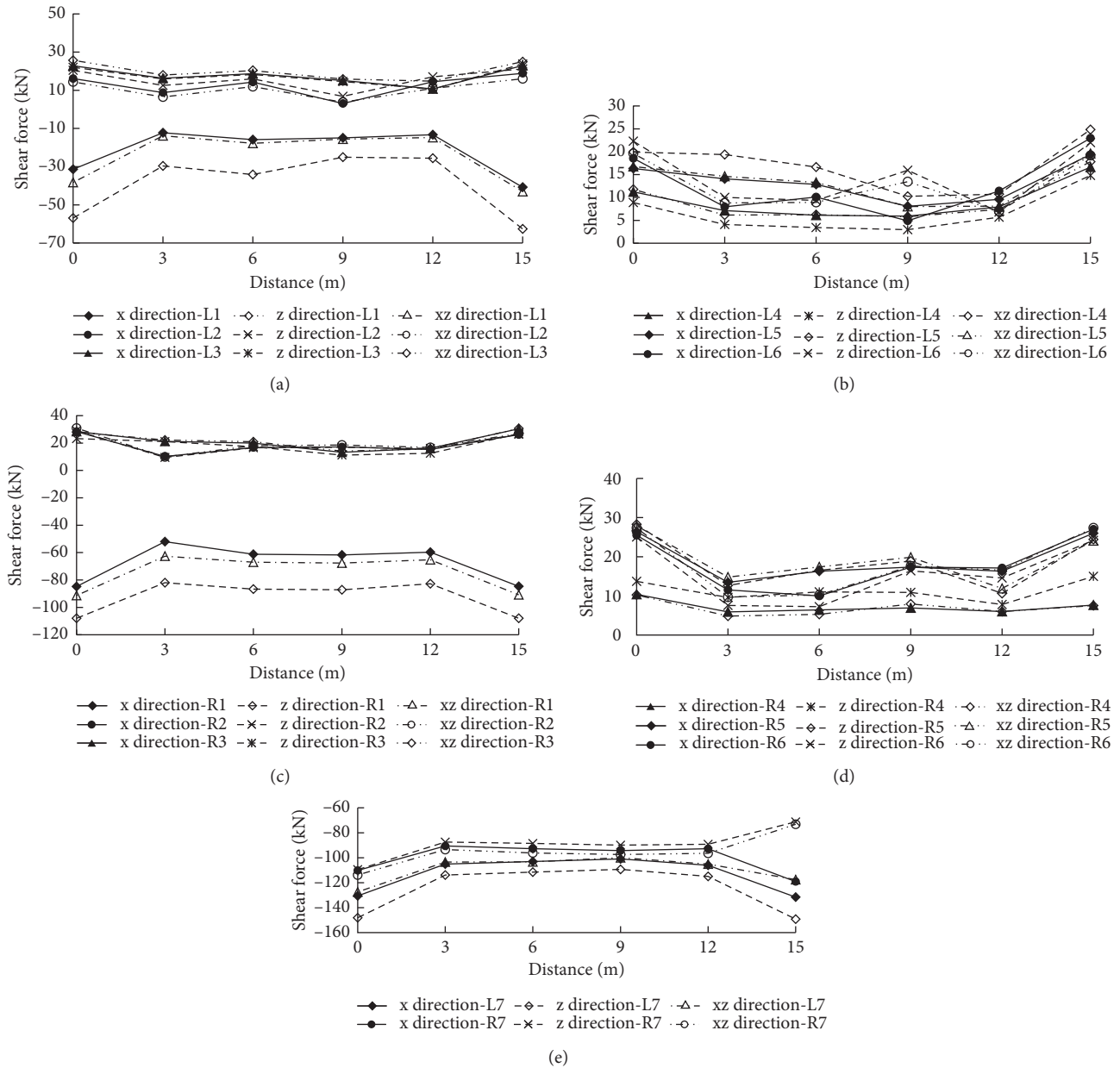


FIGURE 9: The shear force of tunnel lining along longitudinal direction.

Through the force map, the influence of vertical seismic wave to tunnel lining cannot be ignored; it must be considered in structural design.

The charts also show that all of the internal force values of tunnel lining under the seismic wave action in bidirection (XZ direction) are larger than those in single direction. But the region which contains arch foot of both linings and the left part near the free surface of left tunnel is the largest part of internal force in three seismic wave input conditions.

The internal force changes significantly in the left side of the left tunnel lining and the arch foot of the right tunnel lining. The reason is that the upper rock layer of the right hole is thick and has good stability, and it is far away from the existing slope and is less affected by the existing slope.

The left hole is close to the existing slope, and the slope has a great influence on the seismic force response of the right tunnel under the earthquake dynamic action.

### 3.4. Internal Force Changes along the Longitudinal Direction.

Under different loading modes, the internal force change along the longitudinal direction is taken as an index to investigate the difference of seismic force response of tunnel, as shown in Figures 8–10.

As shown in Figure 8, the variation of axial force in the same position is smaller along the longitudinal direction of the tunnel. To the left hole, the axial force reaches the maximum at the arch foot and the value is 502.7 kN at 6 m cross section

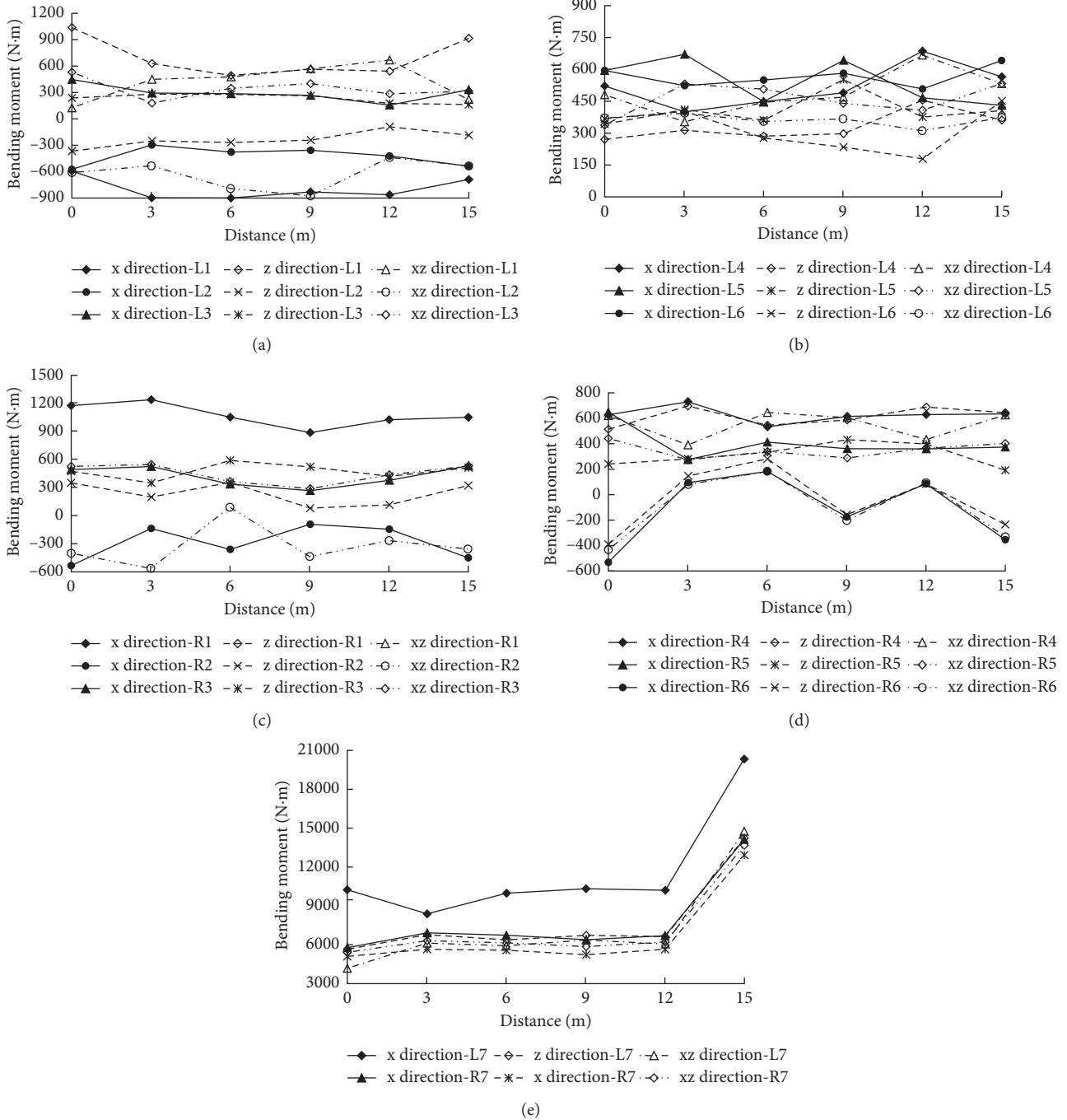


FIGURE 10: The bending moment of tunnel lining along longitudinal direction.

from the tunnel entrance in the X direction seismic wave. To the right hole, the maximum is left arch foot and the value is 550.6 kN at the 9 m cross section from the entrance in the Z direction seismic wave. Through comparison, it can be found that the axial force at the middle part of tunnel lining is larger but smaller at the entrance and exit of the tunnel.

As shown in Figure 9, it can be found that the shear force is larger at the entrance and exit of the tunnel than the other part. To the left hole, the shear force reaches the maximum at the right arch foot and the value is -149 kN at the cross section 15 m from tunnel entrance in Z direction seismic

wave and -148 kN at the cross section of tunnel entrance. To the right hole, the shear force reaches the maximum at the right arch foot and the value is -144 kN at the cross section 15 m from tunnel entrance in the XZ direction seismic wave. From Figure 9, it can be seen that the response of the left hole is more intense than the right hole. The main reason is that in the vertical direction of loading wave, the overlying strata of the right hole is thicker, the action force of the right hole is greater, and the “rise effect” has a significant impact on the shear force response of the right hole. By comparing Figures 8 and 9, it is suggested that the loading direction of single

direction loading method is different, the variation trend of tunnel force are different. It shows that the loading direction of seismic wave has a significant influence on the seismic force response of the tunnel.

As shown in Figure 10, the bending moment increases significantly at the arch foot of the tunnel in all loading modes. The maximum is located at the right arch foot of the left hole and the value is 20,339 N·m at the cross section of tunnel exit in  $x$  direction seismic wave.

By comparing Figures 8–10, it is summarized as follows:

Because distance between the two tunnels is closer, the internal force of right arch foot of left hole, and the left arch foot of right hole is larger than other part of the tunnels because they interact with each other.

Because of the influence of the existing slope on the internal force response of the tunnel, the variation trend of the internal force of the left and the right hole never show a symmetrical trend.

It can be seen that under the action of bidirectional wave loading, the variation trend of internal force in is more complex, but this trend is similar to  $X$  direction wave loading. The reason may be that the response of the vertical direction is stronger than that of the horizontal direction under the action of the bidirectional wave.

#### 4. Conclusions

The large-scale shaking table model test was carried out, and the acceleration response of the unsymmetrical loading neighborhood tunnel with shallow depth model in different directions and different acceleration peaks of Whenchuan seismic wave was obtained.

The three-dimensional numerical model of the unsymmetrical loading neighborhood tunnel with shallow depth was established by using MIDAS-NX. The acceleration and internal forces of the tunnels under the same working conditions were obtained, and the reliability of the numerical model was verified by comparing the acceleration of the tunnel lining.

The tunnel lining dynamic response under different loading modes ( $X$  direction,  $Z$  direction, and  $XZ$  direction) are studied. The axial force, shear force, and bending moment of the tunnel cross section were calculated by the numerical model under the earthquake simulation. The following conclusions are obtained: (1) The internal force of the right arch foot of the left hole and the left arch foot of the right hole is larger than the other part of the tunnels because the distance between the two tunnels is closer and they interact with each other. (2) All of the internal force values of tunnel lining under the seismic wave action in bidirection are larger than those in single direction. The value is not a simple superposition of two directions and has some coupling effect. The influence of the vertical seismic wave cannot be ignored in dynamic response research.

#### Conflicts of Interest

The authors declare that they have no conflicts of interest.

#### Acknowledgments

The authors are grateful for financial support from the National Natural Science Foundation (NNSF) of China through Grant nos. 51204215 and 51404309.

#### References

- [1] H. Min, L. Maqun, W. Anhua et al., "The research of tunnel earthquake damage forms and the reasons," *Technology and Economy in Area Communications*, vol. 57, no. 1, pp. 60–62, 2010.
- [2] W. Zhengzheng, G. Bo, and S. Ranxu, "Shaking table tests on entrance anti-seism of double track tunnels," *China Journal of Highway and Transport*, vol. 22, no. 2, pp. 71–76, 2009.
- [3] L. Lin, H. Chuan, G. Ping et al., "Study of shaking table model test for seismic response of portal section of shallow unsymmetrical loading tunnel," *Chinese Journal of Rock Mechanics and Engineering*, vol. 30, no. 12, pp. 2540–2548, 2011.
- [4] J. Shuping, W. Dongliang, and Z. Shengbao, "Large-scale shaking table test for seismic response in portal section of Galongla tunnel," *Chinese Journal of Rock Mechanics and Engineering*, vol. 30, no. 4, pp. 649–656, 2011.
- [5] X. Hua, L. Tianbin, W. Dong et al., "Study of seismic response of mountain tunnels with 3D shaking table model test," *Chinese Journal of Rock Mechanics and Engineering*, vol. 32, no. 9, pp. 1762–1771, 2013.
- [6] T. Lianjin, H. Sen, Z. Xu et al., "Large-scale shaking table test for dynamic response in portal section of mountain tunnel with different gradients of upward slope," *Rock and Soil Mechanics*, vol. 35, no. 1, pp. 91–98, 2014.
- [7] G. Feng, S. Changxin, T. Xukai et al., "Shaking table tests for seismic response of tunnels with different depths," *Rock and Soil Mechanics*, vol. 36, no. 9, pp. 2517–2523, 2015.
- [8] W. Dong, G. Bo, S. Yu-sheng et al., "Shaking table test study of seismic dynamic response of tunnel entrance slope," *Rock and Soil Mechanics*, vol. 35, no. 7, pp. 1921–1928, 2014.
- [9] M. Guowang, Z. Jiamei, and G. Bo, "Seismic responses of fiber reinforced concrete tunnel lining with shaking table test," *Chinese Journal of Rock Mechanics and Engineering*, vol. 35, no. 6, pp. 1173–1181, 2016.
- [10] J. Xueliang, N. Jiayong, Y. Hui et al., "Large-scale shaking table test study on seismic response characteristics of rock slope with small spacing tunnel," *Engineering Mechanics*, vol. 34, no. 5, pp. 132–147, 2017.
- [11] J. Xueliang, L. Pengyuan, Y. Hui et al., "Large-scale shaking table model test study of unsymmetrical loading neighborhood tunnel with shallow depth," *Chinese Journal of Applied Mechanics*, vol. 34, no. 3, pp. 456–463, 2017.
- [12] F. Wang, X. Jiang, and J. Niu, "The large-scale shaking table model of shallow-bias tunnel with small clear distance," *Geotechnical and Geological Engineering*, vol. 35, no. 3, pp. 1093–1110, 2017.
- [13] H. Min, *Study on Seismic Dynamic Response of Shallow Double-Hole Tunnels*, M.S. thesis, Southwest Jiaotong University, Chengdu, China, 2009.
- [14] W. Yong, *Study on Seismic Response Law of Shallow Double-Hole Tunnels*, Ph.D. thesis, University of Petroleum, Qingdao, China, 2013.
- [15] M. A. Jingson, *Dynamic Response Characteristic Analysis on Complex Lining of Tunnel under Earthquake*, Ph.D. thesis, Chongqing Jiaotong University, Chongqing, China, 2016.
- [16] D. Kunpeng, *Study on Seismic Dynamic Response of Unsymmetrically Loaded Tunnel under Strong Earthquakes*, Ph.D. thesis, Southwest Jiaotong University, Chengdu, China, 2015.

- [17] S. Tiecheng, W. Zhengzheng, W. Wei et al., "Numerical simulation analysis of seismic dynamic response of tunnel portal section with double holes," *Journal of Beijing University of Technology*, vol. 39, no. 2, pp. 220–226, 2013.
- [18] H. Lin, W. Zhong, and P. Cao, "Three-dimensional rock slope stability analysis considering the surface load distribution," *European Journal of Environmental and Civil Engineering*, vol. 20, no. 8, pp. 877–898, 2016.
- [19] G. Lanzano, E. Bilotta, G. Russo, and F. Silvestri, "Experimental and numerical study on circular tunnels under seismic loading," *European Journal of Environmental and Civil Engineering*, vol. 19, no. 5, pp. 539–563, 2015.
- [20] W. Feifei, J. Xueliang, Y. Hui et al., "Test and numerical simulation for acceleration response laws of a shallow buried small spacing tunnel with asymmetrical pressure," *Journal of Vibration and Shock*, vol. 36, no. 17, pp. 238–247, 2017.
- [21] S.-Y. Lin, H.-H. Hung, J. P. Yang et al., "Seismic analysis of twin tunnels by finite/infinite element approach," *International Journal of Geomechanics*, vol. 17, no. 9, p. 04017060, 2017.
- [22] H. Haohua, *The Design and Application Technology on Earthquake Simulation Vibrating Table*, Earthquake Press, Beijing, China, 2008.
- [23] Z. Yin and L. Xilin, *Shaking Table Model Test Method and Technology for Building Structure*, Science Press, Beijing, China, 2012.

## Research Article

# A Modified Newmark Methodology for Permanent Deformation Analysis of Rock-Fill Dams

Hongjun Li , Hong Zhong, Zuwen Yan, and Jianming Zhao

State Key Laboratory of Simulation and Regulation of Water Cycle in River Basin,  
China Institute of Water Resources and Hydropower Research, Beijing 100048, China

Correspondence should be addressed to Hongjun Li; [lihj@iwhr.com](mailto:lihj@iwhr.com)

Received 8 December 2017; Accepted 13 February 2018; Published 1 April 2018

Academic Editor: Haiyun Shi

Copyright © 2018 Hongjun Li et al. This is an open access article distributed under the Creative Commons Attribution License, which permits unrestricted use, distribution, and reproduction in any medium, provided the original work is properly cited.

Newmark sliding block approach has been extensively studied by many researchers in the past decades. Significant progress has been made to alleviate its deficiencies and overcome its simplifying assumptions, but some aspects such as the cyclic shear strength and time history vertical acceleration in the Newmark sliding displacement analysis are seldom considered strictly. In the presented research, a modified Newmark methodology for sliding deformation analysis of rock-fill dams subjected to strong earthquake is proposed. In order to make the seismic safety evaluation of dams more realistic, the influence of cyclic shear strength (earthquake-induced reduction of shear strength) and time history vertical acceleration obtained from the dynamic response analysis on the critical acceleration and accumulative sliding displacement of the flexible sliding body is considered. Detailed comparison between the proposed method and existing methods is performed via the analysis of two typical dams, that is, a virtual rock-fill dam with a height of 100 m which is assumed to be situated on rock formation and a real core rock-fill dam with a height of 150 m built on deep overburden layers. It is demonstrated that the cyclic shear strength and time history vertical acceleration within flexible sliding body, as highlighted in the proposed method, have significant effect on the seismic safety evaluation, critical acceleration, and accumulation of sliding deformation of rock-fill dams subjected to strong earthquake loading. The existing approaches tend to provide unconservative evaluation on the consequences of earthquakes on rock-fill dams.

## 1. Introduction

Nowadays, the evaluation on the seismic performance of rock-fill dams and Earth slopes subjected to strong earthquakes is performed utilizing not only the traditional force-oriented factor of safety, but also the magnitude of the accumulative earthquake-induced sliding displacement [1–3]. A strict and simple prediction of earthquake-induced sliding displacement can directly show the potential consequences of earthquakes on rock-fill dams. In 1965, an original procedure for the prediction of earthquake-induced sliding displacement was formulated by Newmark [4]. Through this research, it is revealed that irregular inertial force induced by earthquake acceleration could exert a driving force sufficient to reduce temporarily the factor of safety below one and then result in several sliding episodes during the shaking. As pointed out by Newmark, sliding

episodes in earthquakes occur when the critical acceleration is exceeded and continues until the velocity of downward movement reduces to zero. So the accumulation of permanent sliding displacement (Newmark sliding displacement), with its magnitude equal to the summation of all downward movements during the shaking, could be a useful index to evaluate the stability of slopes during earthquakes.

In the early Newmark-type method, the flexible sliding body is modeled as a rigid block, and only two parameters are used, that is, the input ground motion and the critical acceleration ( $k_y g$ , the horizontal acceleration that results in unit pseudostatic factor of safety). Due to its effectiveness and simplicity, the Newmark sliding rigid block approach has been extensively adopted and studied by many engineers and researchers in the past decades. Much great progress has been made to alleviate its limitations and overcome its simplifying assumptions; for example, the flexibility of the sliding mass is

firstly considered instead of the assumption of rigid body by Makdisi and Seed [5]. However, the research on the influence of the cyclic shear strength (or dynamic pore pressure) and time history vertical acceleration on the critical acceleration and accumulation of sliding displacement is still limited. Meanwhile, the application of this approach for the seismic stability evaluation of high rock-fill dams with a height over 250 m or around 300 m is also limited. Thus, with the development of testing apparatus and technology for cyclic shear strength of rock-fill materials under cyclic loading, it is suggested that the seismic design and assessment of the effectiveness of mitigation measures for rock-fill dams subjected to earthquake be performed strictly based on the cyclic shear strength [6–9].

On the other hand, a theoretically reasonable and practically feasible method for prediction of earthquake-triggered sliding displacement is required necessarily for the seismic design and stability analysis for emerging high rock-fill dams. Therefore, special emphasis of this paper will be placed on the determination of critical acceleration of flexible sliding body based on the cyclic shear strength and time history vertical acceleration aiming at more realistic evaluation of earthquake-induced sliding displacement of high rock-fill dams.

## 2. Cyclic Shear Strength of Rock-Fill Materials

The first aim of this study is to analyze the effect of cyclic shear strength on earthquake-induced sliding displacements using the modified Newmark method in order to improve the ability of predicting seismic stability of rock-fill dams. It must be noted that the liquefaction-induced instability has not been included in this paper. As we know, in the earthquake, instability occurs when the dynamic shear stresses required to maintain equilibrium of a soil deposit exceed the static shear strength of that deposit. Then it will recombine the structure character of soil's particle until the new equilibrium can reach. The shear strength of soil in this new equilibrium will be regarded as cyclic shear strength.

The cyclic shear strength is an important parameter in seismic design and stability analyses of rock-fill dams. For some typical rock-fill materials, such as fine sand, clay, and sand gravel, the significant cyclic loading induced by irregular strong earthquake usually leads to the obvious degeneration of the undrained shear strength [10, 11]. Some accidents of rock-fill dams occurred due to the decrease of cyclic shear strength. The postcyclic undrained shear behavior of rock-fill materials under cyclic loading has been the focus in the past decades. Nowadays, some considerable advances of testing apparatus and technology for cyclic shear strength of rock-fill materials have been obtained; for example, the cyclic triaxial undrained compress tests and simple shear tests have been used extensively to study the cyclic shear strength of rock-fill materials. From the tests, it is shown that the cyclic undrained shear strength is often related to the confining pressure ( $\sigma'_0$ ), failure number of cycles ( $N_f$ ), and the failure strain criterion (5% or 10%). In general, the correlation of undrained cyclic shear strength ( $\tau_{fs}$ ), confining pressure, and cyclic shear stress ( $\tau_d$ ) acting on the failure surface can be formulated by (1–5). In addition, it is noted that the lower value between the static

shear strength and cyclic shear strength should be adopted in the seismic design and stability analysis of rock-fill dams.

$$\sigma'_{f0} = \sigma'_0 + \tau_0 \sin \phi' \left( \frac{\tau_d > \tau_0}{\sin \phi'} \right), \quad (1)$$

$$\sigma'_{f0} = \sigma'_0 - \tau_0 \sin \phi' \left( \frac{\tau_d \leq \tau_0}{\sin \phi'} \right),$$

$$\tau_{f0} = \tau_0 \cos \phi', \quad (2)$$

$$\alpha = \frac{\tau_{f0}}{\sigma'_{f0}}, \quad (3)$$

$$(\Delta\tau_f)_n = c_r \left( \frac{\tau_d}{\sigma'_0} \right)_n \sigma'_0 \quad (\alpha < 0.15), \quad (4)$$

$$(\Delta\tau_f)_n = \left( \frac{\tau_d}{\sigma'_0} \right)_n \sigma'_0 \cos \phi' \quad (\alpha \geq 0.15),$$

$$\tau_{fs} = (\Delta\tau_f)_n + \tau_{f0} \left( \frac{\tau_d \leq \tau_0}{\sin \phi'} \right), \quad (5)$$

$$\tau_{fs} = (\Delta\tau_f)_n - \tau_{f0} \left( \frac{\tau_d > \tau_0}{\sin \phi'} \right).$$

Here,  $\sigma'_1$  and  $\sigma'_3$  are the major principle effective stress and minor principle effective stress, respectively;  $\tau_d$  is the cyclic shear stress;  $\sigma'_0$  is the initial effective confining pressure with  $\sigma'_0 = (\sigma'_1 + \sigma'_3)/2$ ;  $\tau_0$  is the initial static shear stress with  $\tau_0 = (\sigma'_1 - \sigma'_3)/2$ ;  $c_r$  is the correction coefficient of cyclic shear strength;  $\tau_{f0}$  and  $\sigma'_{f0}$  are the initial shear stress and normal stress acting on the failure surface, respectively;  $(\Delta\tau_f)_n$  is the variation of cyclic shear strength at a given number of cycles;  $n$  is the number of cycles;  $\phi'$  is the effective friction angle; and  $\alpha$  is the initial shear stress ratio on the failure surface.

For the sake of simplicity and convenience in application, based on the available data of rock-fill materials obtained by the dynamic triaxial compress tests and by referring to the mode of Mohr–Coulomb principle, the cyclic shear strength can be represented by a simple equation, as (6). Then, the cyclic shear strength of rock-fill materials can be easily determined from the number of cycles, confining pressure, and shear stress ratio on the failure surface.

$$\tau_{fs} = (\tau_{fs0})_\alpha + \tan \phi_{d\alpha} \sigma'_{f0}, \quad (6)$$

$$(\tau_{fs0})_\alpha = \tau_{fs0} + \zeta\alpha, \quad (7)$$

$$\tan \phi_{d\alpha} = \tan \phi_{d0} + \beta\alpha. \quad (8)$$

Here,  $(\tau_{fs0})_\alpha$  and  $\tan \phi_{d\alpha}$  are the equivalent cyclic cohesion and friction coefficient, respectively, which can be directly introduced into the modified Newmark sliding displacement analysis. Both of them are in proportion to the initial shear stress ratio on the failure surface, as in (7) and (8).  $\tau_{fs0}$  and  $\tan \phi_{d0}$  are the cyclic shear strength parameters as  $\alpha$  equals zero, and  $\zeta$  and  $\beta$  are proportional coefficients.

TABLE 1: Parameters of total shear strength.

Soil	$r$ (g/cm <sup>3</sup> )	$k_c$	$\sigma'_3$ (kPa)	$\sigma'_0$ (kPa)	$\tau_0$ (kPa)	$\tau_{f0}$ (kPa)	$\sigma'_{f0}$ (kPa)	$\tau_{f0}/\sigma'_{f0}$	$N = 30$		
									$\Delta\tau/\sigma'_0$	$\Delta\tau_f$	$\tau_{fs}$
Shell	2.33	1.5	1000	1250	250	196	1095	0.18	0.463	454	649
			2000	2500	500	392	2189	0.18	0.363	711	1103
		2.5	3000	3750	750	588	3284	0.18	0.319	937	1525
			1000	1750	750	588	1284	0.46	0.337	462	1050
			2000	3500	1500	1176	2568	0.46	0.216	592	1768
			3000	5250	2250	1763	3852	0.46	0.156	642	2405

TABLE 2: Parameters of cyclic shear strength.

Soil	$r$ (g/cm <sup>3</sup> )	$N_f$	$\tau_{fs0}$ (kPa)	$tg\phi_{d0}$	$\zeta$ (kPa)	$\beta$
Shell	2.33	30	108.5	0.321	485.6	0.518

TABLE 3: Parameters of the  $E$ - $\mu$  model and equivalent linear model.

Materials	$r$ (g/cm <sup>3</sup> )	$c'$ (kPa)	$\phi'$ (°)	$k$	$n$	$R_f$	$G$	$F$	$D$	$k_{ur}$	$k_1$	$n_1$
Core	1.58	86.6	23.7	202	0.51	0.87	0.25	0.04	2.2	400	1100	0.42
Shell	2.02	5	36	540	0.46	0.79	0.32	0.1	4.7	1100	1600	0.45

Based on the above mentioned description and formulations, the two main steps to obtain the cyclic shear strength are outlined as follows. First, the total shear strength under different confining pressures and consolidation ratios can be obtained from the cyclic triaxial undrained compress tests as shown in Table 1. Second, the parameters of cyclic shear strength can be determined by linear approximation as shown in Table 2.

In some occasions concerning practical rock-fill dam design, it would be convenient for the engineers to adopt directly the static undrained shear strength into the seismic design and stability analysis, if the difference between the cyclic shear strength and its static counterpart of rock-fill materials could be negligible. However, for some particular rock-fill dams, such as rock-fill dam with clay core, sand gravel dam, and rock-fill dam built on the saturated clay or sandy deposits, the impact of cyclic shear strength on the critical acceleration and accumulation of sliding displacement would be so significant that it must be carefully considered as the liquefaction does not occur. For this purpose, available data of dynamic triaxial tests on cyclic shear strength of rock-fill materials were analyzed and a correlation between cyclic shear strength and number of cycles was obtained and listed in Tables 3 and 4.

### 3. Time History Vertical Acceleration

In the existing Newmark-type sliding displacement analysis, the vertical earthquake is usually neglected or considered oversimply in the determination of critical acceleration and accumulation of permanent sliding displacement. Possible effects of vertical earthquake loading on the stability of Earth structures have not been discussed in detail although it had attracted great attention as early as in the 1920s

TABLE 4: Parameters of cyclic shear strength.

Materials	$N$ (times)	$\tau_{fs0}$ (kPa)	$\tan \phi_{d0}$	$\zeta$ (kPa)	$\beta$
Sand layer	20	0	0.209	0	1.604
	30	4.19	0.169	102.7	1.242
Sand gravel	20	55.05	0.383	237.4	0.448
	30	56.66	0.359	217.3	0.167

following the devastating Kanto Earthquake in Japan. Mononobe [12] found that a combination of horizontal and vertical accelerations led to severe damage of Earth retaining structures. Ling et al. [13] and Huang et al. [14] studied the effect of vertical acceleration on the critical acceleration and sliding displacement, in which the vertical acceleration was assumed to act constantly upwards or downwards and its value was taken as a fraction of the peak horizontal acceleration. The value of 2/3 was usually adopted as a reasonable ratio between vertical and horizontal acceleration based on the records of strong motion earthquake accelerations [15, 16].

In addition, more and more results from numerical analyses and shaking table tests revealed that the direction and phase of vertical accelerations acting on the centroid of soil slice within the flexible sliding body vary from time to time and are different for different slices during the seismic excitation, as shown in Figure 1. Consequently, it is necessary to study and clarify the influence of the distribution of time history vertical acceleration on critical acceleration and sliding displacement in order to better reflect the reality.

### 4. The Modified Newmark Methodology

In the model we developed herein, the Bishop pseudo-static limit equilibrium method is used to determine the critical acceleration time history, factor of safety, and

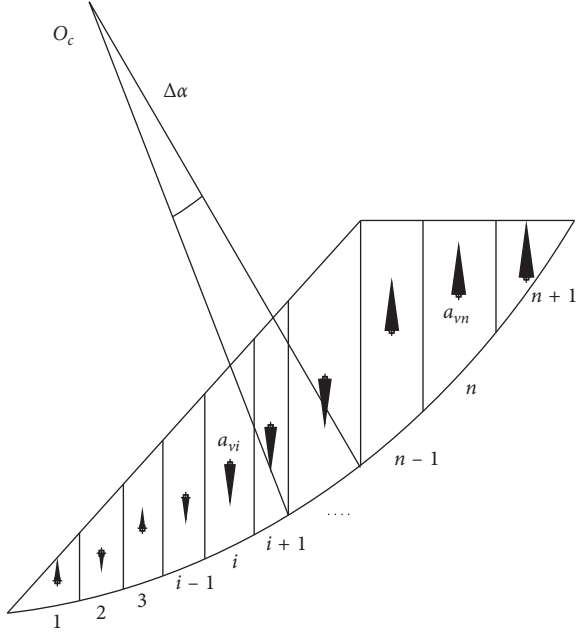


FIGURE 1: Distribution of vertical acceleration within the flexible sliding body.

location of potential slip surface [17–19]. The critical acceleration, which is still defined as the amplitude of horizontal acceleration that drives the potential sliding body into a limit equilibrium state; that is, the factor of safety equals 1.0. Noticeably, in the proposed approach, the effects of cyclic shear strength and time history vertical acceleration are considered strictly, with the detailed process shown as follows.

As shown in Figure 2, the formulation of the pseudo-static limited equilibrium method by Bishop can be rewritten by taking into consideration the cyclic shear strength ( $\tau_{fs}$ ) and time history vertical acceleration ( $a_{vi}$ ) as

$$F_s = \frac{\sum_{i=1}^{n-m} \frac{1.0}{m_{\alpha_i}} \left( ((W_i + G_i) - u_i l_i \cos \alpha_i) \tan \phi'_i + c'_i l_i \cos \alpha_i \right)}{\sum_{i=1}^n \left( (W_i + G_i) \sin \alpha_i + Q_i (R_d^i / R) \right)} + \frac{\sum_{j=1}^{m-p} \tau_{fs}^j l_j}{\sum_{i=1}^n \left( (W_i + G_i) \sin \alpha_i + Q_i (R_d^i / R) \right)} + \frac{\sum_{k=1}^p c_r^k l_k}{\sum_{i=1}^n \left( (W_i + G_i) \sin \alpha_i + Q_i (R_d^i / R) \right)}, \quad (9)$$

$$m_{\alpha_i} = \cos \alpha_i + \frac{\tan \phi'_i}{F_s} \times \sin \alpha_i, \quad (10)$$

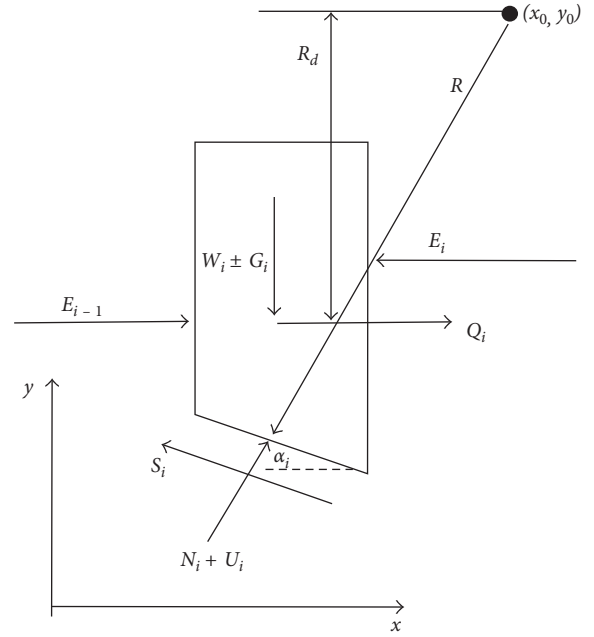


FIGURE 2: Diagram of forces acting on a soil slice.

$$Q_i = k_{h,\max} c_z a_{hi} W_i, \quad (11)$$

$$G_i = \frac{\pm W_i a_{vi}(t)}{g}, \quad (12)$$

where  $c'_i$  and  $\phi'_i$  are the static effective cohesion and friction angle, respectively;  $W_i$  is the soil weight;  $u$  is the hydrostatic pore pressure;  $Q_i$  is the horizontal inertial force obtained by (11);  $G_i$  is the vertical inertial force caused by the time history vertical acceleration, with a positive sign indicating downward direction and vice versa;  $\alpha_i$  represents the inclination of slice as shown in Figure 1;  $c_z$  is the reduction factor of horizontal inertial force, 0.25 is used in the present study;  $a_{hi}$  is the distribution coefficient of horizontal inertial force along the dam height;  $k_{h,\max}$  is the amplitude of the horizontal acceleration coefficient;  $g$  is the acceleration of gravity;  $a_{vi}$  is the time history vertical acceleration at the slice centroid obtained from dynamic response analysis;  $R_d^i$  and  $R$  are the vertical distances of the centroid from the center of the slip circle and the radius of slip circle, respectively;  $n$ ,  $m$ , and  $p$  are the total number of soil slices, number of slices considering the effect of cyclic shear strength, and number of slices where liquefaction occur, respectively;  $\tau_{fs}^i$  is the mobilized cyclic shear strength; and  $c_r$  is the residual strength of soil.

Let the factor of safety ( $F_s$ ) be 1.0, (9) can be rearranged in terms of the peak value of horizontal acceleration coefficient ( $k_{h,\max}$ ), as

$$k_{h,\max}(t) = \frac{\sum_{i=1}^{n-m} \left[ \{c' l_i \cos \alpha_i + (W_i \pm G_i - u_i l_i \cos \alpha_i) \tan \phi'_i\} \sec \alpha_i / 1 + \tan \alpha_i \tan \phi'_i \right]}{\sum_{i=1}^n W_i a_i c_z R_{di}} + \frac{\sum_{j=1}^{m-p} \tau_{fs}^j l_j}{\sum_{i=1}^n W_i a_i c_z R_{di}} \quad (13)$$

$$+ \frac{\sum_{k=1}^p c_r l_k}{\sum_{i=1}^n W_i a_i c_z R_{di}} - \frac{\sum_{i=1}^n (W_i \pm G_i) \sin \alpha_i}{\sum_{i=1}^n W_i a_i c_z R_{di}}.$$

Then, the coefficient of horizontal critical acceleration ( $k_{h,y}$ ) can be determined by the ratio of the summation of horizontal inertial force to the total weight of sliding body, as

$$k_{h,y}(t) = \frac{\sum_{i=1}^n k_{h,\max}(t) c_z a_{hi} W_i}{\sum_{i=1}^n W_i}. \quad (14)$$

Compared to the traditional method, it can be seen that (13) and (14) are both closed-form solutions and can be used to directly determine the coefficient of horizontal critical acceleration ( $k_{h,y}$ ) without any iterative process.

For the convenience of applications, the circular failure mechanism is used in this paper and several necessary transformations are performed. Considering the failure mechanism of circular slip surface, the components of driving angular acceleration ( $\theta_{ave}$ ) and the critical angular acceleration ( $\theta_y$ ) can be derived and expressed as

$$\theta_{ave}(t) = k_{h,ave}(t) \frac{(y_g - y_c)}{R_g^2}, \quad (15)$$

$$k_{h,ave}(t) = \frac{\sum_{i=1}^r m_i a_{hi}(t)}{\sum_{i=1}^r W_i}, \quad (16)$$

$$\theta_y(t) = \frac{\sum_{i=1}^n k_{h,\max}(t) g c_z a_{hi} W_i (y_g - y_c)}{\sum_{i=1}^n W_i R_g^2}, \quad (17)$$

where  $R_g$  is the distance between the centroid of sliding body and the center of the slip surface, respectively;  $y_g$  and  $y_c$  are the vertical coordinate of the slip surface centroid and the center of the slip surface, respectively;  $m_i$  is the lump mass at node  $i$ ;  $a_{hi}$  is the horizontal acceleration of node  $i$  determined by dynamic response analysis; and  $r$  is the number of nodes included in the slip surface.

Then the accumulation of angular sliding displacement ( $\theta$ ) can be obtained by the double integral of (18).

$$\ddot{\theta}(t) = [\theta_{ave}(t) - \theta_y(t)]g, \quad (18)$$

$$\theta = \iint \ddot{\theta} dt, \quad (19)$$

$$S = \theta \cdot R, \quad (20)$$

where  $\ddot{\theta}(t)$  is the time history angular sliding acceleration.

Based on the abovementioned description and formulations, the step-by-step numerical procedure for the modified Newmark sliding displacement approach is outlined as follows:

- (1) Determine the location of critical circular slip surface by (9), coupling with available optimized method
- (2) Conduct the dynamic response analysis and get time history vertical inertial force acting at the centroid of each soil slice by (12)
- (3) Determine the cyclic shear strength mobilized at the bottom of soil slices according to (6~8), and get the horizontal critical acceleration of potential sliding body using (13) and (14)
- (4) Transform horizontal critical acceleration and driving acceleration into angular driving and critical acceleration using (17) and (18), respectively
- (5) Repeat steps (2), (3), and (4) until the end of earthquake shaking and determine the accumulation of sliding displacement using (20)

## 5. Verification and Application

**5.1. Example 1.** A virtual core rock-fill dam with a height of 100 m is investigated. The cyclic shear strength for different number of cycles and the static shear strength are shown in Table 3. The input acceleration time history in the horizontal direction and vertical direction is presented in Figure 3. The amplitude of the acceleration is 0.283 g in the upstream-to-downstream direction, and 0.19 g in the vertical direction. The  $E-\mu$  model and the equivalent linear analyses are performed to estimate the initial stress state and dynamic response of the dam [20]. The parameters used in static and dynamic analyses are listed in Table 5. As shown in Figure 4, the pseudostatic factor of safety and the location of the potential circular slip surface in the upstream dam slope are obtained by the Bishop limited equilibrium method. The Newmark sliding displacement analyses are performed, respectively, by the presented method and the traditional method developed by Makdisi and Seed [5]. Since in the presented method, the two factors, that is, cyclic shear strength and time history vertical acceleration, are considered simultaneously and their effects are coupled. In order to clarify the effect of each factor, a contrast analysis is performed, where only the effect of cyclic shear strength is considered and that of the time history vertical acceleration is ignored.

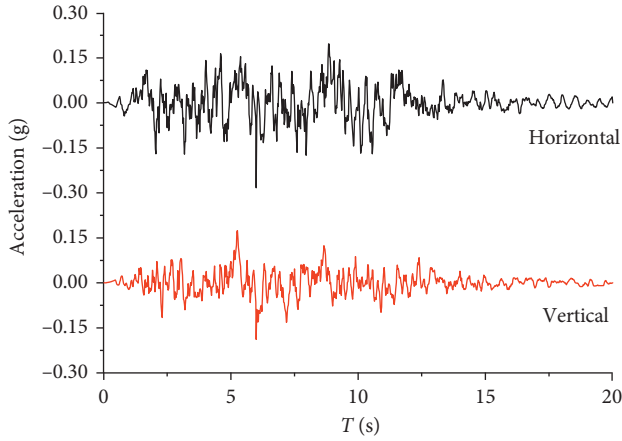


FIGURE 3: Accelerogram of input motion.

TABLE 5: Parameters of static and cyclic shear strength.

Materials	$c'$ (kPa)	$\phi'$ ( $^{\circ}$ )	$N$ (times)	$\tau_{fs0}$ (kPa)	$\tan \phi_{d0}$	$\zeta$ (kPa)	$\beta$
Shell material	5	36	12	0	0.253	115.6	1.621
			20	8.05	0.193	107.8	1.25
Core material	86.6	23.7	12	83.67	0.333	92.9	0.417
			20	83.01	0.320	91.6	0.41

The coefficients of horizontal critical acceleration and accumulation of sliding displacement obtained by the three different analyses are listed in Table 6. It is shown that the critical acceleration obtained by the modified method is remarkably lower than that obtained from the traditional method. The maximum difference could reach 70%, as the cyclic shear strength and time history vertical acceleration are taken into consideration simultaneously. Consequently, the difference in the accumulation of sliding displacement is also considerable. The amplitude of accumulation of sliding displacement obtained from the modified method considering the effects of cyclic shear strength and time history vertical acceleration is nearly three times of that obtained from the traditional method. In addition, from Table 6, it is clear that the accumulation of sliding displacement obtained from the contrast analysis is nearly two times of that from the traditional method, but the difference of critical acceleration and factor of safety determined by the two methods is minor. Thus, it is implied that the prediction of sliding displacement based on cyclic shear strength is important to evaluate the performance of rock-fill dams under strong earthquakes, even if the factor of safety determined based on both static shear strength and cyclic shear strength satisfies the requirements of seismic design.

Figure 5 provides the time history horizontal critical acceleration obtained from the three analyses. It is clear that the critical accelerations determined by the Makdisi and Seed method and the contrast analysis remain unchanged during the earthquake shaking. On the contrary, fluctuation of critical acceleration time history obtained from the modified method can be observed and it is correlated with the input vertical acceleration time history. Furthermore, it

is noted that the minimum critical acceleration obtained from the modified method is nearly 1/3 of that from the Makdisi and Seed method.

As shown in Figure 6, the modified Newmark sliding displacement method gives the highest sliding displacement during the earthquake shaking. It can be observed that the accumulation of sliding displacement obtained by the traditional method stops growing at 10 seconds, whereas the growing trend stops at 15 seconds for the modified Newmark sliding displacement analysis. Compared with the traditional method, the times of sliding episodes and increment of sliding displacement in one sliding episode presented in the modified Newmark sliding displacement analyses are bigger because of the lower time history critical acceleration. It implies that the modified method predicts a sliding episode, whereas the traditional analysis predicts dam slope stability, as the value of driving acceleration lies between the two critical accelerations. In addition, from the engineering point of view, the accumulation of sliding displacement, which is regarded as a key index for the safety evaluation of high core rock-fill dams subjected to design earthquake, obtained by the traditional method tends to be unsafe as the effects of cyclic strength and time history vertical acceleration on the critical acceleration are ignored.

**5.2. Example 2.** The following is a practical core rock-fill dam of 150 m in height which will be built on deep overburden foundation. It is noted that the deep overburden layer of the dam site is thicker than 500 m and has a weak sand inclusion layer with a thickness of 20 m. The maximum cross section and finite element mesh are provided in Figure 7. The dam is mainly composed of core, shell, sand layer, and sandy gravel. The simulation of filling and water storage is conducted by static analysis with the  $E-\mu$  model, and the equivalent linear analyses are performed to obtain the response of acceleration and dynamic shear stress. As shown in Figure 7, the pseudostatic factor of safety and the locations of the potential circular slip surfaces in the upstream and downstream dam slopes are obtained by the Bishop limited equilibrium method. The parameters of static analysis, dynamic analysis, and cyclic shear strength of sand layer are presented in Tables 4 and 7 and obtained from the laboratory triaxial compression test. The design ground motions were selected based on in situ investigations. The acceleration time histories in the horizontal direction and vertical direction are plotted in Figures 8 and 9, respectively, with amplitudes of 0.535 g and 0.36 g, respectively. In the time marching process of equivalent linear analyses, the duration of the earthquake excitation (40 seconds) is divided into 15 periods.

Based on the results obtained from the dynamic triaxial tests and dynamic response analysis, the distribution of ratio of cyclic shear strength to static shear strength ( $\tau_{fs}/(c' + \sigma'_{f0} \tan \phi')$ ) for the sand layer and sand gravel is provided in Figure 10. It is shown that the cyclic shear strength of most of the soil elements located in the sand

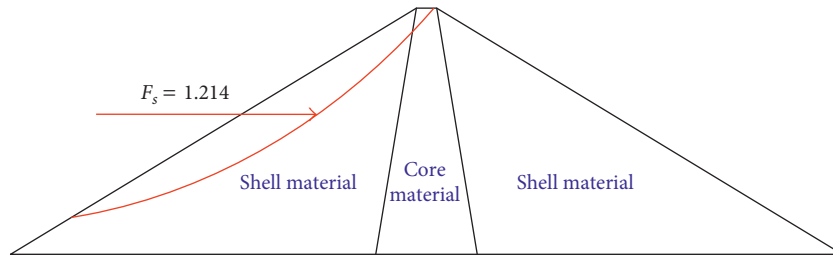


FIGURE 4: Potential circular slip surface and factor of safety of dam under design earthquake.

TABLE 6: Horizontal critical acceleration, sliding displacement, and factor of safety.

Items	Traditional method <sup>1</sup>	Contrast analysis <sup>2</sup>	Modified method <sup>3</sup>
$k_{h,y}$ (g)	0.152	0.134	0.045 <sup>#</sup>
$s$ (cm)	24.2	42.1	68.4
Factor of safety	1.285	1.214	1.214

<sup>1</sup>The traditional method is the approach in which the static shear strength is used. <sup>2</sup>The contrast analysis is the approach in which only the cyclic shear strength is considered in the modified method. <sup>3</sup>The modified method is the approach in which the cyclic shear strength and time history vertical acceleration are considered simultaneously. <sup>#</sup>The minimum critical acceleration during the earthquake shaking.

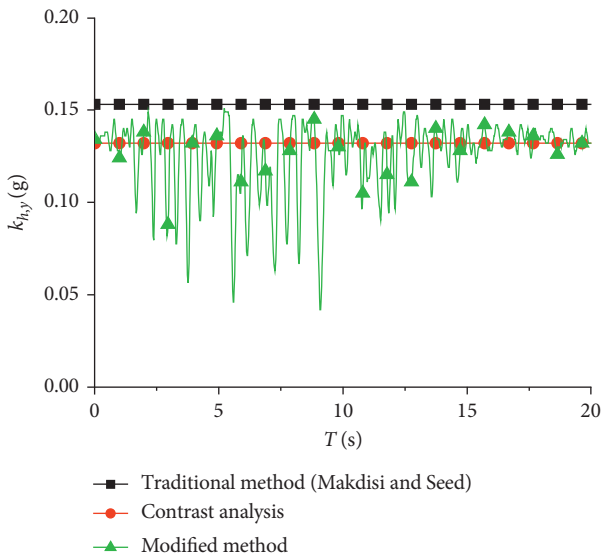


FIGURE 5: Time history horizontal critical acceleration.

layer and sand gravel layer is lower than the static shear strength, but it is noted that the liquefaction does not occur. The difference between the static shear strength and cyclic shear strength is noticeable, and the maximum difference at the toe of the upstream dam is around 50%. Thus, considering the great part of failure surface located in the sand layer and sand gravel layer as shown in Figure 7, the impact of cyclic shear strength on the critical acceleration and sliding displacement should be considered.

The modified Newmark sliding displacement method is used to determine the time history driving acceleration,

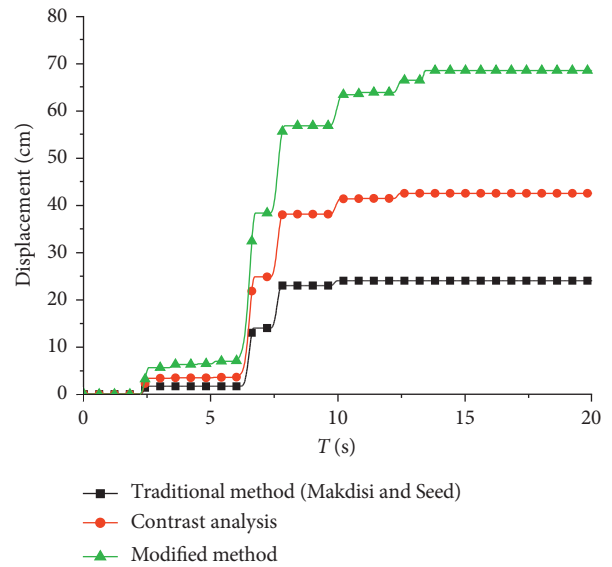


FIGURE 6: Time history sliding displacement.

critical acceleration, and accumulation of sliding displacement, with the results shown in Figures 11–13. Fluctuation of the critical acceleration time history can be observed because of that considering the effect of time history vertical acceleration which is obtained from equivalent linear dynamic response analysis. There are, respectively, two and four obvious intersections between the angular critical acceleration and angular driving acceleration as shown in Figures 11 and 12. It can be observed that the minimum of time history critical acceleration of slip surface in downstream dam slope which corresponds to factor of safety of 0.93 which is smaller than that of slip surface in upstream dam slope which corresponds to factor of safety of 0.88. Meanwhile, the time history driving acceleration of slip surface in the upstream dam slope is bigger than that of slip surface in downstream dam slope during the earthquake shaking. As shown in Figure 13, the magnitudes of sliding displacements of slip surface in upstream dam slope and downstream dam slope are 34.0 cm and 5.5 cm, respectively. It is noted that the increment of sliding displacement of slip surface in upstream dam slope occurred in the first sliding episode is about 32 cm and makes an offer of 95% of total accumulation of sliding displacement. This can be contributed to the remarkable difference of driving acceleration and critical acceleration for the reason that the effects of cyclic shear strength, time

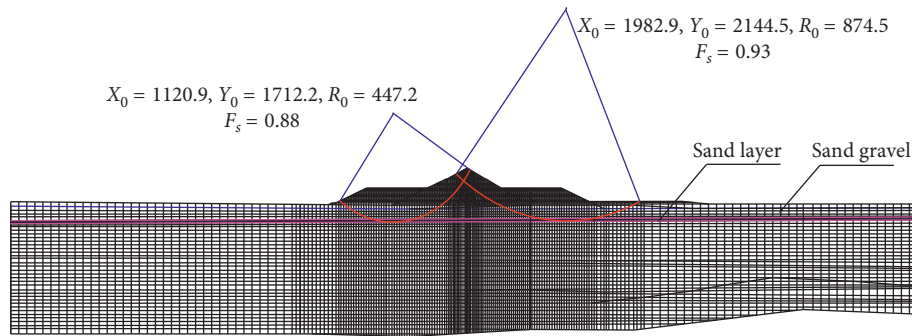


FIGURE 7: Cross section of the dam and potential slip surfaces.

TABLE 7: Parameters of the  $E$ - $\mu$  model and equivalent linear model.

Materials	$r$ (g/cm <sup>3</sup> )	$c'$ (kPa)	$\phi'$ (°)	$k$	$n$	$R_f$	$G$	$F$	$D$	$k_{ur}$	$k_1$	$n_1$
Core	2.2	35	33	447	0.4	0.75	0.39	0.05	1.9	900	1600	0.53
Shell	2.3	0	45	1050	0.37	0.71	0.3	0.09	5.8	2100	4600	0.42
Sand layer	1.55	40	32	280	0.43	0.81	0.42	0.13	2	600	600	0.5
Sand gravel	2.27	0	47	836	0.35	0.79	0.32	0.1	4.8	1700	4544	0.35

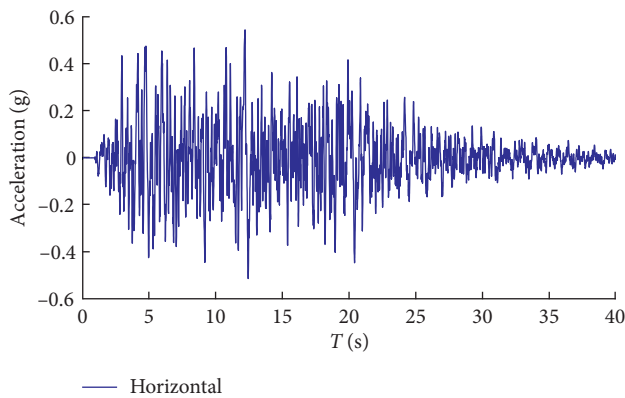


FIGURE 8: Accelerogram of horizontal input motion.

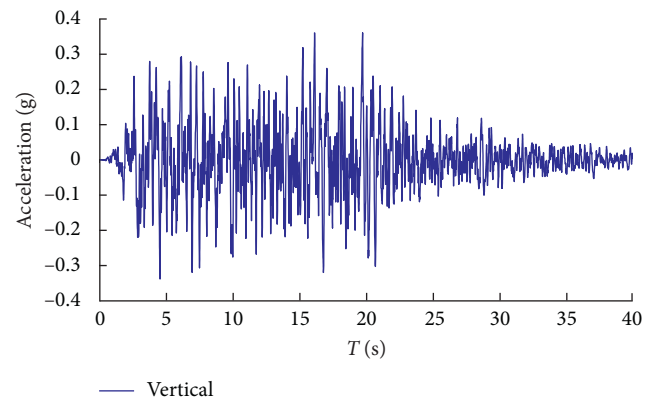


FIGURE 9: Accelerogram of vertical input motion.

history vertical acceleration, and location of flexible sliding body. Consequently, it is justified that the effects of cyclic shear strength and time history vertical acceleration on the critical acceleration and sliding displacement for flexible sliding body are considerable, especially to the foundation of the rock-fill dams with a weak sand layer.

## 6. Conclusions

A modified Newmark-type methodology for sliding deformation analysis of rock-fill dams subjected to strong earthquake is developed. The effects of cyclic shear strength and time history vertical acceleration on the sliding displacement are considered in detail. Based on detailed comparisons between the proposed method and traditional method (Makdisi and Seed's method), it can be seen that the effect of earthquake-induced reduction of shear strength (cyclic shear strength) and time history vertical acceleration

on the critical acceleration and sliding displacement is remarkable. On the other hand, the necessity and feasibility of the proposed method is also verified by the application to the analysis of a real core rock-fill dam which will be built on deep overburden foundation with weak sand layer. It is shown that the cyclic shear strength is generally lower than the static shear strength in the weak sand layer as the liquefaction does not occur during a strong earthquake shaking and the time history vertical acceleration can play an important role in the dam stability evaluation based on the Newmark-type sliding displacement analysis.

As it is known that reliable and convenient prediction of earthquake-induced sliding displacement is crucial for the seismic design of rock-fill dams, it is shown from the numerical examples that there is noticeable difference between the displacement obtained by taking into account the effect of cyclic shear strength and time history vertical acceleration and the displacement obtained by the traditional Newmark

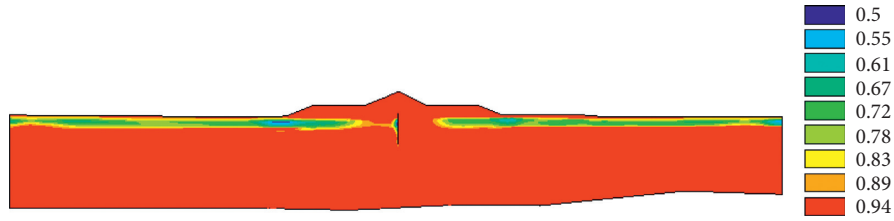


FIGURE 10: The distribution of ratio of cyclic shear strength to static shear strength.

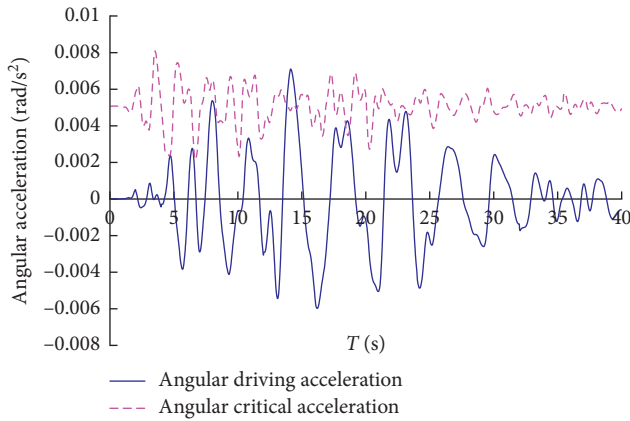


FIGURE 11: Time history angular driving acceleration and critical acceleration of slip surface in upstream dam slope.

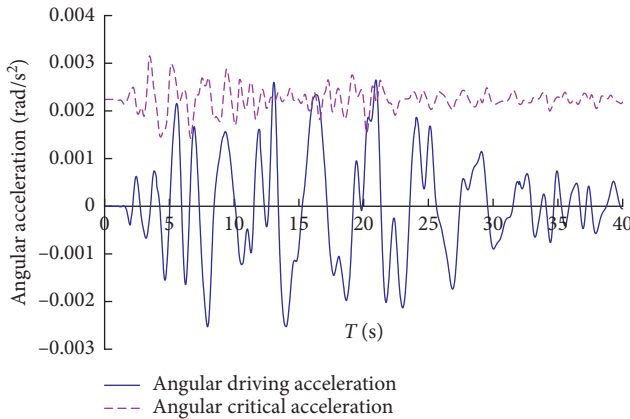


FIGURE 12: Time history angular driving acceleration and critical acceleration of slip surface in downstream dam slope.

method, and this would exert important consequences in the seismic stability analysis of a rock-fill dam:

- (1) When the liquefaction-induced damage does not occur, as the cyclic shear strength is significantly lower than the static shear strength for rock-fill materials and weak sand layer, the analysis presented herein predicts a general failure of dam slope, whereas the traditional Newmark-type analysis would predict dam slope stability.
- (2) In the high rock-fill dams, the time history of vertical acceleration in the flexible sliding body can play an

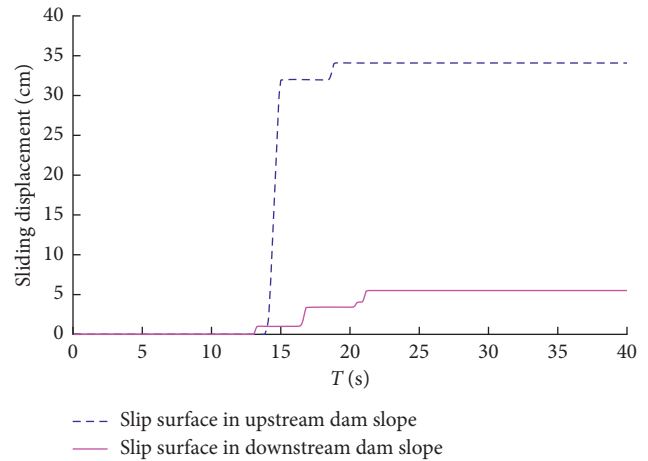


FIGURE 13: Time history sliding displacements of slip surfaces in upstream and downstream dam slopes.

important role in the Newmark-type sliding displacement analysis, and the traditional method could provide unsafe prediction of seismic stability of rock-fill dams.

In a word, the proposed methodology for sliding displacement analysis of rock-fill dams as the liquefaction would not occur leads to more realistic evaluation of the permanent displacement, and it provides a promising alternative to routine seismic design and evaluation of the mitigation measures for high rock-fill dam with a high level of confidence.

### Conflicts of Interest

The authors declare that they have no conflicts of interest.

### Acknowledgments

The financial support by the National Key Research and Development Program of China through Grant no. 2017YFCC0404904, the National Nature Science Foundation of China (51579033), the National Key Basic Research Program of China (no. 2013CB036404), and the Public Service Sector R&D Project of Ministry of Water Resource of China (no. 201501035) and experimental data and technological supports from IWHR Laboratory are gratefully acknowledged.

## References

- [1] A. A. Farghaly, "Evaluation of seismic performance of buildings constructed on hillside slope of Doronka village-Egypt," *ISRN Civil Engineering*, vol. 2014, Article ID 940923, 13 pages, 2014.
- [2] J. Song, Y. Gao, A. Rodriguez-Marek, and T. Feng, "Empirical predictive relationships for rigid sliding displacement based on directionally-dependent ground motion parameters," *Engineering Geology*, vol. 222, pp. 124–139, 2017.
- [3] Y. G. Zhou, J. Chen, Y. She, and A. M. Kaynia, "Earthquake response and sliding displacement of submarine sensitive clay slopes," *Engineering Geology*, vol. 227, pp. 69–83, 2017.
- [4] N. M. Newmark, "Effects of earthquakes on dams and embankments," *Geotechnique*, vol. 15, no. 2, pp. 139–160, 1965.
- [5] F. I. Makdisi and H. B. Seed, "Simplified procedure for estimation dam and embankment earthquake induced deformations," *Journal of the Geotechnical Engineering Division (ASCE)*, vol. 104, no. 7, pp. 849–868, 1978.
- [6] H. B. Seed and R. V. Whitman, "Design of earth retaining structures for dynamic loads," in *Proceedings of the Lateral Stress Ground and Design of Earth Retaining Structures (ASCE)*, pp. 103–147, Ithaca, NY, USA, June 1970.
- [7] W. Wenshao, *The Characteristic of Cyclic Strength and Liquefaction of Soil*, China Electric Power Press, Beijing, China, 1996.
- [8] Z. Li and M. Luan, "Evaluation of aseismic stability of soil embankments considering cyclic degradation of soil strength," *Rock and Mechanics*, vol. 25, no. 2, pp. 409–417, 2004.
- [9] S. Y. Wang and X. B. Lu, "Post-cyclic strength degradation of undisturbed and remolded marine silty clay," in *Proceedings of the 18th International Offshore and Polar Engineering Conference (ISOPE 2008)*, Vancouver, Canada, July 2008.
- [10] A. F. L. Hyde and S. J. Ward, "The effect of cyclic loading on the undrained shear strength of silty clay," *Marine Geotechnology*, vol. 6, no. 3, pp. 299–314, 1986.
- [11] C. Xu, J. Jia, Y. Sun, X. Du, and Y. Gao, "Cyclic strength of saturated sand under bi-directional cyclic loading," *Engineering Geology*, vol. 227, pp. 23–31, 2017.
- [12] N. Mononobe, "Effects of vertical acceleration and theory of vibration," *Proceedings of the Japan Society of Civil Engineers*, vol. 10, no. 5, pp. 1063–1094, 1924.
- [13] H. I. Ling, D. Leshchinsky, and M. Yoshiyuki, "Soil slopes under combined horizontal and vertical seismic accelerations," *Earthquake Engineering and Structural Dynamics*, vol. 26, no. 12, pp. 1231–1241, 1997.
- [14] J. L. Huang, W. Z. Wang, and H. J. Xue, "Dynamic analysis of seismic stability of slopes," *Earthquake Engineering and Engineering Vibration*, vol. 17, no. 4, pp. 113–122, 1997.
- [15] N. M. Newmark and W. J. Hall, *Earthquake Spectra and Design*, Earthquake Engineering Research Institute, Berkeley, CA, USA, 1982.
- [16] J. Ingles, J. Darrozes, and J.-C. Soula, "Effects of the vertical component of ground shaking on earthquake-induced landslide displacements using generalized Newmark analysis," *Engineering Geology*, vol. 86, no. 2-3, pp. 134–147, 2006.
- [17] K. Jinman and M. Nicholas Sitar, "Direct estimation of yield acceleration in slope stability analyses," *Journal of Geotechnical and Geoenvironmental Engineering*, vol. 130, no. 1, pp. 111–115, 2004.
- [18] L. Li, S.-C. Chi, and G. Lin, "The complex method based on ant colony algorithm and its application to the slope stability analysis," *Chinese Journal of Geotechnical Engineering*, vol. 26, no. 5, pp. 691–696, 2004.
- [19] H. Li, H. Zhong, Z. Yan, and X. Zhang, "Particle swarm optimization algorithm coupled with finite element limit equilibrium method for geotechnical practices," *Mathematical Problems in Engineering*, vol. 2012, Article ID 498690, 14 pages, 2012.
- [20] H. Li, S. Chi, G. Lin, and H. Zhong, "A modified approach for determination of nonlinear properties in seismic response analyses for 200 m high core rock-fill dams," *Canadian Geotechnical Journal*, vol. 45, no. 8, pp. 1064–1072, 2008.